The synthesis and spectroscopy of dipyrrins and their metal complexes

A thesis submitted in the partial fulfilment of the requirements for the degree of

Doctor of Philosophy
in Chemistry

MASSEY UNIVERSITY

Tracey Maree McLean

2012

For Mum and Dad

Abstract

Dipyrrin ligands can be considered as 'half-porphyrins'. They absorb light in the visible region due to a strongly allowed $\pi-\pi^*$ transition. With the energy crisis being one of the most important issues of our time, the strong absorption in the visible region endows dipyrrinato complexes with promise in solar energy conversion applications. The focus of this project was to undertake some fundamental synthesis and spectroscopy of dipyrrin ligands and dipyrrinato complexes for their applications in photochemical devices.

The well-known characteristics of Ru(II)-bipyridine chemistry were combined with the light absorbing properties and synthetic versatility of dipyrrin ligands to prepare and test a range of Ru(II)-dipyrrinato-bipyridine complexes as dyes for applications in dye-sensitised solar cells. The preliminary results of the solar cell measurements show evidence that the Ru(II)-dipyrrinato-bipyridine complexes show promise as light harvesters in solar energy conversion applications. A series of Re(I)-dipyrrinato complexes has also been designed and prepared for potential applications as catalysts in carbon dioxide reduction.

Metallodipyrrin complexes also exhibit strong exciton coupling. A library of transition metal dipyrrinato complexes has been prepared to investigate the exciton interactions in dipyrrin systems. Understanding the exciton interactions in dipyrrin systems and the ability to control the exciton interactions are desirable for improving the solar energy conversion efficiency of dye-sensitised solar cells containing Ru(II)-dipyrrinato-bipyridine complexes as the dye.

Raman spectroscopy and more specifically resonance Raman, as a technique for probing the excited state of dipyrrinato complexes, has largely been overlooked in the literature. Therefore the spectroscopy aspect of this thesis has a central focus on the Raman spectroscopy of dipyrrins, including the first full characterisation of dipyrrin ligands by Raman spectroscopy at a variety of wavelengths (visible and near infrared). Strong resonance enhancement was observed for the dipyrrin ligands, which lays the foundation for fundamental single-molecule SERS studies but also for a broad range of bioanalytical applications.

Acknowledgements

I would like to take the opportunity to thank the large number of people who have contributed to my PhD research and thesis. Firstly, I would like to thank my supervisors Associate Professor Shane Telfer and Dr Mark Waterland for their enthusiasm, encouragement, and patience throughout my research years. Thanks for challenging me when I needed it but most importantly always being there when I needed help or advice. Thanks also for the time and energy you have put into my project.

Thanks also to all past and present members of the Telfer/Waterland research empire and other lab colleagues. Many interesting discussions were had over the past few years, some even related to chemistry. Specifically I must thank Dr Carl Otter for the helpful chemistry discussions relating to my project and Dave Lun for being the all-round go to guy for assistance with lab equipment, mass spectrometry, and many other chemistry problems.

A special mention must also go to Dr Pat Edwards for assistance with specialised NMR experiments, Dr Wayne Campbell and Dr Vyacheslav Filichev for their assistance with establishing the new fluorimeter protocol, Nessha Wise for her assistance with undertaking electrochemistry experiments and Professor Simon Hall for answering many electrochemistry related questions. I must also thank Jamie Withers for assisting me with preparing some of the figures presented in this thesis.

I must also acknowledge Dr Matthias Lein (Victoria University of Wellington) for always being available for assisting with the DFT calculations and Professor Keith Gordon (University of Otago) for allowing laboratory visits for data collection, Dr Attila Mozer and his students (Intelligent Polymer Research Unit, University of Wollongong) and Professor Yong Soo Kang and his students (Energy Materials Lab, Hanyang University) for solar cell measurements.

I would like to acknowledge the financial support from Massey University for a Doctoral scholarship and the MacDiarmid Institute to allow me to undertake this project; and the Institute of Fundamental Sciences Postgraduate travel fund, Royal Society of

New Zealand travel grants and Claude McCarthy Fellowship for travel awards to conferences in Dunedin and Japan, and a research visit to the University of Hong Kong.

I have utilised the expertise of many past and present technical and departmental staff from the Institute of Fundamental Sciences and I would like to thank them for their assistance during my research and thesis writing.

Finally, I must thank my family and partner (Kyle) for their support and encouragement over the last few years, and particularly thanks to Mum for flying me home for long weekends on the farm. As many of my friends will know writing a thesis is exceptionally difficult and stressful so thanks for the support when I needed it and the distraction when I needed a break.

Fear is temporary, achievement is permanent

Table of Contents

Abbreviations

acac	acetylacetonato
aq	aqueous
Ar	aromatic
ATR	attenuated total reflection
bipy	2,2'-bipyridine
BODIPY	boron difluoride complex of dipyrrin
Calcd	calculated
CD	circular dichroism spectroscopy
$CDCl_3$	deuterated chloroform
conc.	concentrated
COSY	correlation spectroscopy
dcb	4,4'-dicarboxy-2,2'-bipyridine
DDQ	2,3-dichloro-5,6-dicyanobenzoquinone
DFT	density functional theory
DIPEA	*N*,*N*-diisopropylethylamine
dmcb	4,4'-dimethoxycarbonyl-2,2'-bipyridine
DMF	*N*,*N*-dimethylformamide
DMSO	dimethyl sulfoxide
DSSC	dye-sensitised solar cell
EDD	electron density difference
EF	enhancement factor
en	1,2-diaminoethane
equiv.	equivalent
ESI	electrospray ionisation
EtOH	ethanol
FF	fill factor
FT	fourier transform
FWHM	full-width half maximum
hfacac	hexafluoroacetylacetonato
HOMO	highest occupied molecular orbital

HPLC	high performance liquid chromatography
IC	internal conversion
IR	infra-red spectroscopy
ISC	intersystem crossing
ITO	indium tin oxide
J_{sc}	short circuit current
LUMO	lowest unoccupied molecular orbital
MAD	mean average deviation
MALDI	matrix assisted laser desorption ionisation
MeCN	acetonitrile
MeOH	methanol
MLCT	metal-to-ligand charge transfer
NEt_3	triethylamine
NMR	nuclear magnetic resonance
PDT	photodynamic therapy
Ph	phenyl
ppm	parts per million
RR	resonance Raman spectroscopy
RRIA	resonance Raman intensity analysis
RT	room temperature
S	singlet state
SERS	surface-enhanced Raman spectroscopy
SE(R)RS	surface-enhanced (resonance) Raman spectroscopy
SM-SERS	single molecule surface-enhanced Raman spectroscopy
T	triplet state
TD-DFT	time-dependent density functional theory
TFA	trifluoroacetic acid
THF	tetrahydrofuran
TLC	thin layer chromatography
TPP	tetraphenyl porphyrin
UV-Vis	ultraviolet-visible spectroscopy
V_{oc}	open circuit voltage
μ	transition dipole moment
$\pi-\pi^*$	pi-to-pi star

All the work in this thesis was completed by Tracey M. McLean

except

Chapter 2

- Solid and solution state non-resonance Raman data of **34** were collected by Dr Cushla McGoverin at the University of Otago.
- Time-dependent DFT calculations of **34** were undertaken with the assistance of Dr Mark Waterland.
- TEM images of silver nanoparticles were collected at the Manawatu Microscopy and Imaging Centre with the assistance of Mr Doug Hopcroft.

Chapter 3

- After initial attempts of optimising the geometry of **43**, Dr Matthias Lein (Victoria University of Wellington) was contacted for assistance. He subsequently undertook all DFT and time-dependent DFT calculations of **43**.
- Mr Graham Freeman synthesised the azadipyrrin ligand **44**.
- With the exception of **38** and **44** all the crystal structures presented were determined by Associate Professor Shane Telfer.

Chapter 4

- Serena Smalley established the general synthetic protocol for Ru(II)-dipyrrinato complexes including the synthesis of **46** and **47**.
- Associate Professor Shane Telfer synthesised Ru(II)-dipyrrinato complex **46b**.
- All DFT calculations of **46**-**H** including the Mulliken analysis were undertaken by Dr Mark Waterland.
- All DFT calculations of **46** were undertaken by Sam Lind (University of Otago).
- Resonance Raman data at excitation wavelengths 413 nm, 444 nm and 532 nm were collected by Sam Lind and Deirdre Cleland (University of Otago).
- Solid state absorption spectroscopy on TiO_2 or NiO, device fabrication and solar cell testing were undertaken by members of Dr Attila Mozer's research group (Intelligent Polymer Research Institute, University of Wollongong) and

Professor Yong Soo Kang's research group (Energy Materials Lab, Hanyang University).

Chapter 5

- Janice Moody established the general synthetic protocol for Re(I)-dipyrrinato complexes including the synthesis and characterisation of **59**, **60**, **64**, and **70**.
- Serena Smalley developed the synthesis of dipyrrin ligand **61**.

Publications by Tracey M. McLean related to this PhD thesis:

- McLean, T. M., Waterland, M. R., Telfer, S. G., Gordon, K. C., McGoverin, C. M., Raman spectroscopy of dipyrrins: non-resonant, resonant, and surface-enhanced cross-sections and enhancement factors. *J. Raman Spec.* **2011**, 42, 2154-2164.
- Telfer, S. G., McLean, T. M., Waterland, M. R., Exciton coupling in coordination complexes. *Dalton Trans*. **2011**, 40, 3097-3108.
- Hall, J. D., McLean, T. M., Smalley, S. J., Waterland, M.R., Telfer, S.G., Chromophoric dipyrrin complexes capable of binding to TiO_2: synthesis, structure and spectroscopy. *Dalton Trans*. **2010**, 39, 437-445.
- McLean, T. M., Cleland, D.M., Lind, S.J., Gordon, K.C., Telfer, S. G., Waterland, M. R., Strongly absorbing $\pi-\pi^*$ states in heteroleptic dipyrrin/2,2'-bipyridine ruthenium complexes: excited-state dynamics from resonance Raman spectroscopy. *Chem-Asian J*. **2010**, 5, 2036-2046.
- McLean, T. M., Moody, J. L., Waterland, M. R., Telfer, S. G., Luminescent Re(I)-dipyrrinato complexes. *Inorg. Chem.* **2012**, 51, 446-455.

Chapter 1

Introduction

1.1 Perspective

Approximately 85% of the world's energy needs is met by fossil fuels. In addition to the progressive decline in fossil fuel reserves, the burning of fossil fuels results in pollution and production of greenhouse gases associated with global warming. Global energy consumption is expected to double by mid-century and triple by the turn of the century. Therefore the energy crisis has become the most important issue of this century.[1-5]

The sun, which provides 120,000 terawatts (TW) of power, could provide the solution to the global energy crisis.[4] Just one hour of sunlight striking Earth provides more energy than is consumed by humans in one year.[5] Nonetheless, sunlight is both diffuse and intermittent and therefore conversion to useful energy forms requires capture, concentration and storage of the energy.[3, 4] None of these requirements can be met by current technologies. Addressing these challenges has become one of the most urgent and important areas of modern day science.[6, 7]

Photosynthetic organisms have evolved to capture sunlight very efficiently to drive one of the key reactions to sustain life (equation 1.1). In plants, photosynthesis provides an energy source for the survival of the plant by converting and storing the energy in chemical bonds as carbohydrates. Indirectly, photosynthesis provides a food source for humans as we consume plant biomass.[2, 3, 8] The oxygen produced during photosynthesis is released to the atmosphere.[8]

$$6CO_2 + 6H_2O \xrightarrow{h\nu} \underset{\text{carbohydrate}}{C_6H_{12}O_6} + O_2 \qquad (1.1)$$

At the centre of photosynthesis is the splitting of water by sunlight into oxygen and hydrogen (equation 1.2).[9] This process must be sensitised because water cannot be

electronically excited by solar energy.[4, 10] The overall transformation involves multiple proton and electron transfers and thus a considerable thermodynamic barrier to overcome.[11]

$$\begin{aligned} 4H^+ + 4e^- &\longrightarrow 2H_2 \\ 2H_2O &\longrightarrow 4H^+ + 4e^- + O_2 \\ \hline 2H_2O &\xrightarrow{h\nu} 2H_2 + O_2 \qquad E^\circ = -1.23\ V \end{aligned} \tag{1.2}$$

It should be noted that the redox couples expressed in equation 1.2 are pH dependent (pH = 0) which is not a desirable condition for photocatalytic water splitting.

Hydrogen is often considered to be the ideal fuel to power the future since its combustion generates heat and water.[3, 4, 12, 13] However, the problems associated with generation, storage, and transport of H_2 are significant.[13]

The chemist's challenge is to design a system that mimics the photosynthetic machinery of plants to split water to produce hydrogen and oxygen.[2] Such a system needs to operate at room temperature and use earth abundant materials.[3] This is a very challenging goal.[3, 14] A number of strategies for light driven water splitting is currently being investigated.[2, 3, 9, 15, 16]

Photovoltaic technology is an alternative solar energy conversion strategy that involves the direct conversion of light into electrical energy.[9] Traditional photovoltaic devices are silicon based semiconductors (p-n type semiconductors). This requires high purity crystalline silicon.[4, 5, 7] Efforts into new photovoltaic devices are continuing with thin film designs using cheaper materials for large scale production.[9]

Dye-sensitised solar cells, or Grätzel cells[17], are a more recent class of photovoltaic technology. These cells are based on the sensitisation of wide bandgap semiconductors by dyes which absorb significant fractions of sunlight. The maximum conversion efficiency is currently ~10-11%.[18, 19] However, the efficiency is limited by the long term stability of each of the components of the solar cell.[20, 21] Extensive research into improved efficiencies and long term stability are on-going.[21, 22] With improved conversion efficiencies and long term stability these devices have the potential to be viable cost effective alternatives to silicon based semiconductors.[20]

1.2 Dipyrrins and their complexes

1.2.1 General background and structure of dipyrrins

Dipyrromethene ligands were first reported by Hans Fischer in 1937.[23] In recent literature they are most commonly referred to as dipyrrin ligands and this name is used hereafter. Dipyrrin ligands can be roughly considered as bispyrrolic "half porphyrins" and historically were employed as the synthetic precursors to porphyrins.[24] The basic dipyrrin unit with IUPAC numbering and the historical porphyrin nomenclature (**1**), the core porphyrin structure (**2**) are depicted in Figure 1.1. More recently, dipyrrin chemistry has focussed on the coordination chemistry of dipyrrinato ligands[24] (**3**) and the BF_2-dipyrrinato compounds (BODIPY) (**4**) given their useful photophysical properties.[25]

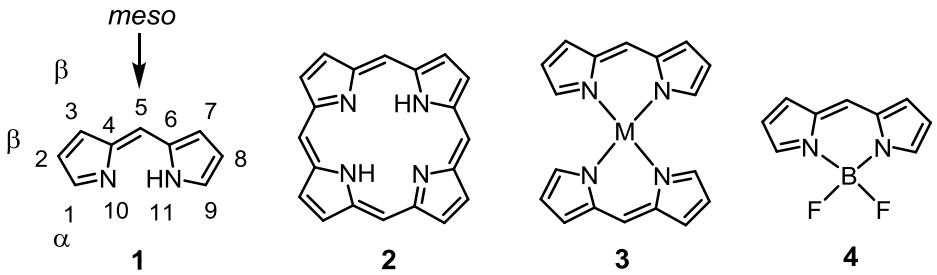

Figure 1.1. Structure and IUPAC numbering system of the basic dipyrrin unit with historical porphyrin nomenclature (**1**), structure of a free base porphyrin (**2**), dipyrrin chelate (**3**), and BODIPY complex (**4**).

Following historic pyrrole nomenclature and the naming of porphyrins, positions 1 and 9 of the dipyrrin framework are sometimes referred to as the α-positions and positions 2, 3, 7, and 8 are referred to as the β-positions, while position 5 is often termed the *meso* position (Figure 1.1). The nature and number of substituents on the dipyrrin significantly affect the stability and reactivity. For example, fully unsubstituted dipyrrin **1** is reported to be unstable due to the susceptibility of electrophilic and nucleophilic attack.[24] Incorporating alkyl substituents at positions 1-3,7-9 prevents electrophilic and nucleophilic attack. By incorporating an aryl substituent at the 5-position, dipyrrins can be isolated with only hydrogen substituents in positions 1-3,7-9.[24]

1.2.2 Synthesis of dipyrrins

The four major synthetic pathways to dipyrrins have been summarised by Brückner *et al*.[26] Of these synthetic pathways the acid-catalysed condensation of 2-formyl pyrrole (**5**) with pyrrole **6** is the most common. This reaction yields a 5-unsubstituted dipyrrin (**7**) isolated as the HBr salt (Figure 1.2). These reactions are generally high yielding but can be limited by purification.[24] Alternatively, 5-substituted dipyrrins (**7**) can be prepared by the acid-catalysed condensation of two equivalents of an unsubstituted pyrrole **6** and a carboxylic acid or an acid halide (Figure 1.2).

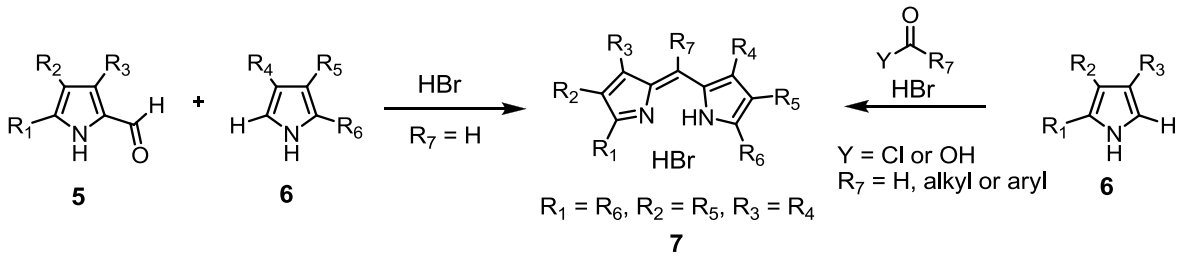

Figure 1.2. The general procedure for the acid-catalysed condensation reactions in the synthesis of asymmetric dipyrrins or dipyrrins bearing hydrogen at *meso* position.

The preparation of 5-aryl substituted dipyrrins is well documented.[26-31] 5-aryl substituted dipyrromethanes, the precursors to 5-aryl substituted dipyrrins, have enhanced the accessibility to 5-aryl substituted dipyrrins. In the traditional synthesis of 5-aryl substituted dipyrromethanes, an aromatic aldehyde (**8**) is reacted with excess of a pyrrole, where it acts as a solvent, in the presence of a mild Lewis acid catalyst (e.g. $InCl_3$) (Figure 1.3).[27] The 5-aryl dipyrromethane product (**9**) can usually be purified by crystallisation. Reaction yields are usually greater than 50%, and the reactions are scalable.

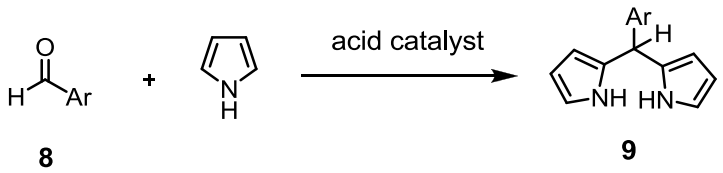

Figure 1.3. The general procedure for the synthesis of 5-aryl substituted dipyrromethanes.

Recently, the synthesis of 5-aryl substituted dipyrromethanes has been improved. By using aqueous HCl as the reaction medium, the condensation of an aromatic aldehyde requires only three equivalents of pyrrole at room temperature.[28] Products are obtained in high yields and usually by simple filtration. This method is appropriate for a wide variety of aromatic aldehydes.

Oxidation of 5-aryl substituted dipyrromethane (**9**) yields the corresponding 5-aryl substituted dipyrrin (**10**) (Figure 1.4). Such compounds are usually stable in their free base form. Oxidation of the dipyrromethane is typically achieved by using DDQ (2,3-dichloro-5,6-dicyano-1,4-benzoquinone).[24, 26, 28] A milder alternative to DDQ is *p*-chloranil (2,3,5,6-tetrachloro-1,4-benzoquinone).[24]

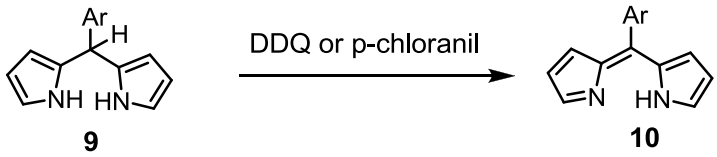

9 **10**

Figure 1.4. Generalised procedure for the synthesis of symmetric dipyrrins via the oxidation of the precursor dipyrromethane.

However, there are noteworthy limitations to the classic two-step acid-catalysed condensation and oxidation reactions to synthesise dipyrrins. These include (i) the requirement for the synthesis of the starting aldehyde if it is commercially unavailable, and (ii) exposure of any functional groups on the aryl ring of the aldehyde to either a Lewis acid or aqueous acid and DDQ or *p*-chloranil. Certain functional groups are incompatible with these conditions and result in reduced yields. For example, the electronic effect of the diphenylamino substituent (-NPh_2) on the aryl ring reduces the reactivity of the precursor aldehyde; therefore more forcing conditions are required. Instead the "traditional" approach to dipyrrin synthesis (Figure 1.3) is required where catalytic quantities of TFA are used to provide the dipyrromethane.[32] Purification after the oxidation step can be particularly arduous, though this is not always apparent from literature reports. Furthermore this particular method for the synthesis of dipyrrins always results in an aryl spacer group between the dipyrrin core and the functional group. This limits the ability to influence the electronic properties of the dipyrrin core by incorporation of electron donating or electron withdrawing substituents.

1.2.3 Dipyrrinato complexes

Dipyrrins are monoanionic when deprotonated and are known to form both homoleptic and heteroleptic complexes with a variety of metal ions.[24, 29, 33-50] The preparation of homoleptic complexes often involves using the metal acetate in methanol given that the product is usually insoluble in methanol and can be easily isolated by filtration; however, other metal salts and solvents are also used.

1.2.4 Complexation geometries of dipyrrinato complexes

The geometry at the metal centre is primarily determined by the preferred coordination environment of the metal ion.[26] The secondary determinant of the geometry at the metal centre is the steric interactions of the substituents at positions 1 and 9 of the dipyrrin ligand.[24] In homoleptic complexes such as [Ni$\mathbf{L}_2$] and [Cu$\mathbf{L}_2$] the steric interactions of substituents as small as hydrogen atoms in these positions result in the formation of complexes with distorted coordination environments. For example, [Cu$\mathbf{L}_2$] complexes adopt a distorted square planar coordination geometry to accommodate the substituents at positions 1 and 9.[26, 36, 51, 52] The geometry of [Ni$\mathbf{L}_2$] complexes is a special case. X-ray crystal structures of an [Ni$\mathbf{L}_2$] complex (**11**) (Figure 1.5) reveals that the coordination geometry is distorted tetrahedral.[26] However, characterisation by NMR spectroscopy is possible for [Ni$\mathbf{L}_2$] complexes.[24, 26] This indicates that the complex is low spin and diamagnetic; therefore the geometry must be (distorted) square planar.[26]

In the case of Pd(II), which typically forms square planar complexes, [Pd$\mathbf{L}_2$] (**12**), the ligands cannot remain coplanar. The four pyrrole nitrogens and the Pd(II) all lie in the same plane, this plane is subsequently referred to as the PdN_4 plane. To accommodate the steric requirements of the hydrogen atoms at positions 1 and 9 the ligands cant away from the PdN_4 plane with an angle of approximately 40°.[43] This angle is the tilt angle[50] (defined as the angle between the PdN_4 plane). The pyrrolic rings of the dipyrrin core also have pronounced curvature. The planes of the pyrrolic rings of each ligand are inclined at an angle of 34° (defined as the angle between the mean planes formed by the atoms in each pyrrole and the adjacent *meso* carbon).[50] These deviations are observed in the crystal structure of **12** (Figure 1.6).

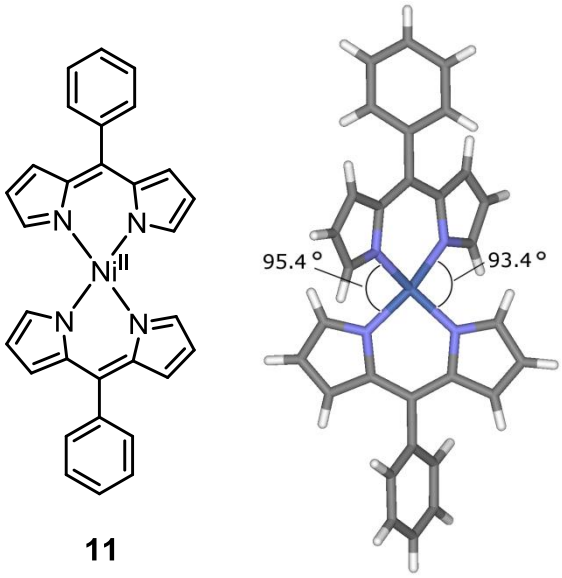

11

Figure 1.5. Distorted tetrahedral coordination geometry of [Ni**L**$_2$] where **L** = 5-phenyl-4,6-dipyrrin.[26]

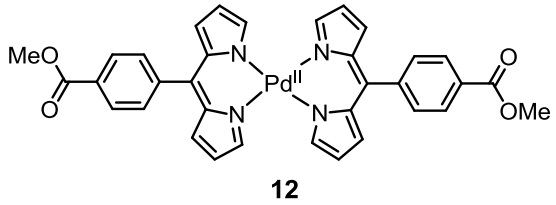

12

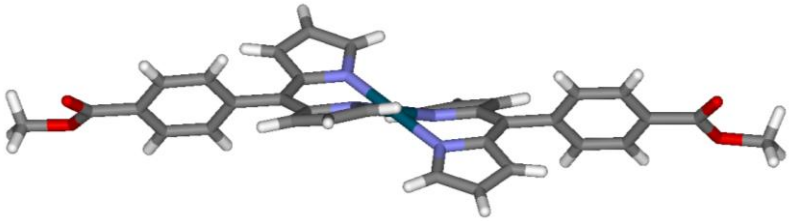

Figure 1.6. Square planar coordination geometry of [Pd**L**$_2$] where **L** = 5-(4-methoxycarbonylphenyl)-4,6-dipyrrin. The crystal structure shows the ligands canted away from the PdN_4 plane and the curvature in the pyrrolic core.[53]

Acetylacetonato ligands (acac) and the hexafluoro derivative (hfacac) are excellent ligands for heteroleptic dipyrrinato complexes as there are minimal steric problems near the metal centre.[54] Figure 1.7 clearly shows the difference in the steric interactions between the α-protons in the heteroleptic complex (**13**) and homoleptic complex (**14**) and the role these protons play in controlling the coordination environment of such complexes.

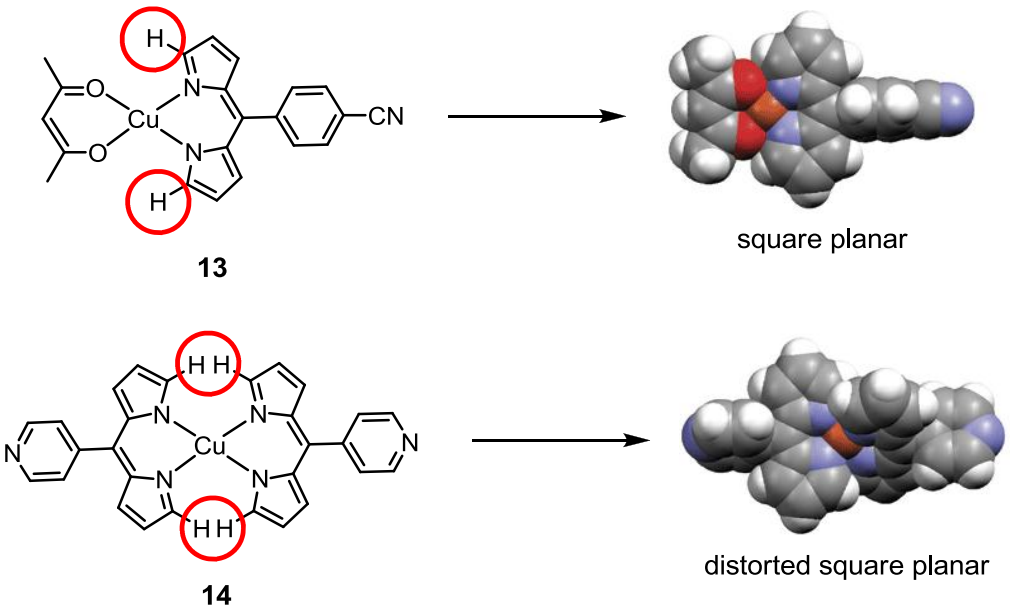

Figure 1.7. Space-filling representations of a heteroleptic Cu(II) (top) and homoleptic Cu(II) (bottom) complex (adapted from reference 52).

1.2.5 BF_2-dipyrrinato complexes

Boron difluoride complexes of dipyrrins, commonly referred to as BODIPYs (**4**), (Figure 1.1) were reported by Treibs and Kreuzer in 1968.[55] The fluorescence properties of these complexes are recognised as their most important characteristic. Generally BODIPY complexes have high fluorescence quantum yields, tuneable emission maxima, and good photochemical stability which has led to commercial use as biological stains,[56, 57] laser dye applications,[58-60] fluorescent switches,[61, 62] and chemosensors (or molecular sensors).[63-67] Research into BODIPYs is currently the most active area of dipyrrin chemistry.[25, 68-70]

The general synthesis of BODIPY complexes (**15**) (Figure 1.8) involves the treatment of a dipyrrin (**16**) with a base and a boron source (usually boron trifluoride). The reaction may also be performed on crude dipyrrins without isolation of the dipyrrin ligand. The synthesis of BODIPYs was revolutionised by the improved synthetic pathways to 5-aryl substituted dipyrrins (Figure 1.3 and Figure 1.4).

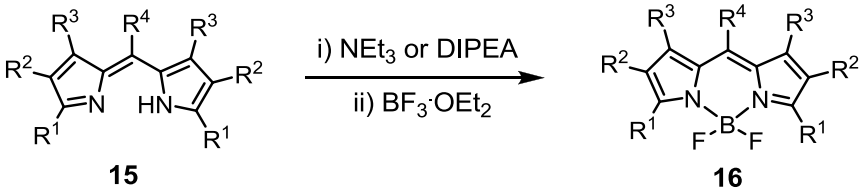

Figure 1.8. The general synthesis of BODIPY complexes.

1.2.6 Azadipyrrins and azadipyrrinato complexes

The synthesis of azadipyrrins (where the methene bridge is replaced with a nitrogen atom) was first described in the 1940s.[71-74] Azadipyrrins can be considered as half phthalocyanines. Phthalocyanines and their derivatives are well known organic dyes.[75, 76] Until the early 2000s these compounds were unstudied for any application. There has been a recent resurgence in the synthesis and studies of azadipyrrins[77, 78] and in particular azaBODIPYs by the O'Shea research group.[79-81] Recent applications of azaBODIPYs include use as agents in photodynamic therapy (PDT),[79, 81] chemosensors,[82] and as *in vitro* fluorophores.[80] In contrast to dipyrrins, few azadipyrrinato complexes are known. To date these include heteroleptic tricoordinate Cu(I), Ag(I), and Au(I) complexes with triphenyl phosphine in the third coordination site,[83, 84] a Re(I) complex,[85] and homoleptic divalent Co(II), Ni(II), Cu(II), Zn(II), and Hg(II).[78, 86] Nonetheless, azadipyrrins and azaBODIPYs are still a relatively undeveloped area of research.

The simplest known and first reported azadipyrrin[71] is the 3,5-tetraphenyl azadipyrrin (**17**). The BODIPY 3,5-tetraphenyl azadipyrrin analogue was reported in 1993[59] (**18**) (Figure 1.9). AzaBODIPYs are prepared from their azadipyrrin analogue in the same way as dipyrrins are converted to their corresponding BODIPY complexes (i.e. treatment with a base and BF_3).

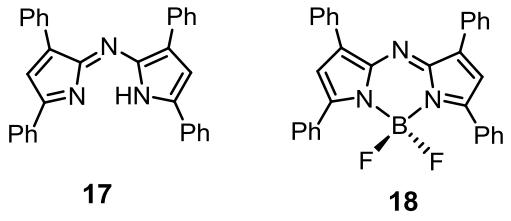

Figure 1.9. Structure of the first reported 3,5-tetraphenyl azadipyrrin and the BODIPY azadipyrrin analogue.

Two general methods for preparing azadipyrrins have been developed (Figure 1.10). Route 1 involves a Michael addition across an α,β-unsaturated ketone (**19**) with nitromethane to give a nitro intermediate (**20**), followed by a reaction with an ammonia source (such as ammonium acetate or ammonium carbamate) to give 3,5-tetraphenyl azadipyrrin (**21**). Alternatively cyanide can be used in place of nitromethane to give a keto-nitrile intermediate. The ease of isolation by precipitation and improved yields were realised when alcohol solvents were used in the reaction. Route 2 involves converting 2,4-diarylpyrrole (**22**) to the 5-nitroso derivative (**23**) then condensing this with another molecule of pyrrole (**22**) to give the 3,5-tetraphenyl azadipyrrin (**21**). This route provides a method to prepare asymmetrical azadipyrrins by condensing the 5-nitroso derivative (**23**) with a different pyrrole fragment. Throughout the literature only aromatic functional groups have been incorporated into the pyrrolic fragments via these synthetic routes.[77, 78]

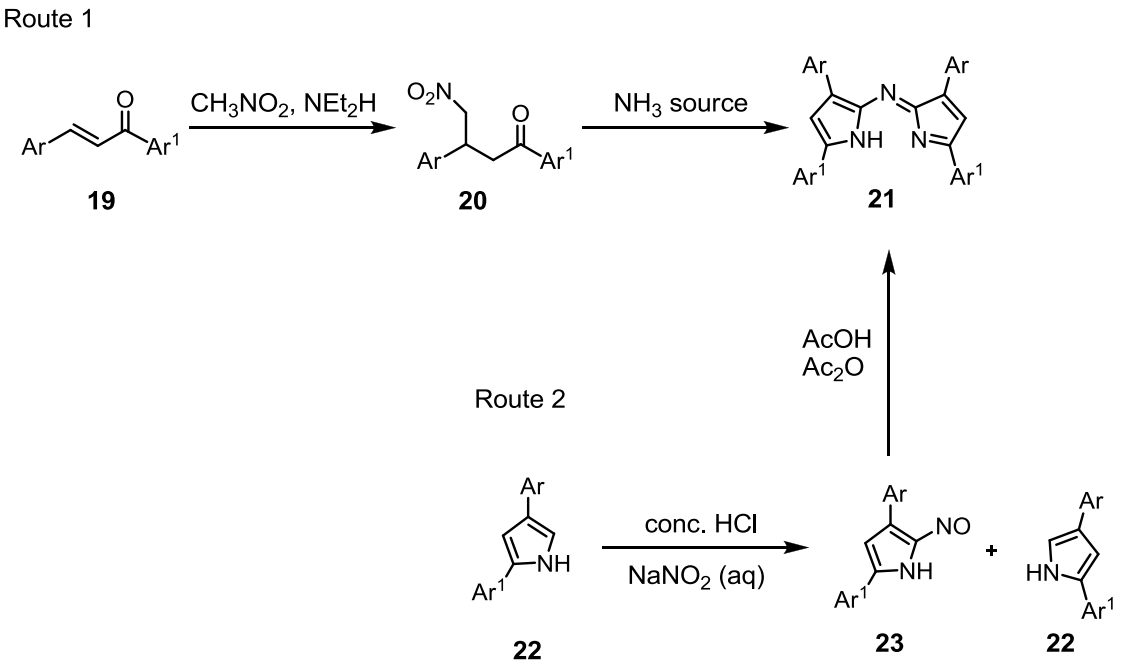

Figure 1.10. The two general procedures for the preparation of azadipyrrins.

1.2.7 Chemical manipulations of dipyrrinato complexes

The modification and elaboration of dipyrrin complexes via chemical manipulations is an underdeveloped area of dipyrrin chemistry. There are three general categories of reactions that have been used: substitutions, functional group interconversions, and

metal-catalysed cross-coupling reactions.[24] In such reactions the metal ion (or BF_2) acts as a protecting group for the dipyrrinato nitrogen atoms. Strongly acidic and/or reductive conditions are avoided as they are known to deprotect the dipyrrinato nitrogen atoms.[24] The present knowledge is largely based on modifying BODIPY complexes (due to the interest in modifying these complexes to tune their optical properties or attach selective binding receptors). A summary of chemical manipulations illustrating the limited number of known reactions to modify dipyrrin complexes can be found in the literature.[24, 25]

Manipulations of functional groups on 5-aryl substituents of dipyrrinato complexes are possible (Figure 1.11). However, generally the equivalent functional group interconversion is not viable on the free ligand. The hydrolysis of the methyl ester dipyrrinato cobalt(III) complex (**24a**) under typical hydrolysis conditions yields the carboxylic acid derivative (**24b**). The carboxylic acid groups can then be converted to amide groups (**24c**), followed by dehydration of the amine groups to yield the cyano derivative (**24d**).[87]

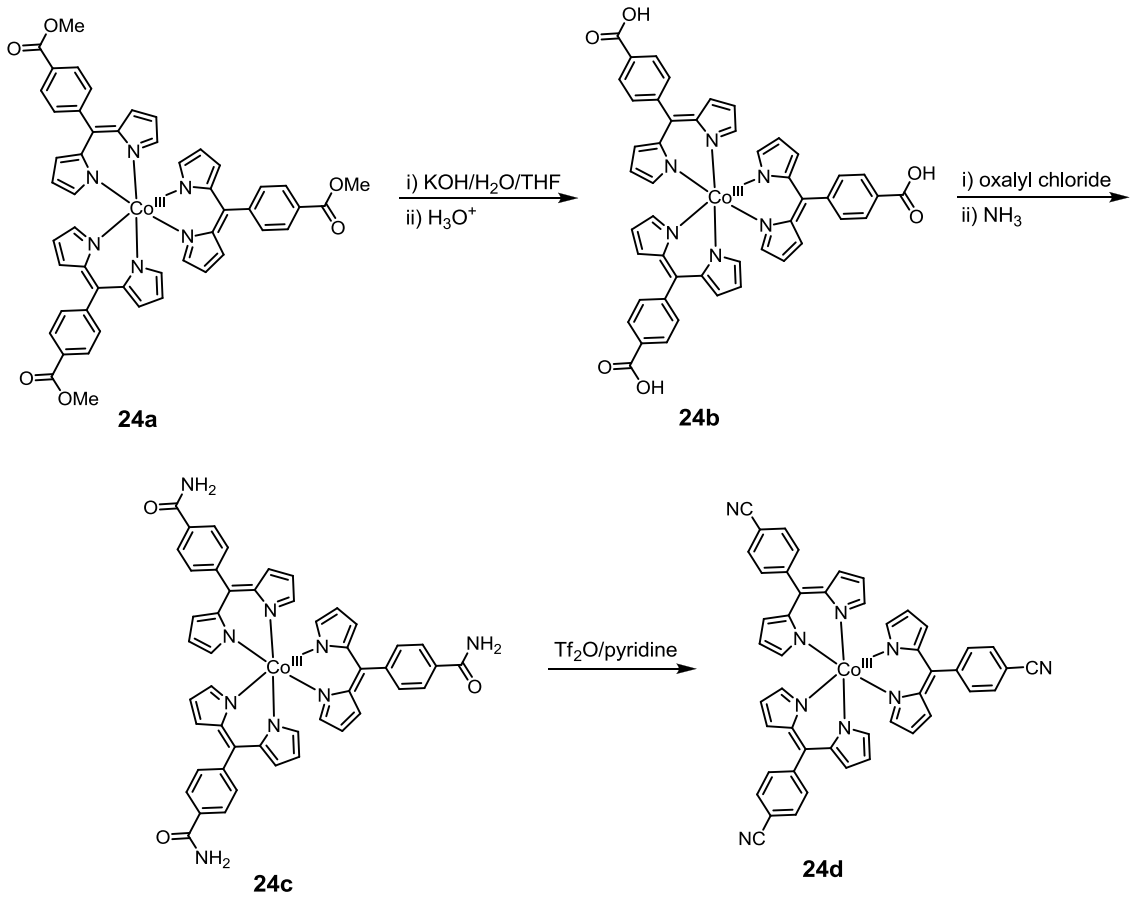

Figure 1.11. Manipulation of a cobalt dipyrrinato complex from a methyl ester (**24a**) to the cyano derivative (**24d**) via a carboxylic acid (**24b**) and amide derivative (**24c**).

1.2.8 Electronic properties of dipyrrins

A unique and defining feature of dipyrrins and azadipyrrins is that they possess a large transition dipole moment across the pyrrolic rings[88] (Figure 1.12), which gives rise to strongly allowed π-π* transitions (~ 20,000 L mol^{-1} cm^{-1} and oscillator strengths, f = 0.5) in the visible region (Figure 1.13). Time-dependent DFT calculations have confirmed the position of the transition dipole moment (see later).

The position of the π–π* transition for dipyrrin ligands is both solvent and pH dependent.[26] The second pyrrolic nitrogen can be protonated with acid which induces both a significant red shift and a substantial increase in the absorption coefficient. The position of the band is relatively insensitive to the functional groups at the *meso* position.[26]

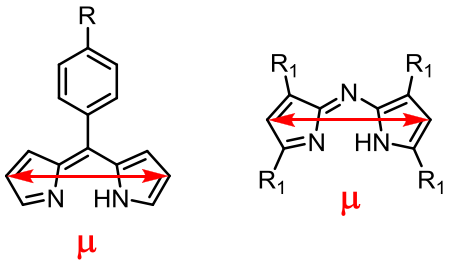

Figure 1.12. Illustration of the position of the transition dipole moment (μ) for the lowest energy π-π* transition of dipyrrins and azadipyrrins.

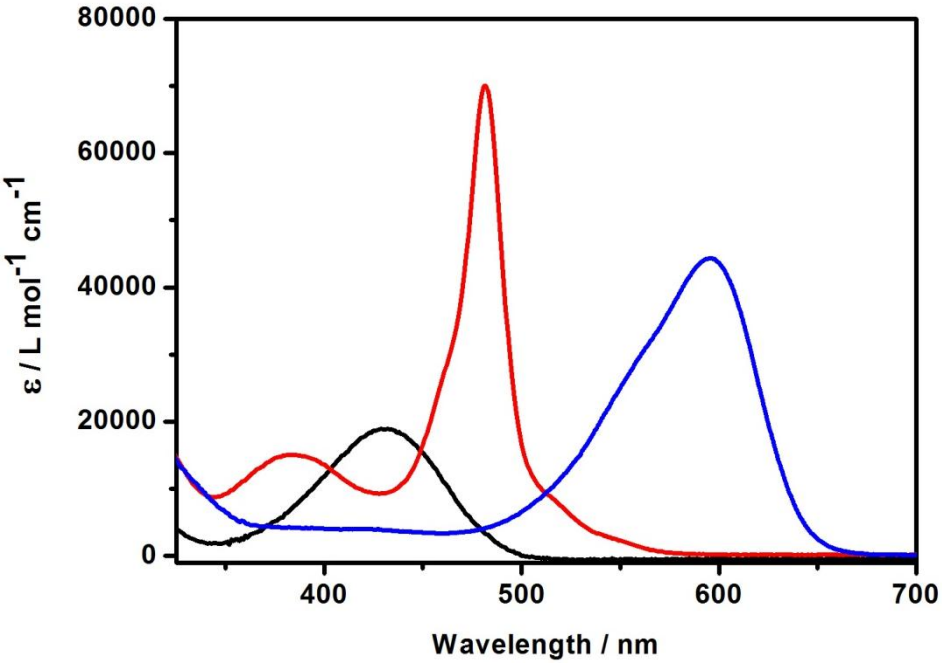

Figure 1.13. Electronic absorption spectra of a dipyrrin ligand (black) in MeOH, an azadipyrrin ligand (blue) and a typical bisdipyrrinato complex (red) in CH_2Cl_2.

1.2.9 Electronic properties of dipyrrinato complexes

The conjugation of the dipyrrin core, analogous to porphyrins, provides dipyrrinato complexes with interesting and useful optical properties. The dipyrrinato complexes have a low energy (~500 nm) absorption band (Figure 1.13) assigned to a π–π* transition located on the dipyrrin core. The area under the π–π* absorption band is proportional to the number of dipyrrinato ligands in the complex.[89]

When two or more dipyrrin ligands come into close proximity, for example by coordinating to a metal centre, the transition dipole moments interact strongly, owing to the strength and close spatial proximity of the chromophores. This leads to new

electronic states that are delocalized across the dipyrrin units. This is termed exciton coupling.[88, 89] Distinct spectral features are seen in both absorption and CD spectra[40, 87, 88] (Figure 1.14). Exciton interactions in dipyrrins have not been investigated in depth in the literature.

Excluding BODIPYs, there has been a limited number of luminescent dipyrrinato complexes reported. To date these include complexes with Zn(II),[33, 41, 90] Rh(III),[43] Pd(II),[48] Al(III),[33] Ga(III),[91] In(III),[91] Ir(III),[50] and Pt(II).[48] Typically the emission quantum yields of these complexes are significantly lower than most BODIPYs. Restricting the rotation of the *meso* phenyl ring relative to the plane of the dipyrrin chromophore is crucial in obtaining enhanced emission from these complexes.[41, 48, 50, 90, 91] For dipyrrinato complexes with heavy atoms, intersystem crossing from the singlet to the triplet excited state is facilitated by strong spin-orbit coupling in the heavy atoms and emission is assigned to phosphorescence.[48, 50, 91]

The emission properties of BODIPYs may have obscured the promising Raman properties of the core dipyrrin unit. Aside from recent publications from our group[42, 53, 92] dipyrrins and dipyrrinato complexes have not been characterised using Raman spectroscopy. Raman spectroscopy, in particular resonance Raman spectroscopy, is a useful technique for investigating the electronic structure of the complex and assigning electronic transitions. Resonance Raman spectroscopy is also a powerful technique for probing the initial nuclear dynamics following excitation (i.e. 0-100 femtoseconds). From this, changes in the nuclear geometry and the relaxation out of the Franck-Condon region can be examined in detail.

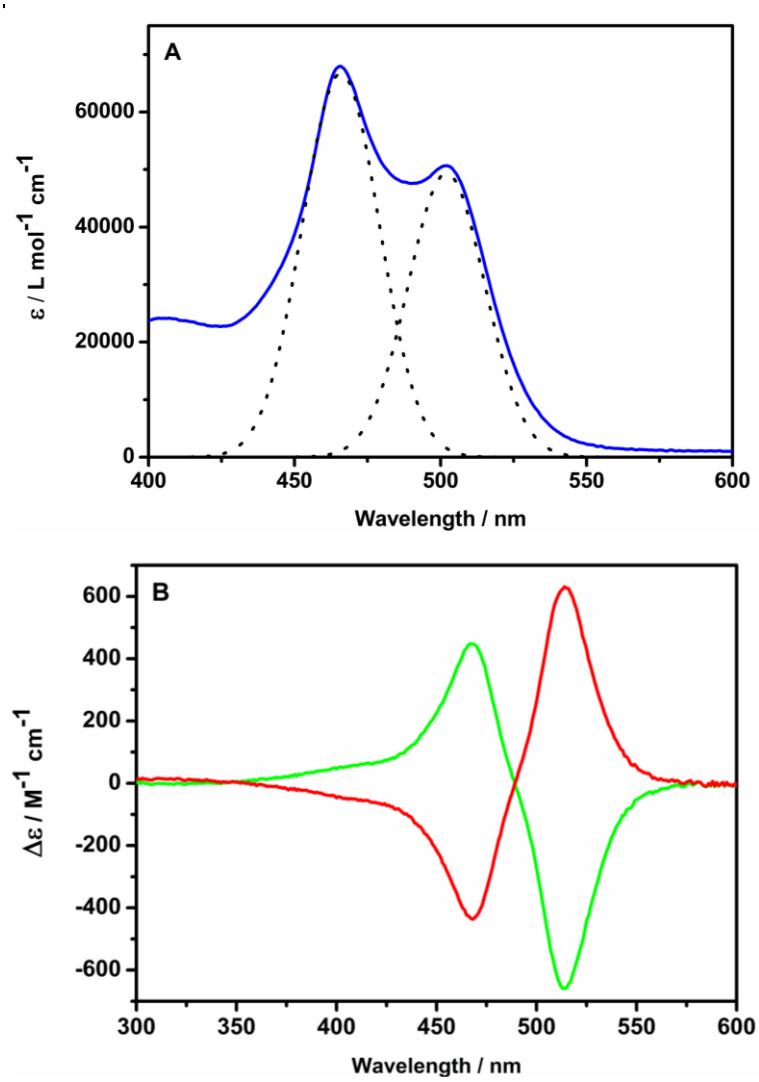

Figure 1.14. Illustration of exciton coupling in [M**L**$_3$] dipyrrinato complexes. (A) electronic absorption spectrum of [Rh**L**$_3$] (blue) where the major components of the observed spectrum are shown as dashed lines,[88] and (B) circular dichroism (CD) spectrum of a Δ-[Co**L**$_3$] (green) and Λ-[Co**L**$_3$] complex (red).[87]

1.2.10 Recent advances in dipyrrin chemistry

Research into the coordination chemistry of dipyrrins and azadipyrrins is rapidly evolving with new and more exotic metal complexes of both homoleptic and heteroleptic dipyrrinato and azadipyrrinato being reported.[24, 40, 44, 49, 50, 93-102] Many of the complexes that have been prepared exhibit interesting spectroscopic properties.

The first alkali metal complexes (Li^+, Na^+, K^+) of dipyrrinato ligands have recently been prepared and investigations into the use of these complexes in salt elimination reactions is being undertaken.[103] A novel example of a heteromultinuclear complex based on a

dipyrrin framework which forms N_2O_2 type complexes with Al(III) has been reported (**25**). These complexes then chelate to Zn(II) (**26**) which enhances the fluorescence relative to the Al(III) complex (Figure 1.15).[33]

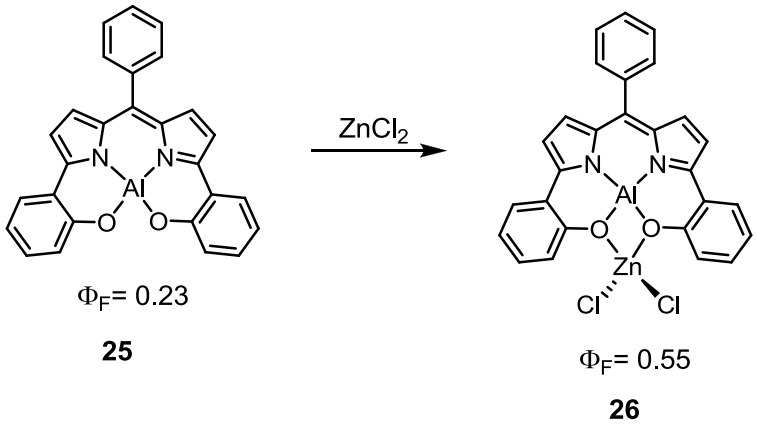

Figure 1.15. A N_2O_2 Al(III)-dipyrrinato complex which further complexes Zn(II) enhancing the fluorescence.

An azadipyrrinato complex of Re(I) has been reported in attempts to combine the well-studied and favourable excited state properties of Re(I) diimine complexes, e.g. $[Re(CO)_3LX]$, where L = 2,2′-bipyridine and 1,10-phenanthroline,[104] with the long wavelength absorption properties of azadipyrrin ligands.

The long-lived excited states and efficient phosphorescent emission characteristics of bis-cyclometallated Ir(III) complexes have been combined with dipyrrin ligands to provide room temperature phosphorescence. The cyclometallating ligand and the *meso* substituent on the dipyrrinato ligand were systematically varied to determine the origin of the emission, which was assigned to a dipyrrin-centred triplet state.[50] The Ir(III) complex **27** with the greatest quantum efficiency (Φ = 0.115) has the phenyl rotation blocked[41, 48, 50, 90, 91] by the mesityl functional group (Figure 1.16). Weak low temperature phosphorescence (Φ = 0.013) from a cyclometallated Pt(II) complex (**28**) has also been reported.[48]

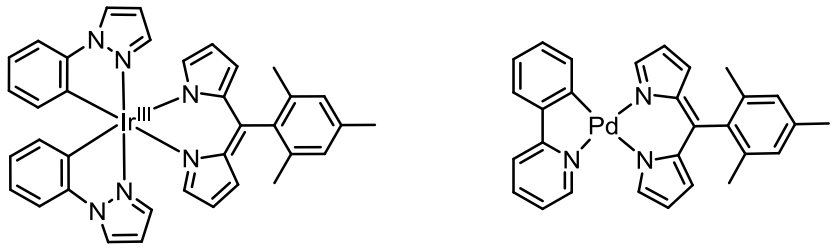

27 **28**

Figure 1.16. A bis-cyclometallated Ir(III)-dipyrrinato complex and a cyclometallated Pd(II)-dipyrrinato complex, which both exhibit phosphorescence.

Heteroleptic η^5-pentamethylcyclopentadienyl dipyrrinato complexes of Rh(III) and Ir(III) (**29**) have been prepared (Figure 1.17). These complexes have been shown to catalyse the reduction of terephthaldehyde to 4-hydroxymethylbenzaldehyde in aqueous and aerobic conditions with greater than 99 percent conversion efficiency achieved.[46]

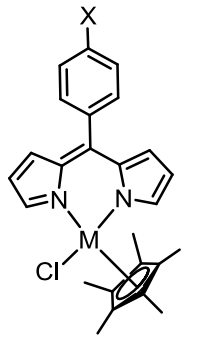

M = Rh(III), Ir(III)

29

Figure 1.17. Heteroleptic η^5-pentamethylcyclopentadienyl dipyrrinato Ir(III) and Rh(III) complexes capable of the catalytic reduction of terephthaldehyde.

Recently, BODIPY complexes with heteroatom substituents at the *meso* position have been reported.[105] Prior to this, the synthesis of dipyrrylthiones (such as **31**) had been described[106] but the synthesis had not been continued to give the corresponding BODIPY. The reaction is outlined in Figure 1.18 where the reaction of pyrrole or substituted pyrrole (**30**) with thiophosgene yields a thioketone (or dipyrrylthione) (**31**). Further reaction with methyl iodide provides an unstable intermediate (**32**) (as the

hydroiodide salt) which is reacted with triethylamine and boron trifluoride etherate to give the thiomethyl BODIPY derivative (**33**).

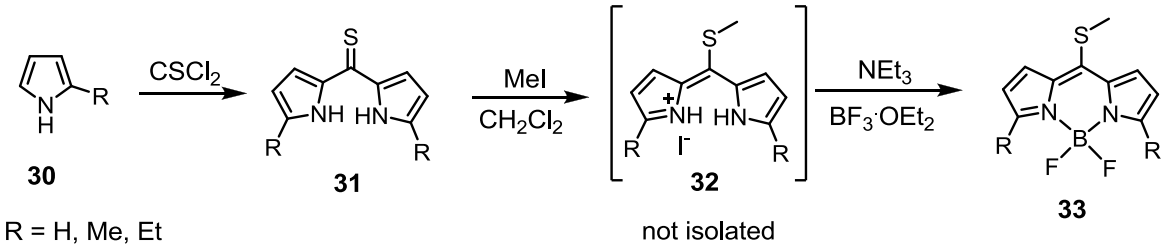

Figure 1.18. Synthesis of a thiomethyl BODIPY complex.

This synthesis has facilitated further elaboration at the *meso* position to provide BODIPY complexes under mild reaction conditions without exposure of the *meso* substituent to acid or oxidation via DDQ or *p*-chloranil.[105] Liebeskind-Srögl cross-coupling reactions with boronic acids have also been utilised to develop novel *meso* substituted BODIPY complexes.[107] Interestingly, this chemistry has not yet been extended to transition metal dipyrrinato complexes.

1.3 Raman spectroscopy

The underlying theory and principles of Raman spectroscopy are related to both fluorescence and infrared spectroscopy. However, unlike these techniques, Raman spectroscopy has not been widely adopted by chemists and is often considered a specialised technique. Raman spectroscopy forms a significant part of this thesis and has been widely used to characterise porphyrins and metalloporphyrins, therefore a full introduction is given here.

1.3.1 Historical background and theory of Raman spectroscopy

The inelastic light scattering phenomenon responsible for Raman spectroscopy was theoretically predicted by Smekal in 1923.[108] However, the phenomenon was not experimentally demonstrated until 1928 by Chandrasekhara Venkata Raman together with Kariamanickam Srinivasa Krishnan.[109]

C. V. Raman

Their experimental setup consisted of a beam of sunlight converged by a telescope objective with an 18 cm aperture and a 230 cm focal length, followed by a second lens with a 5 cm focal length. The sample was placed at this focal point. Complementary light filters were employed to detect the presence of a modified scattered radiation. A blue-violet filter coupled with a yellow-green filter placed in the incident light eliminated the light path through the sample. Moving the yellow-green filter to a position between its original position and the observer resulted in the light path reappearing and was proof of the existence of modified scattered radiation. Raman described the nature of this scattered radiation as "feeble in comparison with the ordinary scattering".[109] Subsequently Raman was awarded a Nobel Prize in Physics in 1930 for this work and the Raman effect was named after him.[110]

1.3.2 Basic theory and principles of Raman spectroscopy

Raman spectroscopy utilises a single frequency of radiation to irradiate the sample. This light interacts with the molecule and polarises the cloud of electrons around the nuclei, forming a 'virtual state' which is a superposition of a molecular state and a photon state. This state is not stable and the photon is released immediately as *scattered* radiation.[111]

When light is scattered by matter the photons are scattered in two ways: elastically or inelastically (Figure 1.19). In elastic scattering, the electron cloud relaxes without any nuclear movement i.e. it does not involve a change in vibrational energy and the molecule returns to its initial energy level. This is also known as Rayleigh scattering and accounts for most of the light scattered from molecules.[111, 112] Inelastically scattered photons account for approximately one in 10^6-10^8 photons, which have a different frequency from that of the incident photons. In this case photons interact with the electron cloud and the nuclei begin to move. This results in a change in energy of the molecule, to higher or lower energy, depending on whether the molecule started in the ground state or in an excited vibrational state. This is known as Raman scattering or the Raman Effect.[111, 112] Raman spectroscopy measures the energy difference between the ground and excited vibrational states.[111]

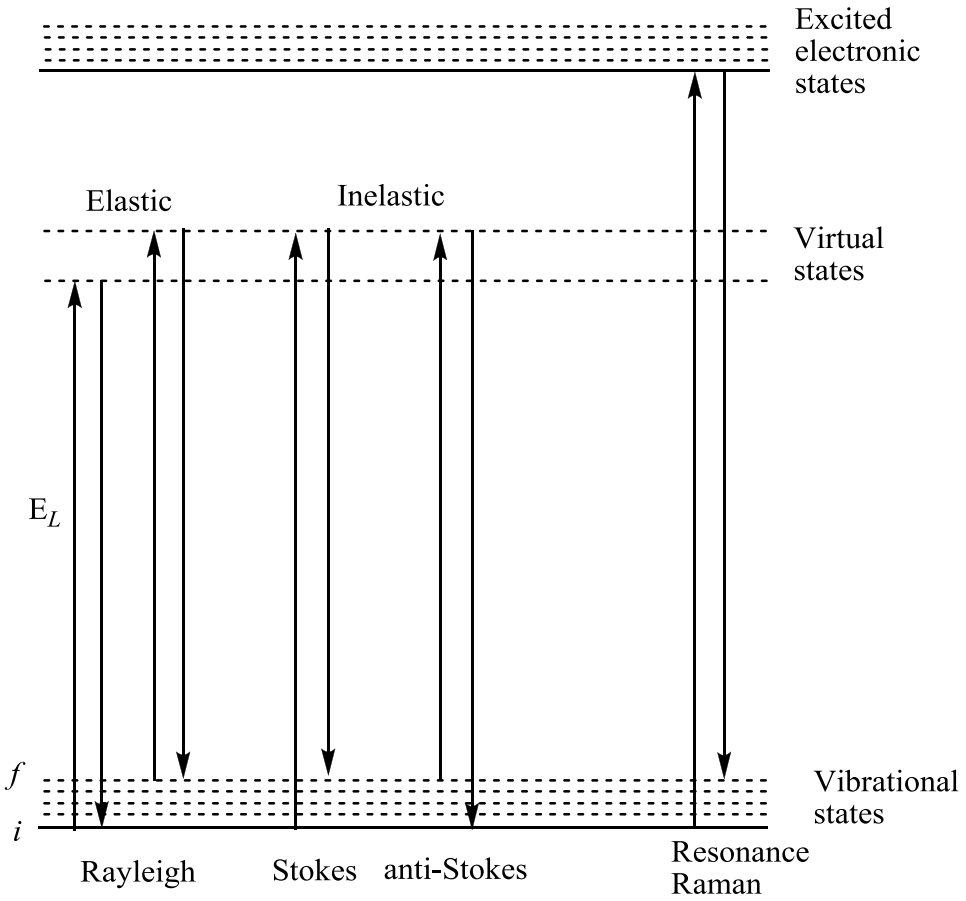

Figure 1.19. Spectroscopic transitions underlying Raman and Resonance Raman spectroscopy.[111-113] *i* and *f* represent the ground and excited vibrational states, respectively. The virtual states are not real states of the molecule and are determined by the frequency of the light source used for excitation (E_L).[111]

Stokes scattering occurs when a molecule begins in the ground vibrational state, *i*, and absorbs a photon promoting the molecule to be in the excited vibrational state, *f*. However, owing to thermal energy, there are some molecules, which exist in the excited state, *f*. Anti-Stokes scattering occurs when scattering from the excited vibrational, *f*, state to the ground vibrational state, *i*, takes place (Figure 1.19). In comparison to Stokes scattering, anti-Stokes scattering is weak; however, anti-Stokes vibrations are more pronounced at higher temperatures. The Boltzmann distribution shows that the excited vibrational state is less populated than the ground state and this explains why anti-Stokes scattering is weaker than Stokes scattering.[111, 112] Usually Stokes scattering is recorded, however, anti-Stokes scattering may be recorded if there is fluorescence interference at longer wavelengths.[111]

1.3.3 Magnitude of Raman scattering

Placzek developed the theory of Rayleigh and Raman spectroscopy by considering ground state polarisability.[114] The classical description of Raman scattering is as follows. An electric dipole is induced, *P*, when an oscillating incident electric field, *E*, interacts with an electron cloud of a chemical bond. This is given by:

$$P = \alpha E \tag{1.3}$$

where α is the polarisability of the molecule. The incident electric field term is given by:

$$E = E_o \cos 2\pi \upsilon_o t \tag{1.4}$$

where υ_o is the frequency of the laser. The molecular vibrations are comprised of normal modes, Q_j, where there are 3N-6 vibrations in a non-linear molecule with N atoms.

$$Q_j = Q_j^{\circ} \cos 2\pi \upsilon_j t \tag{1.5}$$

υ_j is the characteristic harmonic frequency of the *j*th normal mode. For a vibrating molecule, the polarisability term is given by the following Taylor series expansion:

$$\alpha = \alpha_0 + \frac{1}{2}\left(\frac{\partial \alpha}{\partial Q_j}\right)_{Q_j=0} Q_j + \ldots \tag{1.6}$$

Substitution of equations 1.4-1.6 into 1.3 gives:

$$P = \alpha_0 E_0 \cos 2\pi \upsilon_0 t + \frac{1}{2}\left(\frac{\partial \alpha}{\partial Q_j}\right)_{Q_j=0} E_0 \, Q_j^0 \left[\cos\left\{2\pi\left(\upsilon_0 + \upsilon_j\right)t\right\} + \cos\left\{2\pi\left(\upsilon_0 - \upsilon_j\right)t\right\}\right] \tag{1.7}$$

The first term is the Rayleigh scattering, which has the same frequency as the laser frequency. The second term is the anti-Stokes Raman scattering and occurs at a frequency of $\upsilon_o + \upsilon_j$. The third term is Stokes Raman scattering and occurs at a frequency of $\upsilon_o - \upsilon_j$.[113]

Raman intensity, I_R, varies with frequency:

$$I_R = \mu(\upsilon_o \pm \upsilon_j)^4 \alpha_j^2 Q_j^2 \tag{1.8}$$

where μ is a constant. Equation 1.8 illustrates that the Raman intensity varies with the observed frequency (ν_s where $\nu_s = \nu_o \pm \nu_j$) to the fourth power for normal Raman scattering, which in turn depends on the laser frequency (ν_o). The ν^4 dependence is derived from the classical treatment of scattering from an oscillating induced dipole.

Equation 1.8 leads to the major distinction between Raman spectroscopy and infrared spectroscopy. Raman scattering requires a change in the polarisability for an allowed transition.[111] That is, $\frac{\partial \alpha}{\partial Q_j}$ in equation 1.7, must be non-zero to observe Raman bands.[115] Symmetric vibrations usually give the greatest scattering. In comparison, for infrared absorption the most intense absorption is caused by a change in dipole, which results from non-totally symmetric vibrations. Not all vibrations from a molecule are both infrared and Raman active. Therefore the two techniques are complementary methods of investigating the vibrations of a molecule.[111]

Raman cross-section (σ_j) with units of cm^2 $molecule^{-1}$ is often the most important parameter derived from the Raman intensity. The Raman cross-section is proportional to the probability of the scattering of an incident photon as a Raman-shifted photon with a particular Raman shift. The magnitude of σ_j is related to $\frac{\partial \alpha}{\partial Q_j}$.[113]

σ_j is the integrated Raman cross-section, i.e. Raman scattering in all directions and over all scattered frequencies. This would require light collection over all 4π steradians around the sample. This is experimentally impractical. In practise, light is collected over a relatively small angle from one of the several scattering directions from the sample. Accordingly, $\frac{d\sigma_j}{d\Omega}$ is the differential cross-section with units of cm^2 $molecule^{-1}$ sr^{-1}, where Ω represents the angle of collection.

Raman cross-sections for unknown samples are commonly determined via quantitative comparison with a standard/reference with a known Raman cross-section (equation 1.9). These standards are commonly solvents; however external standards are also used.

$$\left(\frac{d\sigma_j}{d\Omega}\right)_{sample} = \left(\frac{d\sigma_j}{d\Omega}\right)_{reference} \cdot \left(\frac{I_{sample}}{I_{reference}}\right) \cdot \left(\frac{c_{reference}}{c_{sample}}\right) \qquad (1.9)$$

Raman cross-section is dependent on the wavelength of laser excitation as resonance effects increase the cross-section, scattering geometry of the experimental set-up, and polarisation.[111, 113]

1.3.4 Resonance Raman spectroscopy and surface-enhanced Raman spectroscopy

There are two serious shortcomings of Raman spectroscopy. The consequence of only one in 10^6-10^8 photons being inelastically scattered is that Raman signals are very weak.

Typical non-resonant Raman cross-sections (using visible excitation) are on the order of 10^{-29} cm^2 molecule^{-1}.[116] This compares to fluorescence cross-sections which are on the order of 10^{-17}-10^{-16} cm^2 molecule^{-1}. Under favourable conditions such as resonance conditions the Raman cross-sections are on the order of 10^{-25} cm^2 molecule^{-1}.[116] Therefore the weak nature of Raman spectroscopy limits the detection of molecules at low concentrations.[111, 113] Secondly, some molecules exhibit fluorescence and even weak fluorescence signals can mask Raman signals.[112, 117]

To overcome the inherent weakness of the Raman effect, there are two possible approaches based on equation 1.3:

$$P = \alpha E \tag{1.3}$$

- modify/increase the polarisability (α) of the molecule. This approach is the basis of the resonance Raman spectroscopy.
- modify/increase the strength of the electric field (E) that the molecule experiences. This approach is the basis of surface-enhanced Raman spectroscopy.

These shortcomings are overcome by resonance Raman spectroscopy (RR), surface-enhanced Raman spectroscopy (SERS), and surface-enhanced resonance Raman spectroscopy (SE(R)RS). SE(R)RS is a combination of both SERS and RR and will not be described further other than to say that the excitation source must be resonant with both the dye and plasmon resonance of the metal surface.[111]

1.3.4.1 Introduction to resonance Raman spectroscopy (RR)

The sensitivity of Raman spectroscopy is greater when the frequency of the excitation is close to that of an electronic transition of the molecule of interest. Resonance Raman occurs when the excitation frequency coincides with an electronic transition of the molecule of interest (Figure 1.19).[118] Pre-resonance Raman occurs when the excitation frequency is close to the electronic transitions of the molecule of interest. The closer the excitation frequency is to the electronic transition the greater the intensity of the Raman bands. The vibrational modes associated with the electronic transition are selectively enhanced in resonance Raman and give rise to Raman bands with a greater intensity. Resonance Raman scattering leads to up to 10^6 times stronger Raman scattering.[112] The resulting spectrum may also be different. For example, overtones and

combinations may be enhanced and bands may be selectively enhanced.[112, 119] See Appendix A1 for resonance Raman theory including Albrecht theory of resonance Raman (A1.1) and resonance Raman intensity analysis (RRIA) (A1.2).

The development of a range of excitation sources coupled with the development of tunable lasers have resulted in exploitation of resonance Raman for many new applications.[111, 112, 120] The main advantage of resonance Raman spectroscopy over traditional Raman spectroscopy is the enhancement of selected Raman bands which allows the detection of analytes present at low concentrations.[120] However, owing to the use of visible or ultraviolet excitation sources, interference from fluorescence is often a problem with resonance Raman.[121]

1.3.4.2 Introduction to surface-enhanced Raman spectroscopy (SERS)

The first Raman spectrum of pyridine adsorbed onto a roughened silver electrode was reported in 1974 by Fleishmann and others.[122] Since then, numerous reports of enhanced Raman signals of molecules adsorbed onto noble metal surfaces have been reported. These metals may be metal surfaces such as thin roughened metal surfaces, metal electrodes[122] or most commonly metal nanoparticles.[123, 124]

The characteristic features of these metal nanostructures are plasmon resonances (more accurately called surface plasmon resonances). Plasmon resonances are coherent oscillations of the surface conduction electrons when excited by electromagnetic radiation[125] (Figure 1.20). Plasmon resonances generate enhanced Raman scattering in a process known historically as surface-enhanced Raman spectroscopy (SERS). This term emphasises the important role of the noble metal substrate in this phenomenon.[117]

The plasmon resonance of metal nanoparticles (especially silver and gold) is a strong and broad band observable using UV-visible spectroscopy. The size and shape of the metal nanoparticles influences the position and intensity of the plasmon resonance via the dielectric constant of the material.[117]

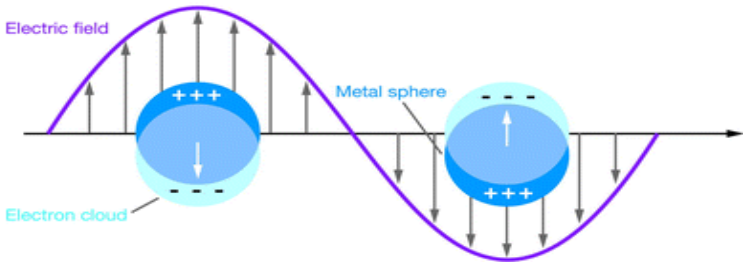

Figure 1.20. A schematic diagram of a localized surface plasmon of spherical nanoparticles by incident electromagnetic radiation.[125] The grey arrows represent the electromagnetic field and the purple line represents the electric field from the incident light.

There is some debate surrounding the mechanism of enhancement of SERS. It is now widely believed that there are three possible contributions to the enhancements observed: (i) surface plasmon resonance in the metal nanoparticle, (ii) charge-transfer resonance which involves the transfer of electrons between the molecule and the conduction band of the metal, and (iii) resonances within the molecule itself.[126] Researchers continue to debate the relative significance of these contributions to the enhancement of the Raman signal.[112, 117, 127] See Appendix A2 for Albrecht theory applied to SERS.

In addition to the three possible enhancement mechanisms of SERS, when metallic nanoparticles are used as the metal substrate, there have been reports of large variations in the enhancement observed.[128, 129] These variations have been ascribed to the random formation of 'hot spots' between the junctions of the nanoparticles.[130] These hot spots give large enhancements, which allow for single molecule detection of analytes.[131, 132] Refer to Figure 1.21 for an illustration of the electromagnetic field enhancement. Controlling hotspots provides the motivation for assembling nanoparticles in a controlled manner.[133]

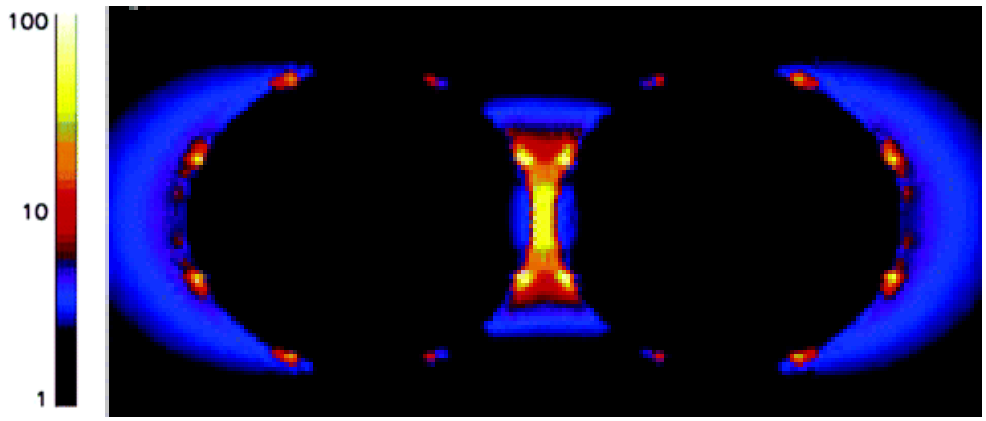

Figure 1.21. The calculated electromagnetic field enhancements of adjacent gold nanoparticles. The colour scale represents the electromagnetic enhancement (adapted from reference 130).

Surface-enhanced Raman spectroscopy has greater sensitivity than normal Raman scattering and resonance Raman scattering. SERS presents abundant spectroscopic information and high sensitivity due to the enhancements resulting from the surface plasmons. This allows SERS to be used for trace analysis of analytes. In particular, this is an effective method for studying molecules of biological importance.[112]

1.4 Electronic absorption spectroscopy

During an electronic transition, a molecule can be excited from the ground state to an electronically excited state by absorbing a photon of light of an appropriate wavelength. This results in the electron density distribution of the ground state and the excited state being different which in turn induces an electric transition dipole moment, μ. The electric transition dipole moment is described by a vector with an orientation corresponding to the direction of the electron displacement and with a magnitude that is proportional to the intensity of the transition.

Electronic absorption spectroscopy measures the absorption of light by a sample as a function of wavelength. If the concentration of the sample (c, mol L^{-1}) and the pathlength of the light traversing the sample (l, cm) are known, then absorbance (A) can be converted to molar absorptivity (ε, L mol^{-1} cm^{-1}) using Beer's Law ($A = \varepsilon cl$).[134] The absorption coefficient (ε_{max}) or the area under the absorption band gives the magnitude of the transition dipole moment.[135]

Electronic absorption spectroscopy is an important technique for identifying the origin of an electronic transition. The position and intensity of the absorption maxima in the absorption spectra relate to the type of electronic transition occurring. For transition metal complexes the following transitions are possible:

- d-d transitions or ligand field transitions. These transitions are characterised by the movement of an electron between the d orbitals of the metal. These transitions are very weak (on the order of 100 L mol^{-1} cm^{-1} for octahedral and square-planar complexes and up to 250 L mol^{-1} cm^{-1} for tetrahedral complexes). Often d-d transitions are masked by the intensity of charge transfer transitions.[136, 137]
- charge transfer (CT) transitions. In such a transition an electron moves between orbitals that are predominantly ligand in character and orbitals that are predominantly metal in character. Transitions are classified as either ligand-to-metal charge transfer (LMCT) and metal-to-ligand charge transfer (MLCT) depending on the direction of electron movement. Charge transfer transitions are usually very intense (on the order of 1000 – 50 000 L mol^{-1} cm^{-1}) and the position of the transition is sensitive to the solvent polarity.[136, 137]
- π-π^* transitions are ligand centred transitions where an electron moves from the bonding π orbitals to the antibonding π orbitals.[138]
- n-π^* transitions occur when an electron is promoted from the non-bonding orbital of N, O, and S atoms to an antibonding π orbital.[139] $n \rightarrow \pi^*$ transitions typically have lower oscillator strengths and can be hidden by the intensity of the π–π^* transition.[138]

1.5 Fluorescence spectroscopy

After a molecule is promoted to an excited electronic state, it may emit a photon of light as one way of returning to the ground state (Figure 1.22). Fluorescence spectroscopy measures this emission of photons from a sample as a function of wavelength. The emitted photon is typically of lower energy than the absorbed photon. The Stokes shift is the difference between the positions of the absorption maximum and the emission maximum of the same electronic transition. This is typically measured in frequency with units of wavenumbers (cm^{-1}).[140]

There are two types of emission, depending on the nature of the excited states. *Fluorescence* is emission from the singlet excited state while *phosphorescence* is emission from the triplet excited state. The triplet excited state is populated from the singlet excited state by a process known as intersystem crossing. Heavy atoms in the molecule such as bromine, iodine and third row transition metals facilitate intersystem crossing.[140] A large Stokes shift[141] combined with temperature dependent emission,[141] quenching of the emission by dissolved oxygen[142] and other quenchers[140] are often indicative of emission from the triplet state.

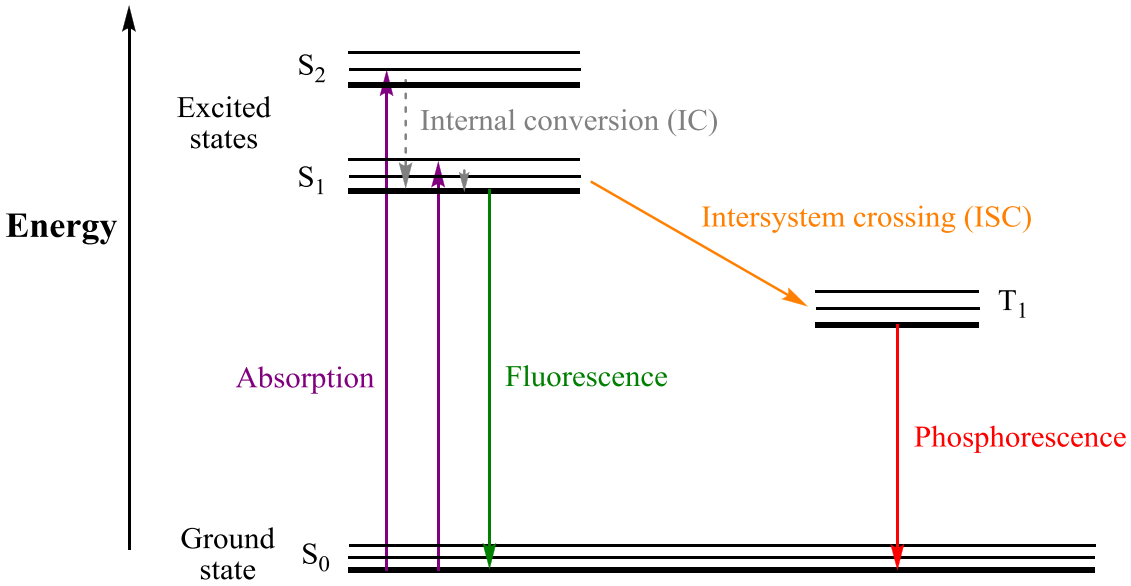

Figure 1.22. A Jablonski diagram illustrating the absorption and emission processes.

The most important parameter determined for an emissive sample is the emission quantum yield (Φ), which can be used to quantify the efficiency of the emission process. The quantum yield is the number of emitted photons relative to the number of absorbed photons.[140] Relative quantum yields are routinely determined against a standard with a known emission quantum yield using (equation 1.10):[143]

$$\Phi_{F(X)} = \left(\frac{A_S}{A_X}\right)\left(\frac{F_X}{F_S}\right)\left(\frac{n_X}{n_S}\right)^2 \Phi_{F(S)} \qquad (1.10)$$

where Φ_F is the emission quantum yield, A is the absorbance at the excitation wavelength, F is the area under the corrected emission curve, and n is the refractive

index of the solvents used. The subscripts s and x refer to the standard and the unknown, respectively.

1.6 Thesis structure

Chapter Two focuses on evaluating the non-resonant Raman, resonant Raman, and surface-enhanced Raman cross-sections and calculating the enhancement factors of dipyrrin ligands. By measuring the resonant Raman cross-sections the goal is to distinguish the electronic (molecular) resonance enhancement from the total resonance enhancement to establish the utility of these ligands for SERS and potentially SM-SERS applications. This work has been published in *J. Raman Spec*. (McLean, T. M., Waterland, M. R., Telfer, S. G., Gordon, K. C., McGoverin, C. M., *J. Raman Spec*. **2011**, 42, 2154-2164).

Chapter Three focuses on the synthesis of a variety of transition metal complexes of dipyrrin ligands and analysis of the resulting exciton interactions using absorption spectroscopy and TD-DFT calculations. Transition metals with well-defined and distinct coordination geometries allow for the control of exciton interactions by tuning the orientation and separation of the chromophores. By controlling the exciton interactions, can dipyrrin systems be designed to mimic these systems and capture a significant fraction of solar energy at the same time? A review of exciton coupling in coordination compounds has been published in *Dalton Trans*. (Telfer, S. G., McLean, T. M., Waterland, M. R., *Dalton Trans*. **2011**, 40, 3097-3108), which features examples of exciton coupling in dipyrrinato complexes. The synthesis of some of the dipyrrinato complexes in this chapter have been published in *Dalton Trans.* (Hall, J. D., McLean, T. M., Smalley, S. J., Waterland, M.R., Telfer, S.G., *Dalton Trans*. **2010**, 39, 437-445).

Chapter Four focuses on the synthesis and characterisation of a family of Ru(II)-dipyrrinato bipyridine complexes for applications in solar energy conversion such as dye-sensitised solar cells (DSSCs) and potentially water-splitting applications. Subsequently, resonance Raman and resonance Raman intensity analysis combined with DFT calculations were employed to examine the excited state dynamics of one of the Ru(II)-dipyrrinato complexes with regard to understanding how effective these materials will be for solar energy conversion applications. The suitability of the dyes as dye-sensitised solar cells was established using electrochemical methods. The solar power conversion efficiencies (η) were measured by means of collaboration with Dr

Attila Mozer at the University of Wollongong and Professor Yoo Soo Kang at Hanyang University. The excited state dynamics from resonance Raman and resonance Raman intensity analysis has been published in *Chem-Asian J.* (McLean, T. M., Cleland, D.M., Lind, S.J., Gordon, K.C., Telfer, S. G., Waterland, M. R., *Chem-Asian J.* **2010**, 5, 2036-2046.)

Chapter Five focuses on the synthesis and characterisation of a series of Re(I)-dipyrrinato complexes for potential applications in the reduction of carbon dioxide. Emission studies particularly the quenching of the triplet state emission by methyl viologen indicate these complexes warrant further investigation as photocatalysts in the reduction of carbon dioxide. Photochemical ligand substitution reactions of the complexes were also investigated. This work has been published in *Inorg. Chem.* (McLean, T. M., Moody, J. L., Waterland, M. R., Telfer, S. G., *Inorg. Chem.* **2012**, 51, 446-455).

Chapter 2

Raman Spectroscopy of dipyrrins: non-resonant, resonant, and surface-enhanced cross-sections and enhancement factors

2.1 Introduction

Since the first report of surface-enhanced Raman scattering (SERS) from single molecules [131, 132] there has been much debate on the magnitude of SERS enhancement factors. For the development of reliable SERS applications, the Raman cross-sections and enhancement factors must be known accurately. But until recently the concept of enhancement factor was not well defined and as a result SERS enhancement factors reported in the literature covered a wide range, from 10^4-10^{14}. There are a large number of factors that contribute to the SERS effect, and therefore SERS enhancement factors, which have been summarised by Le Ru *et al.*[127, 144] Also, the physical mechanisms responsible for the enhancement seen in SERS experiments have been the subject of much debate. Three possible contributions to the enhancement factor have been identified: (i) surface plasmon resonance in the metal nanoparticle, (ii) charge-transfer resonance which involves the transfer of electrons between the molecule and the conduction band of the metal, and (iii) resonances within the molecule itself.[126]

If the issue of hot-spot formation and number of molecules in the scattering volume is momentarily set aside, it is essential to distinguish between enhancement from resonance with the electronic states of the molecule (the resonance Raman effect) and enhancement from resonance with the plasmon modes of the metallic nanostructure (the SERS effect). Further complications arise when the molecular electronic transitions are resonant with the plasmon resonance (surface-enhanced resonance Raman scattering (SE(R)RS)). Most single molecule SERS (SM-SERS) experiments are performed under SE(R)RS conditions and as a result the molecular electronic resonance clearly plays a major role in the extremely large Raman cross-sections obtained from SM-SERS experiments. The best performing and most well researched SM-SERS molecules (e.g. rhodamine 6G, crystal violet) have large fluorescence quantum yields which prevent the measurement of the resonant Raman cross-sections in solution.

Dipyrrin ligands possess strongly allowed π-π* transitions in the visible region, with large transition dipole strengths (absorption coefficients of 20 000 M^{-1} cm^{-1} and oscillator strengths of 0.5). This makes dipyrrin ligands ideal candidates for resonantly enhanced Raman spectroscopies, i.e. resonance Raman and surface-enhanced Raman spectroscopy, both of which rely on enhancement through coupling to dipole-allowed electronic transitions. The advantage of dipyrrin ligands for both resonance Raman and SERS studies is the absence of fluorescence. This allows the resonant Raman cross-sections to be measured accurately, which in turn allows for an accurate assessment of the SERS enhancements.

2.2 Objectives of this work

Surprisingly, prior to our work, there were no publications involving the Raman spectroscopy of dipyrrins. The well-known emission properties of BODIPY complexes and the success of these complexes in fluorescence applications may have obscured the promising Raman properties of the core dipyrrin unit. Our group has recently reported the first Raman spectra[43] and Raman cross-sections for ruthenium-dipyrrin complexes[53] (also see Chapter 4). The ability to obtain a complete characterisation of non-resonant Raman, resonant Raman and surface-enhanced Raman scattering of free dipyrrins is also a very attractive feature for the characterisation of dipyrrinato complexes.

2.3 Background to Raman cross-sections

Raman scattering activity is one of the key parameters in the output of DFT calculations from programs such as Gaussian, typically with the units of Å amu^{-1}. However, there is not a direct relationship between the Raman scattering activity and the relative intensities of the Raman peaks. Rather the Raman scattering activity can be used to determine the non-resonance differential Raman cross-section as follows.

Following the recent publication by Le Ru *et al*[127] the differential Raman cross-section $\left(\frac{d\sigma_{RS}}{d\Omega}\right)$ for a vibrational mode with the frequency $\bar{\upsilon}_i$ is defined as:

$$\frac{d\sigma_{RS}}{d\Omega} = CB_i^2 R_i \bar{\upsilon}_R^4 K(T) \qquad (2.1)$$

C is a constant $\left(C = \frac{\pi^2}{45\varepsilon_o^2} \right)$, $\varepsilon_0 \equiv$ permittivity of free space = 8.8542 x 10^{-12} F m^{-1}.

$B_i^2 = \frac{h}{8\pi^2 c\bar{\upsilon}_{calc}} \left[\text{kg m}^2 \right]$ is the square of the zero point amplitude for the normal mode in reduced mass coordinates.

$\bar{\upsilon}_R$ is the frequency of the Stokes-shifted Raman signal, where $\bar{\upsilon}_R = \bar{\upsilon}_L - \bar{\upsilon}_{calc}$ $\left[\text{m}^{-1} \right]$.

$R_i \left[\varepsilon_0^2 \text{ m}^4 \text{ kg}^{-1} \right]$ is the Raman scattering activity.

$K(T) = \left[1 - \exp\left(\frac{-hc\bar{\upsilon}_{calc}}{kT} \right) \right]^{-1}$ accounts for the thermal population of the vibrational state.[127]

Equation 2.1 gives the differential Raman cross-section in the gas phase. To obtain the predicted liquid phase cross-section a local field correction factor, L, is applied where $L = \left[\frac{(n^2+2)}{3} \right]^4$ and n is the refractive index of the solvent.

Experimental solute differential Raman cross-sections can be obtained relative to solvent cross-sections by:

$$\left(\frac{d\sigma_{RS}}{d\Omega} \right)_{sample} = \left(\frac{d\sigma_{RS}}{d\Omega} \right)_{reference} \cdot \frac{I_{sample}}{I_{reference}} \cdot \frac{c_{reference}}{c_{sample}} \qquad (1.9)$$

where $\left(\frac{d\sigma_{RS}}{d\Omega} \right)_{reference}$ is the differential Raman cross-section of the solvent. These values are reported for a range of solvents (and wavelengths) in the literature. $I_{reference}$ is obtained by integrating the solvent peak corresponding to $\left(\frac{d\sigma_{RS}}{d\Omega} \right)_{reference}$ and I_{sample} is obtained for each peak in the Raman spectrum by integrating each peak. c_{sample} and $c_{reference}$ are the concentration (in mol L^{-1}) of the sample and the concentration of the solvent, respectively. Both non-resonant Raman and resonant Raman cross-sections are obtained in this way while for SERS cross-sections $\left(\frac{d\sigma_{RS}}{d\Omega} \right)_{reference}$ is often an external standard with a known Raman cross-section.

Before proceeding to calculate the resonance Raman and SERS enhancement factors it is important to check the reliability of the experimental non-resonance Raman cross-sections. These can be compared to the calculated non-resonance Raman cross-sections obtained from equation 2.1.

2.4 Experimental details

2.4.1 Computational procedures

All calculations were performed using Gaussian *09*.[145] Calculations were carried out by using density functional theory (DFT), with Becke's three-parameter exchange functional (B3)[146] in combination with the correlation functional of Lee, Yang and Parr (LYP);[147] O3LYP,[148] which has essentially the same form as B3LYP but the OPTX[149] density functional replaces the Becke parameter; and a new hybrid exchange correlation functional M06.[150] The 6-311(+)G (2d,2p) basis set were used for all optimisation and Raman frequency calculations. Self-consistent reaction field methods, more specifically the polarisable continuum model (C-PCM) of Barone,[151] were used to model solvent effects. All geometry optimisations, frequency, and time-dependent calculations were carried out using the C-PCM model. GaussSum2.2.4[152] was used to extract vibrational frequencies and Raman activities from the calculations. The calculated Raman spectrum was scaled by literature values for each functional and basis set,[153-155] and a Gaussian function with FWHM of 5 cm^{-1}. The results of the above calculations were used to analyse and identify the vibrational frequencies, normal modes, and Raman activities. A comparison of the three basis sets was carried out using mean average deviation (MAD) between the experimental non-resonance Raman frequencies and the calculated Raman frequencies (see Figure B1 and Table B1 in Appendix B) and a comparison of the experimental and calculated absorption spectra (see Figure B2 and Table B2 in Appendix B). From this evaluation the B3LYP basis set gave the best results.

Calculations for the electronic excited states were performed using the time-dependent DFT (TD-DFT) calculations with the B3LYP basis set as above. The calculated absorption spectrum is a sum of a series of δ-functions, located at the transition frequencies and scaled by the calculated oscillator strengths. Each δ-function is convoluted with a Gaussian with a FWHM value dependent on the FWHM values of the corresponding peaks of the experimental absorption spectrum. Electron density difference maps were generated by subtracting the ground-state one-particle total density from the one-particle densities for selected excited-states using the Cubeman utility in Gaussian *03*.

2.4.2 Experimental procedures

*2.4.2.1 Synthesis of dipyrrin ligands **34** and **35***

34 and **35** were prepared by following literature procedures[28, 42] and were purified by column chromatography on deactivated neutral alumina using CH_2Cl_2. Spectroscopic data matched that previously published.[26, 28]

2.4.3 General procedures

2.4.3.1 Preparation of samples for non-resonance Raman and resonance Raman spectroscopy

A solution of **34** was prepared in methanol with a concentration of 11.2 mM for non-resonant Raman measurements (1064 nm). A solution of **34** was prepared in dichloromethane with a concentration of 461 μM for resonant Raman measurements using excitation wavelengths of 444 nm, 458 nm, and 488 nm.

2.4.3.2 Preparation of silver nanoparticles

Silver nanoparticles were prepared via the trisodium citrate reduction of silver nitrate according to the method of Lee and Meisel.[156] Briefly, a 1 mM stock solution of silver nitrate and 34 mM solution of trisodium citrate were prepared in Milli-Q water. The silver nitrate stock solution (5 mL) was boiled in a Falconer™ tube before trisodium citrate (0.1 mL) was added and boiled for approximately one hour.

2.4.3.3 Preparation of samples for SERS

The conditions reported by Le Ru *et al.* required for single molecule SERS of rhodamine 6G on silver nanoparticles were used.[157] Briefly, a 40 mM solution of KCl was prepared in Milli-Q water. 0.25 mL of the KCl stock solution was added to a 0.5 mL volume of freshly prepared silver nanoparticles, followed by 0.25 mL of a 2 μM solution of dipyrrin, giving a final concentration of 10 mM KCl and 0.5 μM dipyrrin. This procedure produces consistently large SERS intensities for the cationic rhodamine 6G (sufficient for single-molecule SERS) but no attempt to adjust these conditions to optimize the SERS enhancement of dipyrrins has been made. Excitation wavelengths of 458 nm, 488 nm, and 514.5 nm were used.

2.4.3.4 Raman cross-sections

For non-resonant Raman cross-section measurements in methanol the solute differential Raman cross-sections were obtained relative to solvent cross-sections (equation 1.9) using the solvent band of methanol (1035 cm^{-1}) as an internal standard. The differential cross-section of the solvent band at 1064 nm (7.8 x 10^{-32} cm^2 sr^{-1}) is obtained from the parameters reported by Moran and Kelley[158] (using Mathies and Trulson's A-Term factors).[159] Le Ru *et al*. report an approximate value of 1.8 x 10^{-31} cm^2 sr^{-1} using 633 nm excitation,[127] while Moran's parameters give 7.5 x 10^{-31} cm^2 sr^{-1} for 633 nm excitation. Le Ru *et al.* show that the non-resonant Raman cross-sections of 2-bromo-2-methylpropane (2B2MP) can be accurately calculated using density functional techniques.[127] A B3LYP/6-311(+)G(2d,2p) frequency calculation (with the C-PCM solvent model) of methanol gives a value of 6.9 x 10^{-32} cm^2 sr^{-1} for 1064 nm excitation for the 1035 cm^{-1} band, in very close agreement with the value of Moran, and therefore 7.8 x 10^{-32} cm^2 sr^{-1} has been used in this work. The cross-sections obtained by Moran and Kelley and the data reported here were obtained using similar back-scattering geometries. Dichloromethane was used as an internal standard for measurements of resonant Raman cross-sections. The absolute differential Raman cross-sections of dichloromethane are as follows: 1.789 x 10^{-29} cm^2 sr^{-1} for 444 nm, 1.576 x 10^{-29} cm^2 sr^{-1} for 458 nm, and 1.214 x 10^{-29} cm^2 sr^{-1} for 488 nm.[160] The cross-section of sodium sulfate in water (concentration = 0.100 M) was used as an external standard for the calculation of the SERS cross-sections. The cross-section values are a s follows: 1.606 x 10^{-29} cm^2 sr^{-1} for 458 nm and 1.234 x 10^{-29} cm^2 sr^{-1} for 488 nm.[113]

2.5 Results and Discussion

2.5.1 Synthesis of dipyrrin ligands

The synthesis of ligands **34** and **35** was achieved by literature procedures[28, 31] in two steps (Figure 2.1). The appropriate aldehyde was condensed with pyrrole via an HCl acid catalysed condensation at room temperature, followed by oxidation of the resulting dipyrromethane with DDQ. Purification was achieved via column chromatography on deactivated neutral alumina using CH_2Cl_2.

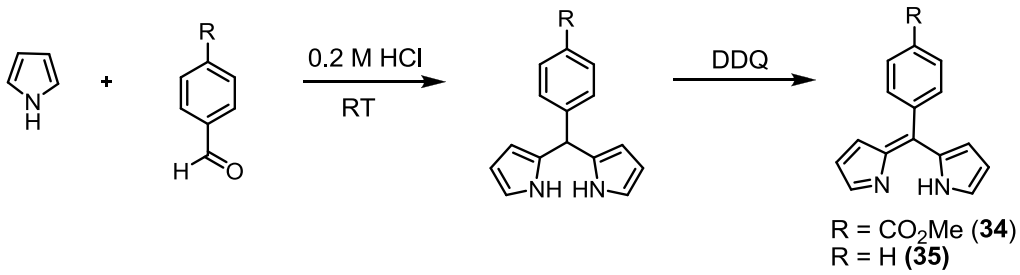

Figure 2.1. Synthetic route to dipyrrins **34** and **35**.

2.5.2 Absorption spectrum and TD-DFT calculations

Figure 2.2 displays the optimised structure of **34** obtained from DFT calculations with the atoms labels used for mode assignments. The pyrrolic rings are co-planar while the phenyl ring makes a torsion angle of 66° with the pyrrolic rings. This reduces the steric interactions of the hydrogen substituents (H_{25}, H_{11}; H_6, H_{18}) but also reduces the conjugation between the dipyrrin core and the phenyl ring.

The position and intensity of the electronic resonance of the molecule play a key role in determining the enhancement in both resonant Raman[161] and SERS.[124, 126, 162] Figure 2.3 shows the experimental and calculated absorption spectra of **34** in methanol.

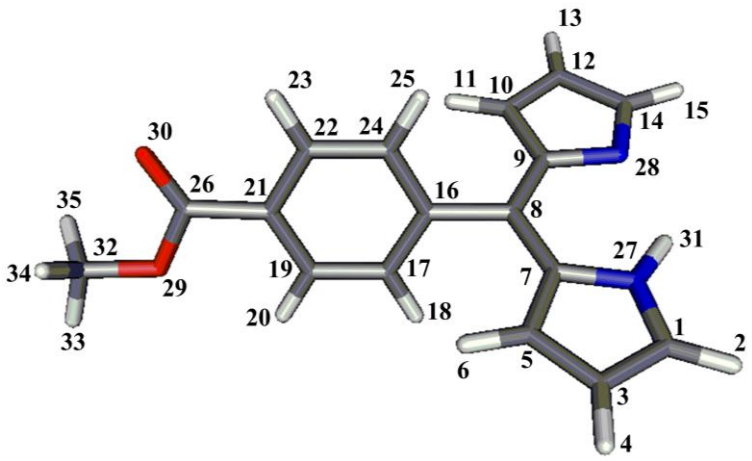

Figure 2.2. Optimised geometry of **34** (DFT/B3LYP 6-311+G (2d, 2p)) with atom labels adopted for mode assignments.

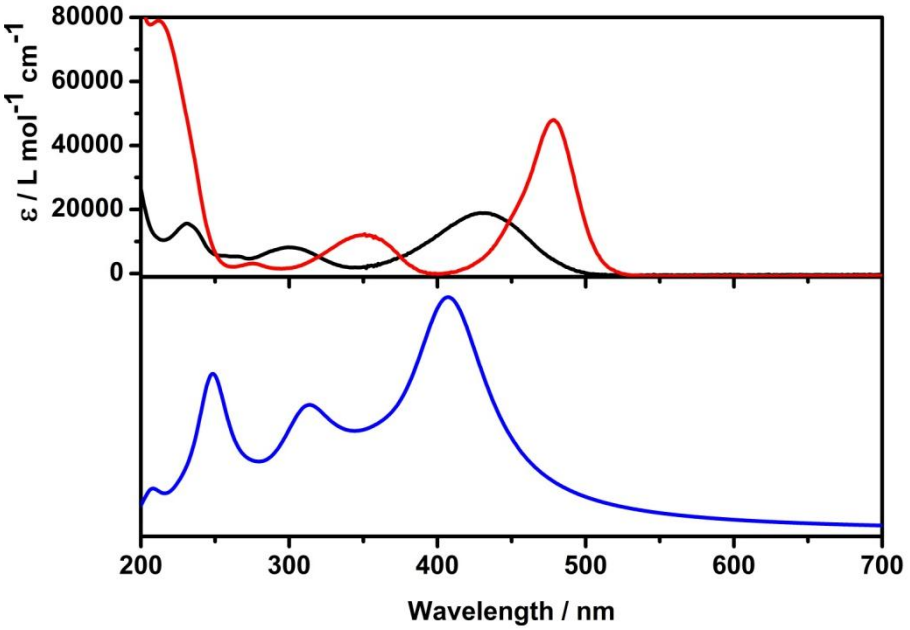

Figure 2.3. Experimental absorption spectra of **34** (top) in methanol (black) and in methanol with TFA (red), and calculated absorption spectra of **34** (bottom) using B3LYP/6-311+G(2d,2p) including C-PCM solvent model. The line shape of the calculated spectrum has been simulated using the calculated oscillator strengths.

Time-dependent DFT (TD-DFT) calculations have been employed to picture the molecular orbitals involved in the electronic transitions of dipyrrin ligand **34**. The DFT calculations show that several one electron configurations contribute to the electronic transitions of **34** (Table 2.1 and Figure 2.4). These one electron configurations are easily visualised using electron density difference (EDD) maps. These maps plot regions of charge-density depletion (green) and accumulation (blue) between the ground and excited-states. Figure 2.5 shows the electron density difference maps for the strongest transitions. The broad dominant transition in the absorption spectrum at 432 nm is assigned as a π-π* transition ($S_0 \rightarrow S_1$). This transition involves the HOMO and LUMO orbitals. The HOMO is confined to the bispyrrolic core of the dipyrrin. The LUMO orbitals involve both the bispyrrolic core and the phenyl ring (Figure 2.4). The calculation predicts this transition to occur at 408 nm. There are two higher energy transitions at 300 nm and 231 nm. The calculation predicts a transition at 339 nm, two closely spaced transitions at 311 and 313 nm, and 248 nm, which are all assigned as π-π* type transitions (Figure 2.5).

Table 2.1. Calculated and experimental absorption parameters for **34**.

Experimental			Calculated		
λ (nm)	ε (L mol^{-1} cm^{-1})[a]	Oscillator strength (f)[a]	λ (nm)	Configuration (% contribution)	Oscillator strength (f)
432	18 900	0.563	408	HOMO→LUMO (95)	0.536
			339	HOMO→LUMO+1 (95)	0.105
			313	HOMO-3→LUMO (97)	0.162
300	8 200	0.382		HOMO-5→LUMO (-23),	
			311	HOMO-2→LUMO (71)	0.054
231	15 600	0.615	248	HOMO-7→LUMO (50),	0.365
				HOMO-3→LUMO+1 (-32),	
				HOMO-2→LUMO+1 (-11)	

[a] The conversion between molar absorptivity (ε) and oscillator strength (f) is outlined in Appendix B2.

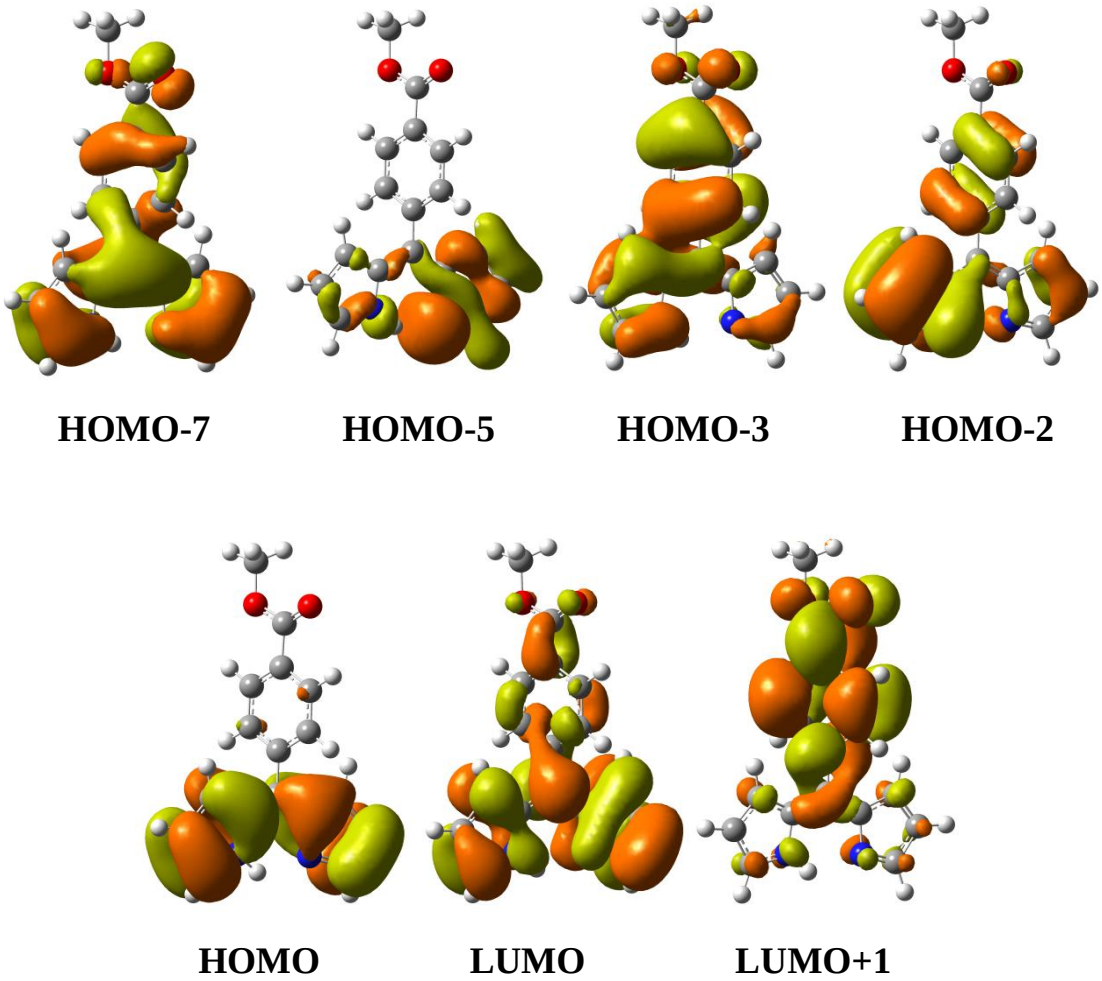

Figure 2.4. Selected molecular orbitals involved in the transitions of **34**.

The plots in Figure 2.5 are a useful guide to interpreting the resonant Raman spectra, as vibrational modes located in regions of large charge-density changes should receive the greatest resonant enhancement. The plots show that there is also significant movement of charge density onto the phenyl ring during the π–π* transition, despite the non-planarity between the phenyl ring and the dipyrrin core. This indicates that functionalising the phenyl ring of the dipyrrin should influence the electronic properties of dipyrrin complexes.

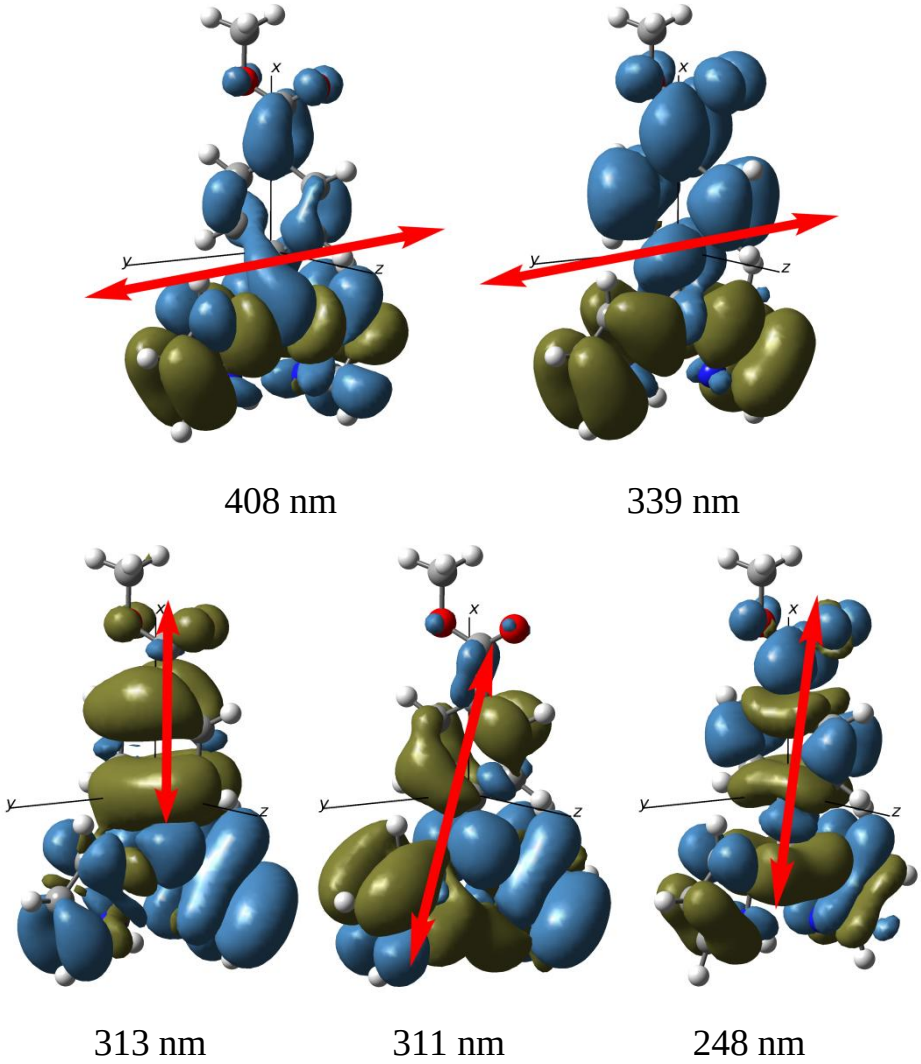

Figure 2.5. Electron density difference plots for **34** with transition dipole moments for each transition indicated in red. The x-plane extends through the phenyl ring, the y-plane extends through dipyrrins pyrrolic core, and the z-plane is perpendicular to the dipyrrins pyrrolic core (coming out of the page). Green represents depletion of electron density and blue represents accumulation of electron density.

The π-π* absorption band at 432 nm was found to be red shifted when acid was added. This was first reported by Brückner *et al*.[26] Significant changes are observed when the basic imine nitrogen of the dipyrrin core is protonated. A red shift of 49 nm is observed in the absorption spectrum (Figure 2.3) of **34** when TFA is added to a methanol solution. The extinction coefficient almost triples while the oscillator strength (f = 0.605) is only slightly larger than the neutral ligand (f = 0.563). A similar red shift is also observed in the π–π* transition upon coordination to a metal centre (Figure 1.13). TD-DFT calculations also predict the pH dependence in the absorption spectrum (Figure B3). The calculations show several configurations which contribute to the electronic transitions of **34** when it is protonated or deprotonated (Table B3). The molecular orbitals and the electron density difference maps associated with the strongest transitions for the protonated and deprotonated ligand are shown in Figure B4-B7. The electron density difference plots of the protonated and deprotonated ligand are very similar to the plots of the neutral ligand. These transitions are all assigned as π–π* type transitions, where for the most part electron density is shifting from the dipyrrin core (green) out towards the phenyl ring (blue).

2.5.3 Non-resonance Raman spectroscopy

The calculated and experimental non-resonant Raman spectra of **34** are shown in Figure 2.6. The calculated frequencies have been scaled by 0.9679. This scaling factor is recommended for the B3LYP/6-311+G (d,p) basis sets and larger.[153] Table 2.2 displays the calculated and experimental non-resonant Raman cross-sections for **34**, mode assignments and mode descriptions as the percentage contribution of redundant internal coordinates to each of the normal modes.

The experimental non-resonant Raman intensities (with 1064 nm excitation) are obtained using the solvent band at 1035 cm^{-1} as an intensity standard. The experimental non-resonant Raman spectrum (in methanol) is limited by concentration and coupled with the weak nature of the Raman effect means only the strongest modes are able to be used to obtain non-resonant Raman cross-sections (using equation 1.9). Only the six strongest modes are observed (q_{66}, q_{69}, $q_{71+}q_{72}$, q_{81}, $q_{82+}q_{83}$, q_{84}) (Figure 2.6C). The Raman cross-sections for these modes are given in Table 2.2 and Figure 2.7 shows the Cartesian displacement vectors for these modes. As expected, modes associated with the dipyrrin core are dominating the non-resonant Raman with some contribution of

modes from the phenyl group. The non-resonant Raman spectrum obtained as a KBr pellet (Figure 2.6B) displays several other Raman active modes. The non-resonant cross-sections for the observed bands in Figure 2.6B were determined by assuming the band at 1576 cm^{-1} has the same cross-section in the solution and solid phases (a reasonable assumption given the experimental error associated with the cross-section measurements). Using a dipyrrin mode as its own internal standard avoids issues with polarisation and concentration when dealing with solid samples. The calculated and experimental values show excellent agreement which provides confidence in the accuracy of the electronic structure calculations.

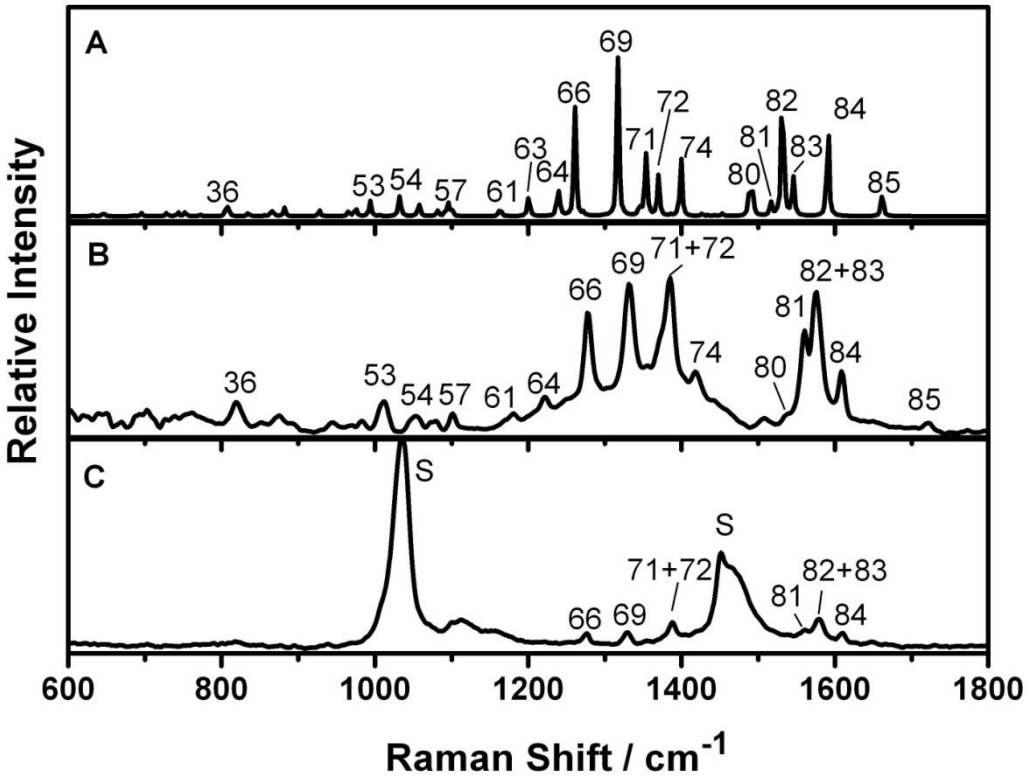

Figure 2.6. Calculated and experimental Raman spectrum of **34** with some normal modes highlighted. (A) Calculated spectrum using DFT/B3LYP 6-311+G (2d,2p) and frequencies are scaled by 0.9679.[153] (B) Non-resonant Raman spectrum as a KBr pellet. (C) Solution non-resonant Raman spectrum [S denotes solvent peaks (MeOH)].

Table 2.2. Mode assignments, mode descriptions and calculated and experimental non-resonant Raman cross-sections for **34**.

Experimental			Calculated[a]			Mode Assignments[e]
Normal Modes	Frequency [cm^{-1}]	$\frac{d\sigma_{nRRS}}{d\Omega}$[b] (solution) [$10^{-28}$ cm^2 sr^{-1}]	$\frac{d\sigma_{nRRS}}{d\Omega}$[c] (solid) [$10^{-28}$ cm^2 sr^{-1}]	Frequency [cm^{-1}]	$\frac{d\sigma_{nRRS}}{d\Omega}$[d] [$10^{-28}$ cm^2 sr^{-1}]	
36	820		0.0189	807	0.0152	$q_{36} = 0.030d_{22,21,26,30}$
42	852		0.0044	866	0.0048	$q_{42} = -0.037d_{8,16,17,18} + 0.044d_{8,16,24,25} + 0.035d_{20,19,21,26} - 0.039d_{26,21,22,23} - 0.036d_{21,22,24,25} + 0.033d_{23,22,24,16}$
44	875		0.0095	881	0.0105	$q_{44} = -0.040d_{2,1,3,4} + 0.033d_{4,3,5,6}$
46	892		0.0033	926	0.0067	$q_{46} = -0.034r_{9,10} - 0.050r_{9,28} + 0.030a_{12,14,15}$
49	945		0.0059	973	0.0100	$q_{49} = 0.056d_{8,16,17,18} + 0.036d_{24,16,17,18} - 0.030d_{16,17,19,20} - 0.088d_{18,17,19,20} - 0.035d_{18,17,19,21} + 0.035d_{20,19,21,22}$
51	983		0.0053	992	0.0192	$q_{51} = 0.101r_{12,14} + 0.032a_{3,5,6} - 0.079a_{10,12,13} + 0.093a_{13,12,14} + 0.048a_{12,14,15} - 0.037a_{15,14,28}$
53	1011		0.0181	1031	0.0251	$q_{53} = -0.062r_{3,5} - 0.056r_{28,31} + 0.109a_{1,3,4} - 0.111a_{4,3,5} - 0.094a_{3,5,6} + 0.074a_{6,5,7}$
54	1052		0.0113	1056	0.0153	$q_{54} = 0.033r_{10,12} - 0.049r_{28,31} + 0.037a_{3,5,6} - 0.035a_{6,5,7} - 0.084a_{9,10,11} + 0.093a_{11,10,12} + 0.058a_{10,12,13} - 0.056a_{13,12,14}$
55	1077		0.0053	1080	0.0059	$q_{55} = -0.047r_{1,3} + 0.063r_{28,31} - 0.032a_{2,1,3} - 0.032a_{3,5,6} + 0.030a_{11,10,12} + 0.030a_{10,12,13} - 0.031a_{13,12,14}$
57	1102		0.0073	1095	0.0133	$q_{57} = 0.046r_{1,27} - 0.121r_{28,31} - 0.062a_{2,1,3} + 0.070a_{2,1,27} + 0.063a_{1,27,31} - 0.054a_{7,27,31}$
60				1160	0.0024	$q_{60} = -0.051r_{9,10} + 0.061r_{9,28} + 0.037a_{8,9,10} - 0.033a_{8,9,28} - 0.055a_{9,10,11} + 0.032a_{11,10,12} - 0.050a_{12,14,15} + 0.040a_{15,14,28}$
61	1179		0.0136	1162	0.0051	$q_{61} = -0.039r_{17,19} + 0.079a_{16,17,18} - 0.081a_{18,17,19} - 0.087a_{17,19,20} + 0.079a_{20,19,21} + 0.071a_{21,22,23} - 0.077a_{23,22,24} + 0.065a_{16,24,25} - 0.065a_{22,24,25}$
63	1222		0.0479	1199	0.0193	$q_{63} = -0.035r_{7,27} + 0.061r_{8,16} - 0.045r_{28,31} - 0.030a_{7,27,31}$
64				1237	0.0158	$q_{64} = -0.034r_{7,27} - 0.034r_{28,31} + 0.037a_{2,1,3} - 0.032a_{2,1,27} - 0.031a_{1,3,4} - 0.057a_{3,5,6} + 0.070a_{6,5,7} + 0.038a_{10,12,13} + 0.035a_{12,14,15}$

						$-0.045a_{15,14,28} - 0.030a_{7,27,31}$
66	1279	0.0313	0.0850	1260	0.0801	$q_{66} = -0.032r_{9,10} + 0.036r_{9,28} - 0.043r_{14,28} + 0.057r_{28,31} + 0.036a_{1,3,4} - 0.039a_{4,3,5} + 0.046a_{3,5,6} - 0.044a_{6,5,7} + 0.032a_{12,14,15} - 0.049a_{15,14,28} + 0.032a_{7,27,31}$
69	1331	0.0310	0.1007	1316	0.1080	$q_{69} = 0.047r_{3,5} + 0.054r_{28,31} + 0.037a_{1,3,4} - 0.034a_{4,3,5} + 0.038a_{6,5,7} - 0.046a_{9,10,11} + 0.042a_{10,11,12} - 0.041a_{12,14,15} + 0.045a_{15,14,28} - 0.031a_{1,27,31} + 0.044a_{7,27,31}$
71+72	1385	0.0778	0.1094	1352 + 1368	0.0802	$q_{71} = 0.055r_{7,8} - 0.033r_{7,27} - 0.039r_{8,16} - 0.035r_{10,12} - 0.031a_{7,8,9} + 0.034a_{15,14,28}$ $q_{72} = -0.055r_{5,7} + 0.050r_{7,27} - 0.058r_{28,31} - 0.039a_{2,1,27} + 0.037a_{4,3,5} - 0.034a_{3,5,6} + 0.063a_{1,27,31} - 0.046a_{7,27,31}$
74	1418		0.0418	1398	0.0364	$q_{74} = 0.054r_{1,3} - 0.037r_{3,5} - 0.035r_{14,28} + 0.036r_{28,31} + 0.042a_{2,1,27} - 0.052a_{1,3,4} + 0.053a_{4,3,5} - 0.032a_{12,14,15} + 0.033a_{15,14,28}$
79	1508		0.0051	1488	0.0199	$q_{79} = -0.038\ r_{8,9} - 0.035a_{16,17,18} + 0.038a_{18,17,19} - 0.035a_{17,19\,20} + 0.031a_{20,19,21}$
80	1538		Weak	1492	0.0111	$q80 = -0.037r_{10,12} - 0.033a_{13,12,14} + 0.034a_{12,14,15} - 0.033a_{16,17,18} + 0.033a_{18,17,19} - 0.035a_{17,19,20} + 0.035a_{20,19,21} + 0.032a_{21,22,23} - 0.035a_{23,22,24} - 0.038a_{16,24,25} + 0.039a_{22,24,25}$
81	1560	0.0393	0.0372	1515	0.0076	$q_{81} = 0.030r_{1,3} - 0.039r_{5,7} + 0.040r_{7,8} + 0.035r_{10,12} + 0.051r_{28,31} + 0.034a_{2,1,27} - 0.042a_{3,5,6} + 0.041a_{6,5,7} + 0.032a_{9,10,11} - 0.041a_{1,27,31} + 0.045a_{7,27,31}$
82+83	1576	0.1125	0.1125	1530 + 1544	0.1083	$q_{82} = -0.031r_{7,8} + 0.053r_{8,9} - 0.034r_{14,28} - 0.032a_{12,14,15}$ $q_{83} = -0.030r_{8,9} - 0.042r_{16,17} + 0.043r_{16,24} + 0.048r_{19,21} - 0.046r_{21,22} - 0.033a_{18,17,19} + 0.036a_{17,19,20} - 0.032a_{23,22,24} + 0.035a_{22,24,25}$
84	1609	0.0221	0.0261	1590	0.0478	$q_{84} = -0.037r_{16,17} - 0.035r_{16,24} + 0.067r_{17,19} - 0.036r_{19,21} - 0.039r_{21,22} + 0.068r_{22,24} + 0.034a_{17,16,24} + 0.055a_{16,17,18} - 0.038a_{18,17,19} - 0.039a_{17,19,20} + 0.056a_{20,19,21} + 0.034a_{19,21,22} + 0.057a_{21,22,23} - 0.040a_{23,22,24} + 0.055a_{16,24,25} - 0.036a_{22,24,25}$

[a] DFT/B3LYP 6-311G (2d,2p) with C-PCM model

[b] Raman cross-sections were calculated using equation 1.9

[c] Raman cross-sections were calculated relative to the 1576 cm^{-1} band, assuming the cross-sections are the same in the solution and solid phases

[d] Raman cross-sections were calculated using equation 2.1 with the local field correction factor applied

[e] Only contributions greater than 0.03 are displayed

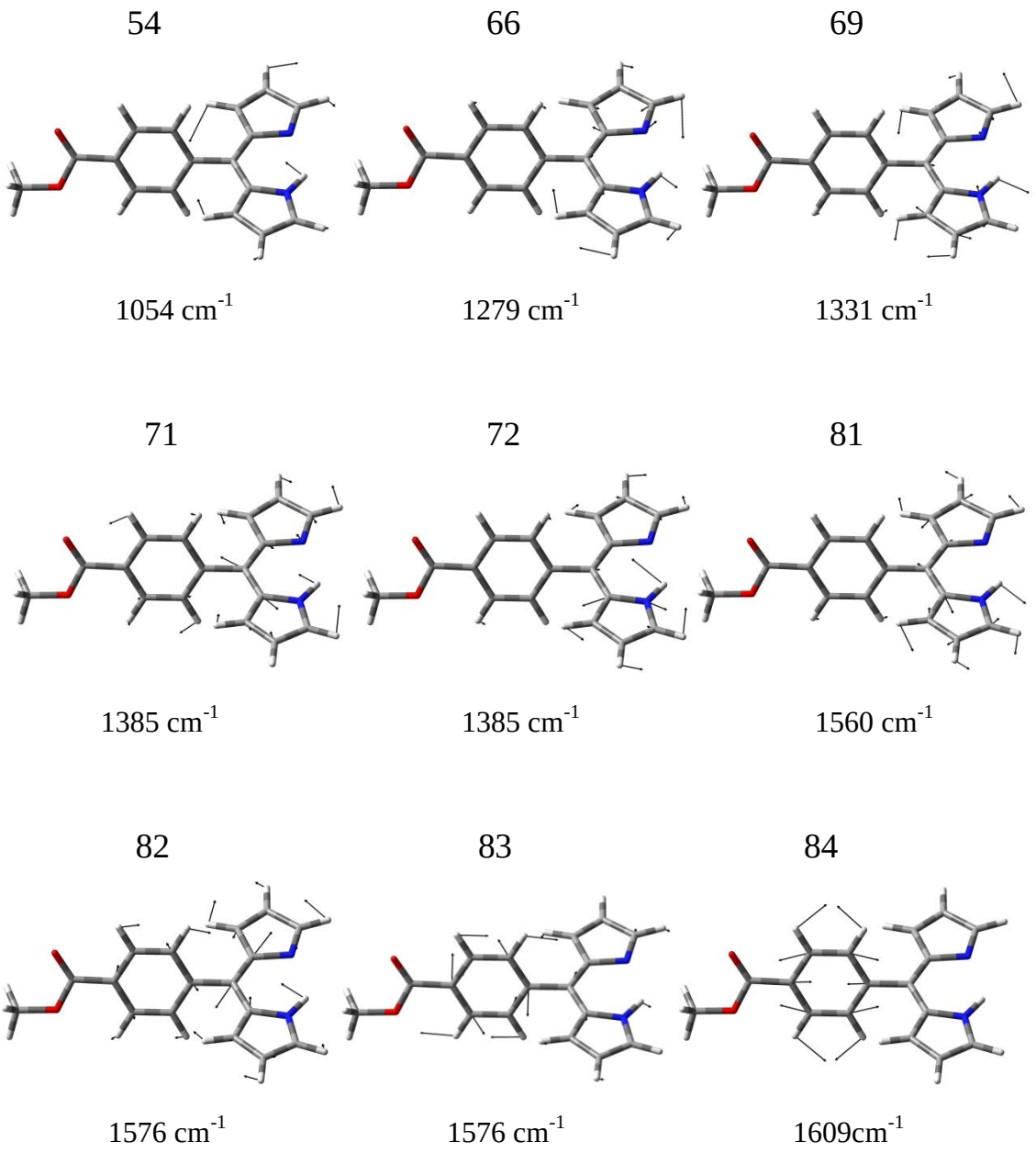

Figure 2.7. Selected normal modes of **34**. Arrows represent the displacement of atoms.

2.5.4 Resonance Raman spectroscopy, resonance cross-sections and enhancement factors

The resonant Raman excitation wavelengths employed (444 nm, 458 nm, 488 nm) are closely resonant with the π-π* transition. They are also on the red edge of the transition of interest which avoids any complication of pre-resonance enhancement from the higher energy transitions. As can be seen from Figure 2.8 most features that are in the non-resonant Raman spectrum (Figure 2.8D) are also common to all the resonant Raman spectra (Figure 2.8A-2.8C).

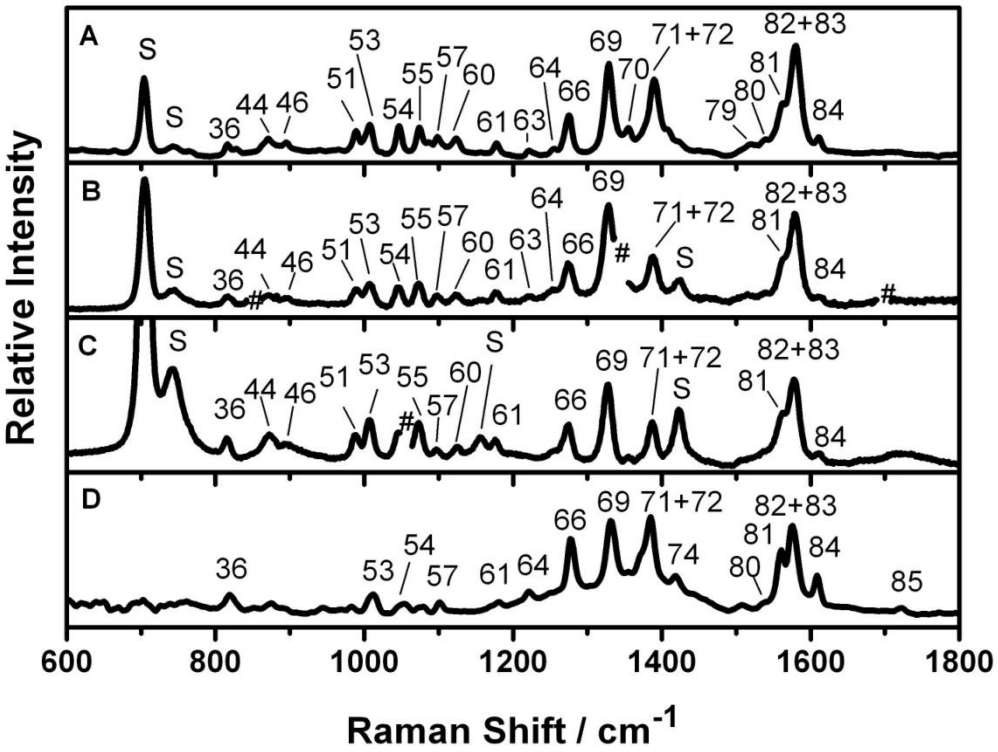

Figure 2.8. Non-resonant Raman and resonant Raman spectra of **34** with normal modes assigned. Resonant Raman spectra were collected at (A) 444 nm, (B) 458 nm, and (C) 488 nm. [S denotes solvent peaks (CH_2Cl_2), # denotes laser lines]. (D) Non-resonant Raman spectrum was recorded as a KBr pellet.

Table 2.3 gives the resonant Raman cross-sections and resonant Raman enhancement factors for **34**, for 444 nm, 458 nm, and 488 nm excitation. At 444 nm the resonant Raman cross-sections are on the order of 10^3-10^5 times larger than the non-resonant Raman cross-sections, consistent with resonance with a strongly allowed π–π^* transition. As the laser excitation moves away from the electronic transition (at 432 nm), the resonant Raman cross-sections decrease by at least an order of magnitude.

The strongest modes in the resonance Raman spectra are mode 82+83 and mode 69. The strong enhancement of these modes is consistent with the electronic structure calculations that show that during the π–π^* transition substantial electron density changes occur in the dipyrrin core and over the phenyl ring. Mode 83 is predominantly a phenyl ring deformation; mode 69 is predominantly a pyrrole ring deformation, while mode 82 has significant deformation of both the phenyl ring and the pyrrole rings. The absence of the C=O bond stretch (of the ester) illustrates that the π-π^* transition does not extend on to the ester, which is again consistent with the electron density plots.

The low symmetry of the dipyrrin systems and the extensive delocalization of the electron density changes provide an explanation for the enhancement of nearly all the vibrational modes. Consequently, all modes are enhanced via A-term scattering (therefore the ground and excited π–π^* state are Frank-Condon coupled). Under Franck-Condon coupling, the oscillator strength of the electronic transition and the mode displacements between the ground and excited-states determine the mode intensities. Both modes 82 and 83 (Figure 2.7) show significant deformation of both the phenyl ring and the pyrrolic core. The large intensity of these modes implies that substantial structural reorganization of the phenyl ring and the pyrrolic core is occurring in the π–π^* excited-state.

Dipyrrins are considered to be "half-porphyrin" systems and therefore it is appropriate to make some comparison between the electronic structures and resonant Raman features of *meso*-substituted dipyrrins and tetraphenylporphyrin species. In tetraphenylporphyrin (TPP) systems the enhanced modes indicate that the excitation into the Soret bands is limited to the porphyrin core and does not typically extend out to the phenyl rings. The phenyl modes in TTP are only weakly enhanced via resonance with the strongly allowed Soret bands (by A-term enhancement), and the enhancement is typically ascribed to intensity borrowing from nearby pyrrole modes.[163-165] Weak electronic conjugation between the phenyl ring and the porphyrin π-system and poor coupling between the phenyl and pyrrole vibrational modes is the cause of the weak enhancement.[164] This is in stark contrast to the strong enhancement of the phenyl modes of *meso*-substituted dipyrrin ligands. In the dipyrrin system the strong enhancement of the phenyl modes together with the electronic structure calculations indicate that the π-systems of the phenyl and dipyrrin core interact strongly. Therefore substituents on the phenyl ring should have an influence on the electronic properties of dipyrrin compounds.

Table 2.3. Experimental Raman cross-sections for non-resonant Raman and resonant Raman data, and resonant Raman enhancement factors for **34**.

Normal modes	Frequency	444 nm		458 nm		488 nm	
		$\frac{d\sigma_{RRS}}{d\Omega}$ [a]	EF[b,c]	$\frac{d\sigma_{RRS}}{d\Omega}$ [a]	EF[b,c]	$\frac{d\sigma_{RRS}}{d\Omega}$ [a]	EF[b,c]
	[cm^{-1}]	[10^{-28} cm^2 sr^{-1}]	[10^4]	[10^{-28} cm^2 sr^{-1}]	[10^4]	[10^{-28} cm^2 sr^{-1}]	[10^4]
36	819	1015	5.4	539	2.9	119	0.6
44	870	2093	22.1	750	7.9	219	2.3
46	895	1607	49.1	102	3.1	302	9.2
49	938	1172	19.7				
51	989	1681	32.0	573	10.9	123	2.3
53	1007	2398	13.3	720	4.0	241	1.3
54	1047	1793	15.8	504	4.4	177	1.6
55	1074	1876	35.6	693	13.1	243	4.6
57	1099	1757	24.0	239	3.3	36	0.5
60	1123	1691		475		80	
61	1178	900	6.6	508	3.7	91	0.7
63	1222	255	0.5	521	1.1		
64	1255	166		590		58	
66	1275	3234	3.8	1731	2.0	208	0.2
69	1329	8882	8.8	5236	5.2	484	0.5
70	1355	1863					
71+72	1390	10126	9.3	2007	1.8	253	0.2
74	1410	629	1.5				
79	1518	936	18.5	380	7.5	9	0.2
80	1538	841				62	
81	1561	3889	10.5	1573	4.2	355	1.0
82+83	1580	13608	12.1	3636	3.2	605	0.5
84	1612	544	2.1	42	0.2	10	0.04

[a] Raman cross-sections were calculated using equation 1.9 and the solvent band of dichloromethane at 701/740 as the reference[158]

[b] $EF = Enhancement\ Factor = \frac{\frac{d\sigma_{RRS}}{d\Omega}}{\frac{d\sigma_{nRRS}}{d\Omega}}$

[c] EF's are relative to the non-resonant (solid) Raman cross-sections

Despite their importance in studies of SERS, to the best of our knowledge there are no reports of direct measurements of resonant Raman enhancement factors for commonly used dyes in SERS experiments. This is because it is not routine to undertake the measurement of the non-resonant cross-sections and also the most common SERS dyes typically have very large fluorescence cross-sections which prevent the measurement of resonance Raman spectra.

There are several reports of resonant cross-sections for strongly enhanced Raman scatterers with visible excitation such as betaine-30 (maximum cross-section ~1.6 x 10^{-25} cm^2 sr^{-1} for the 1320 cm^{-1} band),[166] the non-linear chromophore julolidinyl-n-N,N'-diethylthiobarbituric acid (JTB) (maximum cross-section of ~7 x 10^{-24} cm^2 sr^{-1} for the 976 cm^{-1} band),[158] the azo dye disperse red (a maximum *total* (absolute) cross-section of ~6.0 x 10^{-25} cm^2 for the 1336 cm^{-1} band),[167] and $[Ru(bipy)_3]^{2+}$ (~1.0 x 10^{-24} cm^2 sr^{-1} for the 1544 cm^{-1} band)[168] which are similar in magnitude to the values reported here for dipyrrin **34** (maximum cross-section value is 1.36 x 10^{-24} cm^2 sr^{-1} for the 1580 cm^{-1} band). This implies that dipyrrins have desirable electronic properties and electronic enhancement to be candidates for single-molecule SERS investigations.

2.5.5 Surface-enhanced Raman spectroscopy, surface-enhanced cross-sections and enhancement factors

There are a number of factors that affect the magnitude of the SERS enhancement. A complicating factor is the definition of the enhancement factor itself. Most studies of SERS enhancement factors define the average SERS enhancement factor (equation 2.2) as:[127]

$$EF = \frac{I_{SERS} / N_{Surf}}{I_{RS} / N_{Vol}} \qquad (2.2)$$

where $N_{Vol} = c_{RS}V$ is the average number of molecules in the scattering volume (V) for the non-SERS measurement and N_{surf} is the average number of molecules *adsorbed* in the scattering volume for the SERS measurements. Le Ru *et al*. have presented the problems associated with this definition,[127] with the consequence being that there could be large variations in the enhancement factors reported.

Silver nanoparticles prepared via the citrate reduction of silver nitrate have been reported to be heterogeneous size distribution with diameters between 10-200 nm with various shapes such as rods and triangles.[169] We confirmed the size and shape of our nanoparticles by TEM images (Figure 2.9). In typical samples, the nanoparticles were approximately spherical in shape, though some nanorods were also present. Of the images we analysed, approximately 70% were nanoparticles with an average diameter of 48 ± 9 nm and 30% were nanorods with an average diameter of 41 ± 7 nm and length of 84 ± 28 nm. The total available surface area can be expressed by assuming that all

the nanoparticles are spherical with an effective diameter of 52 ± 10 nm. These uncertainties, together with an estimate of the uncertainty in the Raman intensities, allow us to estimate the uncertainty in the enhancement factors (below). We estimate the uncertainty in the enhancement factors to be approximately 20%.

Knowledge of the size and shape distribution of the nanoparticles enables an estimation of the concentration of the adsorbate required for monolayer coverage of the silver nanoparticles and therefore the SERS enhancement factors can be accurately calculated. The concentration of dipyrrin required for monolayer coverage can be estimated using the following approximations. Assuming spherical nanoparticles with an effective diameter of 52 nm then the total available surface area can be estimated. The approximate nanoparticle concentration can be obtained from the concentration and volume of the silver nitrate stock solution and fundamental constants for bulk silver. The footprint of the dipyrrin molecule can be estimated using the DFT calculation (assuming that the pyrrolic core of the dipyrrin interacts with the nanoparticle surface and that this is the dominant binding mode). The ratio of the surface areas gives the number of dipyrrin molecules required per nanoparticle and finally the concentration of dipyrrin required for monolayer coverage. For monolayer coverage of 50 nm diameter nanoparticles we estimate N_{surf} to be 2.91 x 10^4 dipyrrin molecules per silver nanoparticle and therefore an estimated concentration of 7.6 μM dipyrrin is required for monolayer coverage. Given that our nanoparticles range in size between 50-70 nm, this means that the concentration of dipyrrin required for monolayer coverage is lower, as the nanoparticles get larger. Therefore this estimation is more reliable for larger diameter nanoparticles.

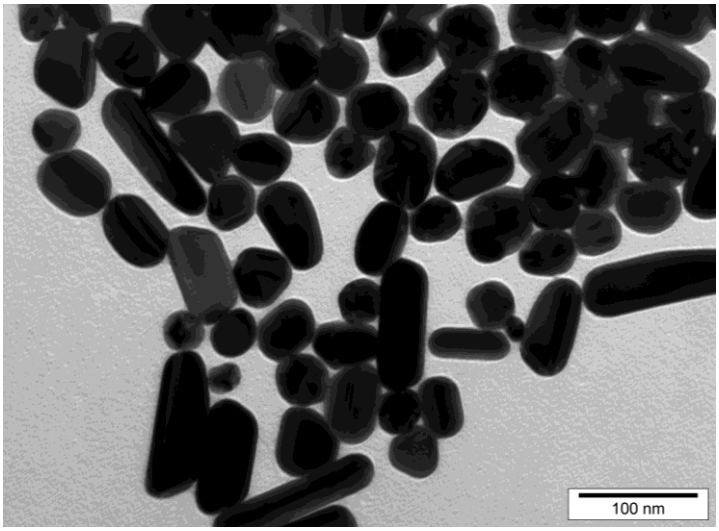

Figure 2.9. A typical TEM image of silver nanoparticles prepared via the Lee & Meisel[156] method.

Table 2.4 displays the Raman cross-sections for Surface-Enhanced Raman Scattering and the electronic and (total) SERS enhancement factors for **34**. Figure 2.10 shows the SERS spectra of **34** with mode assignments shown. The observed SERS cross-sections are approximately 10^1-10^2 orders of magnitude larger than resonance Raman cross-sections. The corresponding electronic and SERS (or *total*) enhancement factors have similar relative values. This illustrates that for dipyrrin ligands the majority of the enhancement arises from electronic origins at least for the conditions used in this study. Le Ru *et al*. have estimated that the maximum average SERS enhancement factors are in the range of ~ 10^{10} – 10^{12} for SERS experiments. A value of 10^{10} is estimated for typical SERS experiments and a value of 10^{12} under the best possible conditions.[127] In our work we have made no attempt to maximise the position of the plasmon with respect to the excitation wavelength or to match the plasmon resonance with the molecular resonance of the dipyrrin ligand. Our maximum enhancement values on the order of 10^6 suggest that there is scope to improve the SERS intensity of dipyrrin ligands.

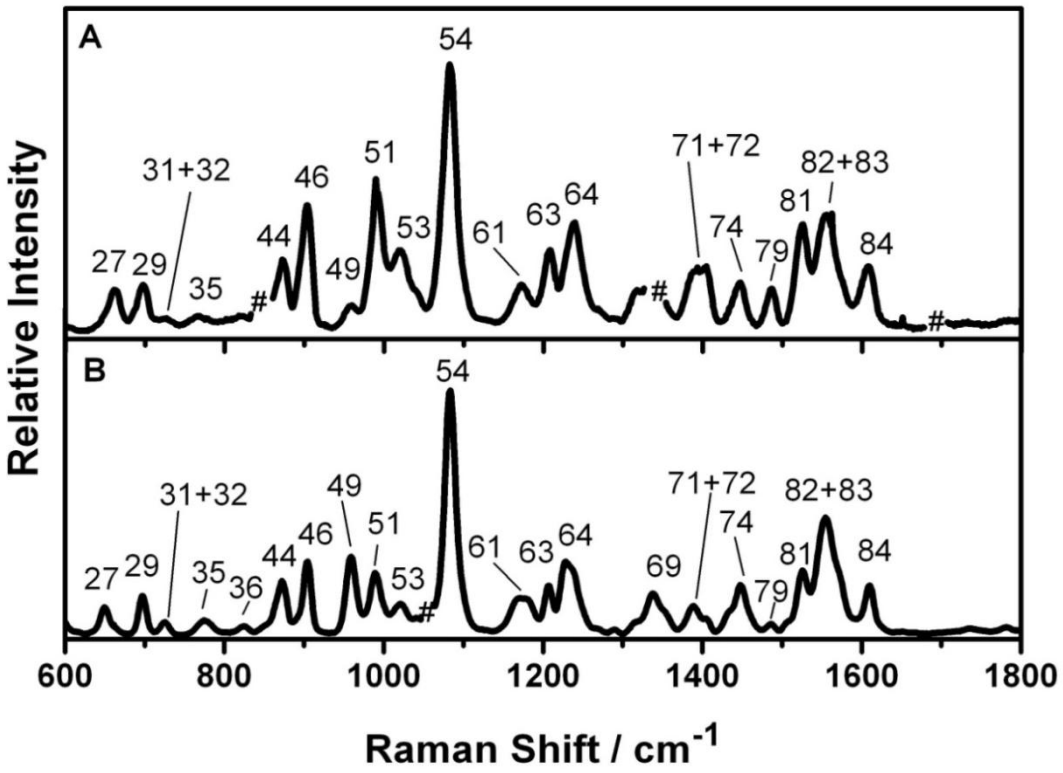

Figure 2.10. Surfaced-enhanced Raman spectra of **34** on silver nanoparticles with normal modes highlighted. (A) 458 nm. (B) 488 nm. [# denotes laser lines].

Modes were assigned based on the DFT calculation; however, there were discrepancies where there were interactions of some modes with the silver nanoparticle surface. For instance the modes 81 and 82+83 have significantly shifted frequencies but they can be assigned based on the pattern they exhibit in the non-resonance Raman spectrum. The SERS spectra show that most of the vibrational modes are enhanced. It is noted that enhancement of most of the vibrational modes in the resonant Raman spectra was also observed. However, the pattern of enhancement is somewhat different and the strong enhancement of mode 54 is particularly evident along with modes 46, and 51, and to a lesser extent, modes 63 and 64. No attempt has been made to complete a detailed analysis of the SERS modes and therefore the underlying enhancement mechanisms have not been determined in this work. However, we can suggest that the possible explanation for the strong enhancement of mode 54 is due to the interaction of the dipyrrin core of **34** with silver nanoparticles. Mode 54 is an in-plane dipyrrin deformation (as are modes 46, 51, 63 and 64) and we reason that since mode 54 is strongly enhanced (as well as the enhancement of modes 46, 51, 63, and 64), that the

dipyrrin core must be interacting/binding to the silver nanoparticles via the nitrogen atoms.

Table 2.4. Normal modes and Raman cross-sections for experimental SERS data for **34**.

		458 nm			488 nm		
Normal Modes	Frequency [cm^{-1}]	$\frac{d\sigma_{SERS}}{d\Omega}$ [a] [10^{-28} cm^2 sr^{-1}]	Total EF [b,c] [10^4]	Electronic EF [d] [10^4]	$\frac{d\sigma_{SERS}}{d\Omega}$ [a] [10^{-28} cm^2 sr^{-1}]	Total EF [b,c] [10^4]	Electronic EF [d] [10^4]
18	402	6499					
19	410	10618					
21	454	1055					
22	492	2851					
23+24	587	398			11985		
25	603	1503					
27	655	5916			8126		
29	697	4946			9734		
31+32	726	1415			2411		
35	772	4244			6098		
36	822	4863	25.8	2.9	1688	9.0	0.6
44	872	7504	79.2	7.9	18483	195.2	2.3
46	903	11464	350.0	3.1	18270	557.8	9.2
51	990	13528	257.5	10.9	21903	416.9	2.3
53	1021	9326	51.6	4.0	11255	62.3	1.3
54	1054	30036	264.8	4.4	97646	861.0	1.6
61	1173	4187	30.7	3.7	9864	72.4	0.7
63	1207	5738	12.0	1.1	9672	20.2	
64	1238	15177			22375		
69	1338	4500	laser[e]	5.2	17404	17.3	0.5
71+72	1389	7236	6.6	1.8	9607	8.8	0.2
79	1485	1758	34.7	7.5	2093	41.3	0.2
81	1525	7822	21.0	4.2	14689	39.5	1.0
82+83	1555	19782	17.6	3.2	67653	60.1	0.5
84	1609	5707	21.8	0.2	12914	49.4	0.04

[a] Raman cross-sections were calculated using equation 1.9 and Na_2SO_4 as an external reference[113]

[b] $Total\ Enhancement\ Factor = \frac{\frac{d\sigma_{SERS}}{d\Omega}}{\frac{d\sigma_{nRRS}}{d\Omega}}$

[c] EF's are relative to the non-resonant (solid) Raman cross-sections

[d] Electronic Enhancement Factor $= \frac{\frac{d\sigma_{RRS}}{d\Omega}}{\frac{d\sigma_{nRRS}}{d\Omega}}$

[e] obscured by laser line

The different intensity patterns under the non-resonant, resonant and surface-enhanced conditions reflect the mechanisms responsible for generating the Raman scattering in each case. Under non-resonant conditions, the polarisability in the ground state controls the intensity of the observed modes, and therefore modes with large polarisabilities are expected to have large intensities. However, under resonant conditions, the origin of the electronic transition controls the mode intensities, and for strongly allowed electronic transitions, such as $\pi-\pi^*$, the scattering will be dominated by A-term scattering.[170] The selection rules for A-term dictate that only modes that are totally symmetric within the ground and excited states will be resonantly enhanced. The large electronic enhancements mean that many modes that were below the noise in the non-resonant spectrum now appear with significant intensity in the resonant Raman spectrum. A similar number of modes are observed between the resonant and surface-enhanced spectra. However, the pattern of enhancements is different and this is a result of additional enhancements from resonance with the plasmon modes of the silver nanoparticles. Under plasmon enhancement conditions, Herzberg-Teller coupling between the ground and other electronic excited-states of the system leads to enhancement of both non-totally symmetric and totally symmetric modes and therefore this explains the appearance of the SERS spectra (relative to the resonance spectrum). The same effect can be used to explain the differences in intensities and enhancement factors obtained with different excitation wavelengths in the SERS measurements. Those modes that show noticeable changes in intensity between 458 nm and 488 nm excitations are modes 46, 50, 51, 79 and 81. Intuitively we expect that the excitation wavelength closest to the plasmon resonance of the silver nanoparticles (around 420 nm) would have the greatest enhancement, however, Table 2.4 shows that the SERS enhancement factors are overall slightly larger for 488 nm excitation than with 458 nm excitation. At 458 nm the excitation is closely resonant with the $\pi-\pi^*$ transition of the dipyrrin, but due to the scattering from coupled plasmon modes[129, 171, 172] of a small fraction of silver nanoparticles (or "hotspots"), the plasmon resonance is likely to be significantly red shifted. The consequence of this is that enhancement via the red shifted plasmon resonance would be expected to be stronger for the 488 nm excitation (i.e. at 488 nm excitation, the electronic resonance with the $\pi-\pi^*$ transition decreases but this decrease is compensated for by being in proximity with the plasmon resonance), and this is observed in the enhancement factors (Table 2.4).

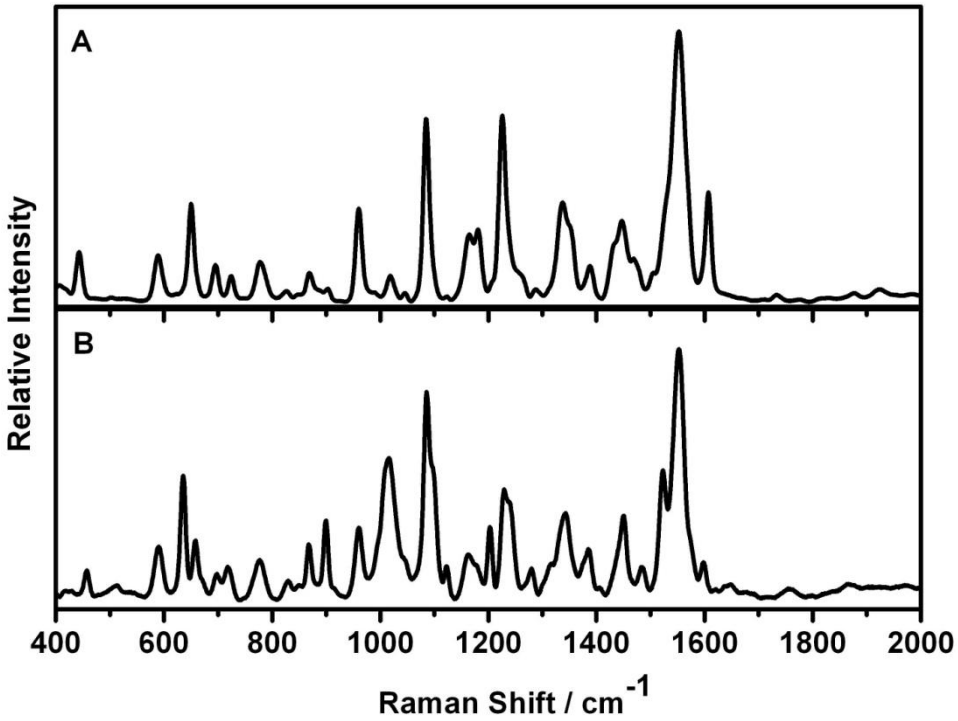

Figure 2.11. SERS spectra of at 514.5 nm for (A) **34**, and (B) **35**.

The SERS spectra of **34** and **35** were briefly investigated to determine how dipyrrins are interacting with the silver nanoparticles. The SERS spectra were observed to be virtually identical for both dipyrrins (Figure 2.11) therefore ruling out an interaction between the carbonyl group and the silver nanoparticle surface as the dominant binding mode. The SERS phenomenon is distance dependent and given that the C=O stretch is absent in SERS spectra of **34** (Figure 2.10) this adds weight to this conclusion.

2.6 Summary

The first full characterisation of dipyrrin ligands by Raman spectroscopy is presented in this chapter. Absolute differential cross-sections are obtained for non-resonant, resonant and surface-enhanced Raman spectra at a variety of wavelengths (visible and near infrared). The experimental non-resonant cross-sections show excellent agreement with the calculated non-resonant cross-section using DFT calculations. The Raman enhancement factors for resonant Raman and surface-enhanced Raman scattering are determined. The magnitudes of the resonantly enhanced cross-sections are similar to those recently reported for strong SERS dyes such as rhodamine 6G and crystal violet. With strong resonant enhancement, absence of fluorescence and facile synthetic

chemistry, dipyrrins possess all the required properties for fundamental studies of single-molecule SERS and also for a broad range of bioanalytical applications.

2.7 Future work

A recent publication reports the simple synthesis of silver nanoparticles which utilises halides to precisely tune the surface plasmon resonance across the visible region of the absorption spectrum.[173] Using this preparation for the silver nanoparticles we could easily match the plasmon resonance with the molecular resonance of the dipyrrin ligand as well as ensuring the position of the plasmon resonance with the excitation wavelength is maximised. In turn this should allow us to complete a more detailed SERS analysis and therefore endeavour to determine the underlying enhancement mechanisms.

Acknowledgements

I wish to thank the following people for their assistance in this chapter: Dr Mark Waterland for running the DFT calculations, Professor Keith Gordon (University of Otago) for allowing a laboratory visit to collect resonance Raman data for **34**, Dr Cushla McGoverin (University of Otago) for collecting non resonance Raman data and Mr Doug Hopcroft from the Manawatu Microscopy and Imaging Centre (MMIC) for acquiring TEM images of the silver nanoparticles.

Chapter 3

Exciton interactions in metallodipyrrins

3.1 Introduction

A characteristic feature of dipyrrins is that they possess a large transition dipole moment. The transition dipole moments of BODIPY chromophores are well defined[25, 174, 175] as lying in the chelate plane and parallel to a line connecting the nitrogen donor atoms (Figure 3.1A). It is assumed that the transition dipole moment of dipyrrin ligands is also found in the same position (Figure 3.1B). DFT calculations of the dipyrrin ligand **34** confirm that the position of the transition dipole moment (for the lowest energy transition) lies within the plane of the dipyrrin core parallel to the nitrogen donor atoms (Figure 3.2). The position of the transition dipole moment generates a strong π-π* transition (ε ~ 20,000 L mol^{-1} cm^{-1} per ligand) in the visible region (~430 nm).

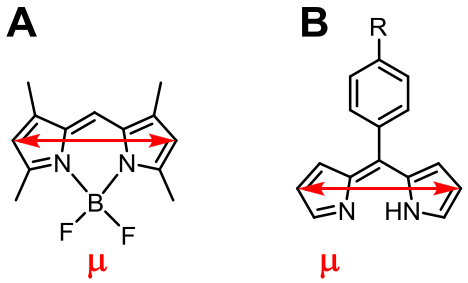

Figure 3.1. (A) The orientation of the transition dipole moment (μ) of BODIPY chromophores (refer to Figure 2 in reference 174). (B) The orientation of the transition dipole moment (μ) for the lowest energy ($S_0 \rightarrow S_1$) π-π* transition of dipyrrins.

When two or more dipyrrin units come into close proximity, for example by coordinating to a metal centre, the transition dipole moments interact strongly, owing to the strength and close spatial proximity of the chromophores (Figure 3.3). This leads to new excited electronic states that are delocalized across the dipyrrin units, described as *molecular excitons*.

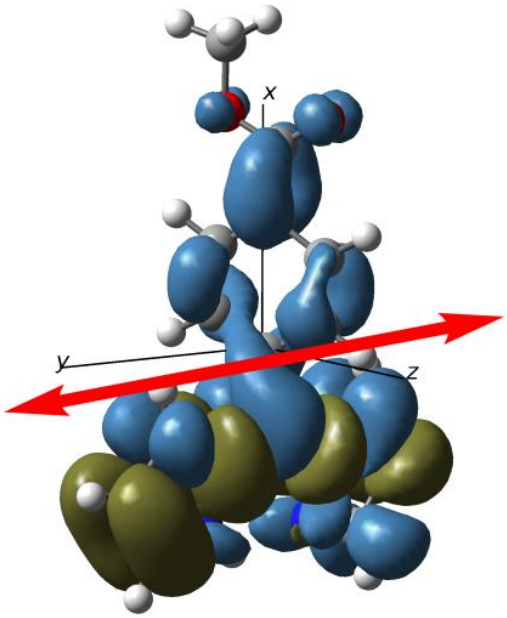

Figure 3.2. DFT output of **34** illustrating the position of the transition dipole moment for dipyrrin ligands. The coordinates of the transition dipole moment (in red) are (*x*, *y*, *z*) (0.262, -2.661, -0.222), and the dipole is oriented approximately along the y-axis.

Exciton interactions are observed in both absorption spectroscopy as the appearance of strong spectral shifts or splitting of the absorption bands and in circular dichroism spectroscopy as positive and negative Cotton effects for a non-racemic complex (Figure 1.14).[88]

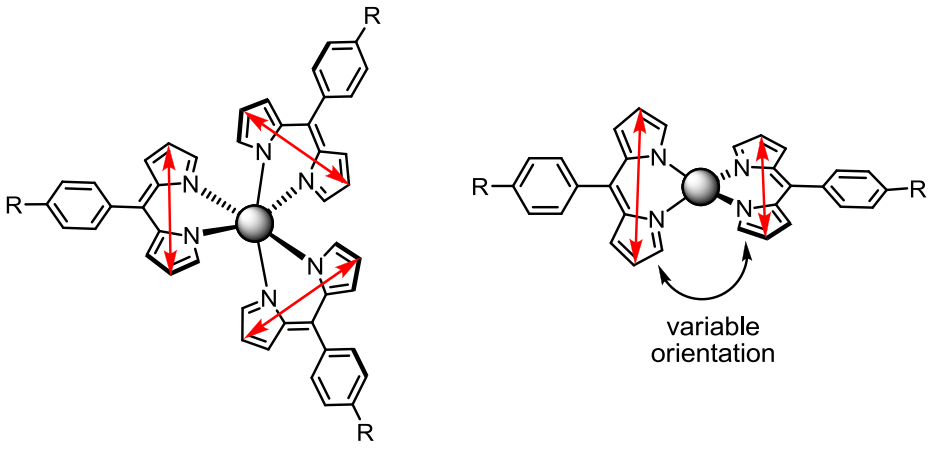

Figure 3.3. Orientation of transition dipole moments for [ML_3] and [ML_2] dipyrrinato complexes.

3.2 Background to exciton coupling

The two simplest cases of exciton coupling occur when a pair of degenerate chromophores are aligned either in (i) a parallel or (ii) a co-linear manner. The two degenerate chromophores couple to give two non-degenerate excited states. Alternatively, three degenerate chromophores (with three-fold rotational symmetry) can couple to give a single non-degenerate excited state (A) and two degenerate excited (E) states (see later). Exciton interactions result in the splitting of the excited state energy levels which are degenerate or near degenerate in the absence of exciton interactions.

If the transition dipoles are parallel (Figure 3.4A), then on electrostatic grounds there will be electrostatic attraction (X′) from "head-to-head" addition of the dipole vectors. This results in a zero net transition dipole and transitions to this state are dipole-forbidden. An electrostatic repulsion (X″) results from "head-to-tail" addition of the dipole vectors. This gives a transition dipole with twice the length relative to an unperturbed chromophore and transitions to this state are dipole-allowed. [Unperturbed chromophore refers to a chromophore where exciton coupling does not exist; e.g. [M**L**X] where **L** is a single dipyrrinato ligand and X is another ligand]. The physical consequences for the electronic absorption spectrum are that the dipole allowed electronic transition will be *blue-shifted* with respect to the transition of an unperturbed chromophore.

If the transition dipoles are co-linear (Figure 3.4B), there will be electrostatic attraction (X′) from "head-to-head" addition of the dipoles which results in a forbidden transition. The electrostatic repulsion (X″) from the "head-to-tail" addition of the dipoles results in an allowed transition. Now the dipole allowed electronic transition for the complex will be *red-shifted* with respect to an unperturbed chromophore. The net length of the summed vectors (dipoles) is proportional to the integrated area of the absorption band of the new exciton states. The integrated area of the absorption band for the new exciton states will be twice that of an unperturbed chromophore.

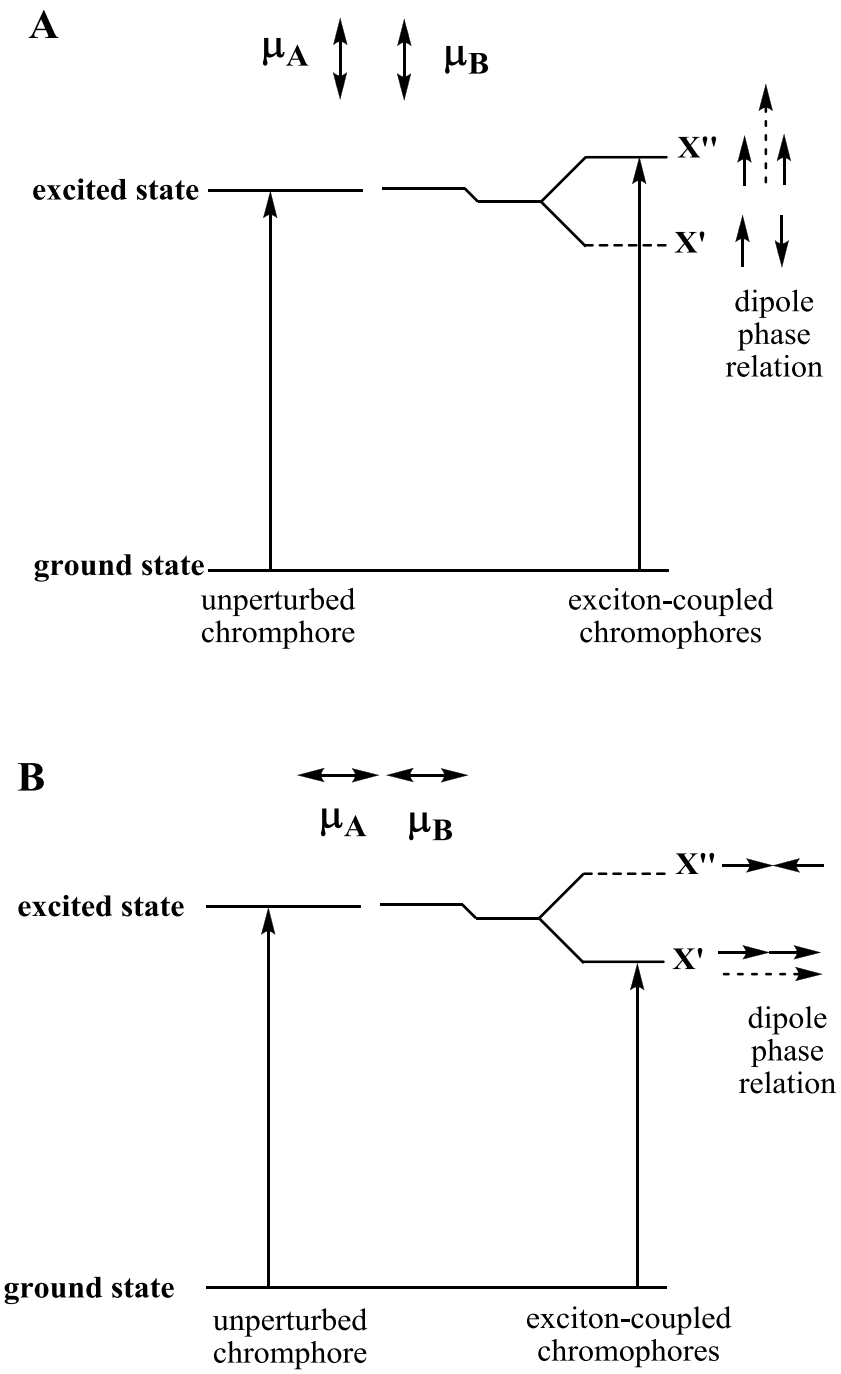

Figure 3.4. Exciton energy diagram where non-degenerate exciton states, X″ and X′, are produced for chromophores in close spatial proximity when the transition dipole moments of the degenerate chromophores are aligned in (A) a parallel manner or (B) a co-linear manner. Allowed transitions are denoted by vertical arrows.

Examples of parallel transition dipoles and co-linear transition dipoles are H-type and J-type dimers in rhodamine 6G[162, 176, 177] (Figure 3.5). The interaction between the transition dipole moments is governed by the geometry of the aggregates. For H-type

dimers, which have a head-to-head addition of their transition dipoles, the absorption is predicted to blue-shift relative to a rhodamine 6G monomer (M). For J-type dimers, which have head-to-tail addition of their transition dipoles, the absorption is predicted to red-shift relative to a rhodamine 6G monomer.

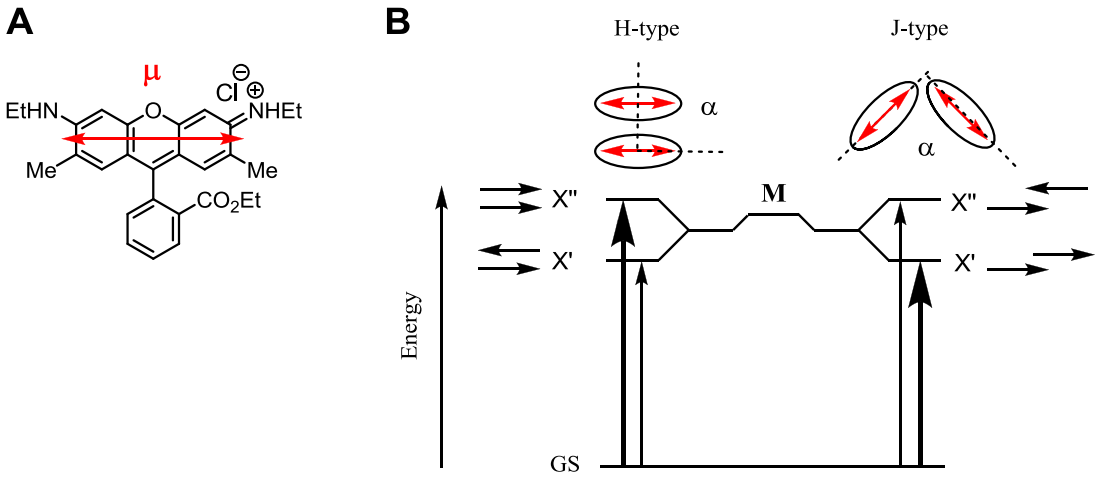

Figure 3.5. (A) Structure and position of the transition dipole moment (μ) in rhodamine 6G. (B) Exciton energy diagram of the electronic states for rhodamine 6G monomer (M) and H-type and J-type dimers.[162] Bold lines represent the transition with the largest oscillator strength (adapted from references 162, 176, and 177).

However, very few examples of exciton coupling are as simple as the interactions of parallel and co-linear transition dipole moments. If we consider a system with two electronic excitations as an example to illustrate exciton coupling interactions for non-planar transition dipole moments then the coupling strength, J, is determined by the electric field of the first transition dipole (oriented along the z-axis, centred at z = 0) (Figure 3.6A) interacting with the second transition dipole centred at a distance, r:[88, 178]

$$J = X'' - X' = -\mu_B \cdot E_A \tag{3.1}$$

where the electric field of the first transition dipole (E_A) is:

$$E_A = \frac{1}{4\pi\varepsilon_0}\frac{1}{r^3}3(\mu_A \cdot \hat{r})\hat{r} - \mu_A \tag{3.2}$$

and the coupling strength is given by:

$$J = \frac{\mu_A \cdot \mu_B}{r^3} - 3\frac{(\mu_A \cdot \hat{r})(\mu_B \cdot \hat{r})}{r^5} \tag{3.3}$$

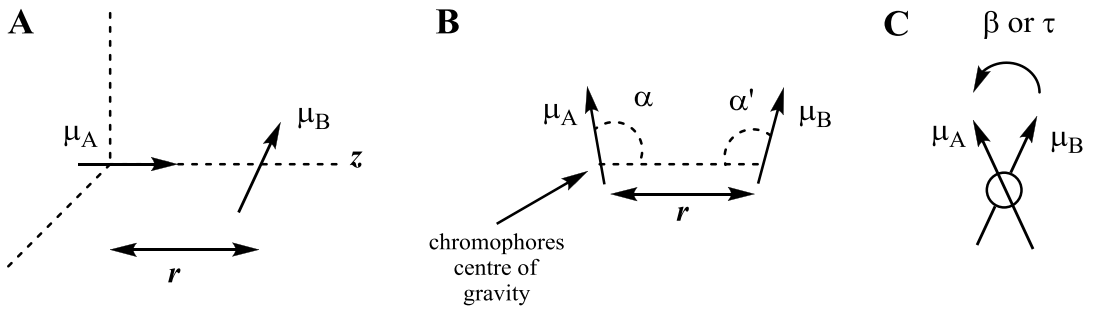

Figure 3.6. The geometrical parameters used to define the orientation of two transition dipole moments.[179]

The exciton energy levels can be found by evaluating the above equations. However, this requires the introduction of coordinates. These coordinates can be derived from computational studies or from geometrical parameters taken from structural data.[179] There is also a variety of similar expressions in the literature for estimating the energy gap between the two exciton states.[180-183]

The above equations depend on the selection of the geometrical parameters. Equation 3.3 introduces an angle for each of the dot products: β is the angle between μ_A and μ_B if their centres of mass are superimposed, α is the angle between μ_A and $\hat{r}$, and α′ is the angle between μ_B and $\hat{r}$, where $\hat{r}$ is the length of this vector (Figure 3.6B and C). Equation 3.3 simplifies to:[88]

$$J = \frac{\mu^2}{r^3}(\cos\beta - 3\cos\alpha\cos\alpha') \tag{3.4}$$

Alternatively, the dihedral angle (τ) between μ_A and μ_B along the vector $\hat{r}$ (Figure 3.6C) can be extracted from structural data and used instead of β. This introduces additional sine factors involving α and α′ to give:[88]

$$J = \frac{2\mu^2}{r^3}(\sin\alpha\sin\alpha'\cos\tau + 2\cos\alpha\cos\alpha') \tag{3.5}$$

The expressions above clearly illustrate that exciton coupling is very sensitive to the relative orientation of the transition dipoles. Therefore the direction of the dipoles needs to be assigned very precisely by a) careful analogy with already established systems, b) using computational chemistry or c) experimentally such as linear dichroism of the chromophore in an oriented medium such as a crystal or a stretched film.[88, 183]

The magnitude of exciton coupling also depends on several other factors described below. Exciton interactions are observed if there are sufficiently strong interactions

between electronic states and exciton coupling is strongest when the electronic transitions of the chromophores are degenerate, i.e. when the chromophores are identical. Exciton coupling is proportional to the square of the transition dipole moment, μ (equation 3.5). Therefore dipoles that have a greater length will have considerable interactions with dipoles in close proximity. This means that exciton coupling is rarely seen for weak electronic transitions such as d-d transitions in metal complexes but is more common for other transitions in transition metal complexes.[40, 43, 87, 88, 179, 184] Organic dyes such as rhodamine 6G are also well known for (intermolecular) exciton interactions via non-covalent interactions.[162, 176, 177] The chromophores must be in close proximity to one another because the energy gap of the exciton states is proportional to $1/r^3$ where r is the distance between the chromophores. Since the exciton model relies on the point dipole approximation, i.e. the distance between the chromophores needs to be large relative to the length of the transition dipole moments. If the chromophores are located too close in space the point dipole approximation does not hold, and the exciton model is not appropriate. Finally, there should be negligible electron delocalisation between the chromophores in the ground state. This approximation holds true for transition metal complexes with chromophoric ligands but can break down for other types of chromophores, i.e. chromophores connected by bridges which allows for a higher degree of conjugation.

3.3 Exciton coupling in dipyrrinato complexes

In the case of transition metal dipyrrinato complexes the transition dipoles are in different planes (Figure 3.7). For bisdipyrrinato complexes, [M**L**$_2$], the coordination geometry which is predominantly dictated by the metal ion, ranges from tetrahedral to square planar. Therefore the dihedral angle (τ) between the two transition dipoles of the ligands ranges from 0° to 90°. The angles α and α' will be 90° for all equilibrium geometries and the distance between chromophores, *r*, will largely be determined by the metal ion.

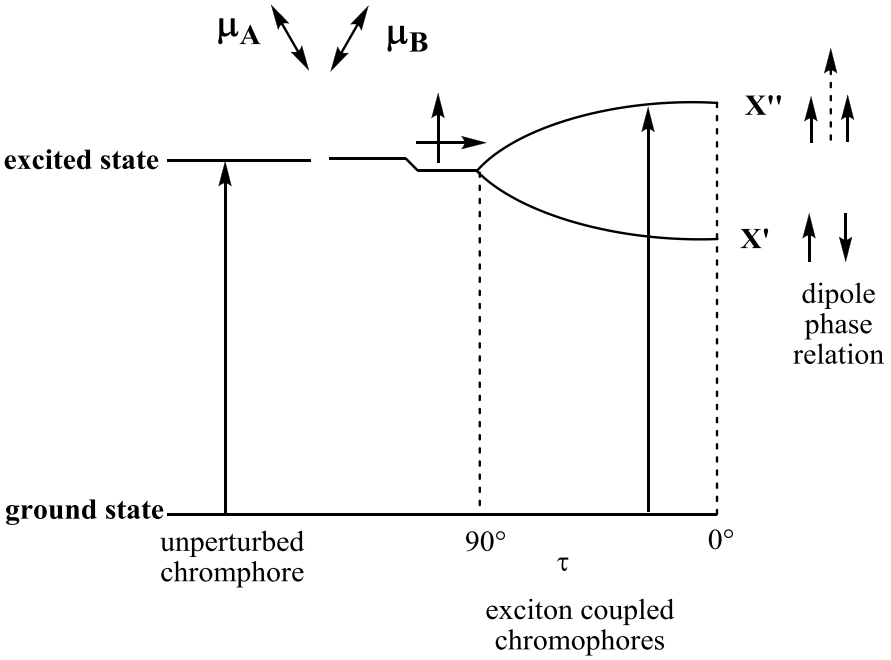

Figure 3.7. Exciton energy diagram where non-degenerate exciton states, X″ and X′, are produced for transition dipole moments aligned in a non-planar manner. Allowed transitions are denoted by vertical arrows.

From the coupling of the two degenerate dipyrrin chromophores then two non-degenerate excited states are expected. Figure 3.7 illustrates the extent of the energy gap between the exciton states, X′ and X″, as a function of the dihedral angle, τ. At τ = 90°, the transition dipoles add in a head-to-head and head-to-tail fashion but these are identical, and therefore there will be no splitting of the excited state (refer to equation 3.5). At this angle the excited states are degenerate and therefore the intensities of the two exciton absorption bands are equal. While at τ = 0°, the arrangement of the transition dipoles is parallel (Figure 3.4A) where only transitions to X″ are allowed, and therefore maximum exciton coupling is reached. Intermediate angles of τ result in an energy gap between the non-degenerate excited states which varies by cos τ. As the angle decreases from 90°, the intensities of the two absorption bands become progressively different; and the transition to the X″ state becomes increasingly more intense than the transition to the X′ state.

3.4 Objectives of this work and target complexes

Transition metals with well-defined and distinct coordination geometries allow for the control of exciton interactions by tuning the orientation and separation of the chromophores. Understanding the exciton interactions in dipyrrinato complexes is important for bridging the gap of knowledge between nature's use of exciton coupling[185] and the application of dipyrrinato complexes in artificial photosynthetic devices and dye-sensitised solar cells. By understanding and controlling the exciton interactions, can we design dipyrrin systems to mimic nature and capture a significant fraction of solar energy at the same time?

A series of transition metal complexes of dipyrrinato ligands was targeted to analyse the exciton interactions observed in electronic absorption spectroscopy. The dipyrrin complexes have well defined coordination geometries ranging from tetrahedral to square planar and octahedral containing one, two or three dipyrrin ligands (Figure 3.8).

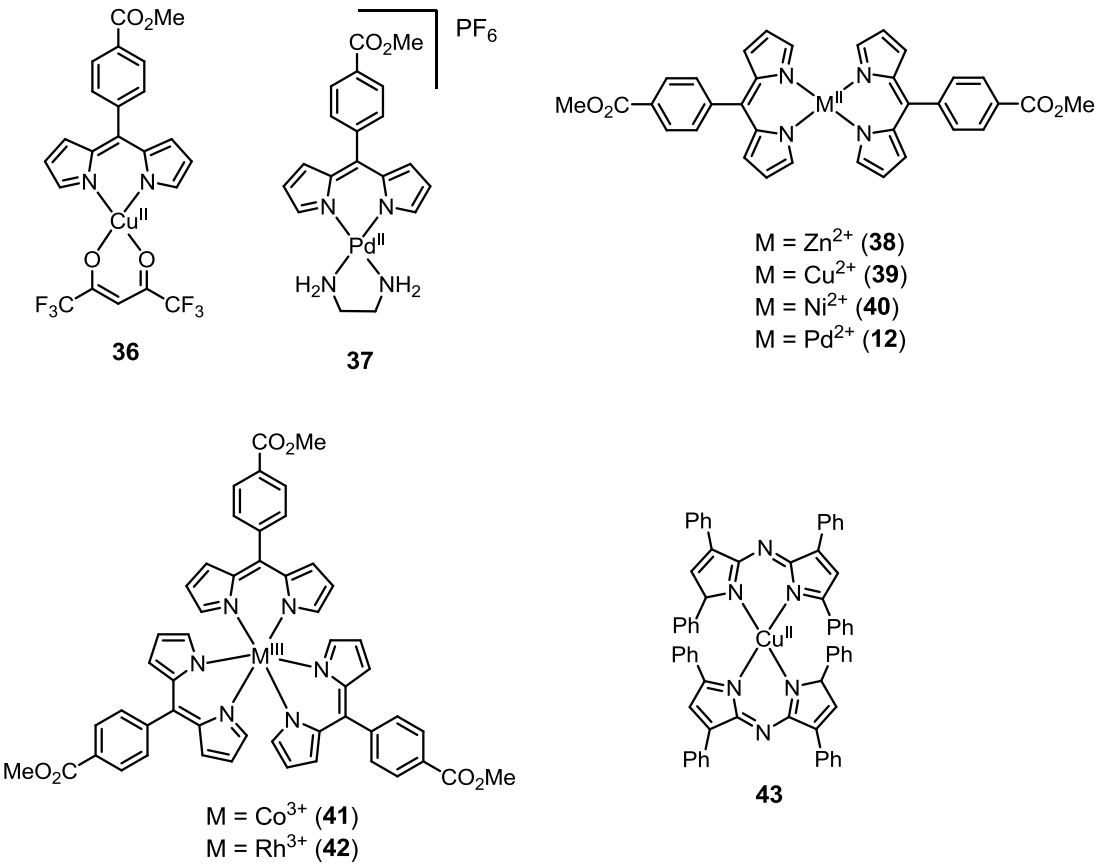

Figure 3.8. Target transition metal complexes of dipyrrinato (and azadipyrrinato) ligands with one, two or three dipyrrinato ligands. The transition metals have a range of coordination geometries from tetrahedral through to square planar and octahedral.

3.5 Experimental procedures

3.5.1 Computational procedures

All calculations were performed using Gaussian *09*. Calculations were carried out by using density functional theory (DFT), with the Becke's three-parameter exchange functional (B3)[146] in combination with the correlation functional of Lee, Yang and Parr (LYP).[147] Attempts were made to optimise the full structure of **43** using an unrestricted 6-311(+)G (d,p) basis set with the C-PCM model.[151] This calculation took three days (or six processor days) to complete the first SCF step and therefore is not computationally viable. Following this, the phenyl groups were removed to reduce the computation time. This structure optimised in six days (or 13.5 processor days) using the basis set described above. However, after the optimisation calculation the angle between the azadipyrrin ligand planes was measured (using Mercury) to be 68.8° while the angle between the azadipyrrin ligand planes of the crystal structure[78] was 48.2°.

With the help of Dr Matthias Lein (Victoria University of Wellington) a basis set consisting of 6-311+G(d,p) for the metal and the azadipyrrin core atoms and 6-31G(d) for the eight phenyl rings was used to optimise the structure, followed by Raman frequency calculations. A smaller basis set of 6-31G(d) for the metal and the azadipyrrin core atoms and 3-21G for the eight phenyl rings achieved similar results. The polarisable continuum model (C-PCM) of Barone[151] were used to model solvent effects. All geometry optimisations, frequency, and time-dependent calculations were carried out using the C-PCM model. GaussSum2.2.4[152] was used to extract vibrational frequencies from the calculations. The calculated Raman spectrum was scaled by 0.9679,[153] and a Gaussian function with FWHM of 5 cm^{-1}. This scaling factor is recommended for the B3LYP/6-311+G (d,p) basis sets and larger.[153] The accuracy of the calculation was checked by analysis and assignment of the vibrational frequencies, and normal modes checking for agreement with the experimental resonance Raman spectra (Appendix C1). Calculations for the electronic excited states were performed using the time-dependent DFT (TD-DFT) calculations with the same basis sets described above. The calculated absorption spectrum is a sum of a series of δ-functions, located at the transition frequencies and scaled by the calculated oscillator strengths. Each δ-function is convoluted with a Gaussian with a FWHM value dependent on the FWHM values of the corresponding peaks of the experimental absorption spectrum.

3.5.2 Experimental procedures

*3.5.2.1 Synthesis of dipyrrinato complexes **36-42** and **12***

*Synthesis of **36***

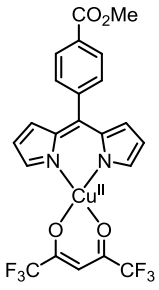

$Cu(hfacac)_2$[186] (0.233 g, 0.471 mmol) was added to a stirring MeOH (15 mL) solution of **34** (0.131 g, 0.471 mmol). Stirring was continued for 10 mins at RT. The solvent was removed on a rotary evaporator. Purification of the product was achieved by chromatography on SiO_2 using CH_2Cl_2 as the eluent. Further purification was achieved by recrystallisation from hot hexane/CH_2Cl_2. Yield: 0.218 g (0.398 mmol, 84%). IR / cm^{-1} 727 (m), 767 (m), 778 (m), 799 (w), 831 (m), 874 (w), 895 (w), 989 (m), 1001 (s), 1026 (s), 1114 (m), 1143 (s), 1182 (m), 1196 (m), 1209 (m), 1253 (m), 1278 (m), 1342 (m), 1378 (m), 1408 (w), 1435 (w), 1463 (w), 1547 (m), 1571 (w), 1611 (w), 1646 (m), 1705 (m); MALDI-MS: *m/z* = 548.09 ([M+]); Anal. Calcd for [**36**] ($C_{22}H_{17}CuF_6N_2O_4$) C, 48.23; H, 2.58; N, 5.11; Found: C, 48.59; H, 2.60; N, 5.20; UV-Vis (CH_2Cl_2) λ_{max} (ε / L mol^{-1} cm^{-1}): 491 (53 400), 317 (20 500), 314 (22 000), 263 (17 500) 235 (38 400).

*Synthesis of **37***

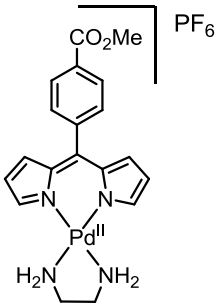

34 (0.114 g, 0.410 mmol), $[Pd(en)(NO_2)_2]$ (0.106 g, 0.410 mmol), and NEt_3 (0.06 mL) were dissolved in MeOH (30 mL). The solution was stirred at room temperature for ~ 22 hours. Excess aqueous NH_4PF_6 was added to the solution with additional H_2O. The solution was left to stand overnight before being filtered and washed with water. Purification of the crude product was achieved via the diffusion of diethyl ether into an acetonitrile solution of the complex. Yield: 0.087 g (0.148 mmol, 36%). ^1H NMR (500 MHz, DMSO-d_6, 25 °C) δ (ppm): 2.73 (s, 4H), 3.92 (s, 3H), 5.61 (s, 4H), 6.46 (dd, *J* = 0.9, 4.4 Hz, 2H), 6.50 (dd, *J* = 1.6, 4.4 Hz, 2H), 7.46 (s, 2H), 7.56 (d, *J* = 8.4 Hz, 2H), 8.08 (d, *J* = 8.4 Hz, 2H); ^{13}C NMR (100 MHz, DMSO-d_6) δ (ppm): 46.81, 52.87, 55.38, 118.94, 128.94, 130.51, 130.84, 131.42, 133.67, 141.95, 146.56, 150.87, 166.33; IR / cm^{-1} 717 (m), 762 (m), 774 (m), 828 (s, br), 896 (w), 1004 (s), 1042 (s), 1060 (w), 1122 (w), 1143 (w), 1187 (w), 1211 (w), 1248 (m), 1284 (w), 1292 (m), 1313 (m), 1346 (m), 1384 (m), 1411 (w), 1435 (w), 1549 (m), 1569 (w), 1585 (w), 1700 (m); MALDI-MS: *m/z* = 443.14 ([M+]); UV-Vis (DMSO) λ_{max}/nm (ε / L mol^{-1} cm^{-1}): 500 (54 900), 385 (7 100), 312 (10 400). Anal.

Calcd for [**37**] ($C_{19}H_{21}F_6N_4O_2PPd$) · $C_4H_{10}O$: C, 41.67; H, 4.71; N, 8.45. Found: C, 41.50; H, 4.53; N, 8.66.

*Synthesis of **38***

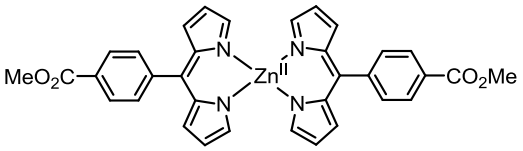

$Zn(OAc)_2 \cdot 2H_2O$ (0.206 g, 0.936 mmol) was dissolved in MeOH (5 mL) and added to a stirring MeOH solution (6 mL) of **34** (0.059 g, 0.211 mmol). A precipitate instantly appeared. The solution was heated at ~50°C for 4 hours before the precipitate was filtered off. Purification of the crude product was achieved by recrystallisation from hot MeOH and CH_2Cl_2. Yield: 0.038 g, 29%. ^{1}H NMR (500 MHz, $CDCl_3$): δ (ppm) 3.98 (s, 6H), 6.41 (dd, *J* = 1.4, 4.1 Hz, 4H), 6.63 (dd, *J* = 0.9, 4.1 Hz, 4H), 7.55 (s, 4H), 7.64 (d, *J* = 8.3 Hz, 4H), 8.14 (d, *J* = 8.2 Hz, 4H), ^{13}C NMR (100 MHz, $CDCl_3$): δ 52.4, 117.6, 128.6, 130.4, 130.8, 132.8, 140.2, 143.7, 147.4, 150.3, 166.9; IR / cm^{-1}: 726 (m), 775 (m), 759 (m), 828, (m), 899 (m), 994 (s), 1026 (s), 1107 (w), 1177 (w), 1191 (m), 1209 (w), 1242 (m), 1279 (m), 1334 (m), 1373 (m), 1403 (m), 1437 (w), 1536 (m), 1569 (w), 1610 (w), 1723 (m); Anal. Calcd for [**38**] ($C_{34}H_{26}N_4O_4Zn$): C, 65.86; H, 4.23; N, 9.04; Found: C, 65.60; H, 4.07; N, 9.05; UV-Vis (CH_2Cl_2) λ_{max} (ε / L mol^{-1} cm^{-1}): 484 (118 900), 465 (73 000), 312 (19 500), 234 (46 100).

*Synthesis of **39***

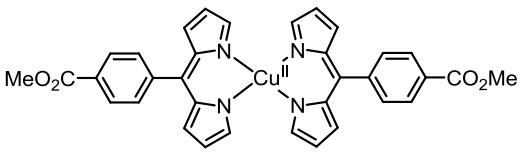

$Cu(OAc)_2 \cdot H_2O$ (0.039 g, 0.195 mmol) was suspended in MeOH (5 mL) and added to a stirring MeOH solution (5 mL) of **34** (0.080 g, 0.287 mmol). Stirring was continued for 16 hours at room temperature. The red precipitate was filtered and washed with MeOH. Purification of the product was achieved by chromatography on SiO_2 using CH_2Cl_2 as the eluent. Further purification was achieved by recrystallisation from hot MeOH/CH_2Cl_2. Yield: 0.087 g (0.141 mmol, 72%). IR / cm^{-1} 725 (s), 761 (s), 777 (m), 830 (m), 894 (m), 965 (w), 996 (s), 1024 (s), 1100 (m), 1177 (m), 1188 (m), 1205 (m), 1241 (s), 1278 (m), 1333 (m), 1372 (m), 1402 (m), 1436 (w), 1535 (s), 1569 (w), 1610 (w), 1713 (w), 1726 (m); MALDI-MS: *m/z* = 619.27 ([M+]); Anal. Calcd for [**39**] ($C_{34}H_{26}N_4O_4Cu$): C, 66.06; H, 4.24; N, 9.06; Found: C, 65.85; H, 4.29; N, 9.09; UV-Vis

(CH_2Cl_2) λ_{max} (ε / L mol^{-1} cm^{-1}): 502 (33 700), 468 (68 100), 368 (13 200), 316 (21 200), 236 (51 700).

*Synthesis of **40***

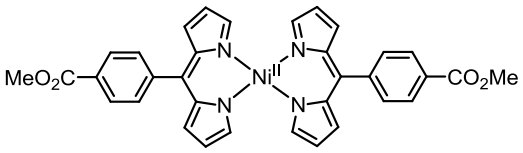

$Ni(OAc)_2 \cdot 4H_2O$ (27.7 mg, 0.111 mmol) was dissolved in MeOH (5 mL) and added to stirring MeOH solution (6 mL) of **34** (0.062 g, 0.222 mmol), where a precipitate instantly appeared. The solution heated at ~50°C for 4 hours. The precipitate was filtered and purification of the crude product was achieved by recrystallisation hot MeOH and CH_2Cl_2. Yield: 0.026 g, 39%. ^{1}H NMR (500 MHz, $CDCl_3$): δ 3.96 (s, 6H), 6.69 (d, *J* = 3.8 Hz, 4H), 7.46 (d, *J* = 8.0 Hz, 4H), 7.80 (d, *J* = 3.6 Hz, 4H), 8.07 (d, *J* = 8.1 Hz, 4H), 9.98 (s, 4H), ^{13}C NMR (100 MHz, $CDCl_3$): δ 52.1, 128.4, 130.3, 130.5, 138.3, 139.7, 140.9, 141.7, 150.9, 166.5, 177.7. IR / cm^{-1} 725 (s), 761 (s), 777 (m), 830 (s), 874 (w), 894 (m), 965 (m), 996 (s), 1024 (s), 1100 (m), 1177 (m), 1188 (m), 1205 (w), 1241 (s), 1278 (s), 1333 (s), 1372 (s), 1402 (m), 1436 (w), 1535 (s), 1569 (m), 1610 (w), 1713 (m), 1726 (m); MALDI-MS: *m/z* = 613.27 ([M+]); Anal. Calcd for [**40**] ($C_{34}H_{26}N_4O_4Ni$) C, 66.59; H, 4.27; N, 9.14; Found: C, 65.52; H, 4.31; N, 9.11; UV-Vis (CH_2Cl_2) λ_{max} (ε / L mol^{-1} cm^{-1}): 477 (45 800), 319 (26 300), 235 (54 400).

*Synthesis of **12***

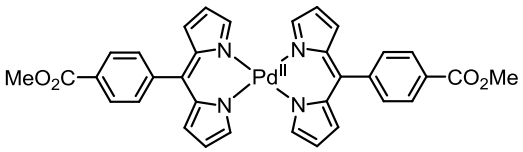

$[Pd(CH_3CN)_2Cl_2]$ (0.0565 g, 0.218 mmol), **34** (0.120 g, 0.431 mmol), and NEt_3 (0.6 mL, 0.430 mmol) were combined in MeOH (35 mL) and stirred at room temperature for one hour. The crude product was isolated by filtration, washed thoroughly with hexane. Purification of the product was achieved by recrystallisation from hot MeOH/CH_2Cl_2. Yield: 0.081 g (0.123 mmol, 57%). ^{1}H NMR (500 MHz, $CDCl_3$, 25 °C) δ (ppm) 3.99 (s, 6H), 6.37 (dd, *J* = 1.6, 4.4 Hz, 4H), 6.65 (dd, *J* = 1.1, 4.4 Hz, 4H), 7.41 (s, 4H), 7.66 (d, *J* = 8.2 Hz, 4H), 8.16 (d, *J* = 8.2 Hz, 4H); ^{13}C NMR (100 MHz, $CDCl_3$, 25 °C) δ (ppm) 52.35, 117.32, 128.76, 130.45 (2C), 131.07, 136.64, 142.04, 146.33, 152.09, 166.74; IR / cm^{-1} 722 (s), 764 (s), 832 (m), 870 (w), 896 (m), 967 (w), 991 (s), 1003 (s), 1033 (s), 1102 (w), 1114 (m), 1177 (w), 1204 (w), 1261 (s), 1280 (s), 1342 (m), 1380 (m), 1403

(m), 1436 (w), 1516 (w), 1542 (s), 1569 (w), 1611 (w), 1717 (m); UV-Vis (CH_2Cl_2): λ_{max}/nm (ε / L mol^{-1} cm^{-1}): 481 (70 000), 383 (15 100), 313 (18 100), 236 (46 600); MALDI-MS: *m*/*z* = 660.30 ([M+]); Anal. Calcd for [**12**] ($C_{34}H_{26}N_4O_4Pd$) · 0.5CH_3OH: C, 61.20; H, 4.17; N, 8.28. Found: C, 60.95; H, 3.96; N, 8.33.

*Synthesis of **41***

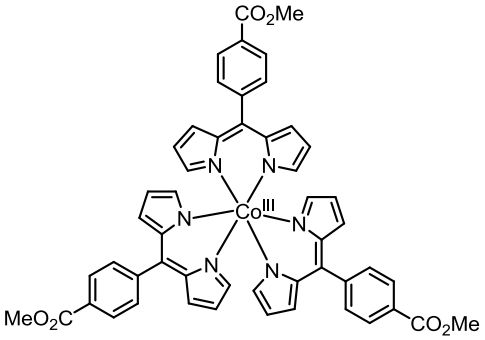

34 (0.400 g, 1.44 mmol) and NEt_3 (0.4 mL) were combined in MeOH (15 mL). $Na_3[Co(NO_2)_6]$ (0.174 g, 0.431 mmol) was dissolved in minimal H_2O and added to the MeOH solution. The mixture was heated at 60 °C under Ar overnight. After cooling to room temperature, water was added to the reaction and the resulting precipitate was filtered and washed with water. Purification of the orange-red solid was achieved via chromatography on SiO_2 using CH_2Cl_2 as the eluent. Yield: 0.125 g (0.140 mmol, 33%). Spectroscopic data matched that previously reported.[29]

*Synthesis of **42***

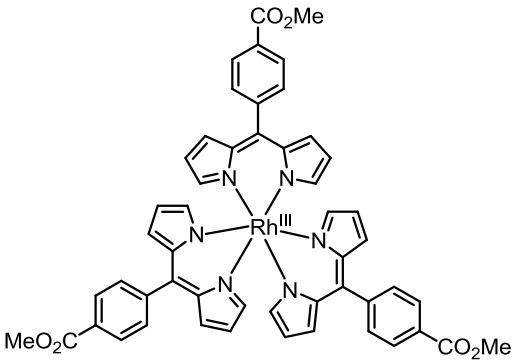

34 (0.593 g, 2.13 mmol), NEt_3 (0.3 mL), and $RhCl_3 \cdot xH_2O$ (0.162g, 0.65 mmol Rh) were combined in isopropyl alcohol and heated to 100 °C overnight. The solvent was removed on a rotary evaporator. Purification of the dark red solid was achieved via chromatography on SiO_2 using CH_2Cl_2/hexane (2/1) as the eluent. Yield: 0.468 g (0.501 mmol, 80%). ^{1}H NMR (400 MHz, $CDCl_3$, 25 °C) δ (ppm) 3.98 (s, 9H), 6.33 (dd, *J* = 1.5, 4.3 Hz, 6H), 6.56 (dd, *J* = 1.5, 4.3 Hz, 6H), 6.60 (s, 6H), 7.53 (d, *J* = 8.3 Hz, 6H), 8.10 (d, *J* = 8.3 Hz, 6H); ^{13}C NMR (100 MHz, DMSO-d_6, 25 °C) δ (ppm) 52.28, 118.26, 128.50, 130.20, 130.40, 131.63, 134.59, 142.92, 146.26, 150.64, 166.82; IR / cm^{-1}: 721 (s), 760 (m), 772 (m), 827 (m), 870 (w), 896 (m), 994 (s),1025 (m), 1031 (m), 1041(m), 1110 (m, br), 1207 (w), 1254 (s), 1278 (m), 1347 (m), 1378 (m), 1412 (w), 1548 (m), 1571 (w), 1722 (m); UV-Vis (CH_2Cl_2) λ_{max}/nm (ε / L mol^{-1} cm^{-1}): 307 (28 800), 404 (25 100), 464 (77 600), 501 (60 300); MALDI-MS: *m*/*z* = 935.41 ([M+]);

Anal. Calcd for [**42**] ($C_{51}H_{39}N_6O_6Rh$): C, 65.53; H, 4.21; N, 8.99. Found: C, 65.65; H, 4.69; N, 8.52.

*3.5.2.2 Synthesis of azadipyrrinato complex **43***

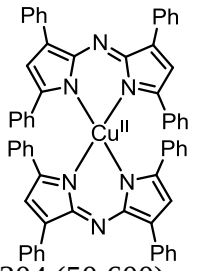

$Cu(OAc)_2 \cdot H_2O$ (0.054 g, 0.272 mmol) was added as a solid to a stirring 2-BuOH solution (8.5 mL) of **44** (0.100 g, 0.222 mmol). The solution was refluxed at 118 °C for 1 hour before being cooled to room temperature. The product was filtered, washed thoroughly with hexane and dried under vacuum overnight. Yield: 0.081 g (0.084 mmol, 38%). UV-Vis (CH_2Cl_2) λ_{max} / nm (ε / L mol^{-1} cm^{-1}): 641 (47 500), 565 (49 400), 304 (50 600), 244 (40 000). Spectroscopic data matched that previously reported.[78]

3.6 Results and Discussion

3.6.1 Synthesis

The preparation of the heteroleptic complexes **36** and **37** (Figure 3.9 and 3.10) was challenging, since heteroleptic complexes have a tendency to form the homoleptic bisdipyrrinato complexes.[36] For example, the synthesis of [Cu**L**(acac)] using stoichiometric quantities of [$Cu(acac)_2$] and the dipyrrinato ligand (**L**) is reported to readily convert to [Cu$\mathbf{L}_2$]. Replacing the acetylacetone (acac) in the Cu(II) starting material with hexafluoroacetylacetone (hfacac) forms the stable complex, [Cu**L**(hfacac)].[36] A variation of this reported procedure[36] was used to prepare complex **36**. In this reaction (Figure 3.9) the hfacac ligands remove the proton from the pyrrolic nitrogen allowing the dipyrrin ligand to coordinate to the metal.

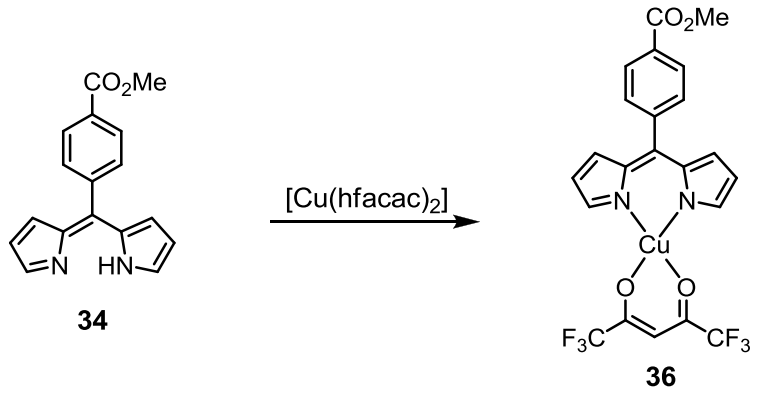

Figure 3.9. The synthetic route to Cu(II)-dipyrrinato complex **36**.

The cationic complex **37** was prepared using stoichiometric quantities of $[Pd(en)(NO_2)_2]$ and **34**, with triethylamine (NEt_3) and stirring at room temperature overnight. The triethylamine serves to deprotonate the dipyrrin ligand. The product was isolated by precipitation with aqueous NH_4PF_6.

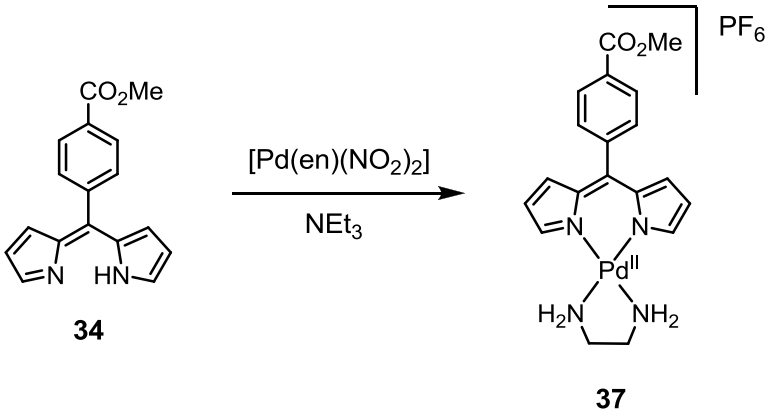

Figure 3.10. The synthetic route to the Pd(II)-dipyrrinato complex **37**.

The synthesis and purification of the complexes **38**-**40** and **12** (Figure 3.11) and **41**-**42** (Figure 3.12) was straightforward owing to the multitude of literature preparations for transition metal complexes of similar dipyrrinato ligands.[24, 26] Typically, the appropriate metal salt is heated in methanol with two (or three) equivalents of dipyrrin ligand **34** and a base (where necessary) (see Table 3.1 for a summary of reaction conditions). Metal acetates are often employed as the metal source since the acetate anions are sufficiently basic to deprotonate the dipyrrin ligand allowing the metal to coordinate. Upon complexation there was an obvious and immediate colour change and

purification was simplified in most cases by the fact that the metal complexes were insoluble in methanol. Filtration followed by column chromatography and/or a recrystallisation step gave the complexes in high purity with moderate to good yields.

The synthesis of complexes **38**-**40** and **12** are variations of preparations of similar dipyrrinato complexes.[26, 47] The synthesis of **41** has been reported in the literature;[29, 30, 87] however, this is the first report of a homoleptic Rh(III) dipyrrinato complex, **42**.[43] This complex was prepared in high yield from a reaction of $RhCl_3$, dipyrrin ligand **34**, and triethylamine (NEt_3) in hot isopropanol (Figure 3.12).

The synthesis of complex **43**[78] (Figure 3.13) from azadipyrrin ligand **44**[72, 73, 80] has been reported in the literature.

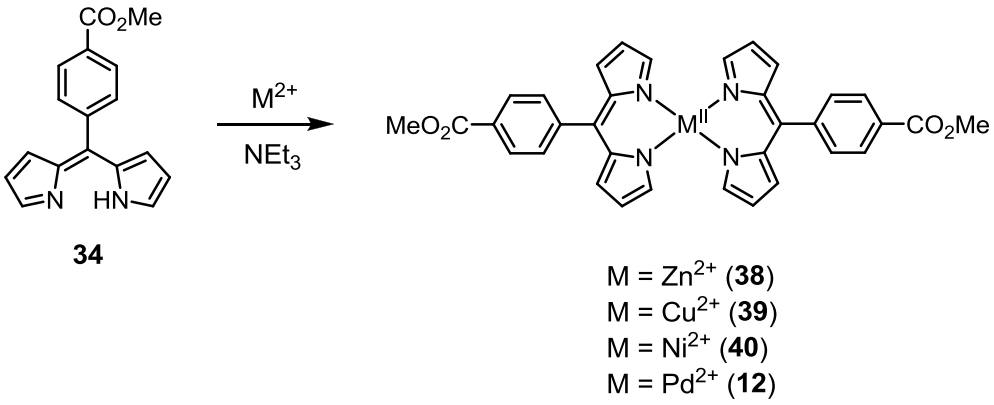

Figure 3.11. The synthetic route to dipyrrinato complexes **38**-**40** and **12**.

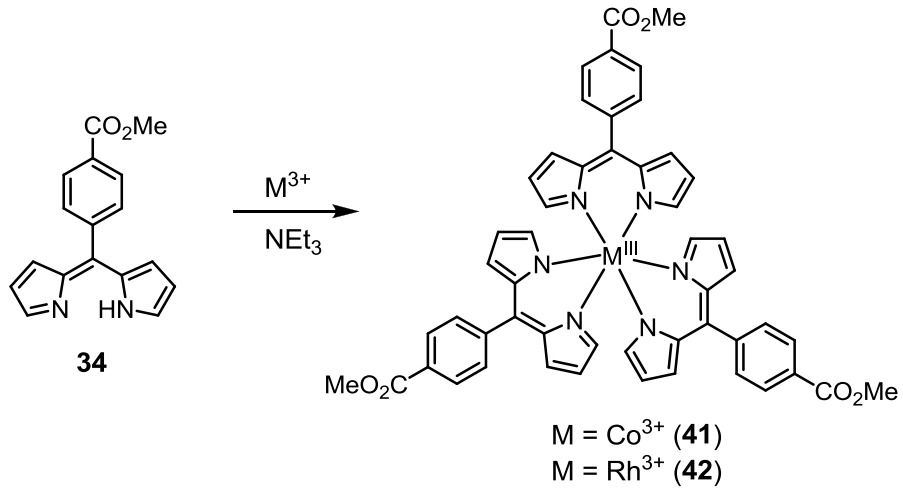

Figure 3.12. The synthetic route to dipyrrinato complexes **41**-**42**.

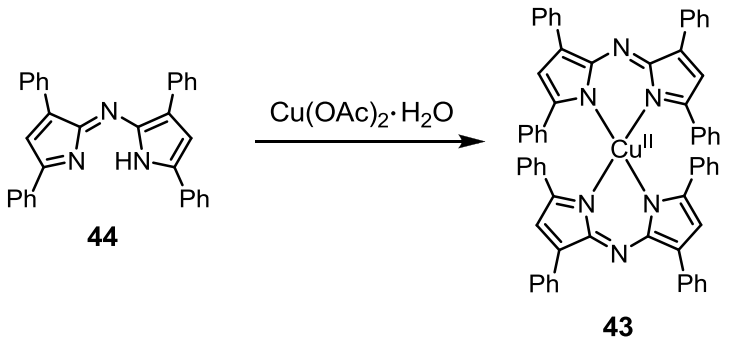

Figure 3.13. The synthetic route to Cu(II) azadipyrrinato complex **43**.

Table 3.1. Reactions for the synthesis of complexes **12** and **36-43**.

Complex	Reagents		Reaction conditions		Yield
	Metal source	Base	Solvent	Temperature, °C (time)	(%)
36	$Cu(hfacac)_2$	–	MeOH	20 (10 mins)	84
37	$Pd(en)(NO_2)_2$	NEt_3	MeOH	20 (overnight)	36
38	$Zn(OAc)_2 \cdot 2H_2O$	–	MeOH	50 (4 hrs)	29
39	$Cu(OAc)_2 \cdot H_2O$	–	MeOH	50 (4 hrs)	72
40	$Ni(OAc)_2 \cdot 4H_2O$	–	MeOH	50 (4 hrs)	39
12	$Pd(CH_3CN)_4Cl_2$	NEt_3	MeOH	25 (1 hrs)	57
41	$Na_3[Co(NO_2)_6]$	NEt_3	MeOH	60 (overnight)	33
42	$RhCl_3 \cdot xH_2O$	NEt_3	iPrOH	100 (overnight)	80
43	$Cu(OAc)_2 \cdot H_2O$	–	2-BuOH	118 (1 hr)	38

3.6.2 Complexation geometries and the orientation of the transition dipole moments

As confirmed by DFT calculations the transition dipole moment (μ) for the lowest energy transition of a dipyrrin ligand lies in the plane of the dipyrrin core parallel to the nitrogen donor atoms. (Figure 3.2). In dipyrrinato complexes the dihedral angle (τ) between the two transition dipoles along the vector $\hat{r}$ (Figure 3.6C) can be obtained from computational studies or crystallographic data.[88] In this case crystal structures of most of the complexes were obtained primarily to confirm the coordination geometries at the metal centres and to evaluate the angle between the transition dipole moments. Mercury™ has been used to estimate these dihedral angles (τ). Since the transition dipole moment lies in the plane of the pyrrolic rings of the dipyrrin core parallel to the nitrogen atoms then defining the mean plane of the core of each dipyrrin ligand (in Mercury) defines the position of the transition dipole moment (represented as the coloured areas in Figure 3.14A). Then the angle formed between these two mean planes (along the vector $\hat{r}$) gives the dihedral angle, τ (Figure 3.14B).

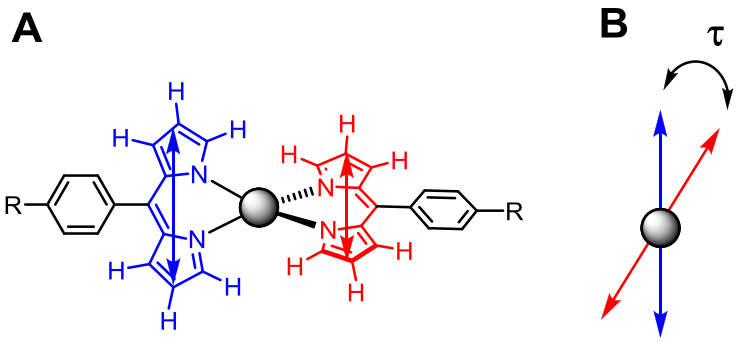

Figure 3.14. (A) Illustration of the atoms included in each dipyrrinato ligand for defining the mean ligand planes and therefore (B) the dihedral angle (τ) between the transition dipole moments.

The geometry about the Cu(II) centre of **36** is square pyramidal. The oxygen of the ester functional group of a dipyrrinato ligand on another complex coordinates in the fifth coordination site (Figure 3.15). The dipyrrinato ligand lies flat but has a small tilt angle[50] (defined in this case as the mean plane between the CuN_2O_2 and the atoms in the core dipyrrin framework) of ~ 9°.

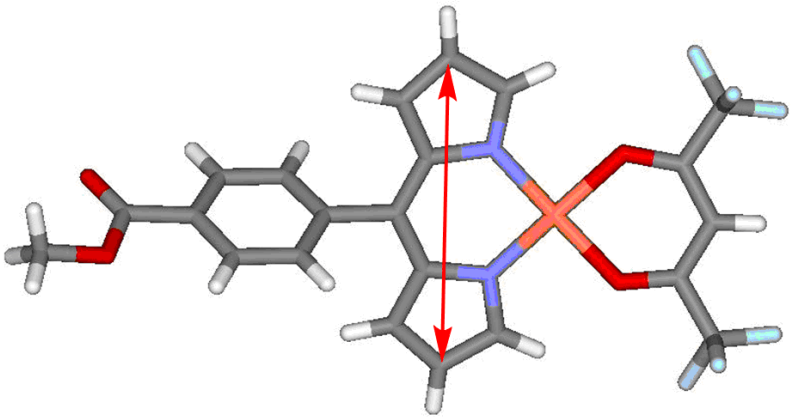

Figure 3.15. The crystal structure of [Cu**L**(hfacac)], **36**, illustrating the position of the transition dipole moment, μ, for the lowest energy π–π* transition in dipyrrin. The geometry at the metal centre is square pyramidal. The carbonyl oxygen atom of the methyl ester of another dipyrrinato ligand coordinates to the metal.

The Pd(II) centre of **37** is strictly square planar (Figure 3.16). The core of the dipyrrinato ligand is perfectly flat but the ligand cants away from the PdN_4 plane with a

tilt angle[50] (defined in this case as the mean plane between the PdN_4 plane and the atoms in the core dipyrrin framework) of ~21°.

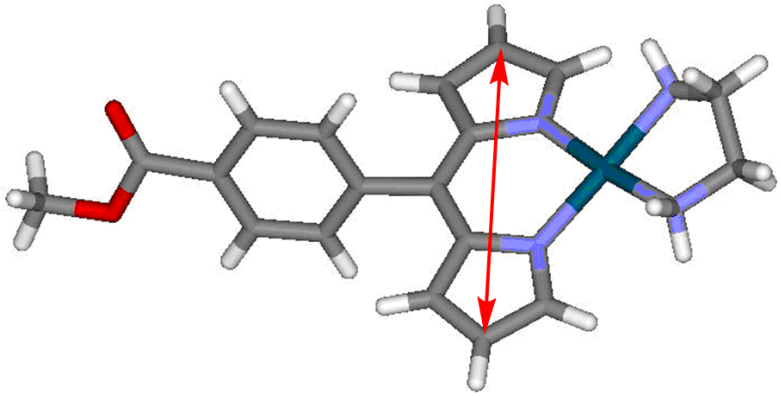

Figure 3.16. The crystal structure of [Pd**L**(en)]$^+$, **37**, illustrating the position of the transition dipole moment, μ, for the lowest energy π–π* transition in dipyrrin. The geometry at the metal centre is strictly square planar.

The geometry of the Zn(II) of **38** has been estimated using a related crystal structure[90] (Figure 3.17) as approximately tetrahedral. Therefore the dihedral angle between the transition dipole moments is approximately 90°.

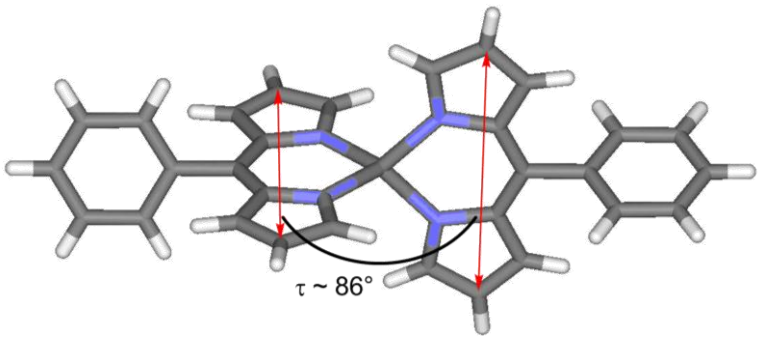

Figure 3.17. The crystal structure of [Zn$\mathbf{L}_2$][90] (as a representative example of **38**), illustrating the position of the transition dipole moment, μ, for the lowest energy π–π* transition in dipyrrin (red). The geometry at the metal centre is approximately tetrahedral.

Each dipyrrinato ligand plane in **39** is essentially flat and the geometry of the Cu(II) centre of **39** is distorted tetrahedral (Figure 3.18). The dihedral angle between the dipole moments ranges between 52-74°.

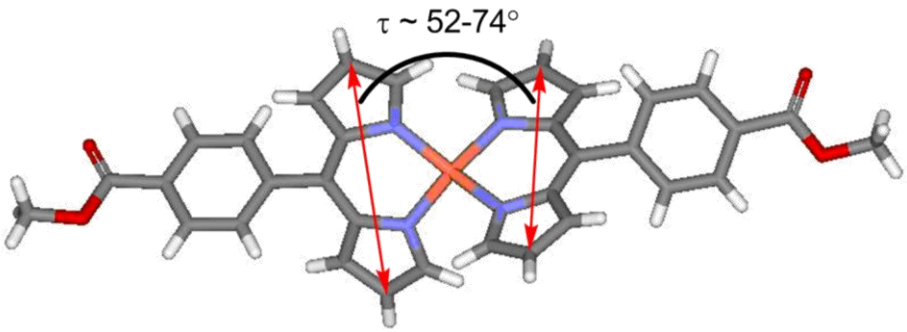

Figure 3.18. The crystal structure of [Cu$\mathbf{L}_2$], **39**, illustrating the position of the transition dipole moments, μ, for the lowest energy π–π* transition in dipyrrin (red). The geometry at the metal centre is distorted tetrahedral.

The geometry of the Ni(II) centre of **40** is a special case. The crystal structure (Figure 3.19) shows that each dipyrrinato ligand plane is flat and the geometry at the Ni(II) centre appears to be distorted tetrahedral. The dihedral angle between the dipole moments ranges between 51-84°. Tetrahedral Ni(II) complexes are high-spin and therefore paramagnetic while square planar Ni(II) complexes are low-spin and diamagnetic.[137] However, sharp, well-resolved peaks were observed in both ^{1}H and ^{13}C NMR spectroscopy for this complex which confirms that the complex is diamagnetic. Therefore the geometry at the metal centre must be (distorted) square planar, in solution at least, instead of tetrahedral.

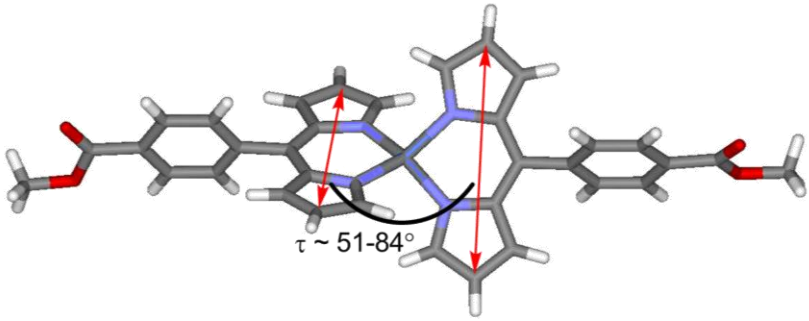

Figure 3.19. The crystal structure of [Ni$\mathbf{L}_2$], **40**, illustrating the position of the transition dipole moments, μ, for the lowest energy π–π* transition in dipyrrin (red). NMR evidence confirms the complex is diamagnetic and therefore the geometry at the metal centre must be closer to square planar than tetrahedral.

The geometry of the Pd(II) centre of **12** is square planar (Figure 1.6 and Figure 3.20) therefore the angle between the transition dipoles is 0°. The crystal structure shows that the two dipyrrinato ligands cannot maintain coplanarity due to the close interligand contacts of the α hydrogens. This forces the ligands to cant away from the N_4 plane with a tilt angle[50] (defined in this case as the mean plane between the PdN_4 plane and the atoms in the core dipyrrin framework) of approximately 40°. The pyrrolic rings of the dipyrrin core also have pronounced curvature. The planes of the pyrrolic rings of each ligand are inclined at an angle (defined as the angle between the mean planes formed by the atoms in each pyrrole and the adjacent *meso* carbon)[50] of 34° to each other. This curvature further reduces the strain induced by the close interligand contacts. This crystal structure parallels the previously reported [Pd(mpm)$_2$] (mpm = 4,4'-dicarboxyethyl-3,3',5,5'-tetraamethyldipyrromethenato), where the dipyrrin ligands have methyl substituents on both α positions.[187]

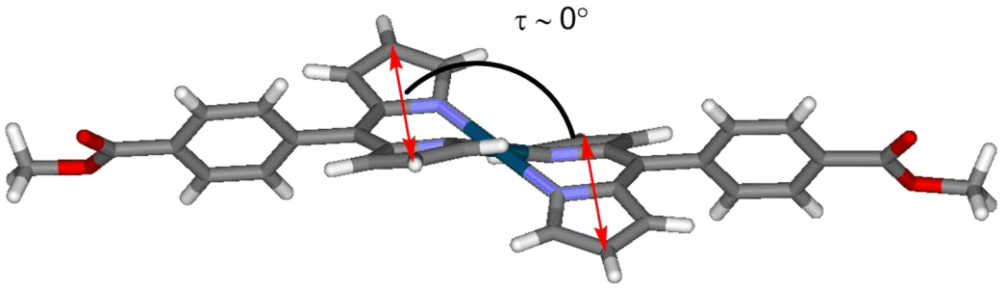

Figure 3.20. The crystal structure of [Pd**L**$_2$], **12**, illustrating the position of the transition dipole moments, μ, for the lowest energy π–π* transition in dipyrrin (red). The geometry at the metal centre is strictly square planar.

The crystal structure[78] (Figure 3.21) of **43** shows the geometry at the Cu(II) centre is distorted tetrahedral and the angle between the transition dipoles is approximately 48°.

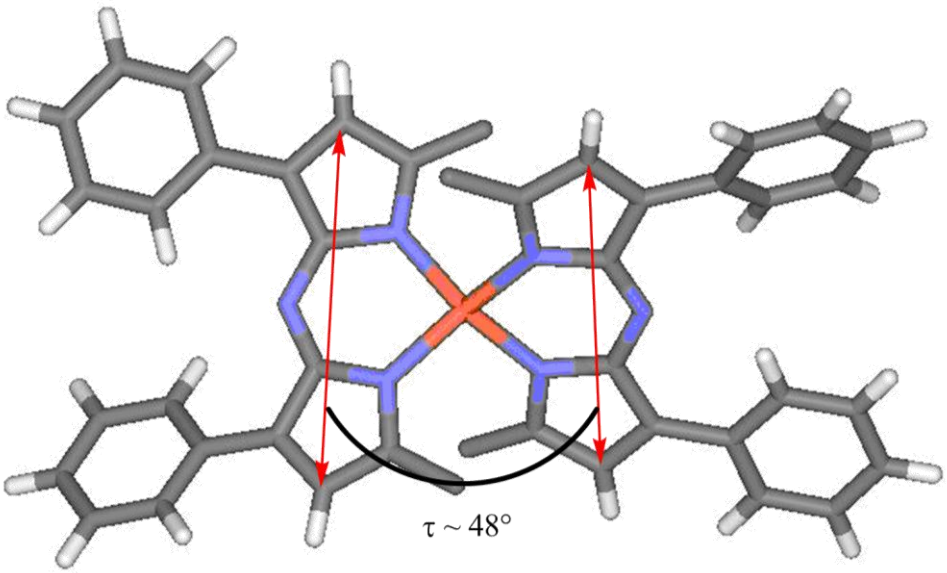

Figure 3.21. The crystal structure of [Cu**Laza**$_2$], **43**, illustrating the position of the transition dipole moments, μ, for the lowest energy π–π* transition in azadipyrrin (red). The phenyl rings have been removed at the α-positions for clarity. The geometry at the metal centre is distorted tetrahedral.

3.6.3 Exciton effects in the absorption spectra of dipyrrinato complexes

Complex **36** and **37**, which exhibit absorption bands at 491 and 500 nm, respectively, represent unperturbed chromophores where the presence of a single dipyrrinato ligand prevents exciton coupling (Figure 3.22).

As discussed above, the coordination geometry at the metal centre for dipyrrinato complexes determines the extent of exciton coupling on the excited state energy levels. The [Pd$\mathbf{L}_2$] complex, **12**, has square planar geometry about the metal centre (Figure 3.20), thus $\tau \approx 0°$ and the arrangement of the transition dipoles is parallel (Figure 3.4A). In this case only the transition to X″ is allowed, therefore there is one sharp absorption band, which is centred at 481 nm. This transition is blue-shifted with respect to the transitions of the unperturbed chromophores. The [Zn$\mathbf{L}_2$] complex, **38** is predicted to have tetrahedral geometry at the metal centre, thus $\tau \approx 90°$.[26, 90] Exciton coupling is expected to be weak or non-existent for this complex due to the degeneracy of the excited states. Therefore this complex possesses a single absorption peak at 484 nm with a high energy shoulder similar to that of BODIPY complexes. This can most likely be attributed to vibronic structure and is common in other zinc(II) dipyrrinato complexes[26, 31, 90] and BODIPY complexes.[58, 188]

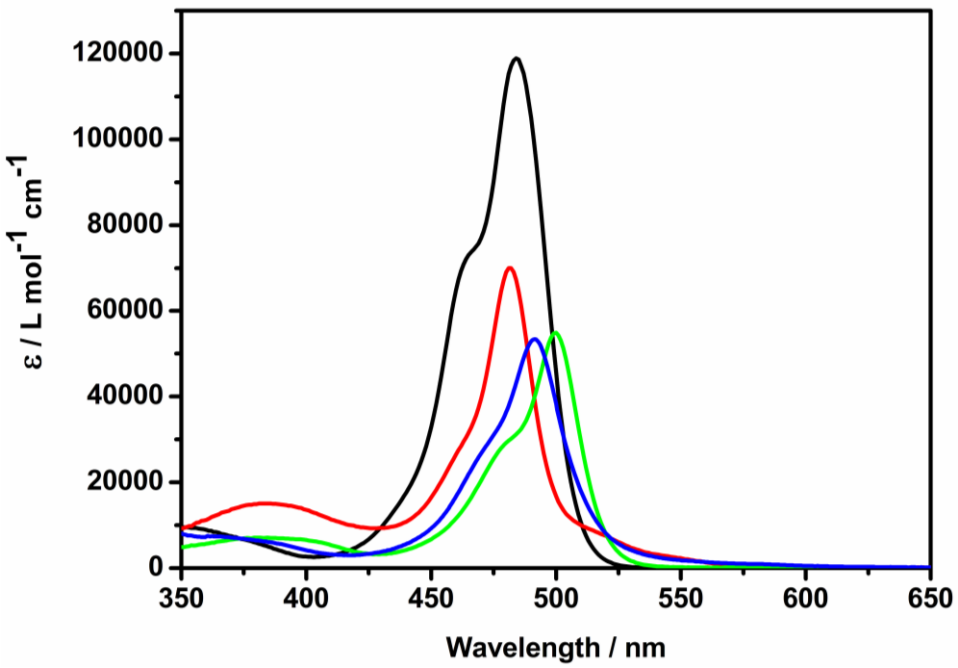

Figure 3.22. Absorption spectra of **36** (blue), **37** (green), **38** (black), and **12** (red) in CH_2Cl_2.

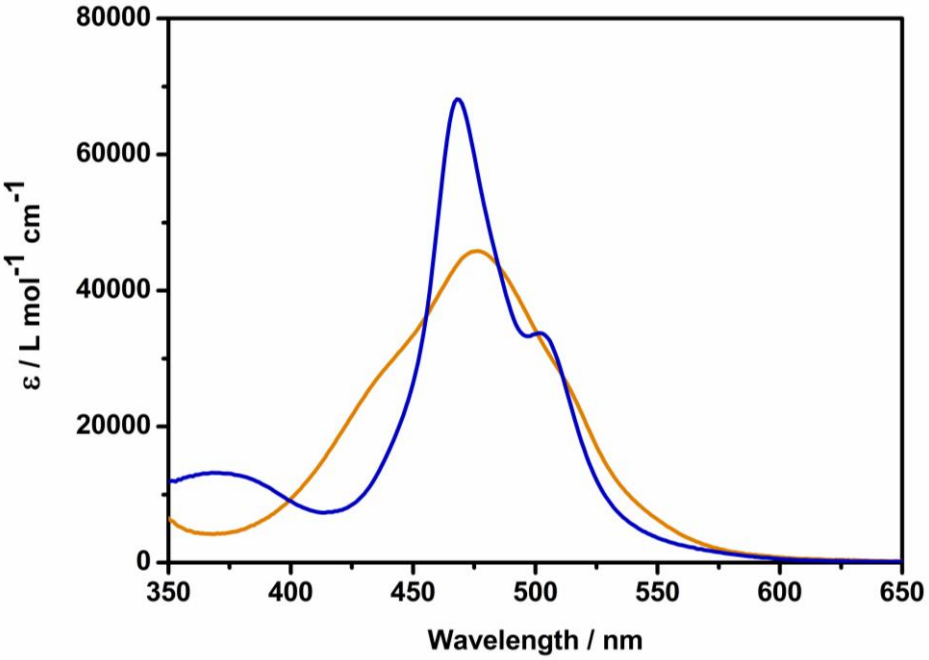

Figure 3.23. Absorption spectra of **39** (blue) and **40** (orange) in CH_2Cl_2.

The [Cu**L**$_2$] and [Ni**L**$_2$] complexes, **39** and **40**, have intermediate geometry about the metal centres. The crystal structures (Figure 3.18) of **39** shows that $\tau \approx 52\text{-}74°$ with a cluster of angles between 67-74°. For this complex there is a strong absorption band at 468 nm and a weaker absorption band 502 nm (Figure 3.23). This weaker band at lower energy is consistent with the angles obtained from the crystal structures. For a similar [Cu**L**$_2$] complex, where the dipyrrin has a phenylacetylenylene group attached to the phenyl spacer group, $\tau \approx 46°$, the absorption bands appear at exactly the same positions with the lower energy band weaker than the higher energy transition.[51]

The crystal structure of **40** (Figure 3.19) shows that the angles between the transition dipoles have a large range between $\tau \approx 51\text{-}84°$. A [Ni**L**$_2$] complex with methyl substituents in the α-positions is reported to have an angle of 76.3° between the ligand planes[189] while another [Ni**L**$_2$] complex with closer similarity to our [Ni**L**$_2$] complex with hydrogens in the α-positions has a much smaller angle of 38.5° between ligand planes.[26] NMR evidence suggests [Ni**L**$_2$] complex **40** is diamagnetic (in solution at least) and the geometry must be (distorted) square planar. The absorption band is broad with a maximum at 468 nm (Figure 3.23). For similar unsubstituted [Ni**L**$_2$] complexes, the absorption spectrum is virtually identical in terms of both position and intensity.[26]

The [Co**L**$_3$] and [Rh**L**$_3$] complexes, **41** and **42**, show prominent exciton coupling in their absorption spectra (Figure 3.24). The exciton coupling for these complexes is easily observable due to both the intensity and energetic separation from other absorption bands. Peaks for **41** are observed at 469 nm and 506 nm while for **42** they are observed at 464 nm and 501 nm, respectively.

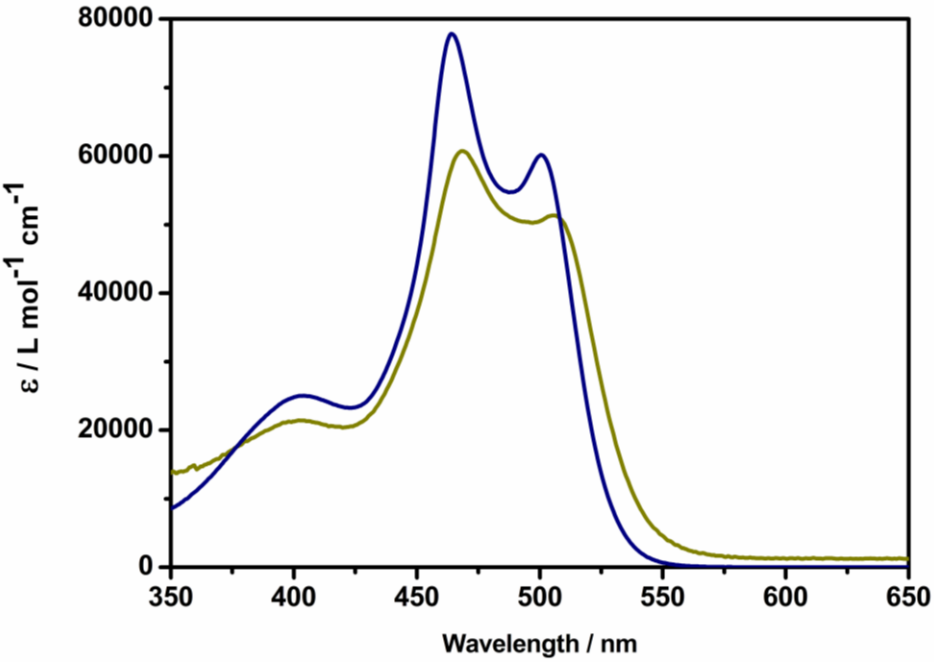

Figure 3.24. Absorption spectra of **41** (green) and **42** (blue) in CH_2Cl_2.

The exciton coupling effects in the CD spectra of octahedral complexes of $[M(bipy)_3]^{n+}$ and $[M(phen)_3]^{n+}$ has been described in the literature by Bosnich.[184] The analysis of absorption spectra of [M**L**$_3$] dipyrrinato complexes follows the same theory. The D_3 symmetry of [M**L**$_3$] dipyrrinato complexes renders three localised transitions which couple in three different ways based on symmetry. The ground state is represented by $\Psi_0 = \chi_1 \chi_2 \chi_3$ and the three excited states are represented as $\chi_1'\chi_2 \chi_3$, $\chi_1 \chi_2'\chi_3$, and $\chi_1 \chi_2 \chi_3'$ where the numbers corresponds to each dipyrrinato ligand, χ is the ground state wavefunction of the dipyrrinato ligand, and the prime indicates an excited-state wavefunction of the dipyrrinato ligand. The three uncoupled excited states are degenerate and the true exciton states are a linear combination of the excited states. The linear combinations describe the coupling between the transition dipole moments of each dipyrrinato ligand. The three coupling modes are determined by symmetry where

two exciton states are produced (X′ and X″), which consist of two degenerate transitions ($\Psi_0 \rightarrow \Psi_E^1$ and $\Psi_0 \rightarrow \Psi_E^2$) and one non-degenerate transition ($\Psi_0 \rightarrow \Psi_{A_2}$) (Figure 3.25).

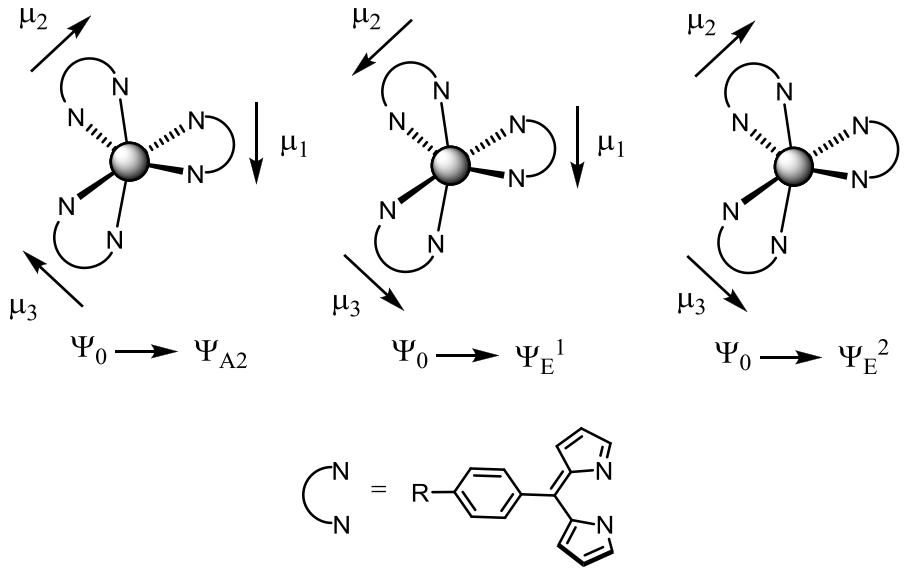

Figure 3.25. A diagrammatic representation of the three coupling modes for an octahedral [M**L**$_3$] dipyrrinato complex (adapted from reference 184). The positive direction is defined as pointing in a clockwise direction.

The higher energy state (X″) results from the dipoles in essentially a "head-to-head" arrangement ($\mu_1 + \mu_2 + \mu_3$) and has A symmetry, while the lower energy state (X′) results from the dipoles in essentially a "head-to-tail" arrangement ($2\mu_1 - \mu_2 - \mu_3$) and ($\mu_2 - \mu_3$) and has E symmetry. Electrostatic considerations suggest that the head-to-head arrangement will be at higher energy than the head-to-tail arrangement.

There are many notable examples in the literature of exciton coupling in related metallodipyrrin complexes with octahedral geometry. Co(III)-dipyrrinato complexes display exciton coupling in both absorption and CD spectra,[29, 87] while Fe(III)-dipyrrinato complexes exhibit even more prominent exciton coupling than the equivalent Co(III) complex.[29] The peaks are visibly more intense, broader, and the energy gap between the states is larger for the Fe(III) complex. The only reported Cr(III) complex shows weak exciton coupling with a shoulder on the low energy side of the main band. The energy gap between the two exciton states is rather small relative to other examples given.[34] Examples of Ga(III)- and In(III)-dipyrrinato complexes have even more pronounced splitting of the exciton energies, X′ and X″. There is clear and

well-defined splitting of the two exciton states with two bands observed with a large energy gap between them.[91] The underlying reason behind the differences between different complexes with the same or very similar ligands is most likely related to *r*, where *r* is the length of the vector connecting the centres of gravity of the ligands.

3.6.4 Exciton effects in azadipyrrinato complexes

The initial hypothesis for the position of the transition dipole moment of azadipyrrin ligands (Figure 3.26) was that the transition dipole moment was polarised analogously to the dipyrrin ligand **34** and BODIPY complexes (as discussed earlier).

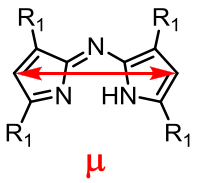

Figure 3.26. Orientation of the transition dipole moment in azadipyrrin ligands.

There are features in the absorption spectra of certain [M**L**$\mathbf{aza}_2$] complexes which are reminiscent of exciton coupling. The Co(II), Ni(II), and Zn(II) complexes of tetraphenyl azadipyrrin **44** have absorption maxima between 596-603 nm with a prominent shoulder on the red edge at approximately 650-700 nm. This transition is ascribed to a π-π transition. The bulky phenyl groups in the α-positions significantly influence the geometries about the metal centres from their ideal geometries. The crystal structures of these complexes show that the angle between the planes of the azadipyrrinato ligands, $\tau \approx 50\text{-}52°$ and the geometry at the metal centre is distorted tetrahedral.[78] A Hg(II) complex of tetraphenyl azadipyrrin with $\tau \approx 54.3°$ and a distorted tetrahedral geometry has a broad absorption spectrum with the absorption maximum at 601 nm but with no obvious shoulder on the red edge.[86]

The Cu(II) complex of tetraphenyl azadipyrrin [Cu**L**aza_2], **43**, features two peaks of approximately equal intensity at 565 nm and 641 nm (Figure 3.27). Based on the exciton model, the large energy gap between the peaks together with their approximately equal intensities indicates strong exciton coupling. The crystal structure (Figure 3.21) of this complex shows that the angle, $\tau \approx 48°$, with a distorted tetrahedral

geometry.[78] This orientation would be expected to give rise to absorption peaks with significantly different intensities. This anomaly has been investigated further using DFT methods.

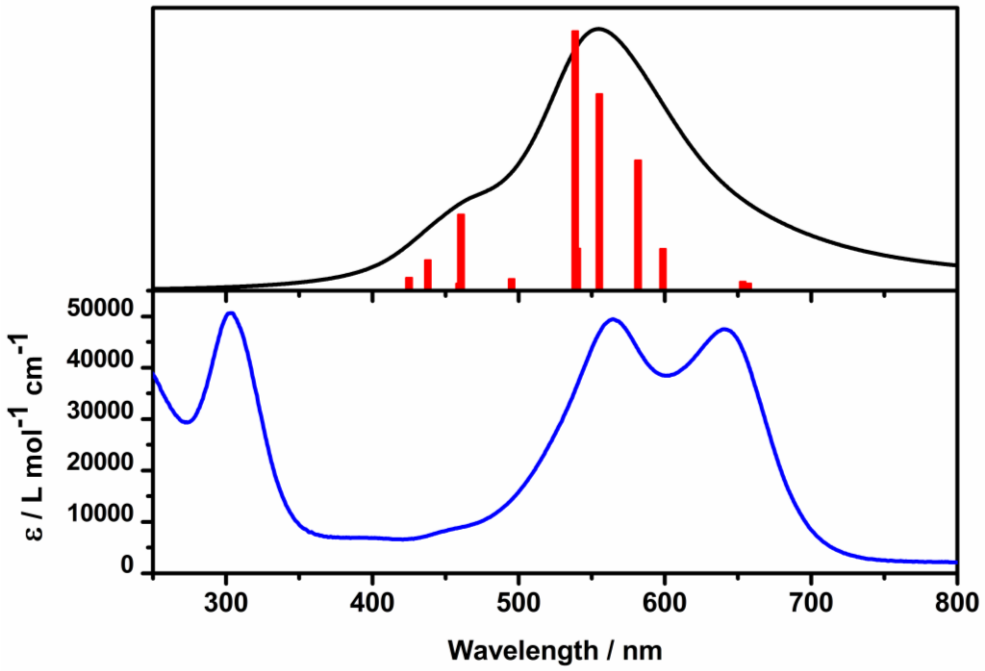

Figure 3.27. Experimental (blue) and calculated (black) absorption spectra of **43** in CH_2Cl_2. The calculated absorption spectra was calculated using DFT/B3LYP 6-311+G (d,p) on Cu(II) and the dipyrrin core atoms and 6-31G(d) on the phenyl ring atoms including C-PCM solvent model. The line shape of the calculated spectrum has been simulated using the calculated oscillator strengths (red).

*3.6.5 DFT investigations of the exciton effects of **43***

The optimised geometry (DFT/B3LYP 6-311+G (d,p) on Cu(II) and the dipyrrin core atoms and 6-31G(d) on the phenyl ring atoms) of **43** is shown in Figure 3.28. For both basis sets the calculated angle between the azadipyrrinato planes is ~56°. This compares to the angle of 48° estimated from the crystal structure (Figure 3.21). The observation that the different sized basis sets arrive at the same angle between the ligand planes almost certainly indicates that the angle obtained in the solid state (from x-ray crystal data) and in solution (from geometry optimisation calculations) is different by approximately 8°. The difference is most likely explained by crystal packing effects in the solid state.

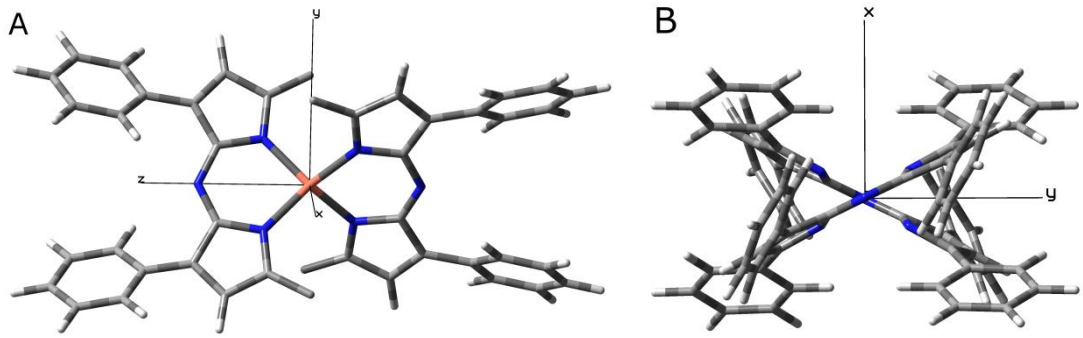

Figure 3.28. Optimised geometry of **43** (DFT/B3LYP 6-311+G (d, p) on the Cu(II) and the dipyrrin core atoms and 6-31G(d) on the phenyl ring atoms) with C-PCM solvent model included. (A) Full view with the phenyl rings in the α-positions omitted for clarity. (B) Side view illustrating the angle ($\tau \approx 56°$) formed between the azadipyrrinato ligand planes. The x-, y-, and z-planes are the C_2 rotation axis.

A TD-DFT calculation with the lowest 48 excited states was used to simulate the calculated absorption spectrum (Figure 3.27) (as outlined in the experimental section). The calculated absorption spectrum shows a broad intense peak centred at 551 nm. This peak consists of five very closely spaced intense transitions. There is a prominent shoulder at higher energy (~460 nm) made up of two intense transitions.

Numerous one electron configurations contribute to these strong electronic transitions of **43** (Table 3.2). The molecular orbitals involved in the strongest electronic transitions are depicted in Figure 3.29. However, the numerous one-electron configurations for each transition make it difficult to interpret without the aid of electron density difference (EDD) or natural transition orbital (NTO) plots. It was computationally expensive to obtain these one-electron configurations (62 days using 16 processors); therefore, it was unviable to obtain the EDD or NTO plots for the purposes of this thesis. The one-electron configurations are further complicated by the unrestricted nature of the calculation. Since Cu(II) has a d^9 electron configuration this complex requires an unrestricted calculation because the spatial and spin components cannot be separated for the doublet configuration. The spin orbitals, rather than the spatial orbitals for restricted calculations, are therefore calculated and shown below in Figure 3.29.

Table 3.2. Calculated and experimental absorption parameters for **43**.

Experimental		**Calculated**			
λ (nm)	ε (L mol^{-1} cm^{-1})	λ (nm)	Configuration (% contribution)	Oscillator strength[a] (f)	Direction of transition dipole moment
641	47 500	599	HOMO-4(β) → LUMO(β) (65)	0.104	+z-plane
		582	HOMO-1(α) → LUMO(α) (16), HOMO(α) → LUMO+1(α) (26), HOMO-1(β) → LUMO+1(β) (11), HOMO(β) → LUMO+2(β) (43)	0.323	+x-plane
565	49 400				
		555	HOMO-4(α) → LUMO(α) (11), HOMO-1(α) → LUMO+1(α) (13), HOMO-3(β) → LUMO+1(β) (18), HOMO-2(β) → LUMO+2(β) (11), HOMO-1(β) → LUMO+2(β) (18)	0.487	+y-plane
		540	HOMO-5(α) → LUMO+1(α) (18), HOMO-2(α) → LUMO(α) (45)	0.104	+z-plane
		539	HOMO-4(α) → LUMO(α) (17), HOMO-3(α) → LUMO+1(α) (14), HOMO-1(α) → LUMO+1(α) (13), HOMO-1(β) → LUMO+2(β) (15)	0.643	-y-plane
		461	HOMO-2(α) → LUMO(α) (41), HOMO-5(β) → LUMO+1(β) (31), HOMO-4(β) → LUMO+2(β) (20)	0.1889	+z-plane
		438	HOMO-5(α) → LUMO+1(α) (45), HOMO-5(β) → LUMO+1(β) (31)	0.0758	-z-plane

[a] Only oscillator strengths greater than 0.075 have been included

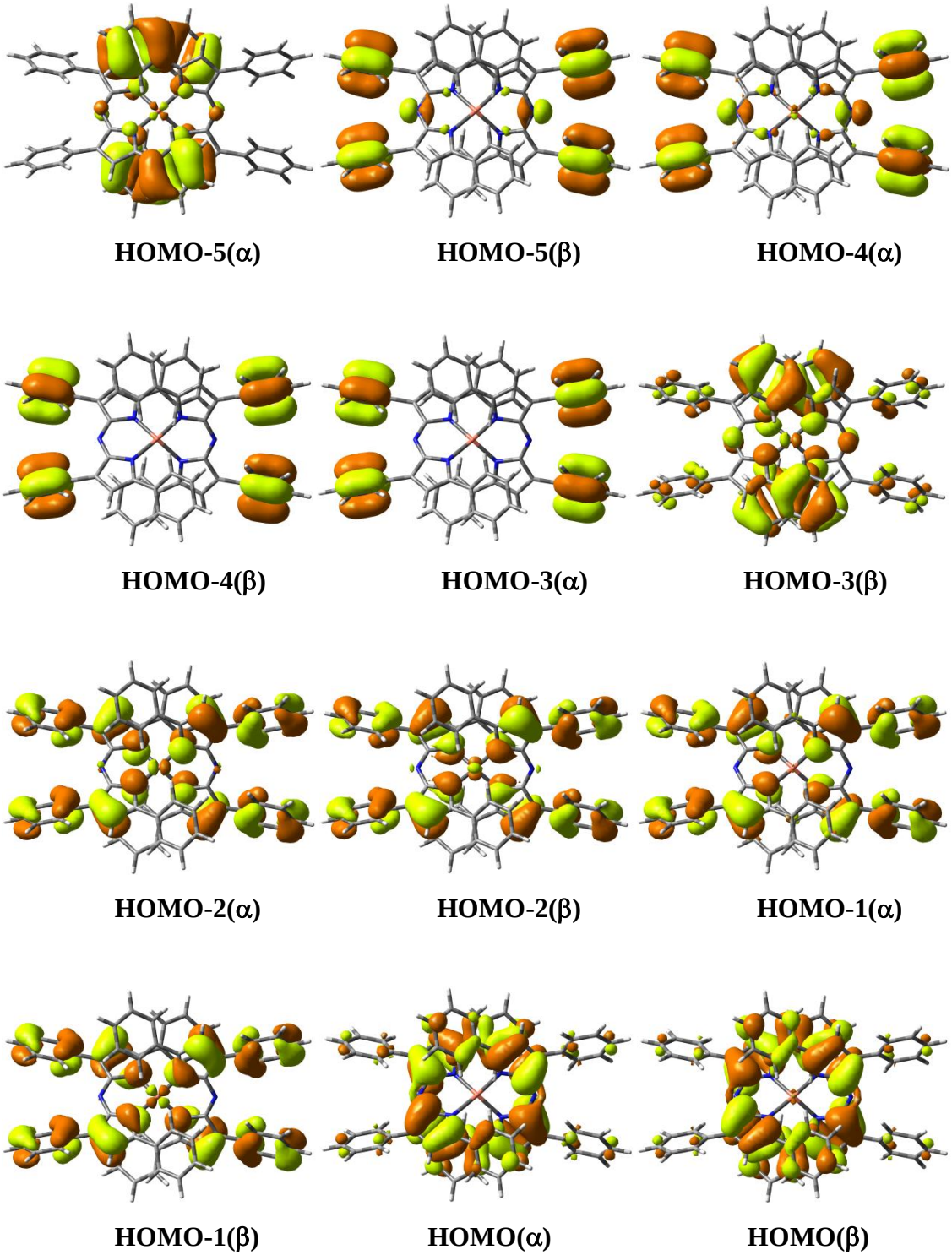

Figure 3.29A. Selected highest occupied molecular orbitals involved in the transitions of **43**.

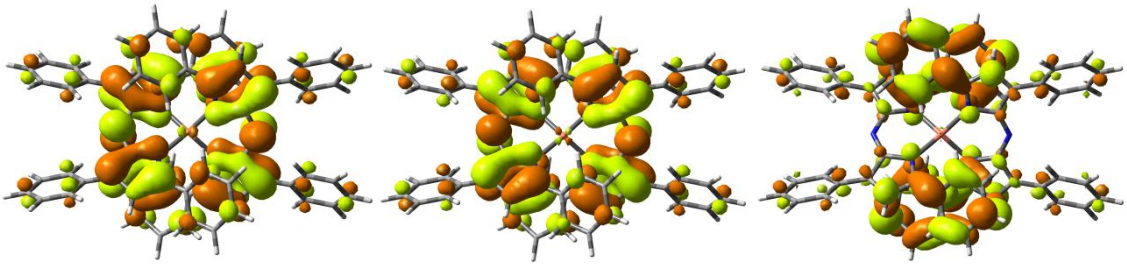

LUMO(α) **LUMO(β)** **LUMO+1(α)**

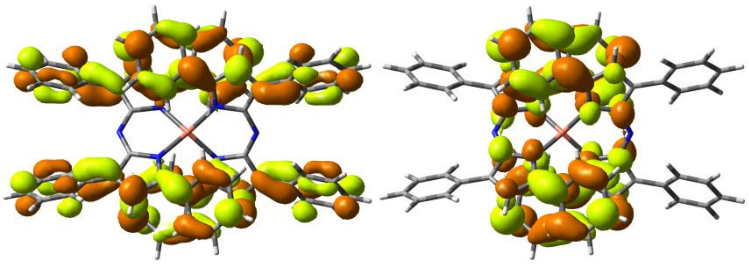

LUMO+1(β) **LUMO+2(β)**

Figure 3.29B. Selected lowest unoccupied molecular orbitals involved in the transitions of **43**.

Nevertheless the orientations of the transition dipole moment in each of the strongest electronic transitions provide insight into the direction of the electron movement in each transition (Figure 3.30 and Table 3.2). Surprisingly, for each transition the transition dipole moment is polarised exclusively along only one of the x-, y-, or z-axes. There are three transitions polarised in the positive z-direction and one in the negative z-direction, there is a transition polarised in the positive y-direction and one in the negative y-direction, and a single transition polarised in the positive x-direction. The "pair" of transition dipole moments in the y-direction or a "pair" of transition dipole moments in the z-direction could combine to give the observed spectrum (Figure 3.27). A further TD-DFT calculation is required to obtain the electron density difference (EDD) plots or natural transition orbital (ETOs) plots for **43**. This will significantly aid in the interpretation of the molecular orbital diagrams. Most importantly it is anticipated that the plots will reveal whether this complex does obey the exciton model If this complex does obey the exciton model then the results should also indicate which pair/s of transition dipole moments are responsible for the exciton coupling.

For the Cu(II) azadipyrrinato complex the TD-DFT results do not support the assumption of a single transition dipole moment for each of the azadipyrrin ligands

polarised along the core of the azadipyrrin ligand (Figure 3.26) parallel to the nitrogen atoms (analogous to that of dipyrrin and BODIPYs). This result *may* imply that this complex does not follow the simple exciton model.

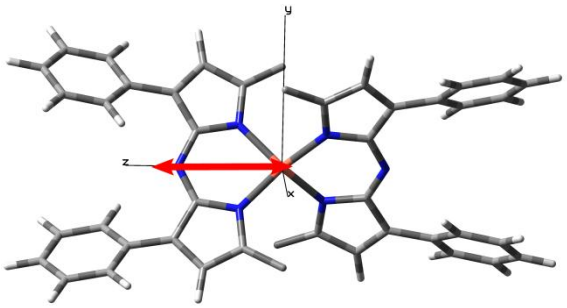

461 nm 540 nm 599 nm

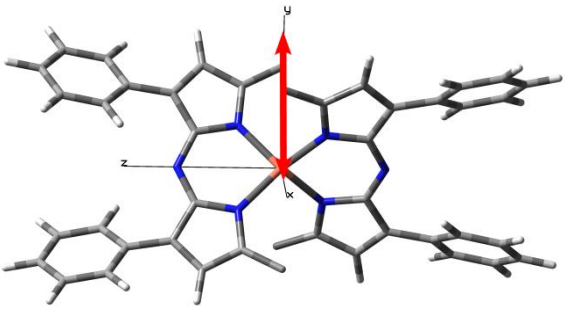

555 nm

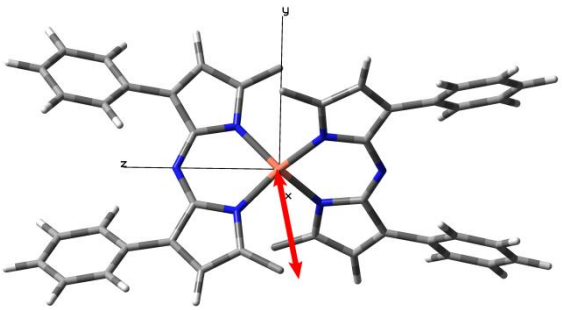

582 nm

Figure 3.30. Illustration of the orientation for the transition dipole moment for the strongest electronic transitions of **43**. The transition at 438 nm (not shown) is polarised along the negative z-direction. The transition at 539 nm (not shown) is polarised along the negative y-direction.

3.7 Summary

The synthesis and characterisation of a library of new transition metal complexes of dipyrrin ligand **34** has been achieved in this chapter to examine the exciton coupling in dipyrrinato (and azadipyrrinato complexes). This includes the first report of a homoleptic Rh(III)-dipyrrinato complex.

DFT calculations of the dipyrrin ligand **34** have confirmed that the transition dipole moment is polarised along the dipyrrin core parallel to the nitrogen donor atoms. The position and strength of the transition dipole moment in dipyrrin ligands gives rise to intense absorption bands (π–π^* transitions) in the visible region of the absorption spectrum. The transition dipole moments are orientated in a non-planar manner upon coordination of dipyrrin ligands to a metal centre. The angle between the transition dipole moments have been determined using crystallographic data.

The exciton coupling of these complexes has been investigated using electronic absorption spectroscopy. Exciton coupling is characterised by strong spectral shifts or splitting of the absorption band. There is a significant blue shift in the absorption of all the [M**L**$_2$] dipyrrinato complexes relative to the unperturbed chromophore. Exciton coupling is most easily observed in [M**L**$_3$] dipyrrinato complexes such as [Co**L**$_3$] and [Rh**L**$_3$] since the absorption band is clearly split into two peaks with a large energetic separation.

The exciton coupling of [M**Laza**$_2$] azadipyrrinato complexes in the literature has been discussed. The [Cu**Laza**$_2$] complex was an anomaly in the series. The absorbance spectrum features two peaks of approximately equal intensity but the angle between the transition dipole moments (determined using crystallographic data) suggests that the absorption peaks would have significantly different intensities. TD-DFT calculations of [Cu**Laza**$_2$] show that there are multiple closely spaced strong electronic transitions. The transition dipole moments responsible for these electronic transitions are not polarised along the azadipyrrin core parallel to the nitrogen donor atoms, rather, each transition dipole moment is polarised along one of the C_2 rotational axes of the complex. The simple exciton model may breakdown for this complex.

3.8 Future work

3.8.1 Exciton coupling in Ru(II)-dipyrrinato complexes

The Ru(II)-dipyrrinato complexes (**46** and **47** in chapter 4) previously reported from our group[42, 43] are expected to have prominent exciton coupling although this is not immediately obvious in their electronic absorption spectra (Figure 4.8). However, circular dichroism (CD) spectroscopy is another useful tool to confirm exciton coupling interactions. This requires resolving the complex into its enantiomers and ensuring the material is enantiopure by HPLC.

A literature procedure for the resolution of $[Ru(bipy)_2(py)_2][Cl_2]$[190] using dibenzoyl-D-tartrate is expected to provide the starting material of **46**. Following this, coordinating the dipyrrin ligand in the normal manner[42] (see chapter 4) should provide the enantiomers of **46**. The carboxyl functional group on the dipyrrinato ligands of **47** provide a convenient point for a chiral base to attach to give the enantiomers of this complex. Scanning a wide range of chiral bases and solvent conditions is expected to provide the enantiomers of **47**.

*3.8.2 Further investigations into the exciton effects of **43** and other azadipyrrinato complexes*

The results from the TD-DFT calculation of the [Cu**Laza**$_2$] complex **43** means that the exciton interactions of the other [M**Laza**$_2$] complexes warrants further investigations Firstly, it is important to reliably establish the position of the transition dipole moment in the azadipyrrin ligand **44** using TD-DFT methods. Following on from this the electronic absorption spectra of the [M**Laza**$_2$] complexes can be re-visited. Further TD-DFT calculations are also required to obtain the electron density difference (EDD) plots or natural transition orbital (ETO) plots for **43**. It is anticipated that these plots will confirm whether **43** does follow the exciton model. If the complex does follow the exciton model then it is hoped that these calculations will reveal which pair/s of transition dipole moments are responsible for the observed absorption spectrum. If the plots show that this complex does follow the exciton model then the calculations may reveal an explanation for why the exciton model breaks down for this complex. This work is currently being pursued.

Resonance Raman spectroscopy and resonance Raman intensity analysis (RRIA) are currently being used to further investigate the nature of the electronic nature of **43**. Preliminary observations suggest that there is strong coupling between the excited states of this complex.

Acknowledgements

I wish to thank the following people for their assistance in this chapter: Associate Professor Shane Telfer for collecting crystal data and solving the crystal structures, Dr Matthias Lein (Victoria University of Wellington) for running the DFT calculations on **43**, and Mr Graham Freeman for the synthesis of **44**.

Chapter 4

Ru(II)-dipyrrinato complexes and their applications

4.1 Introduction

Ru(II), a d^6 metal in the second row of the periodic table, generally forms stable, diamagnetic, and kinetically inert octahedral complexes with extraordinary photochemical and photophysical properties. In particular, Ru(II)-polypyridyl complexes are widely known due to their unique combination of chemical stability, redox properties in both the ground and excited states, luminescence, and long excited state lifetimes. The archetypal Ru(II) complex, $[Ru(bipy)_3]^{2+}$, has attracted the attention of researchers the world over. The rich photophysical and photochemical properties of this complex and its derivatives have been well characterised.[191, 192]

The absorption spectrum of $[Ru(bipy)_3]^{2+}$ is dominated by multiple metal-to-ligand charge transfer (MLCT) and π-π^* transitions from the singlet ground state, S_0. Internal conversion occurs to the lowest singlet state, S_1, followed by intersystem crossing through to a low energy MLCT triplet excited state, T_1. The excited state lifetime of $[Ru(bipy)_3]^{2+}$ is on the order of one microsecond depending on the solvent and temperature.[14, 191] Emission arises from excitation into any of the absorption bands of $[Ru(bipy)_3]^{2+}$. The intensity, lifetime, and position of the emission are essentially temperature dependent.[191]

Ru(II)-polypyridine complexes are the most widely employed photoactive chromophores.[191] This has included a multitude of Ru(II)-polypyridine complexes implemented in dye-sensitised solar cell[18, 22, 193, 194] and water splitting applications.[15, 195, 196] Other photoactive Ru(II) complexes have been successfully targeted for the photocatalytic reduction of small molecules such as CO_2 and CS_2,[197-199] designed to bind to the major or minor groove of DNA[200-205] for biological studies[206] and designed for intercalation into DNA.[207, 208] The long term goal for these target complexes is to find new anti-cancer agents.[209, 210] Ru(II) nitrosyl complexes also show promise as anti-cancer agents. These complexes produce nitric oxide (NO) upon irradiation with light which results in cell death.[211, 212]

4.2 Ru(II) complexes as dyes in DSSCs and as water splitting photocatalysts

4.2.1 Dye-sensitised solar cells (DSSCs)

Dye-sensitised solar cells (DSSCs) are alternatives to silicon solar cells. They both convert solar energy to electrical energy (but via different mechanisms).

In DSSCs, light is absorbed by a photosensitiser (dye) which is anchored to a semiconductor film, typically TiO_2. Upon light absorption, the dye is promoted to an electronically excited state, where charge separation takes place and an electron is injected within femto- to picoseconds[20] into the conduction band of the semiconductor film. The electrons are transported to an external circuit via the anode (generally a conducting glass substrate). A redox electrolyte such as I^-/I_3^- reduces the dye back to its original state.[18] See Figure 4.1 for a schematic representation for the operation of a DSSC. Solar power conversion efficiency (η) is a measure of the energy from sunlight that is converted to electric energy. Solar power conversion efficiency is the ratio of electric power output to the incoming light intensity that strikes the cell and is determined by measuring the photocurrent as a function of the cell voltage (equation 4.1).[213]

$$\eta(\%) = \frac{J_{SC} V_{OC} FF}{I_S} \qquad (4.1)$$

Here, J_{SC} is the short circuit photocurrent which is the maximum current occuring when the voltage across the cell is zero. V_{OC} is the open circuit voltage which is the maximum voltage occurring when the net current through the cell is zero. FF is the fill factor and I_S is the incident solar intensity. The internationally accepted standard test conditions use reference air mass (AM 1.5) sunlight (viewed at 48° overhead) with a value normalised to 1000 W m^{-2} with the temperature kept constant at 25 °C.[214]

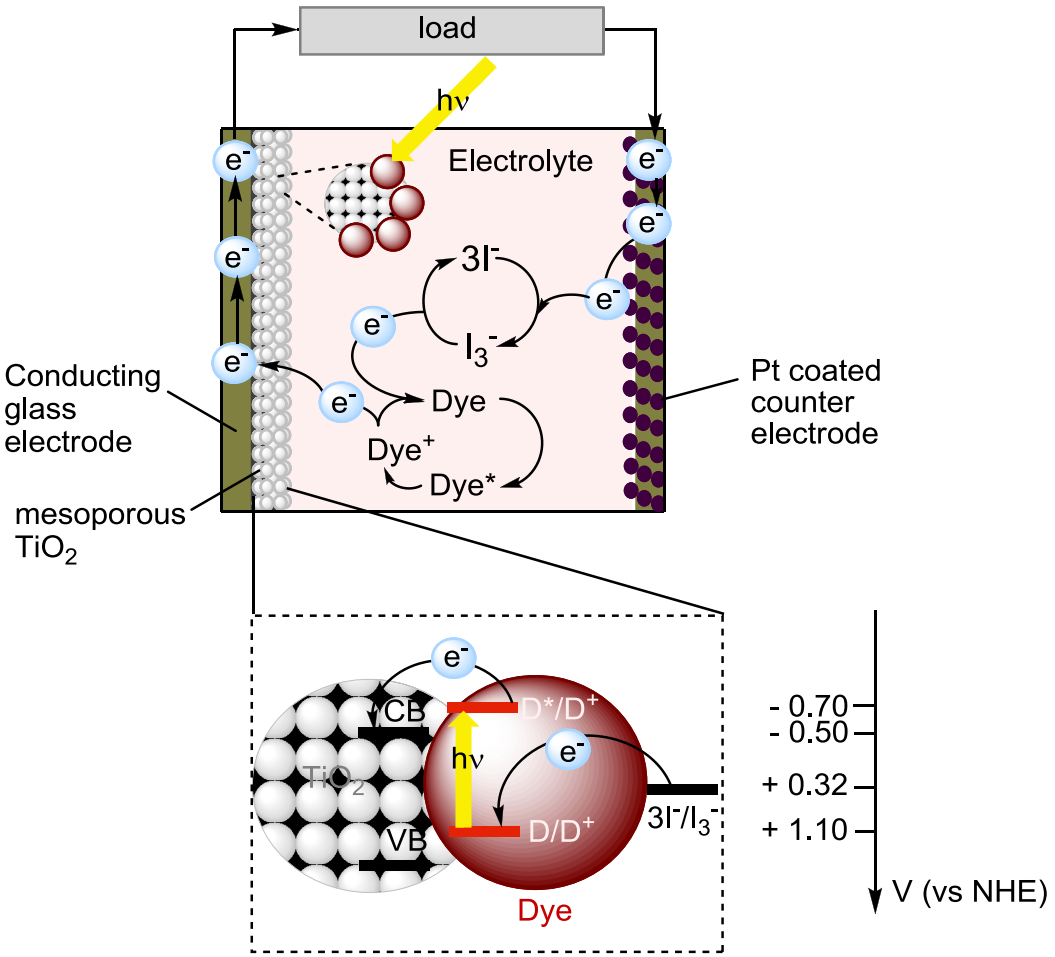

Figure 4.1. A schematic representation of a dye-sensitised solar cell. The potentials for the DSSC are based on **N719**, TiO_2 and I^-/I_3^- redox couple.[19, 194] Light is absorbed by a dye on the surface of TiO_2. Charge separation takes place from the electronic excited state and an electron is injected into the conduction band of the semiconductor film. The electrons are transported to an external circuit via the anode and a redox electrolyte reduces the dye back to its original state (adapted from reference 194).

4.2.2 Ruthenium based DSSCs

Ground breaking work of O'Regan and Grätzel[17] lead to the first ruthenium based polypyridyl dyes. To date many of the most efficient photosensitisers (dyes) have been produced in the Grätzel research lab. The most well-known dyes from the Grätzel lab are discussed below (Figure 4.2). Numerous reviews of dye-sensitised solar cells can be found in the literature.[18, 20-22, 194, 215]

The initial work from the Grätzel lab produced **N3**, which exhibited a broad visible light absorption spectrum, a sufficiently long excited state lifetime of ~20 ns, and strong

adsorption to the semiconductor surface (TiO_2). These properties led to this dye having a solar to electric power conversion efficiency of ~10%.[216] Investigating the protonation state of **N3** on the power conversion efficiency led to an increase in the power conversion efficiency when the dye is doubly protonated (referred to as **N719**).[217]

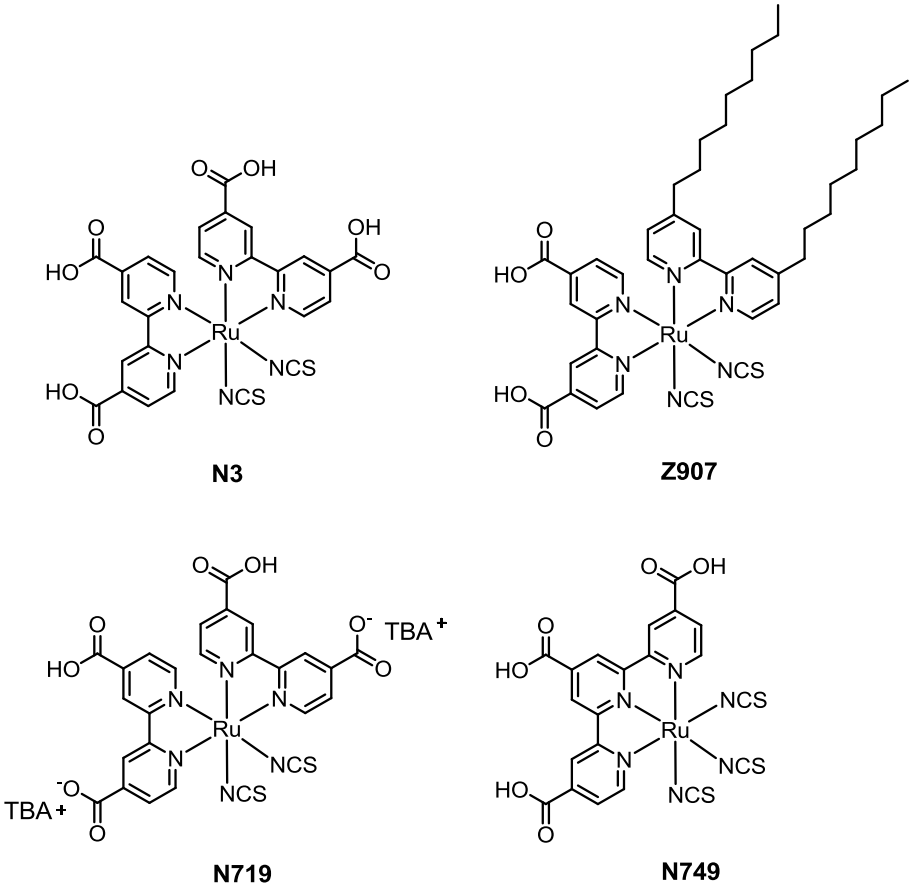

Figure 4.2. The structures of some of the most successful Ru(II)-based photosensitisers from the Grätzel research laboratory.

Extending the spectral response to the near-IR region was one key aspect to improving power conversion efficiencies. **N749** was designed with one terpyridine ligand substituted with three carboxyl ligands and three thiocyanato ligands. This combination has a power conversion efficiency of 10.4%.[218] Increased molar extinction coefficient, prevention of the dye aggregation on the semiconductor surface, and optimisation of the redox potential of the dye has been achieved with **Z907**, which has two hydrophobic alkyl chains on the back of 2,2'-bipyridine. The power conversion efficiency was only

~7% even with a decyl phosphonic acid (DPA) as a co-absorber but this dye showed superior thermal stability.[219]

Many of the published dyes have employed thiocyanato (NCS^-) ligands, despite the known reduced chemical stability of complexes containing thiocyanato ligands. The most promising example without thiocyanato ligands is a cyclometallated Ru(II) complex (**YE05**) with a power conversion efficiency of 10.1% (Figure 4.3).[19, 22] During the injection of the electron into the conduction band of the semiconductor the cyclometallated ligand stabilises the Ru^{3+} excited state generated at this time.[19] Also the fluorine substituents alter the electron-donating properties of the cyclometallated ligand, in such a way that the oxidation potential is more positive than the redox electrolyte. This provides the driving force for the rapid regeneration of the oxidised dye during electron injection into the conduction band of TiO_2.[19, 22] This result gives promise for the production of efficient dyes without thiocyanato ligands.

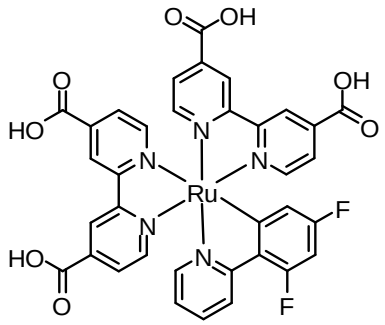

YE05

Figure 4.3. The structure of the most efficient (η = 10.1%) cyclometallated Ru(II) dye.

4.2.3 Water splitting devices

Since the report by Honda and Fujishima of the electrochemical photolysis of water using TiO_2,[220] water splitting devices have been receiving increased attention in a bid to alleviate the world's energy crisis. The goal is to use the concept of artificial photosynthesis to efficiently split water into its component elements hydrogen (H_2) and oxygen (O_2), using solar energy to drive the thermodynamically unfavourable reactions (equation 1.2). In a practical sense, hydrogen is the more valuable of these two components as it can be used in fuel cells.[196]

$$4H^+ + 4e^- \longrightarrow 2H_2 \qquad \text{(reduction)}$$

$$2H_2O \longrightarrow 4H^+ + 4e^- + O_2 \qquad \text{(oxidation)}$$

$$2H_2O \xrightarrow{h\nu} 2H_2 + O_2 \qquad E° = -1.23\ V \qquad (1.2)$$

The process of splitting water is very complex. The overall transformation involves multiple proton and electron transfers which need to be coupled as well as a considerable thermodynamic barrier to overcome.[7, 11, 196] Catalysts are required to achieve this overall transformation.[16]

One approach is to use catalytic transition metal complexes as catalysts to split water.[7, 10] The Ru(II) complex (**45**)[15] and the Pt(IV) complex[221] by Milstein *et al.* represent state-of-the-art examples in terms of advances in water splitting (Figure 4.4).[196] The ruthenium complex that splits water into hydrogen and oxygen though a series of unusual steps, however, is not yet catalytic. The hydrogen is generated thermally and the oxygen is produced photochemically.[15] These complexes utilise 'pincer' ligands. These are tridentate ligands capable of accommodating 4-, 5- and 6-coordinate environments. The most attractive feature of these ligands is the ability to extensively tune the donor groups bonding to the metal centre. In particular the photochemically driven oxygen-oxygen bond forming reductive elimination step is unprecedented and a significant advancement in the goal towards catalysed water splitting. The design of the 'pincer' ligand also addresses the coupling of the proton-electron transfer in an elegant manner, via the sequence of protonation/deprotonation and subsequent aromatisation/dearomatisation of the pincer ligand (Figure 4.4).[15, 196]

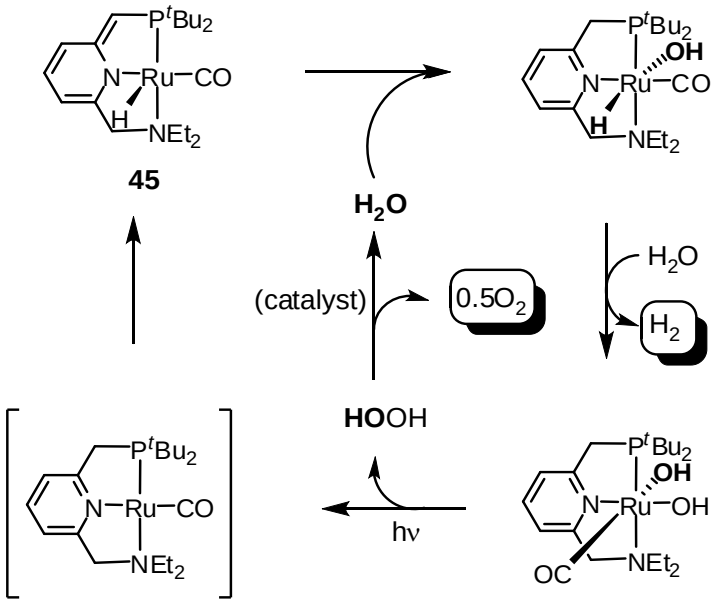

Figure 4.4. The proposed reaction scheme for the splitting of water using a Ru(II) complex **45** with a 'pincer' ligand. The hydrogen is generated thermally while the oxygen is produced photochemically (adapted from references 15, 196).

One of the many other approaches[11, 14, 222-224] is to use photovoltaic devices to capture sunlight and create an electric circuit by separating the csharges. This device may be either a silicon semiconductor,[2] or a DSSC typically on TiO_2.[195] Then transition metal complexes as catalysts are employed to mediate water splitting. Catalysts are employed at either end of the photovoltaic device to prevent the charges from recombining with each other. A catalyst at the anode splits water to produce oxygen and protons in an oxidative process. The protons flow to the other catalyst at the cathode where they combine with the electrons (from the circuit) to make hydrogen in a reductive process.[2, 7, 16, 195, 225] Ultimately this process splits water into hydrogen and oxygen. Significant research is going into perfecting each catalyst independently from the entire water splitting device.[16, 224]

4.2.4 Essential dye characteristics and previous Ru(II)-dipyrrinato complexes

The essential characteristics of the dye in DSSC are:[194]

- an absorption spectrum that extends across the visible wavelength region and even into the near-infrared region (with large molar absorption coefficients).

- anchoring groups such as $–CO_2H$, $–H_2PO_3$, $–H_2SO_3$ to strongly bind the dye to the semiconductor surface (TiO_2, SnO_2, ZnO).
- an excited state energy level that is higher than the energy level of the conduction band of the semiconductor. This ensures that electron transfer from the excited state (D^*/D^+) of dye to the conduction band of the semiconductor is energetically downhill.
- the reduction potential of the oxidised level (D/D^+) lower than the redox potential of the redox couple (I^-/I_3^-).
- photostability as well as electrochemical and thermal stability.

In exploratory work from our group, the coordination of dipyrrinato ligands to Ru(II) was achieved to prepare first generation Ru(II)-bipyridine-dipyrrinato complexes (**46** and **47**) (Figure 4.5).[42, 43] The first generation Ru(II)-dipyrrinato complexes were designed with carboxyl groups ($–CO_2H$) for binding to the semiconductor surface on the dipyrrin moiety.

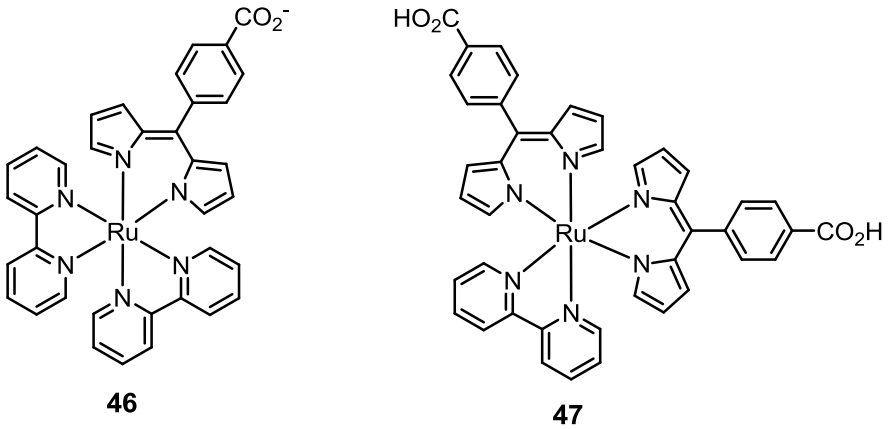

46 **47**

Figure 4.5. First generation Ru(II)-dipyrrinato complexes.

The synthesis of these complexes was achieved using a combination of both conventional and microwave heating. Microwave irradiation of dipyrrin ligand (**34**) and $[Ru(bipy)_2Cl_2]$ in ethylene glycol in the presence of NEt_3 gives **46a**. Standard hydrolysis conditions were employed to hydrolyse the ester group to provide **46**. Standard esterification conditions were used to re-esterify the carboxyl group to provide **46b** (Figure 4.6).[42] A reaction between dipyrrin ligand (**34**) and $[Ru(dmso)_4Cl_2]$ in absolute EtOH produces **48** as an intermediate, followed by a direct reaction with excess 2,2'-

bipyridine at high temperatures provides **47a**. Standard hydrolysis conditions were employed to provide **47** (Figure 4.7).[42, 43]

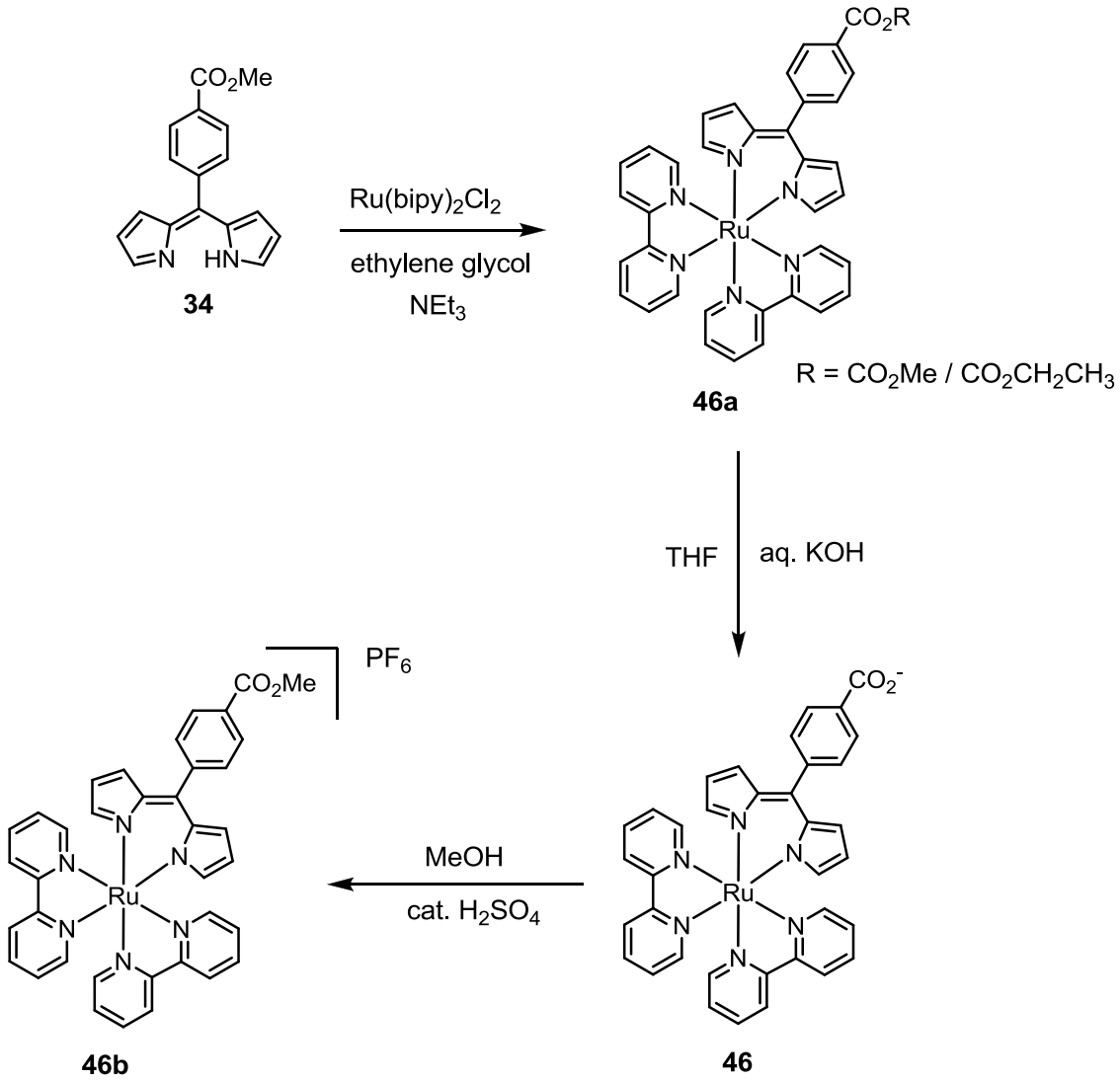

Figure 4.6. Synthesis of first generation Ru(II)-dipyrrinato complex **46**.

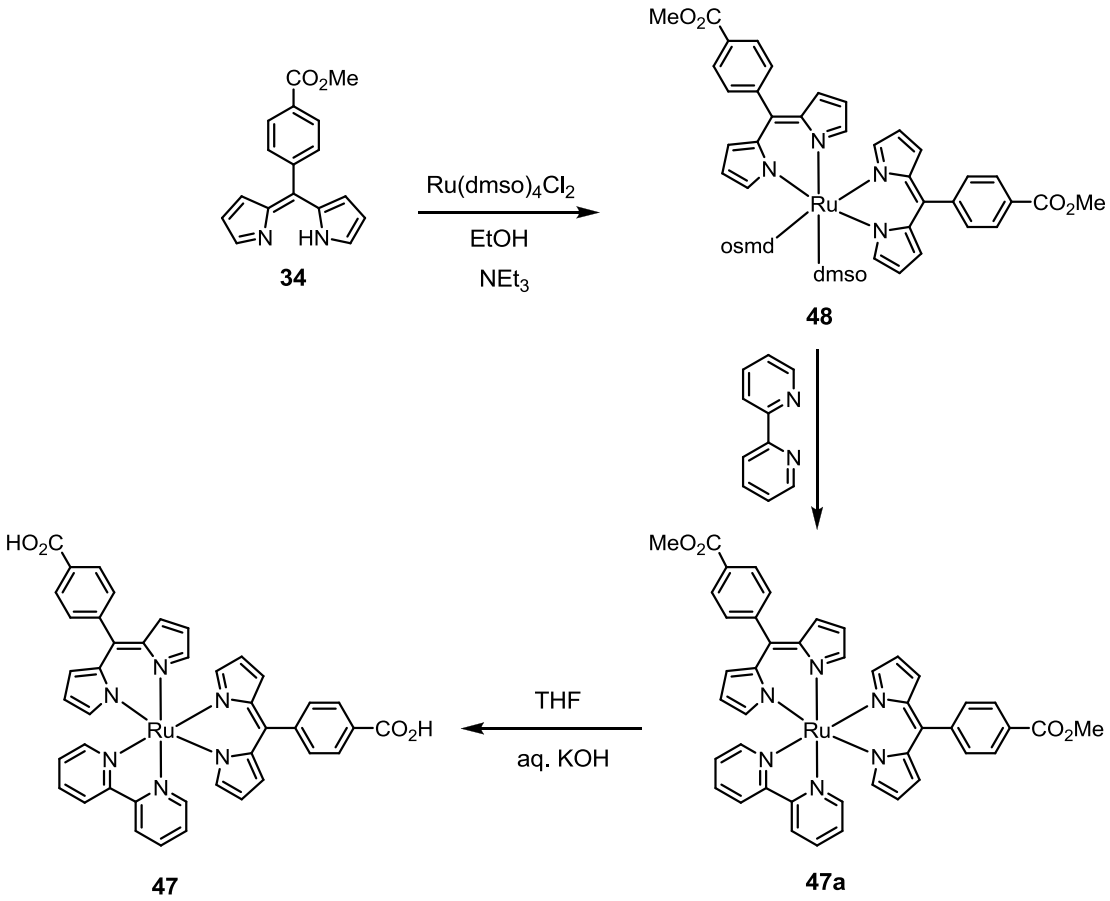

Figure 4.7. Synthesis of first generation Ru(II)-dipyrrinato complex **47**.

Complexes **46** and **47** exhibit two distinct peaks in the absorption spectra (Figure 4.8). The absorption spectra clearly show that the dyes absorption extends across the visible wavelength region with large absorption coefficients. Assignments of the transitions were confirmed using resonance Raman, using appropriate excitation wavelengths into each absorption peak.[42] The peak centred between 445-465 nm for both complexes is ascribed to π–π* transition centred on the dipyrrin chromophore. By incorporating two dipyrrin ligands into the complex (**47**) the intensity of the transition is doubled relative to the intensity of transition for **46** (containing a single dipyrrin ligand). At longer wavelengths, there is a weaker transition ascribed to an MLCT transition from Ru(II) to the bipyridine substituent. For **46** this transition is centred at 517 nm and for **47** this transition is significantly red shifted to 638 nm. It is important to note that a weak Ru(II)-dipyrrin MLCT transition is also observed (see later). The intensity and position of the two transitions can be tuned by changing the number of dipyrrin and bipyridine ligands.

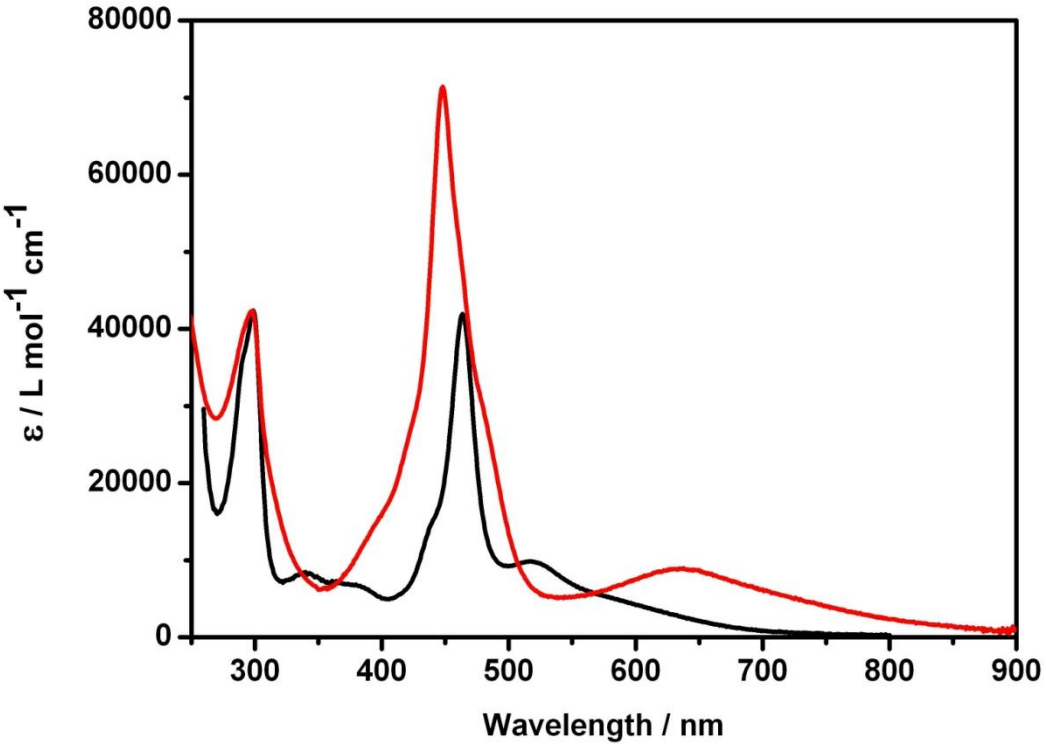

Figure 4.8. Absorption spectra of **46** (black) in DMSO and **47** (red) in MeOH with NaOH.

4.3 Objectives of this work and target complexes

Dipyrrinato complexes of Ru(II) combine the favourable light absorption properties of dipyrrins with the well characterised chemistry of Ru(II)-bipyridine complexes. The light harvesting ability of first generation Ru(II)-dipyrrinato complexes combined with the strongly bind ability of these complexes to TiO_2[43] show that Ru(II)-dipyrrinato complexes may have promising applications as dyes in DSSCs.

4.3.1 Target DSSC complexes

As an extension to the exploratory work in our group, further dipyrrinato complexes were targeted (Figure 4.9). In literature examples of Ru(II) bipyridine DSSCs the carboxyl group is exclusively positioned on the bipyridine substituent to take advantage of the Ru(II)→bipyridine metal-to-ligand charge transfer excited states.[20, 21, 193, 215, 226, 227] However, the position of the carboxyl group can be shifted to the dipyrrinato ligand to alter the mode of charge injection, assuming the electron comes from the π–π* excited state of the dipyrrinato. In first generation Ru(II)-dipyrrinato complexes **46** and

47 the carboxyl functional group on the dipyrrinato ligand provides an alternative point for charge injection into the TiO_2 (Figure 4.10). In the second generation Ru(II)-dipyrrinato complexes (**49** and **50**) the carboxyl groups are on the bipyridine substituents (Figure 4.10) where the electron comes from the metal-to-ligand charge transfer excited states.[20, 193, 226-228]

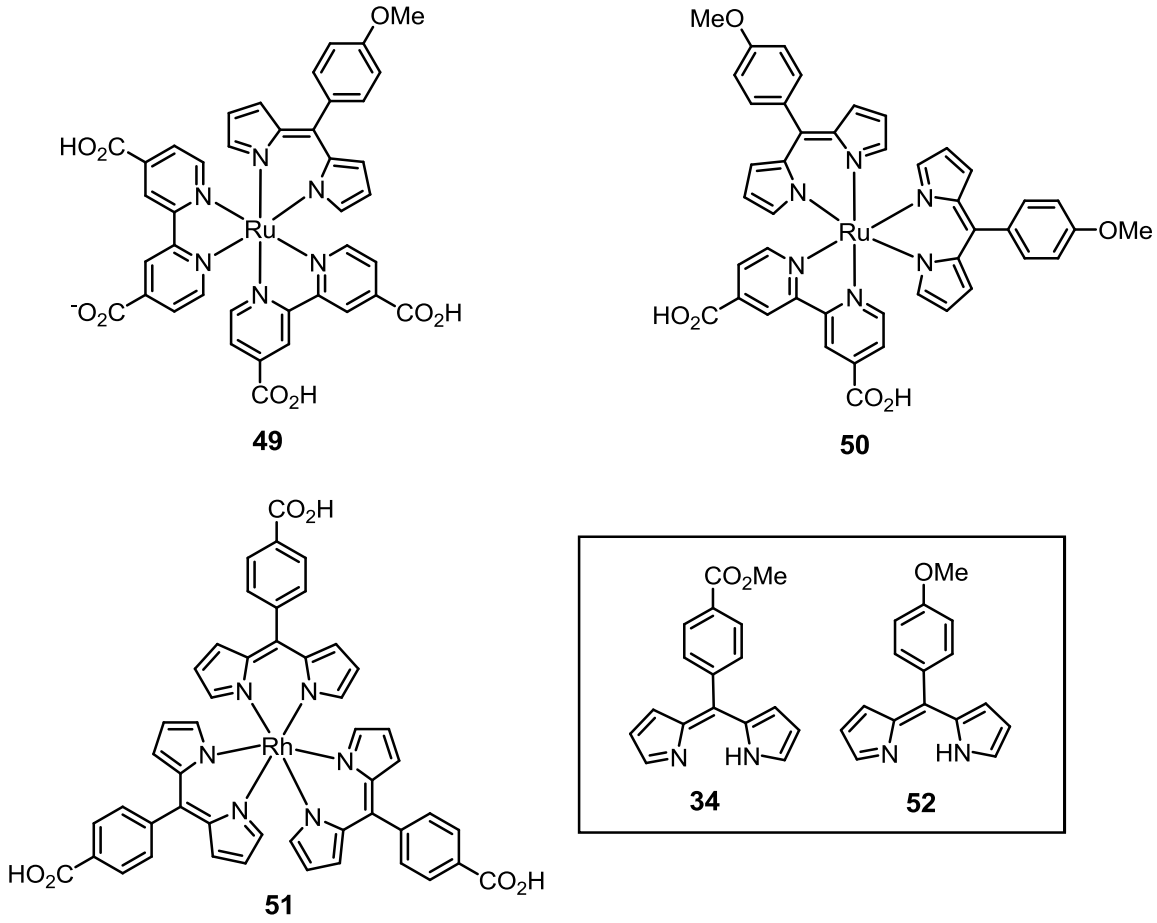

Figure 4.9. Target Ru(II) and Rh(III) dipyrrinato complexes for DSSC applications. Inset: dipyrrin ligands used in target dipyrrinato complexes.

In the same way that the fluorine substituents of the cyclo-metallated ligand in **YE05** alters the electron-donating properties of the ligand,[19] different functional groups can be incorporated on the aryl substituent of the dipyrrinato ligand to tune the electronic and redox properties of the Ru(II)-dipyrrinato complexes. By incorporating electron donating groups into the dipyrrinato ligand this increases the electron density on the ligand and redox processes occur at more negative potentials. The opposite effect occurs when electron-withdrawing groups are incorporated.[46] Complex **49** is analogous

to Grätzel's cyclometalated dye **YE05** where the cyclometalated ligand is replaced with the methoxy functionalised dipyrrin ligand (**52**). By incorporating the electron donating methoxy functional group in ligand **52** the goal was to alter the redox potentials of complexes **49** and **50**. This is to ensure that favourable electron transfer takes place between the excited state (D^*/D^+) of the dye and the conduction band of the semiconductor.[194]

Despite limited applications of rhodium containing complexes in solar energy conversion,[229, 230] a homoleptic Rh(III) complex **51** was targeted where the carboxyl groups on the dipyrrin ligand can anchor to TiO_2 [43] (Figure 4.9). This complex was targeted to identify any structure-activity relationships that might develop between the Ru(II)- and Rh(III)-dipyrrinato dyes.

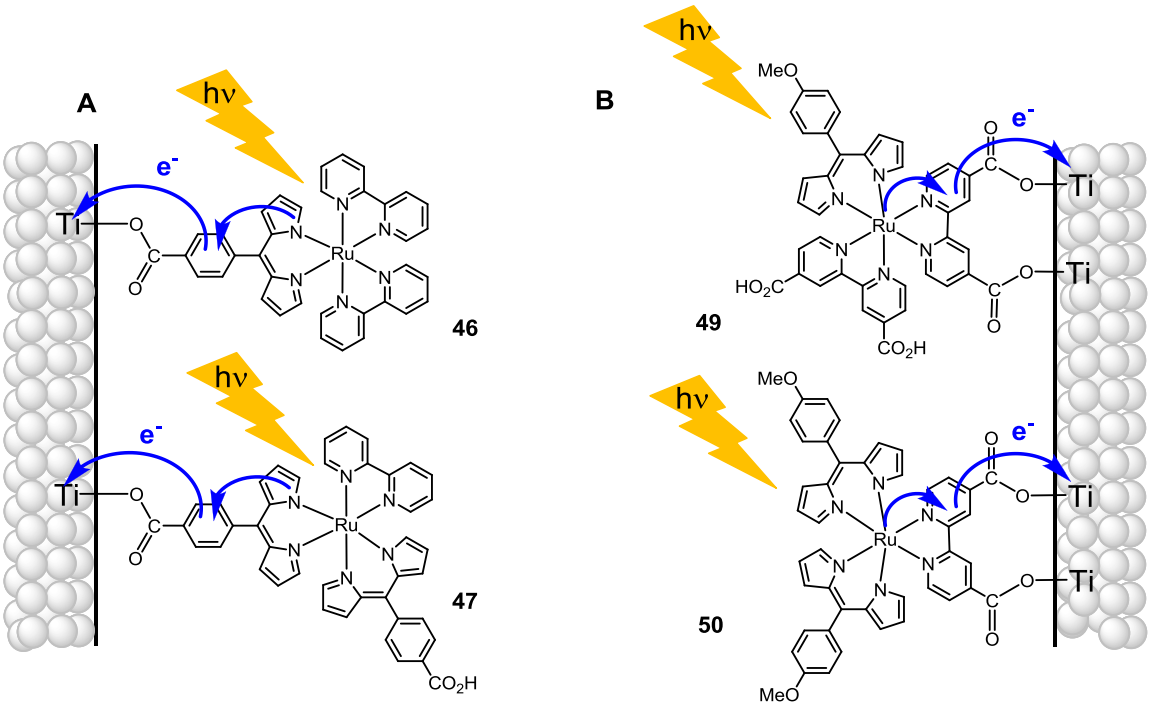

Figure 4.10. Schematic of charge injection modes of Ru(II)-dipyrrinato complexes. Charge injection via the carboxyl groups on the periphery of the (A) dipyrrinato ligand assuming the electron comes from the π–π* excited state and (B) bipyridine ligand where the electron comes from the metal-to-ligand charge transfer excited states.[20, 193, 215, 226-228]

4.3.2 Other targets

To study the ultrafast kinetics of these Ru(II)-dipyrrinato complexes **53** and **54** were targeted to serve as "models" for the DSSC complexes **49** and **50** (Figure 4.11). Complexes **53** and **54** have no carboxyl functional groups on the bipyridine ligand.

The rotation of the *meso*-phenyl substituent is an important non-radiative pathway for the relaxation of dipyrrin-centred excited states.[41, 48, 90, 231] Incorporating the mesityl functional group into dipyrrinato complexes is known to enhance the emission of the complex by restricting the rotation of the phenyl ring.[48, 50, 90, 91] The mesityl functional group is incorporated into the dipyrrin ligand (**56**) in an endeavour to increase emission of complex **55** (Figure 4.11).

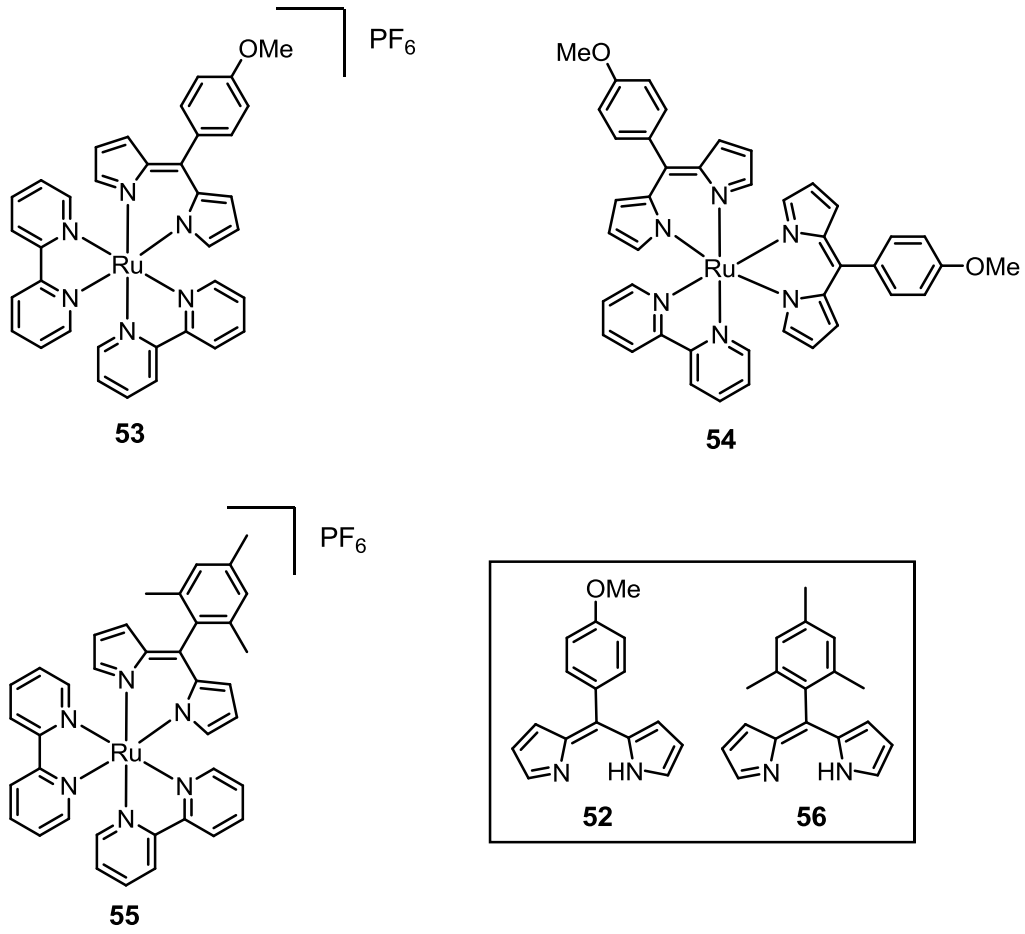

Figure 4.11. Target Ru(II)-dipyrrinato complexes. Inset: dipyrrin ligands used in target dipyrrinato complexes.

4.4 Experimental details

4.4.1 Computational procedures

All computations were performed with the Gaussian *03*[232] suite. Density Functional Theory was used exclusively using the B3LYP hybrid functional. Calculations using LANL2DZ for **46** experienced convergence problems, so replacing the LANL2DZ basis set on all of the non-heavy atoms (in this case C, H, N and O atoms) with 6-31G resolved these issues. Therefore the basis set consisted of LANL2DZ for the ruthenium atoms and 6-31G +(d) for all the other atoms for **46**. For **46**-**H** calculations the LANL2DZ basis set was used for all atoms. Self-consistent reaction field methods, more specifically the polarisable continuum model (C-PCM) of Barone[151] were used to model solvent effects. All geometry optimisations, frequency, and time-dependent calculations were carried out using the C-PCM model. GaussSum2.2.4[152] was used to extract vibrational frequencies and Raman activities from the calculations. The calculated Raman spectrum was scaled by 0.9723[233] and convoluted with a Gaussian function with FWHM of 5 cm^{-1}. Excited-state energies and oscillator strengths were calculated using time-dependent methods. The calculated absorption spectrum is a sum of a series of δ-functions, located at the transition frequencies and scaled by the calculated oscillator strengths. Each δ-function is convoluted with a Gaussian with a FWHM value dependent on the FWHM values of the corresponding peaks of the experimental absorption spectrum. Electron density difference maps were generated by subtracting the ground-state one-particle total density from the one-particle densities for selected excited-states using the Cubeman utility in Gaussian *03*.

4.4.2 Experimental procedures

*4.4.2.1 Synthesis of dipyrrin ligands **52** and **56***

52 and **56** were prepared by following literature procedures[28, 31](as briefly summarised in chapter 2) and purified by adaptations of literature procedures.

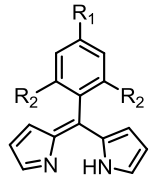

R_1 = OMe, R_2 = H (**52**)
R_1 = R_2 =CH_3 (**56**)

Purification of **52** was achieved by dissolving the crude solid in $CHCl_3$ with sonication for 30 mins and filtration. This step was repeated two or three times. The product (solid) was dissolved in CH_2Cl_2 and adsorbed on to silica and further purified by column chromatography on silica using CH_2Cl_2 as

the eluent. The solvent polarity was gradually increased to CH_2Cl_2/MeOH (95/5) to elute the product as a dark yellow/brown band. The fractions were left to stand overnight to precipitate out the product as a yellow/orange solid. Spectroscopic data matched those previously published.[28]

Purification of **56** was achieved by dissolving in CH_2Cl_2 adsorbing the crude product on to silica and purified by column chromatography on silica using CH_2Cl_2 as the eluent. The solvent polarity was gradually increased to CH_2Cl_2/MeOH (98.5/1.5) to elute the product as a dark yellow band. Spectroscopic data matched those previously published.[31]

*4.4.2.2 Synthesis of complexes **49-51** and **53-55***

*Synthesis of **49***

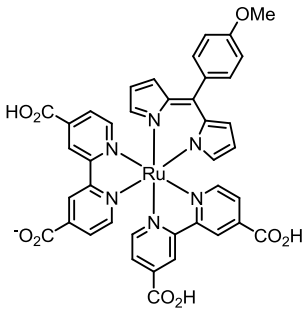

$[Ru(bipyCO_2Me)_2Cl_2]$[234] (0.056 g, 0.078 mmol) was dissolved in CH_2Cl_2 (40 mL) and AgOTf (0.052 g, 0.203 mmol) was added as a solid. The solution was stirred at room temperature for 2 hours before the mixture was filtered through Celite and the solvent was removed on a rotary evaporator. **52** (0.038 g, 0.152 mmol), and Na_2CO_3 (0.092 g, 0.868 mmol) were then added in DMF/H_2O (6 mL/3 mL) and the reaction was heated to 140 °C for 30 mins in a microwave reactor (closed vessel, power = 200W, pressure = 250 psi). The solvent was removed by vacuum distillation and solid was dissolved in water and cooled in an ice-water bath. Aqueous 0.15 M HPF_6 was added to adjust to pH 3. The resulting precipitate was isolated by centrifugation and washed with water acidified to pH 3 using HPF_6. Further purification of the solid was achieved by sonication of the solid in MeCN. Yield: 0.043 g (0.044 mmol, 56%). ^{1}H NMR (500 MHz, D_2O/NaOH, 25 °C) δ (ppm): 3.90 (s, 3H), 6.23 (d, *J* = 4.2 Hz, 2H), 6.40 (d, *J* = 4.1 Hz, 2H), 6.47 (s, 2H), 6.88 (d, *J* = 8.6 Hz, 2H), 7.22 (d, *J* = 8.6 Hz, 2H), 7.60 (dd, *J* = 1.5, 5.9 Hz, 2H), 7.66 (dd, *J* = 1.4, 5.8 Hz, 2H), 7.90 (d, *J* = 5.8 Hz, 2H), 8.04 (dd, *J* = 5.9 Hz, 2H), 8.78 (dd, *J* = 1.2, 7.1 Hz, 4H); ^{13}C NMR (125 MHz, D_2O/NaOH, 25 °C) δ (ppm): aggregation at high concentrations prevented a spectrum from being recorded; IR / cm^{-1}: 719 (w), 734 (w), 754 (w), 776 (m), 819 (m), 859 (w), 871 (w), 890 (w), 943 (w), 988 (m), 995 (m), 1036 (m), 1182 (w), 1246 (s, br), 1348 (m), 1377 (m), 1408 (w), 1540 (m), 1606 (w), 1724

(m, br), 3077 (w), 3102 (w); UV-Vis (H_2O/NaOH) λ_{max}/nm (ε / L mol^{-1} cm^{-1}): 310 (55 200), 387 (17 000), 456 (42 200), 521 (17 700); ESI-MS: *m*/*z* = 839.66 ([M+H])

*Synthesis of **50***

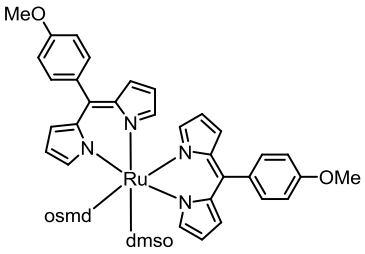

$[Ru(dmso)_4Cl_2]$[235] (0.101 g, 0.208 mmol), **52** (0.111 g, 0.443 mmol), NEt_3 (0.1 mL) were combined in absolute EtOH. The reaction was heated to 82 °C for 10 mins in a microwave reactor at standard pressure (open vessel, power = 200W). The reaction mixture was cooled to room temperature, filtered through a plug of deactivated neutral alumina and washed with acetone. The solvent was removed on a rotary evaporator. Hexane was added to the solid material and sonicated (to remove free dmso) and complex **57** was filtered off and washed with hexane. Further purification could be achieved via chromatography on deactivated neutral alumina using CH_2Cl_2/hexane (1/1) and increasing the gradient to CH_2Cl_2. Yield: 0.158 g (0.209 mmol, 40-75%). ^{1}H NMR (500 MHz, $CDCl_3$, 25 ℃) δ (ppm): 2.55 (s, 6H), 2.80 (s, 6H), 3.90 (s, 6H), 6.23 (dd, *J* = 1.6, 4.4 Hz, 2H), 6.49 (t, *J* = 1.4 Hz, 2H), 6.54 (td, *J* = 1.6, 4.1 Hz, 4H), 6.73 (dd, *J* = 1.5, 4.4 Hz, 2H), 6.94 (td, *J* = 1.6, 7.2 Hz, 4H), 7.30 (m, 4H), 8.80, (t, *J* = 1.5 Hz, 2H); ^{13}C NMR (125 MHz, $CDCl_3$, 25 ℃) δ (ppm): 45.29, 45.62, 55.37, 112.50, 117.99, 118.10, 131.22, 131.53, 131.92, 132.18, 132.59, 135.97, 136.99, 146.50, 151.78, 155.27, 159.60

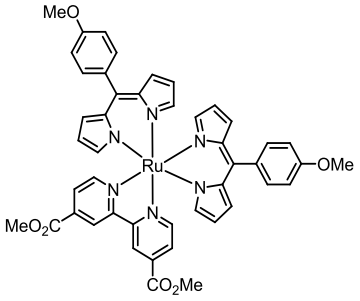

57 (0.702 g, 0.929 mmol) and 4,4'-dimethoxycarbonyl-2,2'-bipyridine[236, 237] (0.252 g, 0.926 mmol) were combined in DMF (11 mL). The reaction was heated to 150 °C for 20 mins in a microwave reactor at standard pressure (open vessel, power = 200 W). Most of the DMF was distilled off before H_2O was added and precipitate filtered off. The solid was dissolved in CH_2Cl_2 and dried over $MgSO_4$. The solution was concentrated and then filtered through an alumina plug which was washed with CH_2Cl_2. The combined eluents were concentrated on a rotary evaporator. Purification of the dark green solid (**50a**) was achieved via chromatography on deactivated neutral alumina using CH_2Cl_2/hexane (3/1) as the eluent. Yield: 0.204 g (0.234 mmol, 25%). ^{1}H NMR (500 MHz, $CDCl_3$, 25 ℃) δ (ppm): 3.88 (s, 6H), 4.00 (s, 6H), 6.09 (dd, *J* = 1.6, 4.3 Hz,

2H), 6.19 (t, *J* = 1.4 Hz, 2H), 6.35 (dd, *J* = 1.5, 4.4 Hz, 2H), 6.47 (dd, *J* = 1.4, 4.3 Hz, 2H), 6.64 (t, *J* = 1.2 Hz, 2H), 6.69 (dd, *J* = 1.4, 4.4 Hz, 2H), 6.92 (d, *J* = 8.2 Hz, 4H), 7.37 (m, 4H), 7.68 (dd, *J* = 1.7, 6.1 Hz, 2H), 8.42 (dd, *J* = 0.6, 6.0 Hz, 2H), 8.64, (d, *J* = 1.3 Hz, 2H); ^{13}C NMR (125 MHz, $CDCl_3$, 25 °C) δ (ppm): 52.89, 53.43, 55.34, 112.41, 112.46, 116.17, 118.10, 121.32, 124.29, 129.32, 131.62, 131.69, 132.01, 132.04, 136.21, 136.67, 146.41, 146.96, 151.64, 153.32, 159.40, 160.42, 165.20; ESI-MS (acetone/MeOH): 872.92 *m*/*z* ([M+]); UV-Vis (CH_2Cl_2) λ_{max}/nm (ε / L mol^{-1} cm^{-1}): 323 (25 500), 446 (83 600), 669 (11 200).

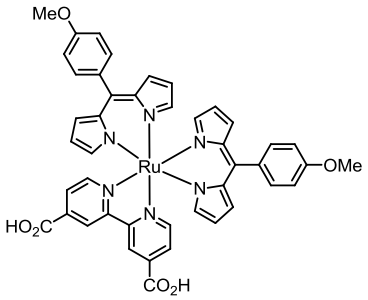

50a (0.211 g, 0.242 mmol) was dissolved in THF (8 mL) and 1M KOH (8 mL). The reaction was heated to 68 °C for 20 mins in a microwave reactor at standard pressure (open vessel, power = 200 W). The THF was removed on a rotary evaporator before being acidified with 1 M HCl. The dark green solid was filtered off and washed thoroughly with water and hexane. Purification of the dark green solid (**50**) was achieved by diffusion of hexane vapours into a solution of the complex in acetone. Yield: 0.123 g (0.146 mmol, 60%). ^{1}H NMR (500 MHz, DMSO-d_6, 25 °C) δ (ppm): 3.94 (s, 6H), 6.14 (dd, *J* = 1.4, 4.2 Hz, 2H), 6.32 (m, 4H), 6.35 (dd, *J* = 1.1, 4.1 Hz, 2H), 6.49 (d, *J* = 3.9 Hz, 2H), 6.62 (s, 2H), 7.02 (dd, *J* = 1.2, 7.3 Hz, 4H), 7.32 (d, *J* = 7.6 Hz, 2H), 7.37 (d, *J* = 7.8 Hz, 2H), 7.63 (dd, *J* = 1.4, 5.8 Hz, 2H), 7.92 (d, *J* = 5.8 Hz, 2H), 8.57 (s, 2H); ^{13}C NMR (125 MHz, DMSO-d_6, 25 °C) δ (ppm): aggregation at high concentrations prevented a spectrum from being recorded; IR / cm^{-1}: 714 (m), 770 (m), 816 (m), 889 (w), 986 (m), 1004 (w), 1028 (s), 1110 (w), 1175 (m), 1245 (s, br), 1291 (w), 1345 (m), 1375 (m), 1404 (w), 1511 (m), 1536 (m), 1604 (m), 1711 (w), 2849 (w), 2917 (w); UV-Vis (DMSO) λ_{max}/nm (ε / L mol^{-1} cm^{-1}): 321 (25 100), 448 (73 300), 656 (10 700); MALDI-MS: *m*/*z* = 844.29 ([M+]) Anal. Calcd for [**50**]: ($C_{44}H_{34}N_6O_6Ru$) · $2H_2O$: C, 60.06; H, 4.35; N, 9.55. Found: C, 60.25; H, 4.26; N, 9.40.

*Synthesis of **51***

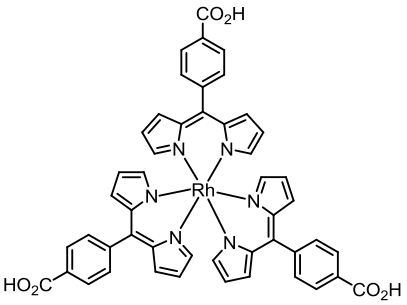

42 (0.0458 g, 0.049 mmol) was dissolved in a mixture of THF (15 mL) and 1 M aqueous KOH (15 mL) and heated to reflux overnight. The reaction mixture was then cooled to room temperature and the THF was removed under reduced pressure before being acidified with 1 M aqueous HCl solution. The resulting orange precipitate was isolated by filtration, washed thoroughly with H_2O, and air-dried. Yield: 0.041 g (0.046 mmol, 94%). An analytically pure sample was obtained by diffusing pentane vapours into a solution of the complex in acetone. ^{1}H NMR (400 MHz, DMSO-d^6, 25 °C) δ (ppm) 6.44 (m, 6H), 6.52 (m, 6H), 6.59 (m, 6H), 7.54 (d, *J* = 7.4 Hz, 6H), 8.06 (d, *J* = 7.4 Hz, 6H); ^{13}C NMR (100 MHz, DMSO-d^6, 25 °C) δ (ppm) 118.81, 128.49, 130.15, 130.95, 131.50, 133.99, 141.58, 146.25, 149.92, 166.91; ESI-MS (DMSO): *m*/*z* = 891.7 ([M-H]$^-$); UV-VIS (DMSO): λ_{max}/nm (ε / L mol^{-1} cm^{-1}): 313 (27 400), 404 (25 600), 466 (69 400), 502 (52 200); Anal. Calcd for [**51**] ($C_{48}H_{33}N_6O_6Rh$) · $3.5H_2O$: C, 60.32; H, 4.22; N, 8.79. Found: C, 60.12; H, 3.93; N, 8.55.

*Synthesis of **53***

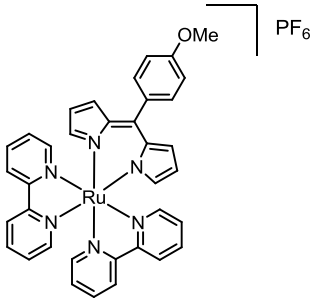

$[Ru(bipy)_2(py)_2][(PF_6)_2]$ (0.405 g, 0.470 mmol),[190, 238] **52** (0.118 g, 0.471 mmol), NEt_3 (0.130 mL) were combined in ethylene glycol (10 mL). The reaction was heated to 100 °C for 8 mins in a microwave reactor (closed vessel, power = 200 W, pressure = 250 psi). Excess aqueous NH_4PF_6 was added and the solution was stirred at for 3 hours at room temperature. The precipitate was filtered off and washed thoroughly with water. Purification of the brown solid was achieved via chromatography on deactivated alumina using CH_2Cl_2 as the eluent. The product eluted as a red/brown band when the polarity of the solvent was increased to CH_2Cl_2/MeOH (99.5/0.5). Further purification was achieved by recrystallisation of the product in hot hexane/CH_2Cl_2. Yield: 0.041 g (0.051 mmol, 11%). ^{1}H NMR (500 MHz, acetone-d$_6$, 25 °C) δ (ppm): 3.89 (s, 3H), 6.29 (dd, *J* = 1.4, 4.4 Hz, 2H), 6.47 (t, *J* = 1.4 Hz, 2H), 6.62 (dd, *J* = 1.4, 4.4 Hz, 2H), 7.03 (d, *J* = 8.8 Hz, 2H), 7.36 (d, *J* = 8.8 Hz, 2H), 7.46 (m, 2H), 7.57 (m, 2H), 8.01 (m, 2H), 8.07 (m, 6H),

8.70 (m, 4H); ^{13}C NMR (125 MHz, acetone-d_6, 25 °C) δ (ppm): 55.71, 113.52, 118.83, 124.34, 124.46, 127.39, 127.73, 132.18, 132.55, 136.59, 136.97, 137.15, 148.01, 149.55, 152.22, 152.82, 158.51, 159.22, 160.92; UV-Vis (CH_2Cl_2) λ_{max}/nm (ε / L mol^{-1} cm^{-1}): 525 (14 500), 459 (47 000), 353 (14 200), 297 (55 000); ESI-MS(MeOH): 663.66 *m/z* ([M+]); Anal. Calcd for [**53**]: ($C_{36}H_{29}NF_6N_6OPRu$): C, 53.53; H, 3.62; N, 10.41. Found: C, 53.66; H, 3.71; N, 10.53

*Synthesis of **54***

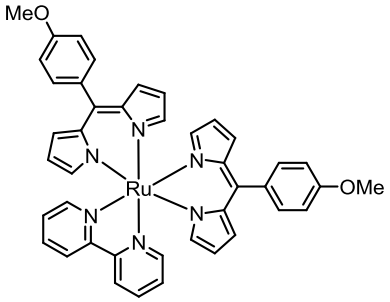

57 (0.154 g, 0.209 mmol) and 2,2'-bipyridine (0.033 g, 0.211 mmol) was combined in DMF (5 mL). The reaction was heated to 150 °C for 9 mins in a microwave reactor at standard pressure (open vessel, power = 200 W). Most of the DMF was distilled off before H_2O was added and precipitate filtered off. The solid was dissolved in CH_2Cl_2 and dried over $MgSO_4$. The solution was concentrated and then filtered through an alumina plug and washed with CH_2Cl_2. The solvent was removed on a rotary evaporator. Purification of the dark green solid was achieved via chromatography on deactivated alumina using CH_2Cl_2/hexane (3/1) as the eluent. Further purification was achieved by recrystallisation of the dark green solid (**54**) in hot MeOH and CH_2Cl_2. Yield: 0.072 g (0.095 mmol, 46%). ^{1}H NMR (500 MHz, acetone-d_6, 25 °C) δ (ppm): 3.88 (s, 6H), 6.13 (dd, *J* = 1.5, 4.1 Hz, 2H), 6.29 (dd, *J* = 1.2, 4.4 Hz, 2H), 6.41 (t, *J* = 1.5 Hz, 2H), 6.44 (dd, *J* = 1.3, 4.4 Hz, 2H), 6.58 (dd, *J* = 1.3, 4.4 Hz, 2H), 6.73 (t, *J* = 1.2 Hz, 2H), 7.01 (m, 4H), 7.35 (m, 6H), 7.80 (dt, *J* = 1.6, 8.2 Hz, 2H), 8.17 (dq, *J* = 0.6, 5.7 Hz, 2H), 8.45 (d, *J* = 8.0 Hz, 2H); ^{13}C NMR (125 MHz, acetone-d_6, 25 °C) δ (ppm): aggregation at high concentrations prevented a spectrum from being recorded; UV-Vis ($CHCl_3$) λ_{max}/nm (ε / L mol^{-1} cm^{-1}): 646 (10 700), 450 (78 700), 329 (16 100), 292 (33 100); ESI-MS (acetone with trace TFA/MeOH): *m/z* = 756.80 ([M+]); Anal. Calcd for [**54**]: ($C_{42}H_{34}N_6O_2Ru$): C, 66.74; H, 4.53; N, 11.12. Found: C, 66.56; H, 4.45; N, 11.07.

*Synthesis of **55***

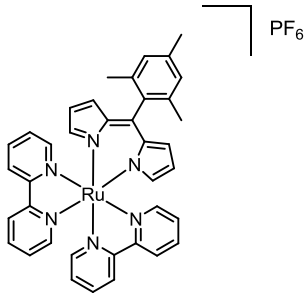

$[Ru(bipy)_2(py)_2][(PF_6)_2]$ (0.380 g, 0.441 mmol),[190, 238] **56** (0.118 g, 0.450 mmol), NEt_3 (0.150 mL) were combined in ethylene glycol (10 mL). The reaction was heated to 100 °C for 10 mins in a microwave reactor (closed vessel, power = 200 W, pressure = 250 psi). Excess aqueous NH_4PF_6 was added and the solution was stirred for 3 hours at room temperature. The precipitate was filtered off and washed thoroughly with water. Purification of the brown solid was achieved via chromatography on deactivated alumina using CH_2Cl_2 as the eluent. The product (**55**) eluted as a red/brown band when the polarity of the solvent was increased to CH_2Cl_2/MeOH (99.5/0.5). Yield: 0.116 g (0.142 mmol, 31%). ^{1}H NMR (500 MHz, acetone-d_6, 25 ℃) δ (ppm): 2.02 (s, 6H), 2.34 (s, 3H), 6.26 (dd, *J* = 1.6, 4.3 Hz, 2H), 6.42 (dd, *J* = 0.8, 4.9 Hz, 4H), 6.97 (s, 2H), 7.47 (t, *J* = 6.6 Hz, 2H), 7.54 (t, *J* = 6.6 Hz, 2H), 8.07 (m, 8H), 8.70 (t, *J* = 6.9 Hz, 4H); ^{13}C NMR (125 MHz, acetone-d_6, 25 ℃) δ (ppm): 19.07, 20.27, 118.39, 123.46, 123.67, 126.30, 126.87, 127.53, 129.51, 135.02, 135.58, 135.74, 135.88, 136.35, 137.13, 145.63, 148.56, 151.37, 152.02, 157.68, 158.34; UV-Vis (CH_2Cl_2) λ_{max}/nm (ε / L mol^{-1} cm^{-1}): 296 (54 800), 348 (9 900), 387 (9 600), 461 (48 200), 525 (15 100); ESI-MS(MeOH): 675.83 *m/z* ([M+]). Anal. Calcd for [**55**]: $(C_{38}H_{33}F_6N_6PRu) \cdot 0.33H_2O \cdot 0.33C_6H_{14}$: C, 56.22; H, 4.52; N, 9.84. Found: C, 56.21; H, 4.08; N, 10.03.

4.4.3 General procedures

4.4.3.1 Resonance Raman solutions

A solution of **46** was prepared in DMSO a concentration of 1.86 mM for resonant Raman measurements at excitation wavelengths of 413 nm, 444 nm, 458 nm, 488 nm, 514.5 nm, and 532 nm. Only 458 nm, 488 nm and 514.5 nm wavelengths are presented in this thesis.

4.4.3.2 Electrochemistry

Electrochemistry as carried out with the assistance of Nessha Wise is detailed in Appendix D1 and cyclic voltammograms are given in Appendix D2.

4.4.3.3 Solid state UV-Vis, device fabrication and solar cell testing

Solid state UV-Vis, device fabrication and solar cell testing of complexes was undertaken by members of the Dr Attila Mozer research group at the Intelligent Polymer Research Institute, University of Wollongong or members of the research group of Professor Yoo Soo Kang at the Energy Materials Lab, Hanyang University. The procedures are outlined in Appendix D3-D4.

4.5 Results and Discussion

4.5.1 Synthesis

The synthesis of ligands **52** and **56** were achieved by literature procedures[28, 31] in two steps (as briefly summarised in chapter 2) (Figure 4.12). Purification of the ligands is laborious. Adaptations of the literature procedures (as discussed in the experimental section) were used to purify the ligands.

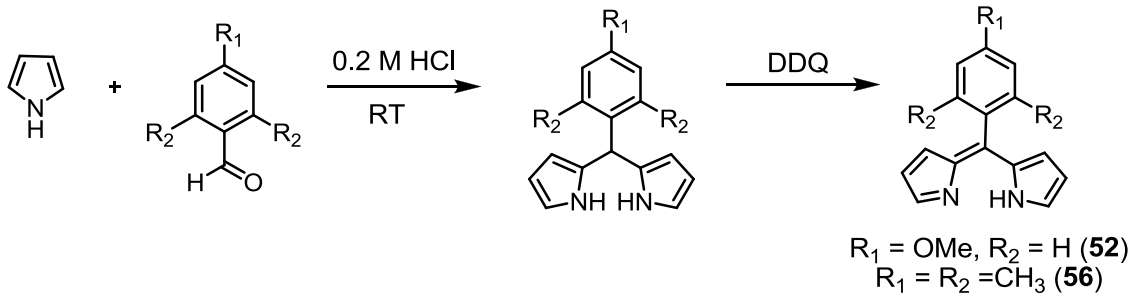

Figure 4.12. Synthetic route to dipyrrin ligands **52** and **56**.

Exploratory work from previous members of our research group established a synthetic methodology for the synthesis of **46** and **47** (as outlined in Figures 4.6 and 4.7). Adaptations of these procedures,[42, 43] using microwave irradiation at every step of the synthesis, reliably produced complexes **50** and **53-55**. Overall, the use of microwave irradiation significantly reduced the reaction times and improved the quality of the products.

The synthesis of **50** is outlined in Figure 4.13. Intermediate complex **57** was obtained in moderate yield by the coordination of dipyrrin ligand **52** to $[Ru(dmso)_4Cl_2]$ in absolute ethanol using microwave irradiation. The next intermediate complex (**50a**) was obtained by an adaptation of the established procedure. The coordination of

4,4'-dimethoxycarbonyl-2,2'-bipyridine (abbreviated as dmcb) to **56** was achieved with microwave irradiation in DMF. The final step in the synthesis of **50** was the hydrolysis of the two ester functionalities to yield the carboxyl functional groups for binding to the semiconductor surface. Standard hydrolysis conditions were employed. However, appropriate reaction conditions were established using microwave irradiation, which significantly reduced the reaction time down to 20 minutes.

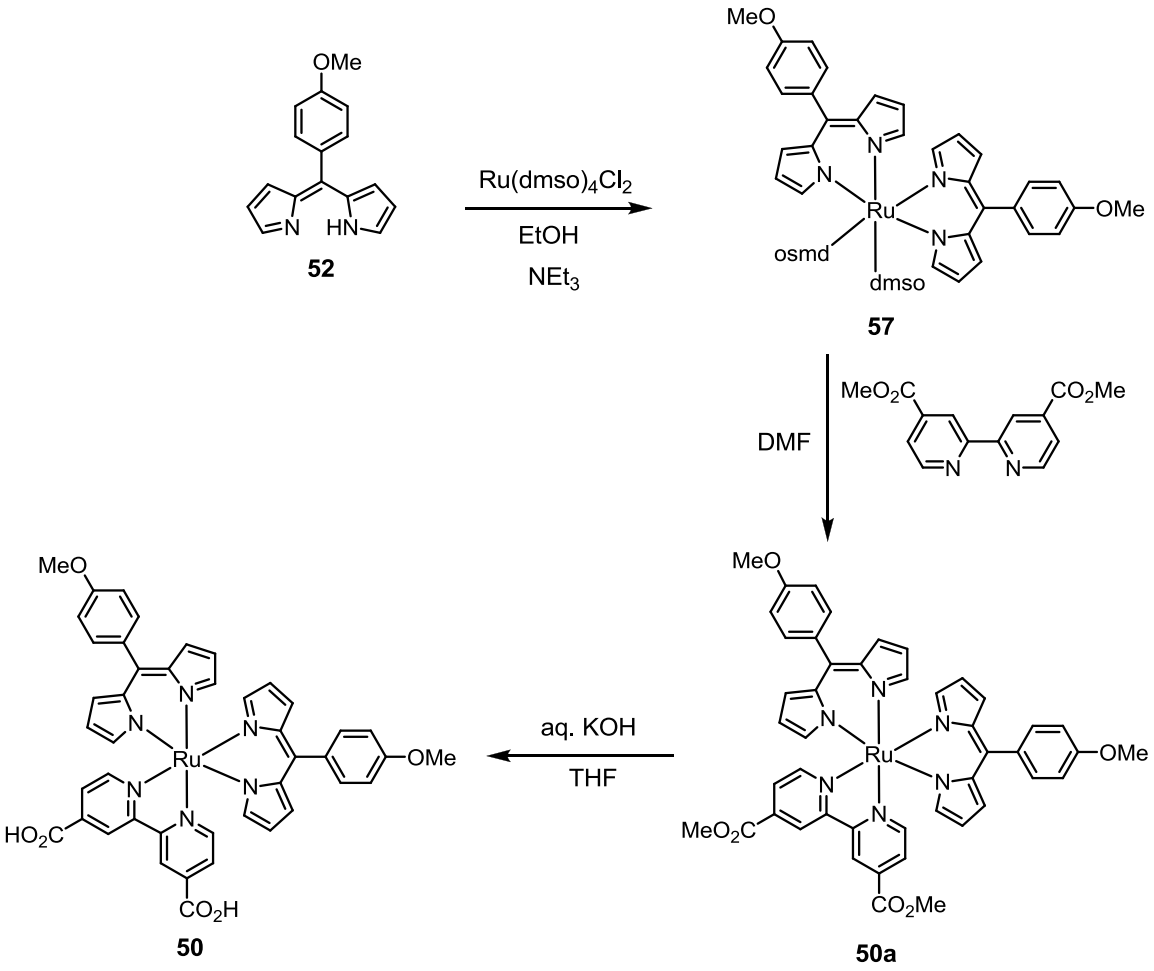

Figure 4.13. The synthetic route to Ru(II)-dipyrrinato complex **50**.

The synthesis of **54** is outlined in Figure 4.14. The coordination of 2,2'-bipyridine to the intermediate complex **57** was achieved using the same conditions established for the synthesis of **50a**.

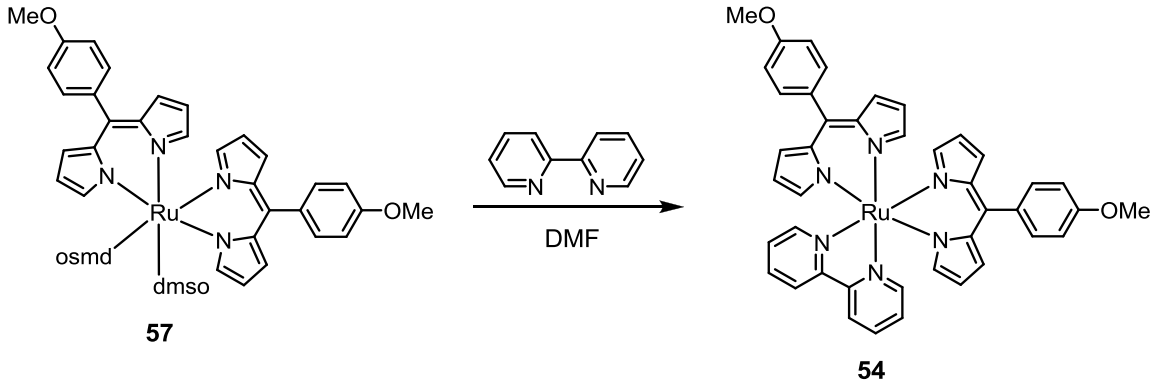

57 **54**

Figure 4.14. The synthetic route to Ru(II)-dipyrrinato complex **54**.

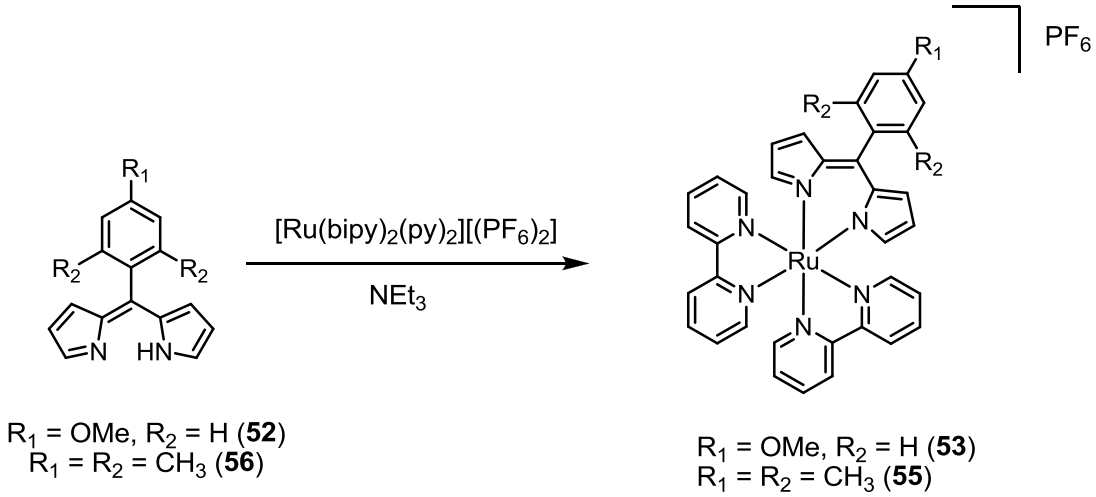

R_1 = OMe, R_2 = H (**52**)
R_1 = R_2 = CH_3 (**56**)

R_1 = OMe, R_2 = H (**53**)
R_1 = R_2 = CH_3 (**55**)

Figure 4.15. The synthetic route to Ru(II)-dipyrrinato complexes **53** and **55**.

The synthesis of **53** and **55** is outlined in Figure 4.15. Small scale test reactions using $[Ru(bipy)_2Cl_2]$ as the starting material established that significant impurities result from the free chloride ligands. For this reason a slight adaptation of the synthetic methodology of **46** (as outlined in Figure 4.6) was made. $[Ru(bipy)_2Cl_2]$ was replaced with $[Ru(bipy)_2(py)_2][(PF_6)_2]$ to remove any source of chloride ions from the reaction. This also prevents competition between the Cl^- and PF_6^- as counter anions. Additional aqueous NH_4PF_6 was required to precipitate the product.

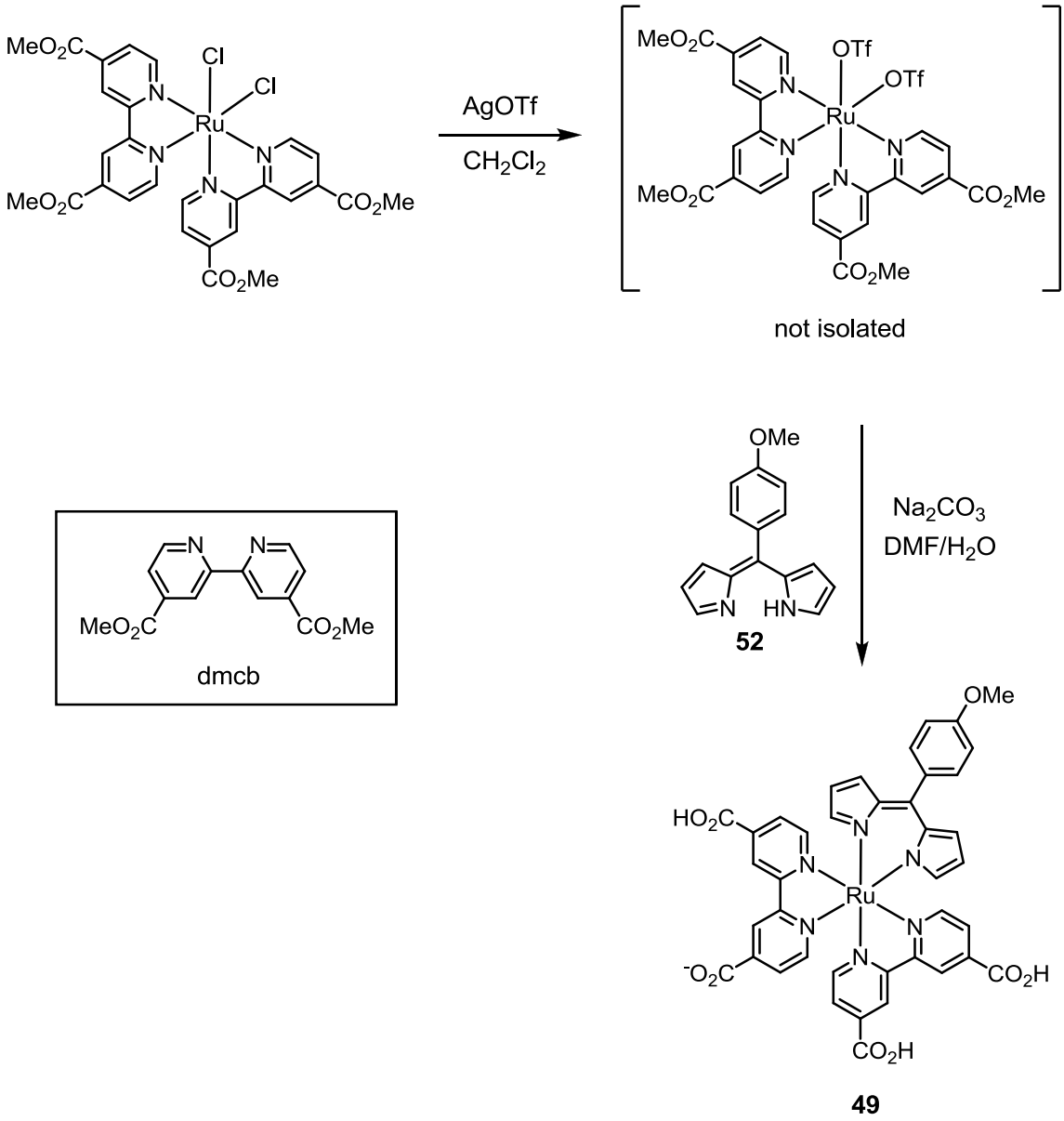

Figure 4.16. The synthetic route to Ru(II)-dipyrrinato complexes **49**. Inset: structure of 4,4'-dimethoxycarbonyl-2,2'-bipyridine (dmcb).

The synthesis of **49** (Figure 4.16) was an adaptation of a literature preparation for the synthesis of $[Ru(dcb)_2(acac)]^+$, (dcb is 4,4'-dicarboxy-2,2'-bipyridine).[239, 240] The starting material, $[Ru(dmcb)_2Cl_2]$, was stirred at room temperature in dichloromethane in the presence of silver triflate to remove the coordinated chloride ligands. Silver triflate and other silver salts are often used in ruthenium chemistry to remove the coordinated chloride ligands.[240] The intermediate complex, $[Ru(dmcb)_2OTf_2]$, was not isolated before the dipyrrin ligand was introduced. A microwave reaction in 2:1

DMF:H_2O with excess sodium carbonate (Na_2CO_3) was employed to coordinate the dipyrrin ligand (**52**). These reaction conditions were sufficient to fully hydrolyse all four of the ester groups on the two 4,4'-dimethoxycarbonyl-2,2'-bipyridine (dmcb) ligands. The product was precipitated at pH 3 from aqueous media using aqueous HPF_6. Purification of this complex is achieved by washing the complex with acetonitrile; however, an analytically pure sample could not be obtained for microanalysis.

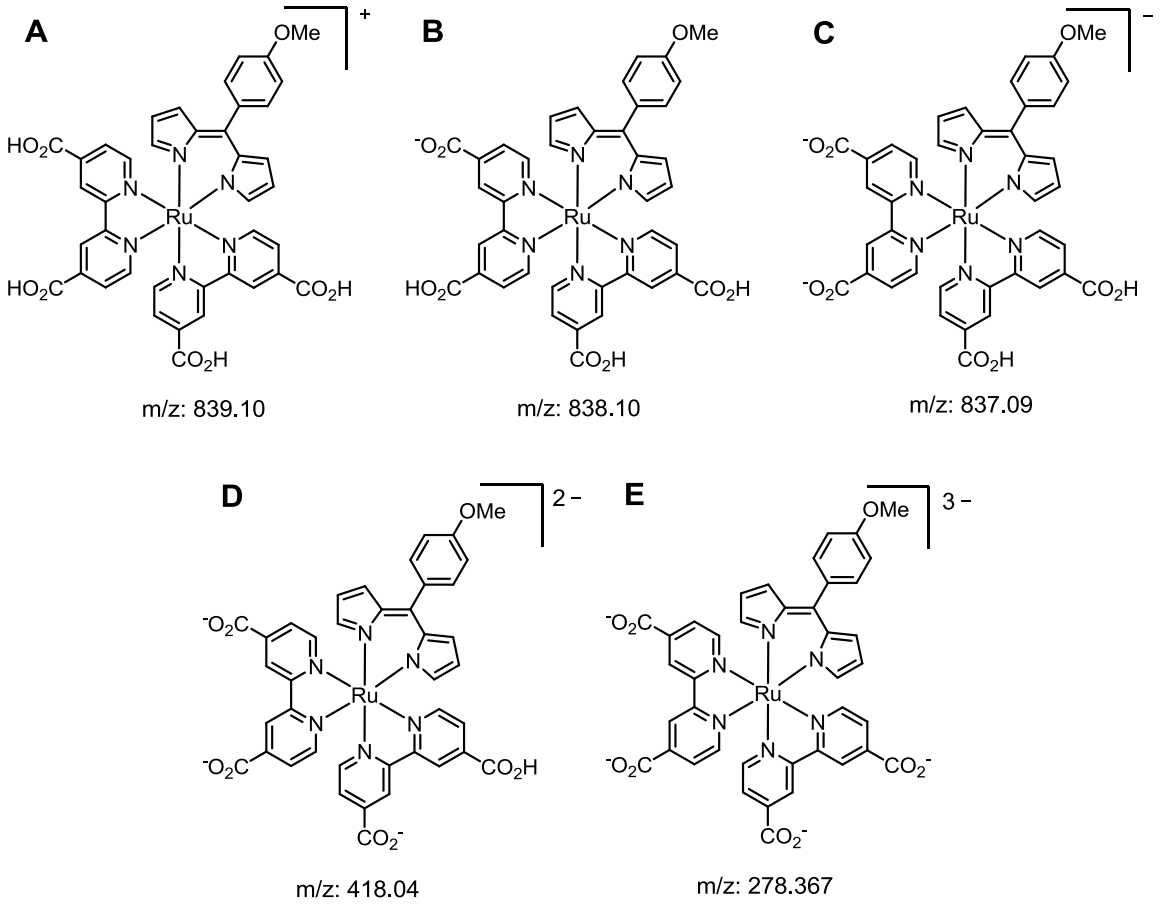

Figure 4.17. Illustration of the protonation states of **49** and expected mass/charge. Mass spectroscopy and ^{31}P NMR and ^{19}F NMR spectroscopy were used to establish that B is the most likely protonation state of complex **49**.

The degree of protonation of **49** was investigated to determine the structure of the complex. The complex could exist in one of five protonation states (Figure 4.17). The protonation state of the carboxyl groups in **49** were determined using mass spectroscopy, and ^{31}P NMR and ^{19}F NMR spectroscopy. Mass spectrometry (ESI) in

negative mode eliminated possibilities C, D and E (Figure 4.17) because no signals were observed for these structures. In positive mode a signal was observed at 839.66 *m/z* which is proposed to be [M+H] for B. The absence of both phosphorus and fluorine in ^{31}P NMR and ^{19}F NMR spectroscopy confirmed that there is no PF_6 in the complex. Furthermore, similar NMR shifts are observed if the complex is precipitated out with aqueous HCl rather than HPF_6. From this we conclude that the complex most likely has a single carboxylate deprotonated to give an overall neutral complex (Figure 4.17B).

The synthetic route to the Rh(III) dipyrrinato complex **51** is outlined in Figure 4.18 (the synthesis of **42** is outlined in chapter 3). Standard hydrolysis conditions were employed to hydrolyse the ester functional groups.

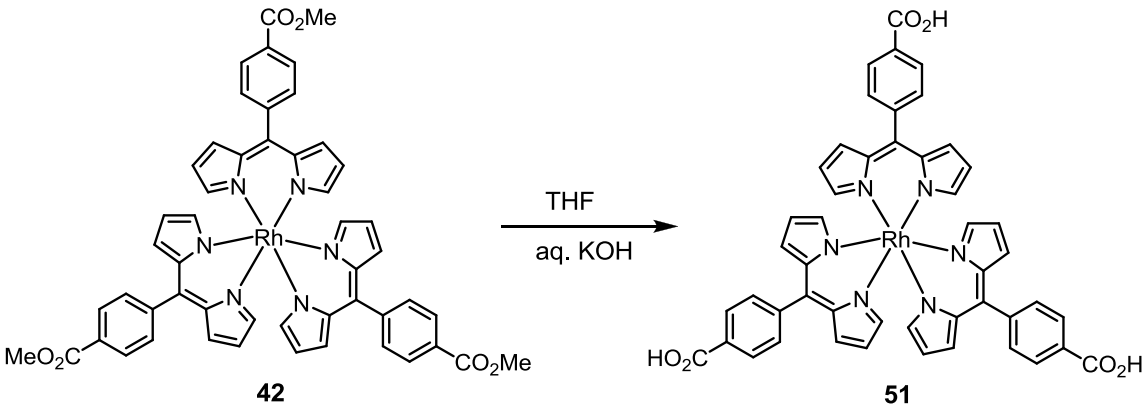

Figure 4.18. The synthetic route to Rh(III)-dipyrrinato complexes **51**.

4.5.2 Characterisation

Complexes **49**-**51** and **53**-**55** were fully characterised by NMR, mass spectrometry, elemental analysis, and UV-Vis spectroscopy. All data were consistent with the structures in Figure 4.9 and Figure 4.11. Of notable interest are the features in the UV-Vis spectra of the Ru(II)-dipyrrinato complexes. The similarity of these spectra of these new complexes to the first generation complexes (**46** and **47**) is striking. All five new complexes show two distinctive features (Figure 4.19 and Table 4.1) with a peak centred between 448-461 nm ascribed to an intraligand π-π* dipyrrin transition and a weaker transition at longer wavelengths ascribed to an MLCT transition from Ru(II) to the bipyridine substituent.[42]

The position and intensity of the π–π* transition is relatively insensitive to the functional group on the dipyrrinato ligand (Table 4.1). When comparisons are made

between complexes with the same number of dipyrrinato ligands with different functional groups only small shifts of less than 10 nm are observed. For example a shift of 8 nm is seen between complexes **46** (carboxyl group on the dipyrrinato ligand) and **49** (methoxy group on the dipyrrinato ligand). Larger shifts are observed for complexes with one dipyrrinato ligand compared to two dipyrrinato ligands (Table 4.1). A shift of 16 nm is observed between complexes **46** (one dipyrrinato ligand) and **47** and **50** (two dipyrrinato ligands). As expected, the intensity of the π–π* transition for complexes with two dipyrrinato ligands (**47** and **54**) is approximately double that of complexes with one dipyrrinato ligand (**46**, **49**, **53**, and **55**). This transition is also broadened for complexes **47** and **54**. This broadening is attributed to exciton coupling (refer to Chapter 3).

Table 4.1. Positions of the absorption bands in the visible region of Ru(II)-dipyrrinato complexes **46**-**47**, **49**-**50** and **53**-**55** and Rh(III)-dipyrrinato complex **51**.

Complex	π–π*	MLCT
46	464	517
47	448	638
49	456	521
50	448	656
51	466, 502	-
53	459	525
54	450	646
55	461	525

The position and intensity of the Ru(II)-bipyridine MLCT transition is sensitive to whether the complex contains either one or two bipyridine substituents (Table 4.1). In $[Ru(bipy)_3]^{2+}$the Ru(II)-bipyridine MLCT transition is observed at 443 nm.[241] The MLCT transition of all the new complexes is significantly red-shifted with respect to this transition in $[Ru(bipy)_3]^{2+}$. For complexes (**49**, **53**, and **55** this transition is centred between 521-525 nm while for complexes (**50** and **54**) this transition is centred between 646-656 nm. In some cases this MLCT transition is also sensitive to whether the bipyridine substituents have carboxyl groups attached. A shift of 18 nm is observed between **47** (where no carboxyl group is attached) and **50** (where a carboxyl group is attached). But these complexes have different functional groups on the dipyrrinato ligand. A smaller shift is observed when the same functional group is on the dipyrrinato ligand. For example **50** (where a carboxyl group attached) and **54** (where no carboxyl

group is attached) have the methoxy functional group on the dipyrrinato ligand and a shift of 10 nm is observed.

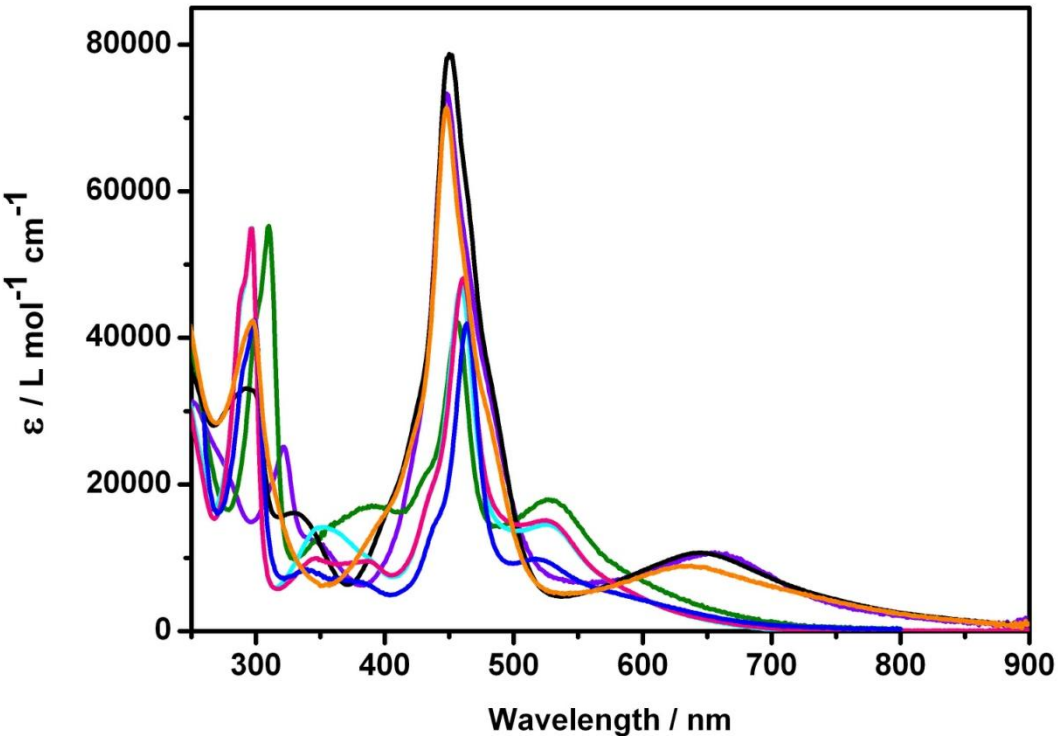

Figure 4.19. Absorption spectra of **46**-**47**, **49**-**50** and **53**-**55** (with **46** and **47** included for comparison purposes). **46** (dark blue) in DMSO, **47** (orange) in MeOH with NaOH, **49** (green) in H_2O with NaOH, **50** (purple) in DMSO, **53** (light blue) in CH_2Cl_2, **54** (black) in $CHCl_3$, and **55** (pink) in CH_2Cl_2.

*4.5.3 Analysis of the electronic structure of **46***

Previous work[42] from our group used resonance Raman to identify the two dominant transitions in the UV-Vis spectra as a π-π* transition centred on the dipyrrin chromophore and the MLCT of the Ru(II)-bipyridine. These transitions were found to be largely uncoupled. This suggests that the orbitals involved in each transition are distinct and localised to different spatial regions of the complex and are therefore non-interacting. To further probe the electronic structure of these first generation Ru(II)-dipyrrinato complexes a detailed analysis of the absorption spectra, quantitative analysis of the resonance Raman scattering, and computational chemistry of **46** (and related complexes **46**-**H** and **46b** in Figure 4.20) were examined. The nature of the electronic excited states and photophysical properties of these Ru(II)-dipyrrinato complexes are

important to understand in considering these complexes for solar energy conversion applications.

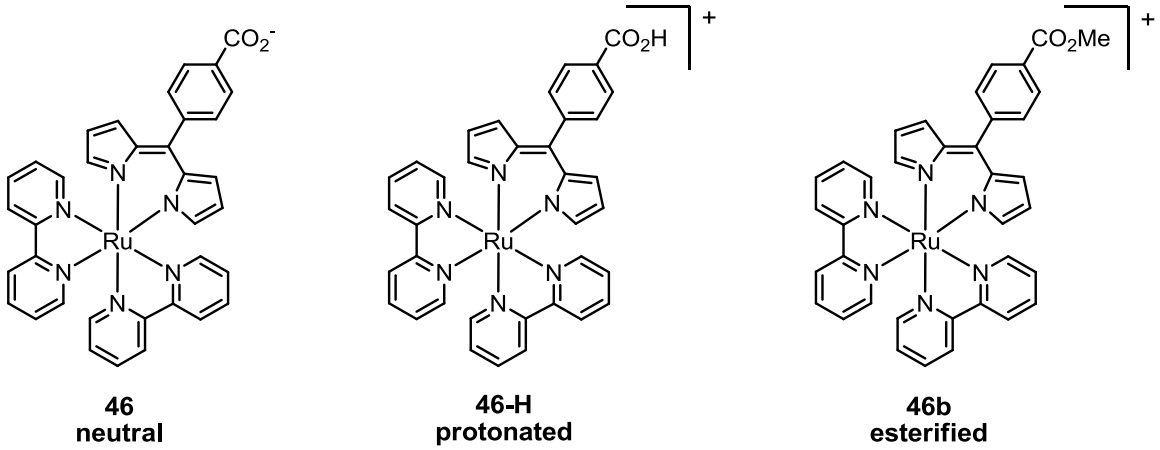

Figure 4.20. Structure of **46** and related complexes **46-H** and **46b**.

*4.5.4 Time Dependent DFT (TD-DFT) calculations of **46** and **46-H***

It has become well-known that time-dependent DFT (TD-DFT) methods yield substantial errors in calculating transition energies and intensities for charge transfer transitions and zwitterionic species.[242-244] For solar energy conversion applications, the carboxylate group is an essential structural feature as it strongly anchors the dye to the surface of TiO_2.[22] Consequently, the calculations were performed on the neutral deprotonated (**46**) and the protonated complex (**46-H**), while experimental data were acquired from the neutral deprotonated complex as this form is the most likely to bind to TiO_2. The optimised structures (Figure 4.21) are virtually identical apart from the clear differences associated with the protonation of the carboxyl group. The optimised structure of **46** closely agrees with the structure of this complex determined by X-ray crystallography.[42] The pyrrolic rings of the dipyrrin core are coplanar, while the dihedral angle between the dipyrrin core and the phenyl ring is 74°.

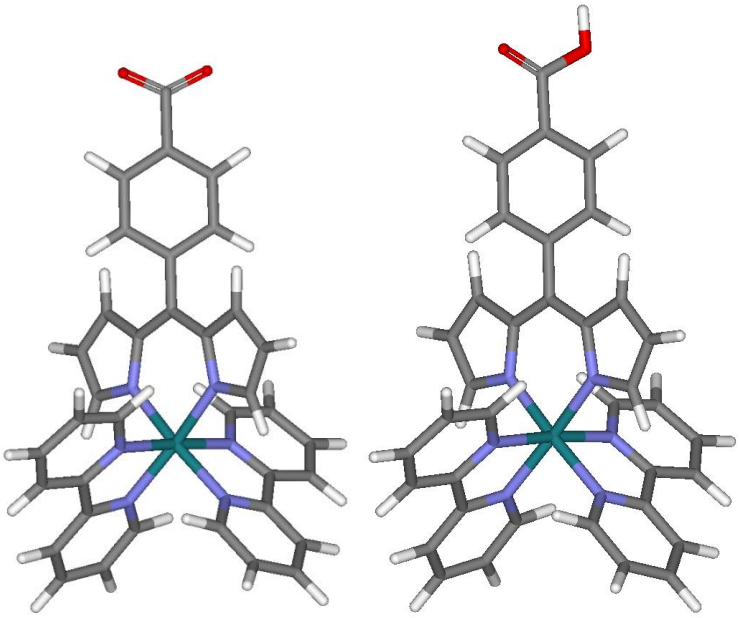

46 **46-H**

Figure 4.21. Optimised geometries of **46** and **46-H**.

4.5.5 Absorption spectroscopy and TD-DFT calculations

Figure 4.22 shows the experimental and calculated absorption spectra in DMSO, while Table 4.2 shows the experimental and calculated absorption parameters of **46** and **46-H**. The experimental spectrum (Figure 4.22A) is effectively a superposition of the two main transitions: an intense narrow transition at 464 nm, characteristic of all dipyrrin complexes; and a broad transition at 517 nm. Based on qualitative resonance Raman, these transitions were assigned as a $\pi-\pi^*$ dipyrrin transition and a ruthenium bipyridine MLCT transition, respectively.[42] These transitions have oscillator strengths (f) 0.35 and 0.14, respectively. A very weak transition (on the shoulder of the 517 nm transition) is observed at 590 nm (f = 0.05). This weak transition can be assigned as an MLCT transition (see below). There are weak transitions in the region of 340-375 nm, which can probably be ascribed to "Rydberg-like" transitions (see later). Rydberg transitions are characterised by a change in the quantum number (n) and following the transition the electron density typically just extends from its origin outwards in all directions.

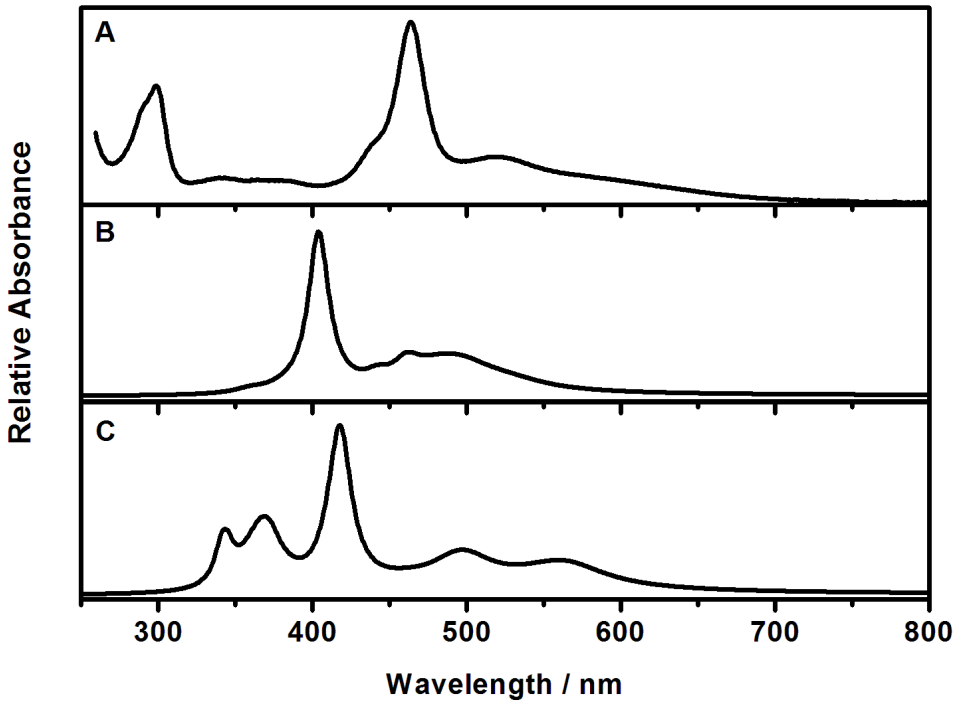

Figure 4.22. Calculated and experimental absorption spectra of **46** and **46**-**H**. (A) Experimental spectrum of **46** in DMSO, (B) calculated spectrum of **46** with C-PCM solvent model (DMSO); and (C) calculated spectrum of **46**-**H** with C-PCM solvent model (MeOH).

Table 4.2. Experimental and calculated absorption parameters for **46** and **46-H**.

	Experimental		Calculated			
	λ / nm	**f[a]**	**λ / nm**	**f[a]**	**Configuration (% contribution)**	**Assignment**
46[b]	590	0.055	523	0.016	HOMO-1→ LUMO (87)	
	517	0.136	499	0.076	HOMO-1→ LUMO+2 (76)	
			483	0.073	HOMO-3→ LUMO (-19), HOMO-2→ LUMO (49), HOMO-2→LUMO+2 (-14)	
			453	0.025	HOMO-5→ LUMO+2 (61), HOMO-2→ LUMO+2 (26), HOMO-5→ LUMO (-12), HOMO-1→ LUMO+2 (-10)	
			473	0.011	HOMO-3→ LUMO (11), HOMO-3→ LUMO+2 (66), HOMO-2→ LUMO (10), HOMO-2→ LUMO+2 (-11)	
			461	0.040	HOMO-3→ LUMO (58), HOMO-2→ LUMO (25)	
			442	0.021	HOMO-3→ LUMO+1 (72)	
	464	0.351	404	0.326	HOMO-3→ LUMO+2 (15), HOMO-2→ LUMO+2 (44)	
	439	0.081	385	0.019	HOMO-5→LUMO (24), HOMO-5→LUMO+2 (71)	
	376	0.122	360	0.016	HOMO-3→LUMO+3 (12), HOMO-2→LUMO+3 (-20), HOMO-1→LUMO+4 (-15), HOMO→LUMO+5 (43)	
46-H[c]			565	0.076	HOMO-1→LUMO (80), HOMO-1→LUMO+1 (15)	MLCT (Ru-dipyrrin)
			561	0.016	HOMO-2→LUMO+1 (11), HOMO-1→LUMO+2 (78)	
			541	0.013	HOMO-2→LUMO+2 (19), HOMO-1→LUMO (11), HOMO-1→LUMO+1 (66)	
			497	0.127	HOMO-2→LUMO+1 (76)	MLCT (Ru-bipyridine)
			461	0.020	HOMO-2→LUMO+2 (64), HOMO-1→LUMO+1 (11)	
			418	0.278	HOMO-3→LUMO (62)	$\pi-\pi^*$
			411	0.025	HOMO→LUMO+4 (93)	
			369	0.143	HOMO-2→LUMO+3 (29), HOMO-2→LUMO+4 (16), HOMO-1→LUMO+5 (14), HOMO-1->LUMO+6 (13), HOMO→LUMO+7 (18)	"Rydberg"

[a] Only calculated oscillator strengths of greater than 0.01 are reported.
[b] Calculated in DMSO
[c] Calculated in MeOH

As shown in Table 4.2, the TD-DFT calculations show that several configurations contribute to the electronic transitions. The molecular orbitals for **46** and **46-H** (Figure 4.23 and 4.24) are significantly different despite the electronic absorption spectra and resonance Raman spectra being very similar for these species (see later). It was anticipated that these molecular orbitals would also be similar to each other. Previous TD-DFT calculations have shown the π-π* dipyrrin (or azadipyrrin) transition of the free ligand, BF_2 complex, or metallocomplex predominantly involves the HOMO-LUMO molecular orbitals,[84, 188, 245] whereby occupied orbitals have amplitude centred only on the dipyrrin core and unoccupied orbitals have amplitude on the dipyrrin core which sometimes extends out to the phenyl ring (if present). The molecular orbitals of ligand (**34**) shown in chapter 2 (Figure 2.5 and Table 2.1) also shows that the π-π* transition also consists largely of a HOMO-LUMO transition.

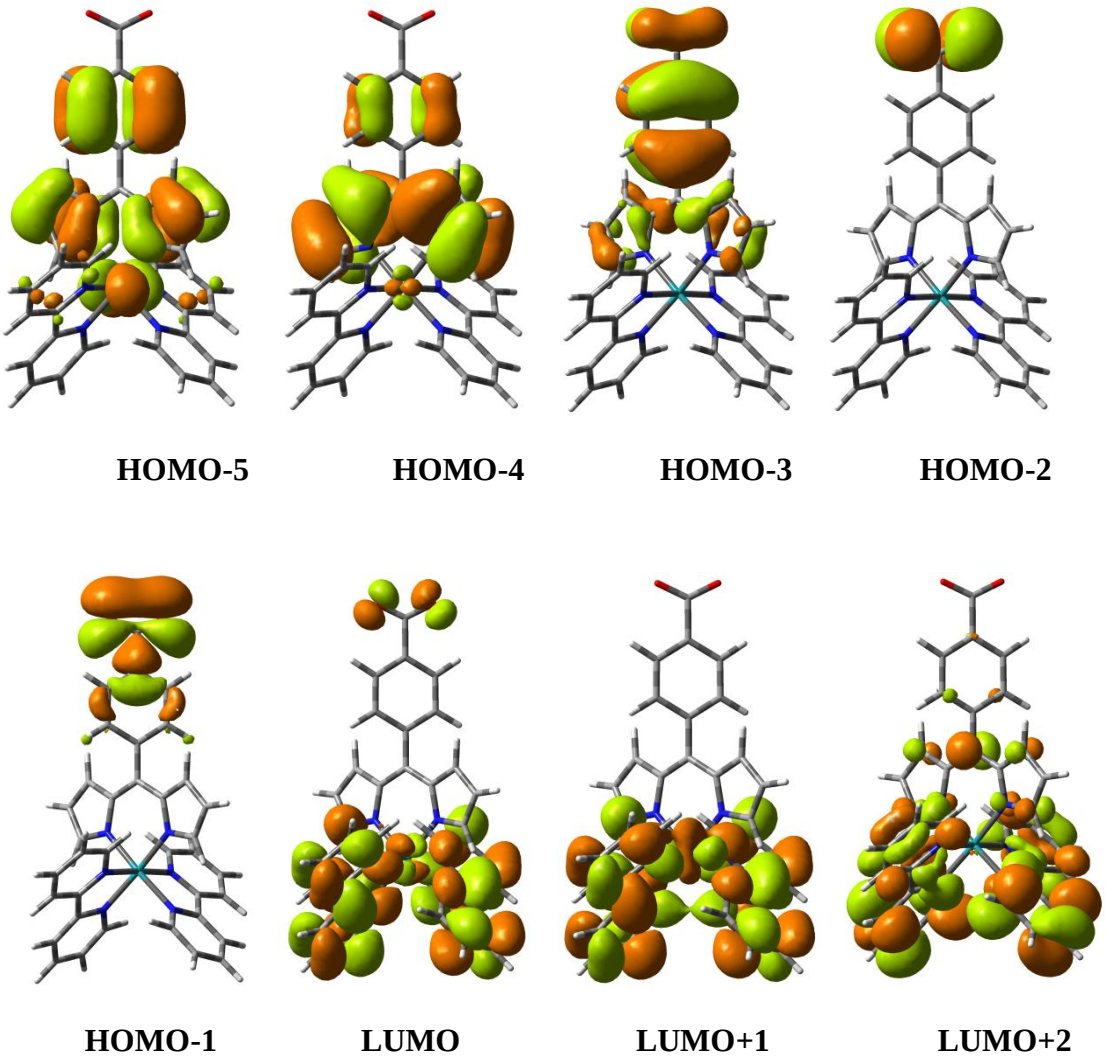

Figure 4.23. Selected molecular orbitals involved in the absorption spectrum of **46**.

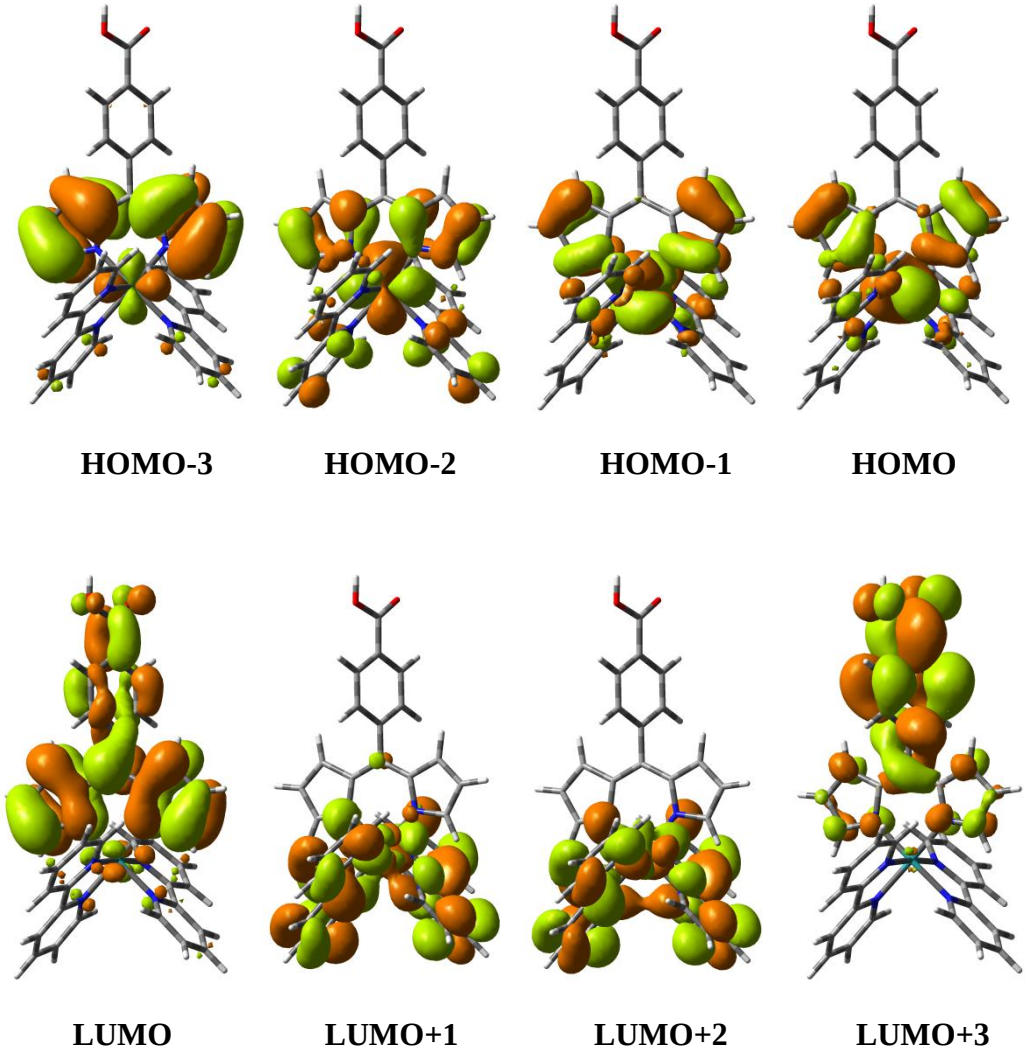

Figure 4.24. Selected molecular orbitals involved in the absorption spectrum of **46**-**H**.

The molecular orbitals of **46** are not a fair representation of the actual molecular orbitals (Figure 4.23) involved in the transitions. For **46**, the calculated transition probably assigned to the π-π* transition (404 nm) due to the large oscillator strength predicts occupied orbitals have substantial amplitude around the phenyl ring and carboxylate substituent of the dipyrrin ligand, while the unoccupied orbital has large bipyridyl amplitude. The two calculated transitions (523 nm and 499 nm) in the region of the ruthenium bipyridine MLCT transition have significant amplitude around the carboxylate substituent of the dipyrrin ligand, while the unoccupied orbital has large bipyridyl amplitude. Clearly this is not a ruthenium bipyridine MLCT transition. Presumably the poor agreement between previous calculations and these calculations can be explained by the fact that **46** is neutral overall but zwitterionic and the charges

are separated over a large distance. As mentioned earlier, this is a limitation of DFT calculations.[242-244]

The molecular orbitals of **46**-**H** (Figure 4.24) show far better agreement with published calculations of dipyrrinato complexes. The calculated transition for the π-π* transition (418 nm) is dominated by changes in density on the dipyrrin ligand. The HOMO-LUMO of the BF_2 dipyrrin complex[188] correspond closely to the HOMO-3 and LUMO orbitals of **46**-**H**. However, our calculation shows that the HOMO-3 to LUMO transition is less dominant than the HOMO-LUMO transition of the BF_2 dipyrrin complex. This is most likely a consequence of the high energy ruthenium 4d and bipyridyl π-orbitals interacting with the dipyrrin π-orbitals. The MLCT transitions calculated to be at 497 nm and 565 nm are dominated by bipyridyl and ruthenium orbitals and orbitals that perturb electron density across the bipyridyl orbitals, respectively. However, there is some dipyrrin character in the 565 nm transition.

Overall the multiple configurations make a simple interpretation using the molecular orbitals difficult. The TD-DFT calculations of **46**-**H** are more easily visualised by using electron density difference plots (Figure 4.25). These plots clearly show the dipyrrin π–π* nature of the transition at high energy and the MLCT character of the low energy transition. In the π–π* transition the electron density shifts from the dipyrrin core (green) out towards the phenyl ring and carboxyl substituent (blue). In the MLCT transition the electron density shifts from the metal centre (green) and terminates on the bipyridine ligands (blue).

The occupied molecular orbitals (Figure 4.24) for the Rydberg transition of **46**-**H** are centred predominantly on the Ru(II) centre with some dipyrrinato and bipyridine character. The unoccupied molecular orbitals for the Rydberg transition (not shown) are centred either exclusively on the bipyridine ligands or dipyrrinato ligand. The EDD plot of this transition (Figure 4.25) shows that the electron density moves from the Ru(II) centre (green) and extends out onto the dipyrrinato and bipyridine ligands (blue).

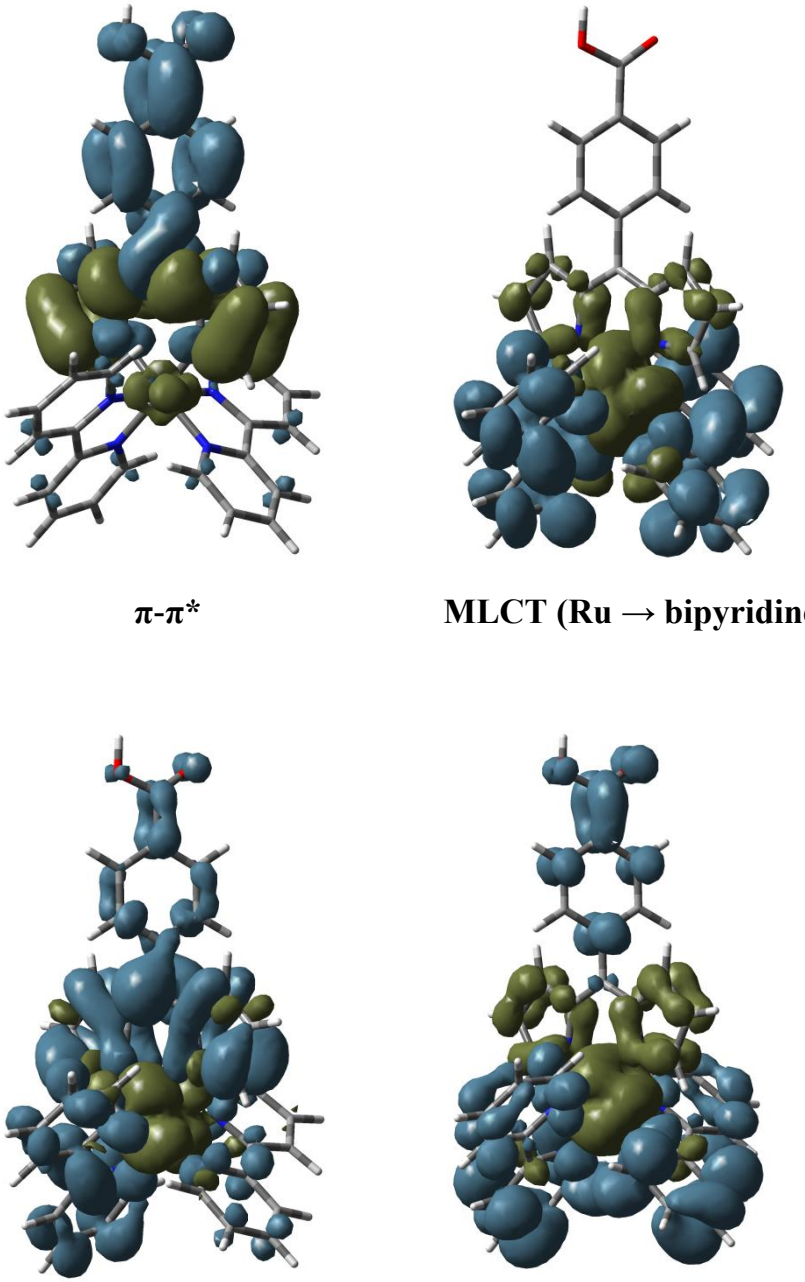

Figure 4.25. Electron density difference plots for the π-π*, MLCT transitions and Rydberg transition of **46-H**. Green represents depletion of electron density and blue represents accumulation of electron density.

Further analysis of the nature of the electronic transitions was undertaken via a simple Mulliken analysis of **46-H** (Table 4.3). The complex has been separated into fragments of the Ru(II) atom, each bipyridine ligand, the dipyrrin core, and finally the phenyl and

carboxyl are grouped together. The changes in electron density for the strongest transitions for these fragments of **46**-**H** were calculated.

The data in Table 4.3 further support the conclusions of the analysis above. The two low energy transitions are shown to have significant MLCT character. In both transitions the Ru(II) centre loses significant electron density, while the bipyridine ligands equally gain electron density. In the case of the transition at 565 nm, the dipyrrin core and the phenyl ring gains most of the electron density, therefore this is a Ru(II)-dipyrrin MLCT. The transition at 497 nm is almost purely a ruthenium-bipyridine MLCT. The Mulliken analysis confirms that the 418 nm transition is a $\pi-\pi^*$ transition. The dipyrrin core loses electron density which is gained by the phenyl ring. In the UV region of the absorption spectrum, the Mulliken analysis shows that the transition can be ascribed as a "Rydberg-like" transition where the transition is MLCT in nature but utilises both the bipyridine and dipyrrin orbitals.

Table 4.3. Mulliken analysis of **46**-**H** showing the fractional changes in charge density for the excited states.

	λ^a / nm	*f*	Ru	bipy1	bipy2	dipyrrin	phenyl
"Rydberg"	369	0.142	67→2 (-65)	7→31 (24)	7→31 (24)	18→5 (-13)	0→30 (30)
$\pi-\pi^*$	418	0.278	12→1 (-11)	1→6 (5)	1→6 (5)	85→68 (-17)	1→19 (18)
MLCT1	497	0.127	67→5 (-62)	9→44 (35)	9→45 (36)	15→5(-10)	0→1 (1)
MLCT2	565	0.076	67→2 (-65)	6→10 (4)	6→10 (4)	21→66 (45)	0→12(12)

[a] Calculated wavelengths

Figure 4.26 shows the effect of protonation and esterification on the electronic structure of the complexes. Protonation and esterification barely perturbs the electronic structure of the molecule. The resonance Raman spectra (Figure 4.27) of these complexes are very similar, which also confirms that the electronic structure is unperturbed upon protonation or esterification.

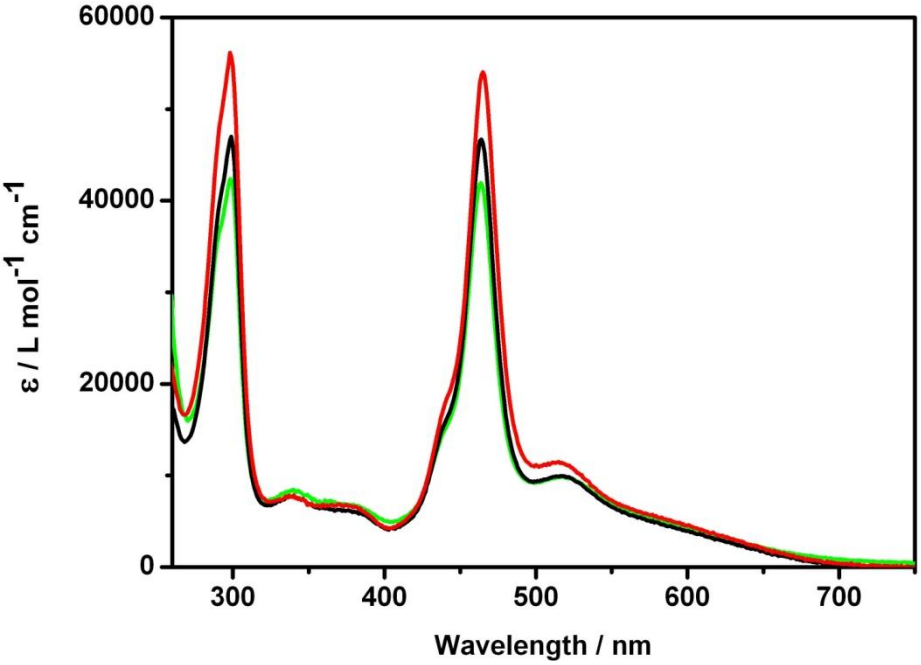

Figure 4.26. Effect of protonation and esterification on the electronic structure of **46** and its derivatives; absorption spectra of neutral (**46**, green) protonated with 0.1% (v/v) TFA, (**46-H**, black) and esterified complexes (**46b**, red) in DMSO.

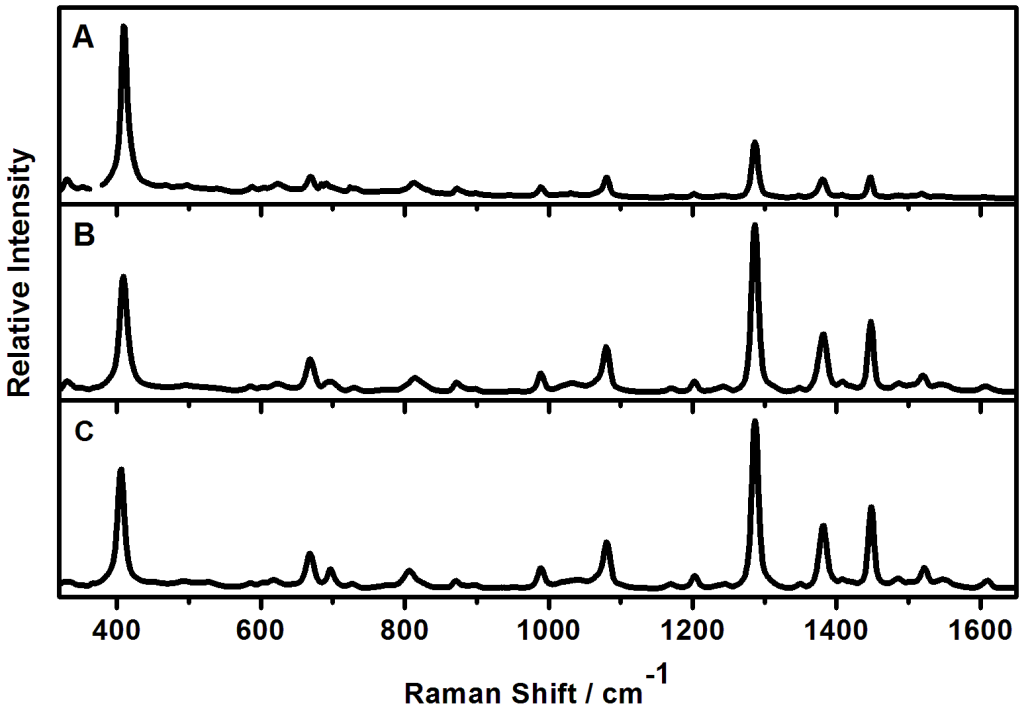

Figure 4.27. Effect of protonation and esterification on the electronic structure of **46** and its derivatives; resonance Raman at 458 nm in DMSO (A) neutral (**46**), (B) protonated with 0.1% (v/v) TFA (**46-H**), and (C) esterified complexes (**46b**).

4.5.6 Resonance Raman spectroscopy

The resonance Raman spectra of **46** are shown in Figure 4.28. There are a number of notable features in the resonance Raman spectra. Firstly the characteristic enhancement patterns obtained with 458 nm and 514.5 nm excitation suggest that the electronic structure of the molecule is represented by two independent chromophores. The spectrum acquired with 458 nm excitation is dominated by vibrational modes of the dipyrrin ligand, while the spectrum acquired with 514.5 nm is dominated by vibrational modes of the bipyridyl ligand. The enhanced bipyridyl modes resemble the resonance Raman spectrum of $[Ru(bipy)_3]^{2+}$;[246] consistent with resonant enhancement of an MLCT transition terminating on the bipyridine ligand. The modes which receive the greatest enhancement are the most effective at transforming the molecule from its ground state to its excited state geometry.

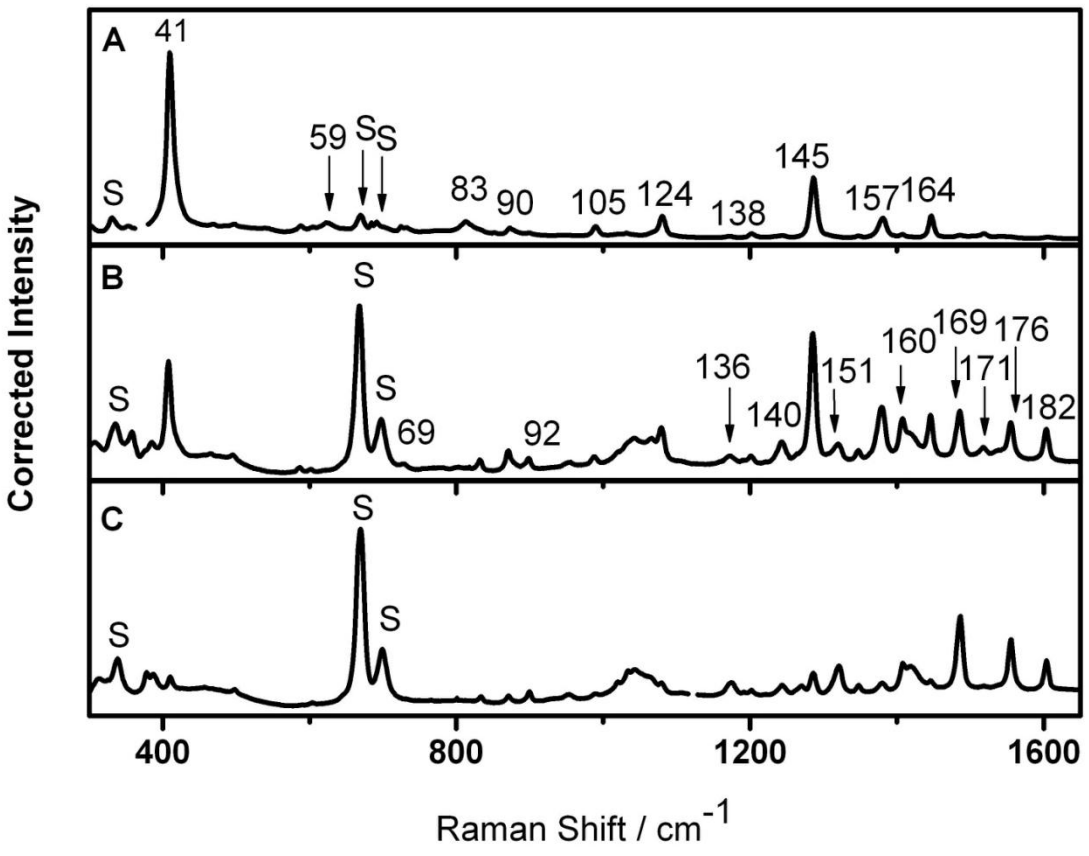

Figure 4.28. Resonance Raman spectra of **46** in DMSO with excitation at (A) 458 nm, (B) 488 nm, and (C) 514.5 nm. [S denotes solvent peaks (CH_2Cl_2)]. Note that not all wavelengths are shown.

Mean average deviation (MAD) is used as a measure of the correlation between the calculated and experimental values. For the assigned modes of **46**, the MAD is 5 cm^{-1}. Considering the accuracy of the calibration and resolution of the Raman spectrometer used in this study (~4 cm^{-1}), this indicates a close correlation between the calculated and experimental spectra.

The most striking feature of the resonance Raman spectra is the very strong enhancement of the low frequency mode at 409 cm^{-1} (assigned as q_{41}), particularly with 458 nm excitation. The q_{41} mode (Figure 4.29) involves torsion about the transannular bond between the dipyrrin core and the phenyl ring of the dipyrrin ligand. Other strongly enhanced modes observed with 458 nm excitation: 1081 cm^{-1}, 1287 cm^{-1}, 1380 cm^{-1}, and 1447 cm^{-1} ($q_{124,}$ q_{145}, q_{157}, q_{164}, respectively) are all pyrrolic ring deformations and can be described as "dipyrrin modes". This is expected because the 458 nm excitation is on resonance with the π–π^* transition of the dipyrrin ligand. The mode enhancements confirm that the π–π^* transition of the dipyrrin ligand are confined to the dipyrrin core and therefore only atoms of the dipyrrin core are displaced.

A different enhancement pattern is observed using 514.5 nm excitation, which is closely resonant with the MLCT transition. The strongest enhanced bands include: 1320 cm^{-1} (most likely a pair of modes, q_{151} + q_{153}), 1486 cm^{-1} (q_{169}), 1555 cm^{-1} (a pair of modes, q_{176} + q_{177}) and 1603 cm^{-1} (q_{182}). All of these enhanced modes involve distortion of the bipyridyl ring. The enhancements of these modes are consistent with resonance with only the MLCT state. Figure 4.29 depicts some of these enhanced vibrational modes.

Dipyrrin modes:

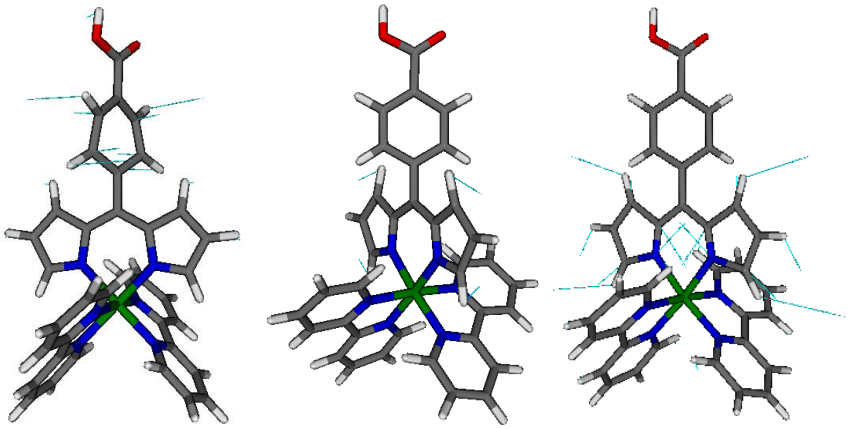

41 **124** **145**

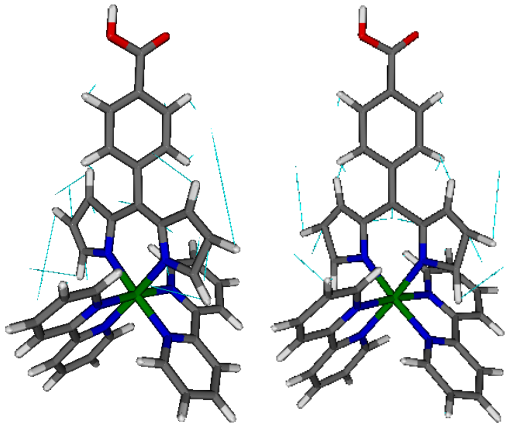

157 **164**

Bipyridine modes:

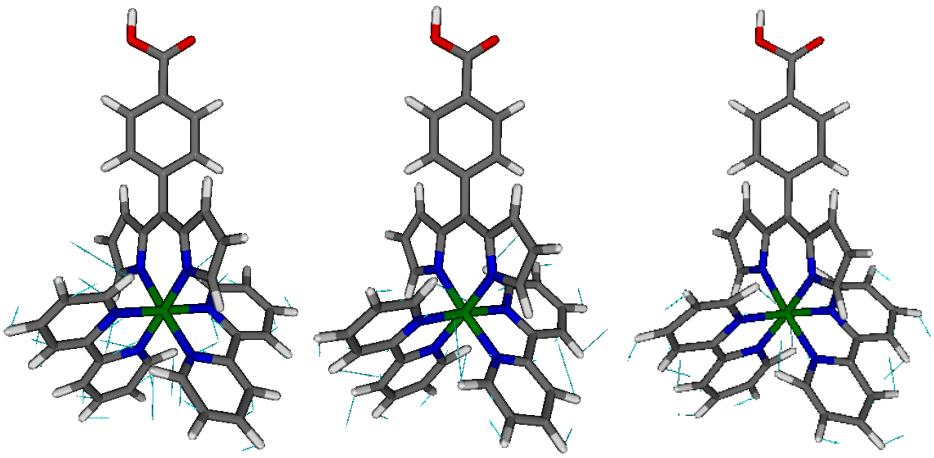

146 **165** **169**

Figure 4.29. Plots of the selected normal modes of **46-H**.

4.5.7 Resonance Raman intensity analysis (RRIA)

Resonance Raman intensities depend on the square of the transition dipole moment. Therefore the two states with the strong dipole-allowed transitions as shown by the TD-DFT calculations are expected to dominate the resonance Raman. The resonance Raman intensities provide a method for a detailed examination of the output from the TD-DFT calculations. We utilised an empirical model consisting of two electronic states (i.e a simple two level system) to simulate the resonance Raman intensities (and absorption spectrum). The simulated and experimental absorption spectra are given in Figure 4.30.

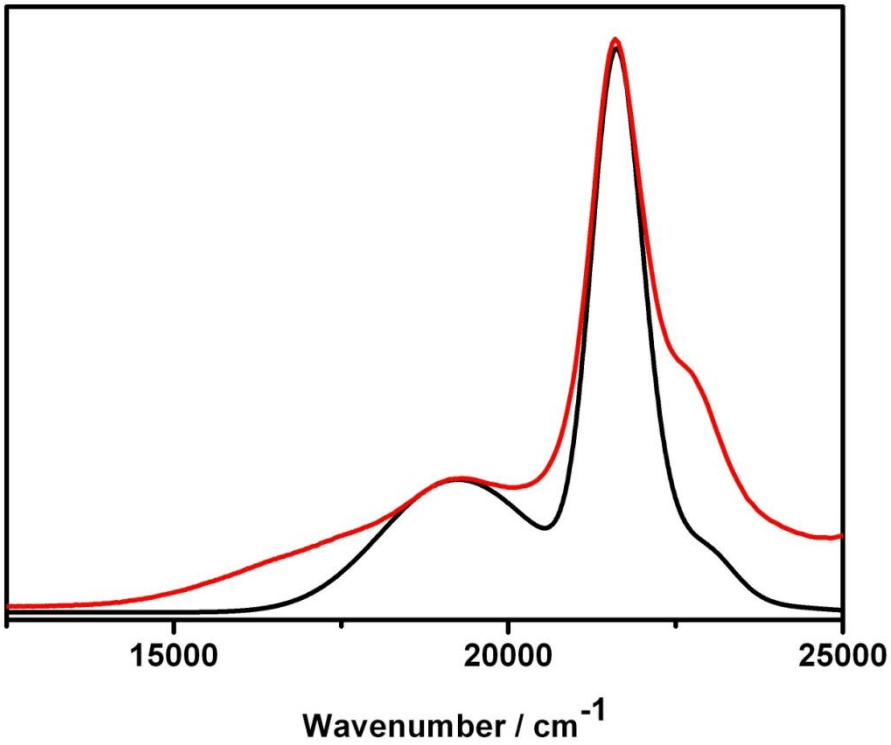

Figure 4.30. Simulated (black) and experimental (red) absorption spectrum of **46**.

The resonance Raman intensity analysis supports the independent nature of the π–π* and MLCT states. The simulated Raman excitation profiles (Figure 4.31) reveals that a quantitative analysis of the resonance Raman intensities is consistent with the observation that the π–π* and MLCT states dominate the electronic structure of **46**. It is important to note that the low Raman frequencies are not observed for certain wavelengths due to notch-filter bandpass cut-offs preventing data acquisition. The Raman excitation profiles show that there are two distinct patterns: either a single strong

peak at higher energy in the excitation profile, which is indicative of these modes being resonance enhanced by only the π–π* dipyrrin transition; or two peaks are observed, which demonstrates that there is resonant enhancement from both the MLCT and π–π* transitions.

If the states are strongly coupled then the resonance Raman intensities would be expected to be sensitive to the angle between the transition dipole moments. Initially, the simulation was run with an angle of 127° (53°) between the two states (π–π* and MLCT), as suggested by the DFT calculations (by measuring the angle between the respective transition dipole moments using Mercury). Subsequently, values of 0° and 90° were modelled. Remarkably the resonance Raman intensities were insensitive to this parameter and produced virtually identical excitation profiles. We also observed there is no dependence on the relative sign of the mode displacement (Δ) parameter.

In general, the resonance Raman intensity of a mode is proportional to $\omega^2\Delta^2$ where ω is the frequency of the mode and Δ is the dimensionless mode displacement. Mode displacements are used to simplify the resonance Raman analysis. The mode displacements (Table 4.4) are largely reflected in the mode intensities (scaled by the ω^2 factor). For the MLCT and π-π* states, the dynamics in the Franck-Condon region are also largely independent despite the small energy gap between the states. Therefore we conclude that for resonance Raman scattering, at least, the MLCT and π–π* states are independent.

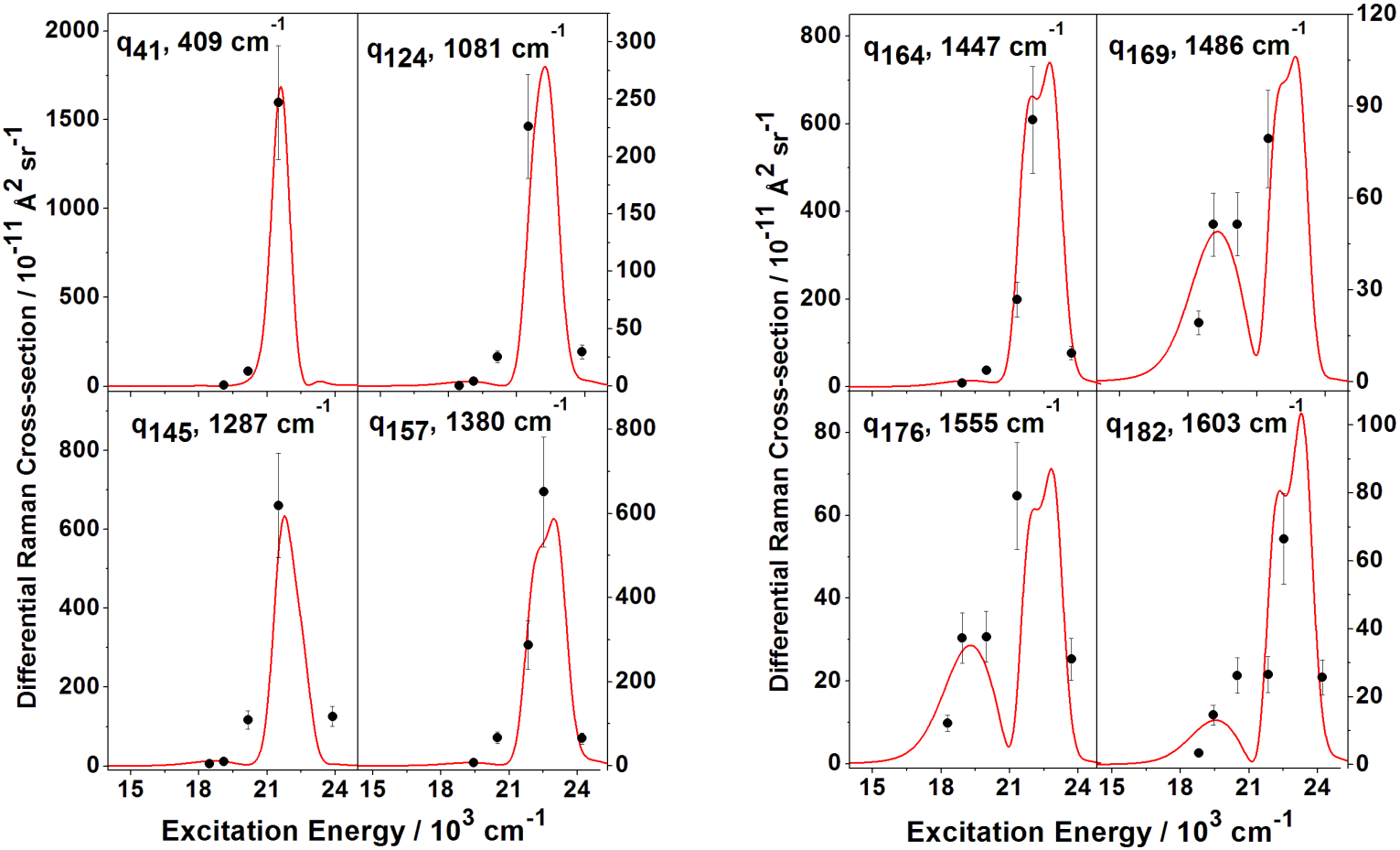

Figure 4.31. Raman excitation profiles of **46**. Solid red lines represent simulated profiles. Points are experimental values (with estimated errors) at discrete excitation wavelengths.

Table 4.4. Electronic and nuclear parameters for the resonance Raman intensity analysis of **46**.

Mode	Calculated frequency[a] (cm^{-1})	Experimental frequency (cm^{-1})	MLCT			π-π*		
			Δ[b]	CF[c]	λ_v[d] (cm^{-1})	Δ[b]	CF[c]	λ_v[d] (cm^{-1})
41	409	409	0.2	0	8.2	0.47	0.12	45.2
42	426	420	0.2	0.1	8.4	0.28	0	16.5
47	466	466	0.26	0.06	15.8	0.105	0	2.6
51	495	497	0.29	0.085	20.9	0.08	0.03	1.6
52	509	518	0.18	0.065	8.4	0.073	0	1.4
59	620	624	0	0	0	0.16	0	8
69	725	730	0	0	0	0.22	0	33.4
73	752	752	0.1	0.075	3.8	0.045	0	0.8
83	811	815	0	0	0	0.16	0	10.4
90	885	874	0	0	0	0.09	0	3.5
92,93	902	900	0.17	0.035	13	0.05	0	1.1
105	989	990	0.12	0.08	7.1	0.079	0	3.1
113,114	1019	1018	0.15	0.08	11.5	0.03	0	0.5
117	1034	1033	0.17	0.08	14.9	0.07	0	2.5
121,122	1058	1058	0.17	0.125	15.3	0.04	0	0.8
124	1080	1081	0.11	0.035	6.5	0.145	0	11.4
136	1180	1175	0.16	0.1	15	0.022	0	0.3
138	1196	1203	0.08	0.02	3.8	0.055	0.015	1.8
140	1235	1245	0.11	0.05	7.5	0.03	0	0.6
145	1274	1287	0.16	0.06	16.5	0.2	0.08	25.7
151,153	1319	1320	0.18	0.1	21.4	0	0	0
157	1369	1380	0.1	0.06	6.9	0.16	0	17.7
160	1410	1409	0.14	0.05	13.8	0.05	0	1.8
164	1432	1447	0.08	0.1	4.7	0.24	0	44.3
169	1490	1486	0.27	0.15	54.2	0.08	0	4.8
171	1510	1519	0.06	0.05	2.7	0.07	0	3.7
176,177	1555	1555	0.21	0.11	34.3	0.07	0	3.6
182	1595	1603	0.15	0.07	18	0.09	0	6.5
Total vibrational reorganisation energy (cm^{-1})				332.7			239.4	
Electronic origin (E_{00}) (cm^{-1})				16330			21270	
Homogeneous broadening (Γ_0) (cm^{-1})				2600			875	
Electronic dipole length (μ) (Å)				1.030			1.186	
Classical reorganisation energy (cm^{-1})				3048.0			345.2	

[a] DFT/B3LYP (as detailed in the experimental section) with scaling factor of 0.9723[233] applied
[b] Dimensionless displacement
[c] Condon Factor
[d] Reorganisation energy for mode, v

Assuming that the potential energy surfaces are harmonic in nature, the magnitude of the mode displacement will determine the excited state dynamics for all Franck-Condon active modes. The majority of modes have displacements in the range of 0.05-0.25, which is consistent with other reports of mode displacements.[168, 247-249] However, mode q_{41} has a significantly larger mode displacement (in the π-π* state) than the other modes (Table 4.4). The dimensionless displacement of 0.47 is almost double that of the next

largest displacement. Accordingly, this mode is expected to dominate the dynamics in the Franck-Condon region.

The results of the DFT frequency calculation show mode q_{41} to be a transannular torsion of the phenyl ring on the dipyrrin ligand (Figure 4.29). The large displacement of q_{41} indicates firstly that this mode is strongly enhanced upon excitation into the π-π* state. The strong enhancement of the mode also indicates there is a substantial change in the π electron density of the phenyl ring and around the transannular bond upon excitation into the π-π* state. Therefore immediately after the excitation into the π–π* state, the angle between the phenyl ring and the plane of the dipyrrin core must be altered, which generates the substantial dynamics along the q_{41} mode. It is interesting to note the effect of protonation and esterification on the intensity of the q_{41} mode. Figure 4.27 shows there is a substantial decrease in the intensity of the q_{41} mode as the carboxylate group is protonated and esterified. This indicates that in the excited state, the displacement of mode q_{41} decreases for complexes **46-H** and **46b**. Metallodipyrrin species have been shown to exhibit strong inter-molecular π-stacking interactions when the phenyl ring substituent is neutral[250] (i.e. **46-H** and **51**) and these interactions may inhibit the torsional motion of the phenyl ring in the excited state.

4.5.8 Excited state dynamics in other dipyrrinato complexes

An extensive study of the excited state dynamics of boron dipyrrin complexes as a function of the dihedral angle between the dipyrrin core and the phenyl substituent in the *meso* position has been undertaken in the literature.[188] The results reveal that in the ground state geometry for a boron dipyrrin complex with a phenyl substituent at the *meso* position, the dihedral angle is 55° (125°), some 35° from perpendicularity. While in contrast there is a deep minimum in the lowest excited singlet state (S_1) when the dihedral angle is 180° (which is equivalent to 0°) (refer to Figure 9 in reference 188). At this angle, the potential energy minimum corresponds to the delocalisation of the LUMO out onto the phenyl ring (as seen in Figure 8 in reference 188). Where there is a minimum in the excited state surface (180°) there is rapid transfer of the excited state population (via non-radiative processes) from the S_1 state to the S_0 state. This is accompanied by enhanced electron delocalisation out to the phenyl ring at this dihedral angle. This provides a clear reason for the low quantum yield efficiency for this complex.

If the mesityl functional group is incorporated into the phenyl ring (three methyl groups at the *ortho*- and *para*-positions) then the rotation of the phenyl ring is restricted. The methyl groups effectively forces an orthogonal arrangement between the dipyrrin core and the phenyl ring to give the ground state conformation. However, the lowest singlet excited state is no longer a conformation with 180° dihedral angle between the dipyrrin core and the mesityl group. Therefore, fluorescence from the S_1 state is observed as the molecule returns to S_0.

Recent studies of bis(dipyrrinato) zinc complexes, further demonstrate the link between the excited state dynamics and the substituent at the *meso* position.[41, 90] The rotation of the phenyl ring is restricted by incorporating mesityl substituents onto the phenyl ring and consequently the excited state lifetime of a bis(dipyrrinato) zinc complex was increased ~50-fold.[90] Similar effects have been observed in heteroleptic cyclometallated dipyrrin species.[48, 50] We have also observed weak emission underneath the resonance Raman from complex **55** (Figure 4.32). The resonance Raman of complex **46** is included for comparison of a non-emissive Ru(II) dipyrrinato complex. The intensity of the q_{41} mode is significantly reduced for **55** and therefore displacement along the mode is reduced. Resonance Raman shows that the transannular rotation controls the excited state dynamics directly from the Franck-Condon region.

These previous studies have identified the influence of the phenyl ring substituent on the excited state lifetimes and fluorescence yields and our resonance Raman analysis complements the conclusions of these studies. Resonance Raman provides the underlying mechanism: specifically, motion along the q_{41} mode quickly relaxes the system to a minimum on the excited state surface. The deep minimum in the lowest excited state coincides with a maximum on the ground state surface and the "energy gap" law ensures rapid non-radiative decay from the excited state to the ground state. Although the q_{41} mode dominates the resonance Raman spectra, other modes are coupled with this mode through changes in electron density across the entire chromophore. Consequently, in-plane distortions and bending modes of the dipyrrin core (q_{146}, q_{157}, q_{169}) are also active in the Franck-Condon region.

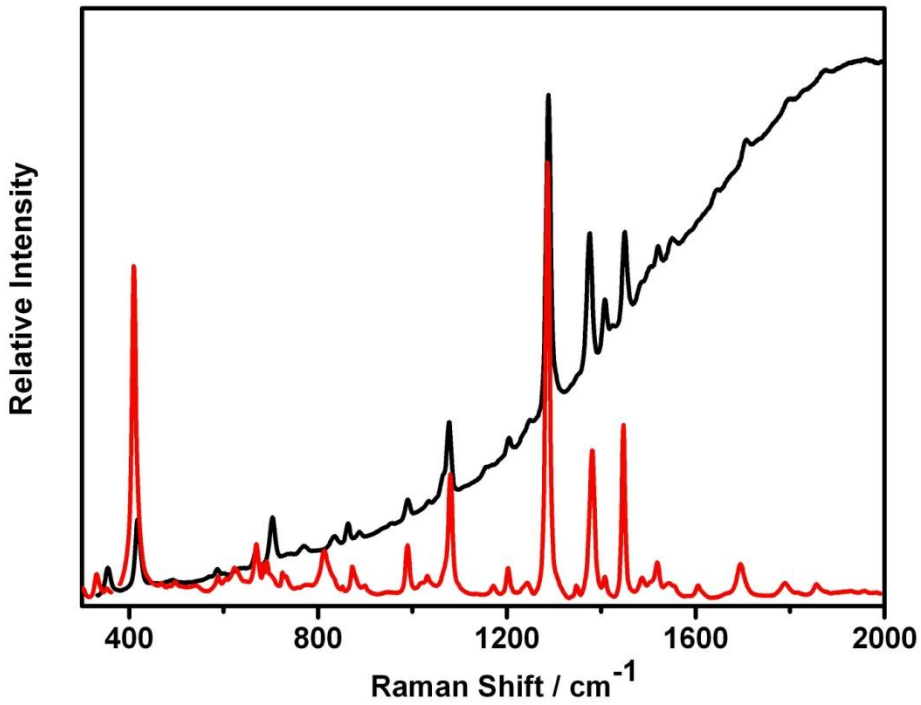

Figure 4.32. Resonance Raman spectra at 458 nm of **46** (red) in DMSO and **55** (black) in CH_2Cl_2.

4.5.9 Application of Ru(II)-dipyrrinato complexes in solar energy conversion

The electronic absorption spectra (Figure 4.19) of the Ru(II)-dipyrrinato complexes illustrates the light harvesting capability of these dyes. By altering the number of dipyrrin ligands in the coordination sphere, the MLCT absorption band is shifted further into the red thereby capturing a greater proportion of the solar spectrum. Preliminary work by our group has demonstrated that dipyrrinato-based complexes with carboxyl functional groups attached to the dipyrrin strongly bind to TiO_2 surfaces.[43] These are two crucial aspects of an efficient solar cell dye and these observations suggest that Ru(II)-dipyrrinato complexes may have promising applications as dyes in DSSCs.

Furthermore, the torsion motion in mode q_{41} (Figure 4.29) and the large displacement of this mode illustrates there is a large change in the π electron density of the phenyl ring upon excitation into the π-π* state. The electron density difference plot of the π–π* state (Figure 4.25) also confirms the electron density extends out to the phenyl ring during the transition. This shift in electron density out onto the phenyl ring in the π–π* state indicates that sensitisation of TiO_2 by these Ru(II)-dipyrrinato complexes may occur directly from the π–π* state (Figure 4.10A), depending on competing rates of

relaxation and injection. Therefore Ru(II)-dipyrrinato complexes with carboxyl groups on the phenyl ring may offer an alternative method of electron injection into TiO_2.

4.5.10 Solid state absorption spectroscopy

The light harvesting ability of the dyes adsorbed on TiO_2 (n-type semiconductor) and NiO (p-type semiconductor) films was checked by recording their solid state absorption spectra. The spectra of the dyes on TiO_2 films are shown in Figure 4.33. The solid state absorption spectrum of **51** on TiO_2 shows that there is significant enhancement of the absorption relative to the other complexes on TiO_2. It is important to note that the absorbance is near the upper detection limit of the spectrometer. The observation of high absorbance indicates very high dye loading on the TiO_2, possibly more than monolayer coverage. The carboxylic acid groups promote hydrogen bonding between other molecules of **51** resulting in multilayer coverage of the dye on the surface of the TiO_2. There is a pronounced red shift in the onset of the absorption band (~585 nm) with respect to the solution state absorption spectrum (~550 nm). The solution state absorption spectrum has been reported in reference 43. The absorption spectrum has also lost its distinctive two bands with the low energy band at 466 nm (in solution) not resolved.

The solid state absorption spectra of the dyes (**47** and **51**) on NiO films (Figure 4.34) show some notable differences compared to the spectra on TiO_2 and in solution. The transition assigned to $\pi-\pi^*$ of the dipyrrin chromophore in solution (448 nm) is significantly red shifted (to 477 nm) for complex **47**. The longer wavelength transition (~ 640 nm) of **47** more closely resembles the solution phase spectrum (rather than the solid state spectrum on TiO_2). Only one peak is resolved in the solid state spectrum of **51** on NiO with a slight red shift (~ 525 nm) relative to the TiO_2 spectrum (~ 510 nm). The absorption spectrum of complexes **46** and **50** on NiO show negligible absorption (near the noise limit of the instrument) and therefore are not shown.

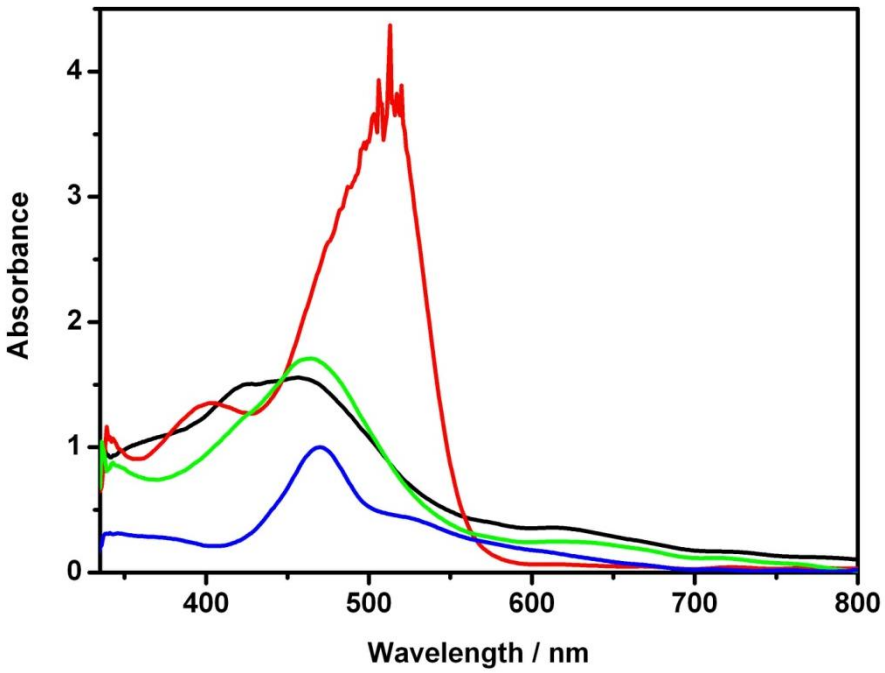

Figure 4.33. The solid state absorption spectra of dyes **46** (blue), **47** (green), **50** (black), and **51** (red) adsorbed to TiO_2.

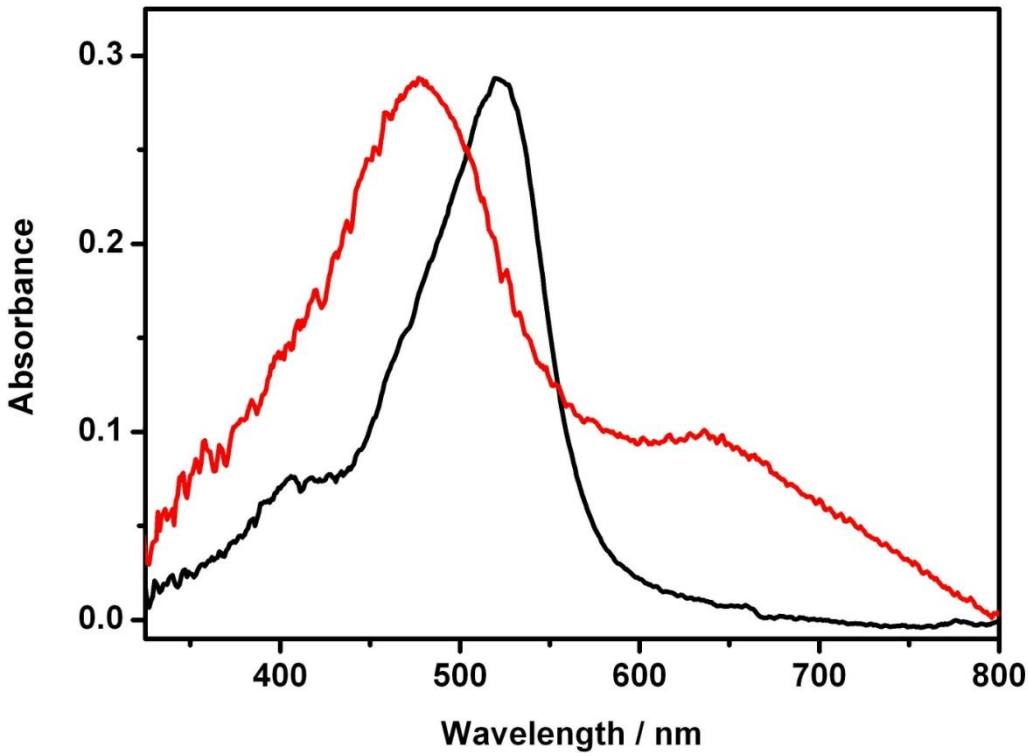

Figure 4.34. The solid state absorption spectra of dyes (**47**, red; **51**, black) adsorbed to NiO.

4.5.11 Electrochemistry

The electrochemistry of the dye-sensitised solar cell complexes was investigated by (staircase) cyclic voltammetry (Figure D1-D7). Where possible, the measurements have been made on the methyl esters of the complexes for solubility reasons. Two examples of both the methyl ester and carboxyl forms of the complexes have been measured (**47** and **47a**; and **50** and **50a**) to assess the effect of the functional group on the electrochemistry results. The limited solubility of some of the complexes in MeCN prevented all the dyes being measured in this solvent, therefore either MeCN or DMF was used. All potentials are reported against the NHE reference electrode. Experimental potentials, which were obtained using a ferrocene internal standard, were converted to potentials versus NHE by adding 0.63 V (MeCN) or 0.40 V (DMF).

A comparison between the redox potentials of $[Ru(bipy)_3]^{2+}$ and Grätzel's dyes (**N719** and **YE05**) and the Ru(II)-dipyrrinato dyes can be made. Reversible metal centred oxidation processes attributed to Ru^{2+}/Ru^{3+} are observed at 1.52 V for $[Ru(bipy)_3]^{2+}$ [251] and 1.12 V and 1.08 V,[19] for **N719** and **YE05**, respectively. By comparison with the metal centred oxidation processes of these literature examples[19, 251] the oxidation process centred between 0.246 V and 0.965 V (vs NHE) is most likely assigned as an irreversible or quasi-reversible metal-centred (Ru^{2+}/Ru^{3+}) process (Table 4.5). The dipyrrinato ligands have a significant influence on the potentials of this oxidation process. For Ru(II)-dipyrrinato complexes with two dipyrrinato ligands (**47**, **47a**, **50**, **50a**) this metal-centred oxidation process occurs in the range of 0.246-0.543 V (vs NHE). For the complexes with two dipyrrinato ligands (**46b** and **49**) the potentials are significantly more positive where they fall in the range of 0.87-0.96 V (vs NHE). Differences are observed in the metal centred oxidation process for the methyl ester and carboxyl forms of complexes **47** and **47a**; and **50** and **50a** (Table 4.5). The potential of the methyl ester forms (**47a** and **50a**) is 0.25-0.30 V (vs NHE) more positive than the carboxyl forms (**47** and **50**).

The cyclic voltammograms of the free dipyrrin ligands **34** and **52** were also measured (Figure D8-D9). A reversible reduction process takes place in the range of -0.554 V and -0.776 V (vs NHE). The free dipyrrin ligands also have two irreversible oxidations around 0.58 V (vs NHE) and 1.50 V (vs NHE) for both ligands. The reduction of the bipyridine ligands in $[Ru(bipy)_3]^{2+}$ occurs between -1.00 V and -1.50 V where three reversible reduction peaks are observed.[251] For **N719** and **YE05** the reduction of the 4,4'-dicarbonyl-2,2'-bipyridine ligand is reported at -0.70 V and -1.20 V,[19] respectively

in DMF. Therefore the reversible reduction feature over the range of -0.632 V and -1.039 V (Table 4.5) of the Ru(II)-dipyrrinato complexes cannot be unambiguously assigned to either the reduction of the bipyridine or the 4,4'-dicarbonyl-2,2'-bipyridine ligands or the dipyrrinato ligands in these Ru(II)-dipyrrinato complexes.

Table 4.5. Redox potentials ($E_{1/2}$) for Ru(II)- and Rh(III)-dipyrrinato complexes and dipyrrin ligands.

Complex or ligand	Solvent	First oxidation process	First reduction process
		vs NHE [b]	vs NHE [b]
42[a]	MeCN	1.154	-0.005
46b	MeCN	0.965	-0.663
47	DMF	0.248	-1.014
47a	MeCN	0.506	-0.632
49	DMF	0.874	-0.985
50	DMF	0.246	-1.039
50a	MeCN	0.543	-0.716
34			-0.554
52			-0.776

[a] Complex **42** is Rh based

[b] Values are reported against NHE using literature values (relative to the Fc/Fc^+ redox couple) after the addition of Fc/Fc^+ as a standard. [+0.63 V (vs NHE) in MeCN)[252] and +0.40 V (vs NHE) in DMF)[253]].

Cyclic voltammetry is a useful tool for estimating the suitability of a complex as a solar cell dye. The HOMO potential must be more positive than the redox mediator to ensure favourable regeneration kinetics of the oxidised dye by the redox mediator. The LUMO potential must be more negative than the conduction band of the semiconductor (TiO_2) to obtain efficient electron injection into the conduction band.[194] The ionisation potential is an approximation of the HOMO level. This can be estimated from the oxidation onset potential (E_{onset}^{ox}) of the metal centred process.[254] The electronic bandgap can be estimated from the onset wavelength (λ_{onset}) of the lowest energy band in the absorption spectra. Therefore the LUMO potential can be estimated retrospectively.[254] These energy levels have been estimated from solution state cyclic voltammetry (CV) and are summarised in Table 4.6 and Figure 4.35. Due to the solubility of complex **51** and **46** the energy levels of these complexes has been estimated using their methyl ester analogues (**42** and **46b**, respectively).

Table 4.6. Summary of the energy levels obtained from cyclic voltammetry.

Complex	E_{onset}^{ox} (vs NHE) / V	Onset of absorption / nm	Ionisation Potential / eV [a]	Bandgap / eV [b]	LUMO / V [c]
46[d]	0.764	700	5.323	1.776	-1.01
47	-0.07	800	4.488	1.554	-1.63
49	0.544	700	5.103	1.776	-1.23
50	-0.157	800	4.402	1.554	-1.71
51[e]	0.985	550	5.544	2.260	-1.29

[a] Ionisation Potential (eV) = HOMO (eV) = E_{onset}^{ox} (vs NHE) + 4.5588 eV [254, 255]

[b] Band gap (eV) = $\frac{1243}{\lambda_{onset}\,(\text{nm})}$

[c] LUMO (V) = E_{onset}^{ox} (vs NHE) - band gap (eV)

[d] The energy levels of **46** have been estimated from the energy levels of **46b**

[e] The energy levels of **51** have been estimated from the energy levels of **42**

The energy level diagram (Figure 4.35) shows that for the mono-dipyrrinato dyes (**46**, **49** and **51**) that electron injection into the conduction band of the TiO_2 and dye regeneration from the redox mediator should be favourable. However, for bis-dipyrrinato complexes **47** and **50**, the HOMO potential is more negative than the traditional I^-/I_3^- redox mediator therefore regeneration of the dye is predicted to be unfavourable.

It is important to note that there is only a weak dependence on the oxidation potential of the dye, $E^{ox}(D/D^+)$, in preventing recombination.[256] The ability to change the oxidation potential of the dye is restricted by the need to achieve favourable energetics for electron injection and dye regeneration. Therefore the separation of the hole on the oxidised dye from the electron injected into the TiO_2 plays an important role in impeding the rate of charge recombination between the injected electrons and the oxidised dye.[21]

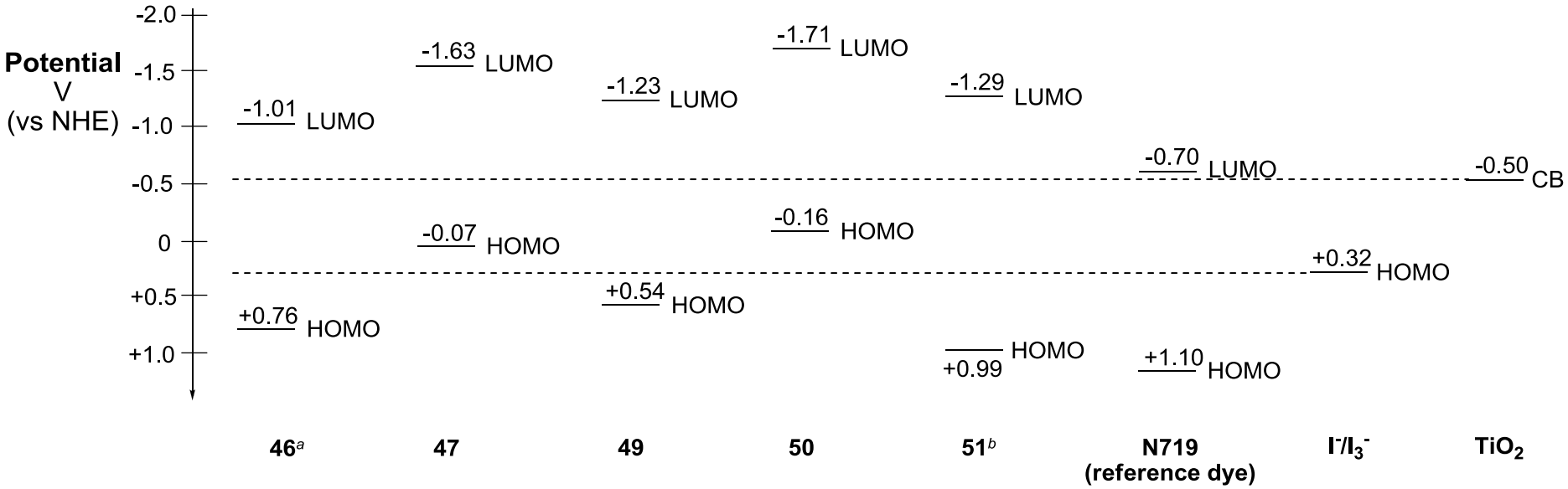

Figure 4.35. Energy level diagram for complexes **46**, **47**, **49**, **50** and **51** (vs NHE). The energy levels of a reference dye (**N719**), the redox mediator (I^-/I_3^-), and the conduction band (CB) of TiO_2 has been included for comparison purposes. The HOMO potential is E_{onset}^{ox} (vs NHE). The LUMO potential is obtained by subtracting the band gap from the E_{onset}^{ox} (vs NHE).[a,b] The energy levels of **46** and **51** are estimated from their methyl ester analogues (**46b** and **42**).

Charge recombination is one of the key loss mechanisms (Figure 4.36) limiting the performance of DSSCs. Electron injection into the conduction band of the TiO_2 (2) occurs within femto- to picoseconds.[20] Following this there are two possible recombination pathways. The recombination of the electron with the oxidised dye (D^+) (4), or the recombination of the electron with the redox couple (I^-/I_3^-) (5).[257] These recombination processes occur in the millisecond to microsecond time domain.[18, 20, 257, 258] Other loss mechanisms include decay of the excited state of the dye (D^*) back to the ground state before the electron is injected to the TiO_2 (6)[21, 257] and aggregation of the dye on the TiO_2 surface. This leads to deactivation of the excited state of the dye.[21] There is a possibility that these dipyrrinato dyes could be aggregating on the surface of the TiO_2.[250] Aggregation is commonly prevented in literature examples of Ru(II) DSSCs by including bulky terminal groups[259, 260] and this method could be employed for Ru(II)-dipyrrinato complexes.

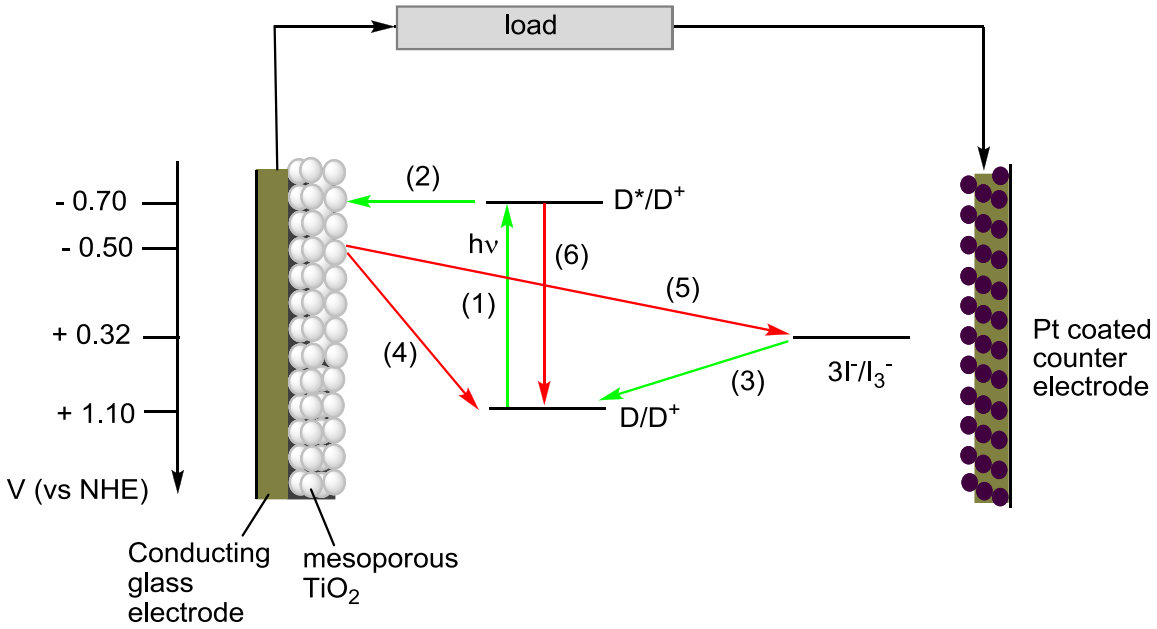

Figure 4.36. Schematic diagram showing the desired processes (green arrows) and undesirable processes (red arrows) which occur during the operation of a DSSC. (1) absorption of light, (2) electron injection from the dye excited state into the conduction band of TiO_2, (3) regeneration of the dye cation by electron transfer from the redox couple, (4) recombination of the electron with the dye cation, (5) recombination of the electron with the redox couple (I^-/I_3^-), and (6) decay of the excited state back to the ground state (adapted from references 21, 257).

4.5.12 Solar cell testing

Current-voltage curves are plotted in order to extract the necessary parameters required to characterise the dyes performance. The short circuit current (J_{SC}) is the starting point of a current-voltage curve. The short circuit current is found when the voltage applied to the cell is zero. For an ideal cell the short circuit current is the maximum current produced by the cell. From here the voltage is increased and the current is monitored until the open circuit voltage is reached (V_{OC}). The open circuit voltage (V_{OC}) is found when there is no current passing through the cell.[213] A typical current-voltage curve (of a metalloporphyrin dye) is given in Figure 4.37. The current-voltage curves for the dipyrrinato dyes are given in Appendix D3 (Figures D11-D22).

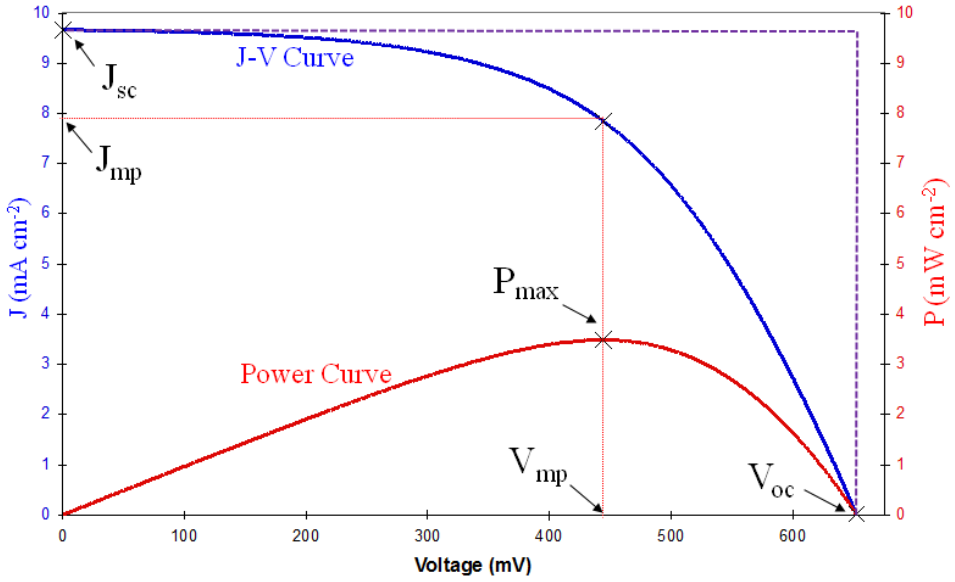

Figure 4.37. Typical current voltage curve (blue) of a metalloporphyrin showing the short-circuit current (J_{SC}) and the open circuit voltage (V_{OC}), and a power curve (red) showing the maximum power (P_{max}). The ratio of the red dotted box relative to the purple box gives the fill factor (FF).[261]

The fill factor (FF) is one of the most important parameters derived from the current-voltage curve of a solar cell.[213, 261] The fill factor (equation 4.2)[22, 213] is the ratio of the electric power produced at the point of maximum power (P_{max}) (red dotted box in Figure 4.37) on the power curve relative to the product of open circuit voltage (V_{OC}) and

the short circuit current (J_{SC}) on the current-voltage curve (purple box in Figure 4.37).[261]

$$FF = \frac{P_{\max}}{V_{OC} J_{SC}} = \frac{V_{mp} J_{mp}}{V_{OC} J_{SC}} \quad (4.2)$$

where J_{SC} is the short-circuit current (A/cm^2 or mA/cm^2), V_{OC} is the open circuit voltage (V or mV) and P_{max} is the maximum power (W/cm^2 or mW/cm^2) on the power curve. This value is calculated as the product of the photocurrent and photovoltage at the voltage where the power output of the cell is maximal.[22]

The value of the fill factor reflects the extent of the losses occurring from the DSSC.[22] An ideal cell would have a fill factor of unity but this is unachievable for practical cells.[261] Silicon solar cells have a fill factor of ~ 0.7.[261] Low V_{OC} values suggest there is a mismatch in the energy levels while low J_{SC} values indicate there are significant losses occurring from the cell, for example charge recombination (see above). The performance of the dyes as sensitisers for both TiO_2 and NiO DSSCs is given in Table 4.7.

The performance of complexes **46**, **47**, and **50** on both semiconductor surfaces was poor with solar conversion efficiencies of less than 0.06 % (on TiO_2). The energy levels of complexes **47** and **50** (Figure 4.35) indicated that the regeneration of the dye cation by the redox mediator would be unfavourable. The low V_{OC} values for these dyes (~ 0.4 V) confirms that there is a disparity between the energy levels of dye, the redox mediator and/or the conduction band of the semiconductor. The low J_{SC} value of complex **46** suggests other losses are occurring from the cell.

Under standard testing conditions the best Ru(II) DSSCs (on TiO_2) have J_{SC} values in the range of 16-22 mA cm^{-2} and V_{OC} values of 0.7-0.86 V. These J_{SC} and V_{OC} values correspond to fill factors between 0.65-0.8.[22] The best performing dye in this dipyrrinato series is complex **49** with a solar conversion efficiency of 0.6%, which is still significantly lower than the best dyes in the literature.[17-19, 22, 216-219, 262] The fill factor for this complex of 0.69 is slightly larger than the reference dye (**N719**) which indicates that the complex should perform well. The V_{OC} value for complex **49** of 0.42 is less than half the magnitude of the V_{OC} value of reference dye (**N719**); however, the J_{SC} value for complex **49** is nearly seven times smaller than the J_{SC} value of the reference dye. In particular the low J_{SC} value of complex **49** suggests that there are losses occurring from the cell.

The Rh(III)-dipyrrinato complex **51** (on TiO_2) has an average efficiency of 0.245%. The J_{SC} values obtained for **51** are much smaller than the reference dyes (Table 4.7) and the best Ru(II) dyes reported in the literature.[22] The fill factor for this complex is larger than the reference dye (**N719**). However, the J_{SC} and V_{OC} values, which are much lower than the values recorded for the reference dye, indicate there are losses from the cell.

Table 4.7. Solar cell performance on TiO_2 and NiO[a].

Device	Dye	V_{OC} (V)	J_{SC} [b]	Fill Factor (FF)	η (%)
TiO_2	**46**	0.3	0.0140	0.42	0.017
	47	0.395	0.21	0.62	0.05
	47	0.400	0.22	0.64	0.06
	49[c]	0.42	2.1	0.69	0.6
	50	~0	0.051	0.2	~0
	51	0.515	0.63	0.71	0.23
	51	0.505	0.66	0.78	0.26
	N719 [d,e]	0.72	15.6	0.61	6.8
	395 [e]	0.615	3.25	0.7	1.4
NiO	**46**	0.063	136	0.33	0.0028
	47	0	0	0	0
	50	0	0	0	0
	51	0.081	129	0.33	0.0034
	395 [e]	0.094	623	0.32	0.0180

[a] The fabrication of the solar cells is outlined in Appendix D3.
[b] Units for TiO_2 cells = mA cm^{-2}, units for NiO cells = μA cm^{-2}.
[c] Complex **49** was tested at Hanyang University under standard testing conditions.
[d] Reported solar cell efficiency is 10.1-11.2% (depending on the size the device).[18] The value reported in this table was obtained under standard testing conditions at the University of Wollongong.
[e] Structures of the reference dyes are given in Appendix D6.

Complexes **47** and **50** on NiO both show solar conversion efficiencies of zero since the V_{OC}, J_{SC}, and fill factors for these complexes are zero. Complexes **46** and **51** on NiO show the fill factor is comparable with that of the reference dye (**395**); however, the solar conversion efficiencies are much lower than **395** (Table 4.7). The J_{SC} values for both of the complexes are four- to five-fold lower than the value for the reference dye (**395**). The V_{OC} values for both of the complexes are slightly lower than the value for the reference dye (**395**). The particularly low J_{SC} values indicate that significant current losses are occurring.

The results reported in this thesis indicate which dyes are worthy candidates for further testing in regard to optimising the testing conditions for improving the solar conversion efficiency. Multiple testing of each dye in a new solar cell device is also required for reproducibility.

The complexes with the carboxyl groups on the dipyrrinato ligand (**46**, **47**, and **51**) generate a photocurrent when irradiated following sorption onto TiO_2. Despite the poor energy conversion efficiencies this result is promising since it indicates that electron injection into the TiO_2 is occurring. The best of these complexes is the Rh(III)-dipyrrinato complex **51**. Since there are few examples of Rh(III) complexes as sensitisers for dye-sensitised solar cells in the literature then the result from this first generation Rh(III)-dipyrrinato complex indicates that further work on the design of Rh(III)-dipyrrinato complexes is warranted in an attempt to improve the solar conversion efficiency. For complexes **46** and **47**, where the electron injection is anticipated to be from the π–π^* excited state of the dipyrrin, the poor solar conversion efficiencies may indicate that this method of electron injection is inferior to the "traditional" electron injection from the (Ru(II)→bipyridine) MLCT excited state of the Ru(II)-bipyridine of the dye.

The best dyes employed as sensitisers for dye-sensitised cells in the literature have exploited the MLCT excited state of Ru(II) bipyridine dyes. The best dye in this series of dipyrrinato dyes, complex **49** where the carboxyl groups are attached to the bipyridine ligands, most likely exploits the (Ru(II)→bipyridine) MLCT excited state.

4.6 Summary

The synthesis and characterisation of a series of Ru(II)-dipyrrinato complexes have been achieved. Ru(II)-dipyrrinato complexes are attractive targets for solar energy conversion since they absorb light across a large proportion of the visible region. Resonance Raman, resonance Raman intensity analysis and DFT calculations reveal that upon excitation of the dipyrrinato ligand there is a large shift of electron density from the dipyrrin core out towards the phenyl ring. This shift in electron density indicates that if the phenyl ring of the dipyrrinato ligand is functionalised with a suitable group for binding to TiO_2 then electron injection may occur directly from the π–π^* excited state.

To the best of our knowledge, these are the first Ru(II)-dipyrrinato and Rh(III)-dipyrrinato complexes tested in solar energy conversion. Despite poor energy conversion efficiencies from this series of dipyrrinato dyes the results are promising since they indicate that electron injection into the TiO_2 is occurring.

4.7 Future work

Optimising the testing conditions is required to fully evaluate this series of dipyrrinato solar cell dyes. Different semiconductor surfaces (such as ZnO and SnO_2), electrolytes, and solvent systems need to be explored to improve the solar conversion efficiencies. For reliable results each complex should be tested multiple times to ensure reproducibility. From these results the position of the carboxyl binding group, the effect of the functional group on the dipyrrinato ligand can be fully evaluated and the best method of charge injection in dipyrrinato complexes can be inferred.

Future synthetic targets include dipyrrinato ligands substituted with a diphenylamino functional group (Figure 4.38) to investigate the role charge separation plays in Ru(II)-dipyrrinato complexes as DSSC dyes.

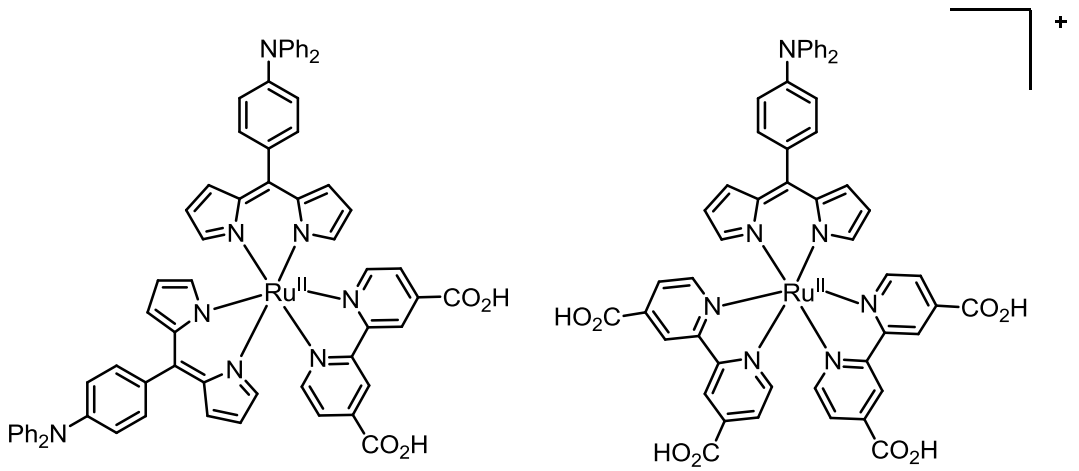

Figure 4.38. Structure of two future target complexes with diphenylamino substituents on the dipyrrinato ligand where charge separation should be more favourable.

Metallophthalocyanine dyes sensitised onto TiO_2 has shown that phthalocyanine dyes and their derivatives warrant investigation as solar cell dyes.[259, 263, 264] Recall that azadipyrrin ligands can be considered to be half phthalocyanines. As such suitably

designed azadipyrrin ligands complexed with Ru(II) are worthy targets to investigate for DSSC applications and water splitting devices (Figure 4.39). Recently there has been a focus on producing light-harvesting complexes which absorb solar radiation in the red to IR wavelengths[21, 260, 263-265] and it is anticipated that Ru(II)-azadipyrrinato complexes will have a significantly red shifted absorption maximum with respect to Ru(II)-dipyrrinato complexes. The synthetic protocol established in this thesis and by past members should provide routes to these future target complexes. Post-synthetic modifications of the methyl substituents (in the β-positions) of the azadipyrrinato ligand could afford the appropriate groups for binding to TiO_2.

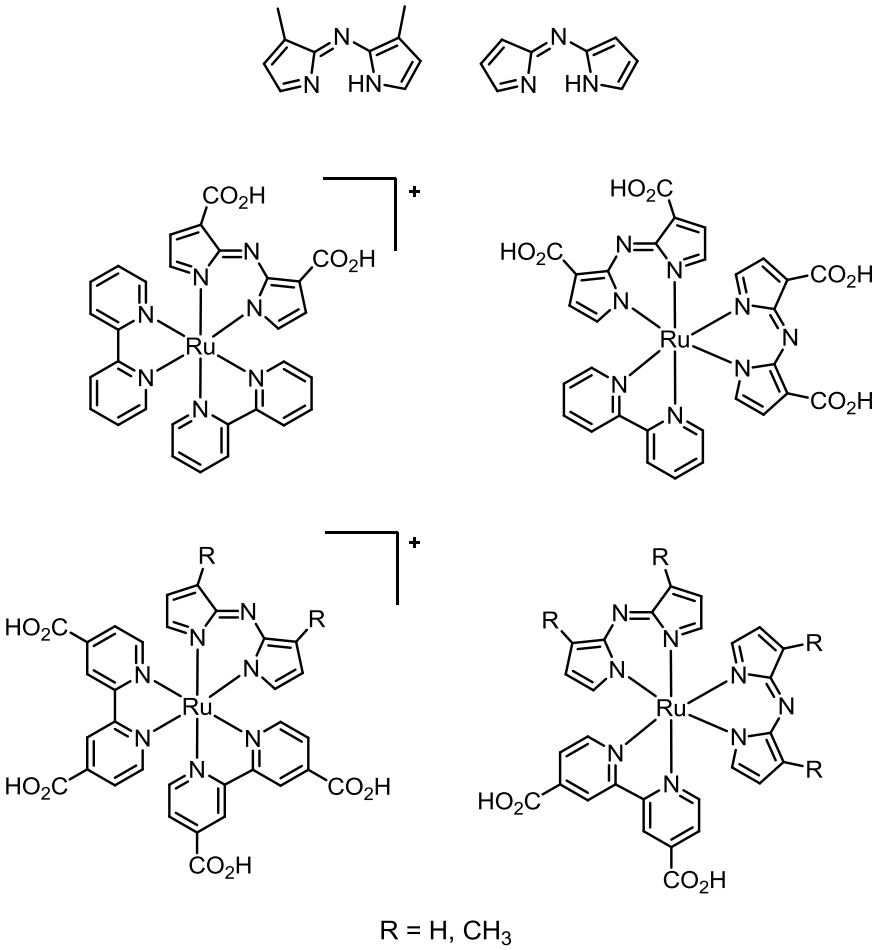

Figure 4.39. Structure of the target azadipyrrin ligands and future target Ru(II)-azadipyrrinato complexes.

The long term focus for the synthesis and characterisation of new dipyrrinato complexes in solar energy applications requires fast and ultrafast kinetic measurements for

complexes reported in this thesis. Information on the excited state lifetimes and excited state dynamics is crucial for designing next generation dipyrrinato complexes and improving the performances of these complexes in photochemical devices.

Acknowledgements

I wish to thank the following people for their assistance in this chapter: Serena Smalley for establishing the synthetic protocol for Ru(II)-dipyrrinato complexes including the synthesis of **46** and **47**. I would also like to acknowledge Dr Mark Waterland for the DFT calculations on **46-H**, Sam Lind and Deirdre Cleland (supervisor: Professor Keith Gordon, University of Otago) for collecting resonance Raman data at excitation wavelengths of 413, 444, and 532 nm, the preliminary resonance Raman intensity analysis, and DFT calculations of **46**; Matt Griffith and Lei Tong (supervisor: Dr Attila Mozer, Intelligent Polymer Research Institute, University of Wollongong); Professor Yong Soo Kang and his students (Energy Materials Lab, Hanyang University) for solar cell measurements; Dr Wayne Campbell (Massey University) for valuable discussions on the solar cell results and providing Figure 4.36; and Nessha Wise and Professor Simon Hall (Massey University) for assistance with electrochemistry measurements and valuable discussions on electrochemistry results.

Chapter 5

Luminescent Re(I)-dipyrrinato complexes and their applications

5.1 Background to Re(I)-polypyridine complexes

Re(I), a d^6 metal in the third row of the periodic table, generally forms stable complexes with polypyridine or other diimine ligands often with three carbon monoxide co-ligands.[104, 266] These types of Re(I) complexes have rich and well characterised photochemical properties and continue to be an intense area of research.[104, 266] Upon light absorption, the Re(I) centre, can transfer electron density from its d orbitals to the low-lying π* orbitals of aromatic ligands such as bipyridine to form a metal-to-ligand charge transfer (MLCT) excited state. Irradiation into the MLCT manifold of many Re(I) complexes of the type $[Re(bipy)(CO)_3Cl]$ or $[Re(bipy)(CO)_3PR_3]^+$ results in photochemical ligand substitution reactions.[104, 267-271]

Re(I)-polypyridine complexes and their derivatives have interesting photophysical properties such as intense luminescence[269, 270, 272-276] and have found applications in solar energy conversion[277] and photocatalysis.[198, 278, 279]

5.1.1 Applications of Re(I)-polypyridyl complexes

5.1.1.1 Catalytic reduction of CO_2

Complexes of the type *fac*-$[Re(bipy)(CO)_3L]^{n+}$ where L = NCS^-, Cl^-, $P(OEt)_3$, $P(O\text{-}iPr)_3$ are known to catalytically reduce CO_2 to CO upon absorption of visible light.[278-281] The proposed mechanism for this catalytic cycle (Figure 5.1) begins with the reductive quenching of the triplet (^{3}MLCT) excited state by triethanolamine (TEOA), to produce the one electron reduced (OER) species, $[Re(bipy)(CO)_3L]^{\bullet-}$. Elimination of L^- from the OER species, to give $[Re(bipy^{\bullet-})(CO)_3]$, is a key step in the photocatalytic reaction. It is assumed the CO_2 coordinates in the vacant coordination site resulting in the CO_2 adduct. At this point the OER species donates an electron to the CO_2, to produce CO and $0.5O_2$. The starting material (**58**) is regenerated by the re-coordination of the eliminated L anion.[279] Recently, binuclear and tetranuclear Ru(II)- and Re(I)-

polypyridine complexes have also shown capacity to catalytically reduce CO_2[199, 281] and in some cases these complexes are remarkably efficient.[282]

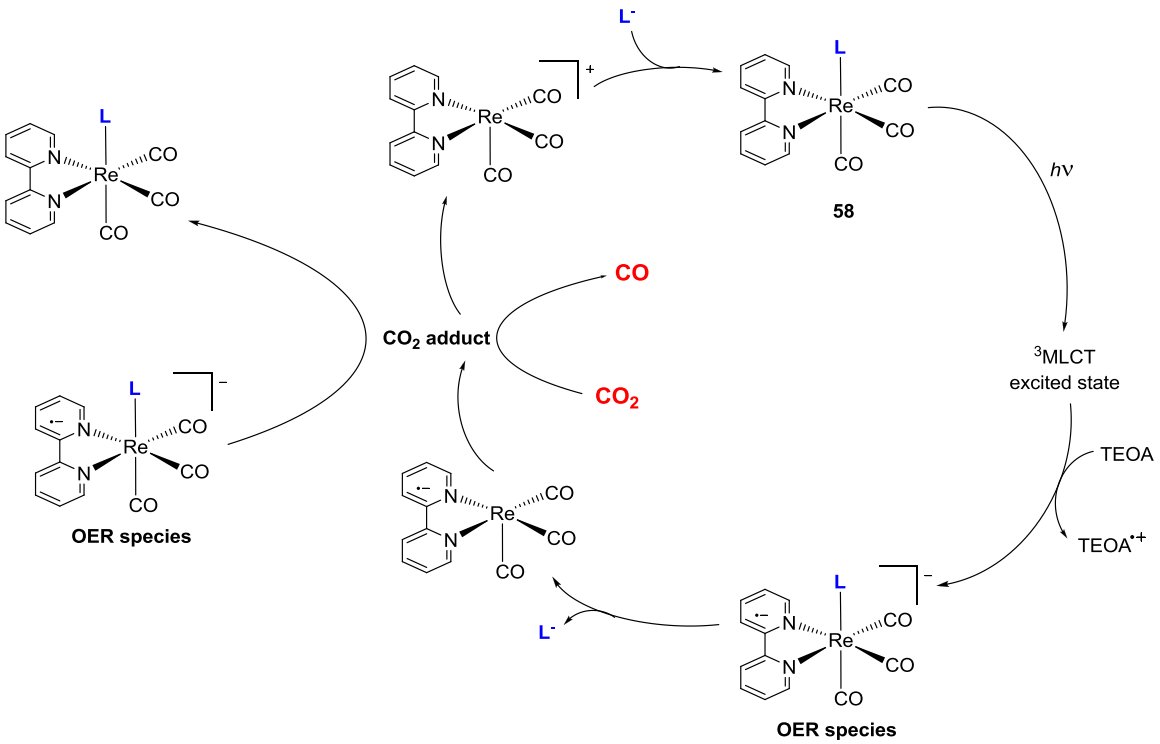

Figure 5.1. The catalytic reduction of CO_2 by a Re(I)-polypyridine complex (**58**).

5.1.1.2 Photochemical ligand substitution (PLS) reactions

Efficient photochemical ligand substitution is observed for *fac*-$[Re(bipy)(CO)_3(PR_3)]^+$ complexes. This yields *cis-trans*-$[Re(bipy)(CO)_2(PR_3)L]^{n+}$ where PR_3 is a tertiary phosphine or phosphite and the entering ligand L is chloride, pyridine, or CH_3CN.[269] The substitution reaction occurs by the loss of the CO group *trans* to the axial PR_3 ligand. Labelling studies (^{13}CO) were consistent with a dissociative mechanism where the axial CO *trans* to the phosphorus ligand was labilised.[270] Mechanistic studies strongly suggest that the photochemical ligand substitution reaction occurs from an excited state (probably ^3MC) which is thermally accessible from the lowest ^3MLCT excited state (Figure 5.2), particularly when the photosubstitution reaction involves a dissociative mechanism.[283]

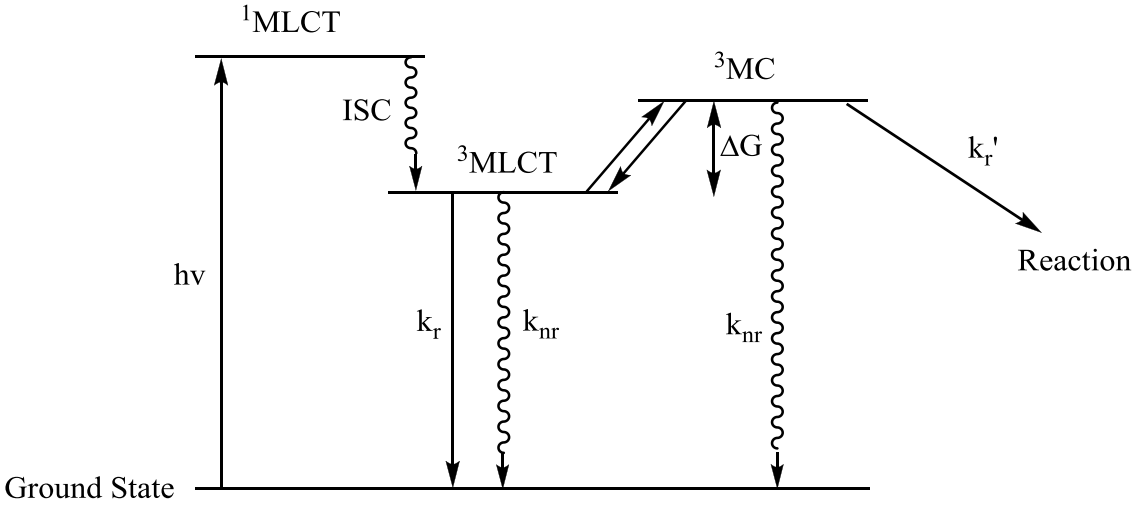

Figure 5.2. A simplified Jablonski diagram describing the activated loss of the carbonyl ligand *trans* to the PR_3 of *fac*-$[Re(bipy)(CO)_3(PR_3)]^+$.

Moderately efficient photochemical ligand substitution was also reported recently by Ishitani and others for *fac*-$[Re(bipy)(CO)_3Cl]$ and *fac*-$[Re(bipy)(CO)_3Y]^+$ to yield *fac*-$[Re(bipy)(CO)_2LCl]$ where Y is pyridine or CH_3CN and the entering ligand L is pyridine or CH_3CN. Mechanistic studies illustrated that in this case the photochemical ligand substitution differs from previously described studies in that it does not proceed from the lowest ^{3}MLCT excited state. Rather the reactions probably proceed from higher vibrational levels of the ^{1}MLCT state or higher electronic states such as π–π^* or higher lying Re-bipy or Re-CO ^{1}MLCT states.[268]

5.1.1.3 Solar cells

Re(I)-diimine complexes have been successfully incorporated into solar cells. While there are limited examples of applications as photosensitisers in DSSCs,[284] there are multiple instances of applications in bulk heterojunction solar cells.[277, 285, 286]

5.2 Objectives of this work and target complexes

The applications of Re(I)-polypyridyl complexes combined with the strong light absorbing properties of dipyrrin ligands ($\varepsilon \approx 20\ 000\ M^{-1}\ cm^{-1}$ in the visible region) provide the rationale for exploring Re(I)-dipyrrinato complexes. Such complexes are expected to have interesting spectroscopic properties with potential applications in

catalytic reduction of CO_2 and as sensitisers in DSSCs or water splitting devices. The incorporation of dipyrrinato ligands has the advantage over Re(I)-polypyridyl systems in that it will move the light absorption into the visible region of the spectrum, which is crucial for further development of devices which rely on solar radiation.

In exploratory work in our group, the coordination of dipyrrinato ligands to Re(I) was achieved to prepare the first known Re(I)-dipyrrinato complexes (Figure 5.3). There is one example of a non-emissive Re(I)-azadipyrrinato complex in the literature.[85]

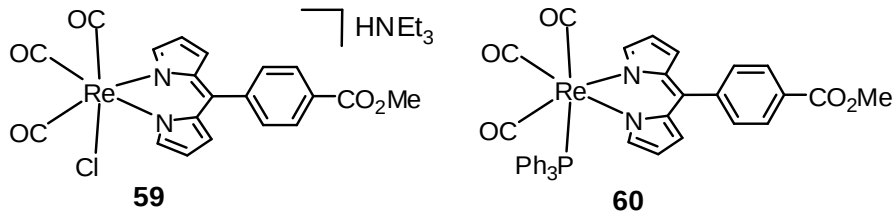

Figure 5.3. First generation Re(I)-dipyrrinato complexes **59** and **60**.

As an extension to this exploratory work in our group, further Re(I)-dipyrrinato complexes were targeted with a variety of different dipyrrin ligands (Figure 5.4). This chapter focuses on the synthesis, characterisation, and spectroscopic properties of a series of new Re(I)-dipyrrinato complexes. It was anticipated that the electronic (and redox) properties of the complexes could be tuned by incorporating different functional groups on the aryl substituent of the dipyrrin ligand (Figure 5.4A). The ester functional group in ligand **34** is electron withdrawing. The methoxy and diphenylamino substituents in ligands **52** and **61**, respectively, are both electron donating groups. Diphenylamino substituents are also well known for extending the charge separation distance in complexes in DSSCs.[21, 287] The rotation of the *meso*-phenyl substituent is an important non-radiative pathway for the relaxation of dipyrrin-centred excited states.[41, 48, 90, 231] Re(I)-dipyrrinato complexes of ligand **56** were targeted since the rotation of the phenyl ring is restricted using the mesityl functional group. This is one common method employed in the literature[41, 48, 50, 90, 91] for enhancing the emission of dipyrrinato complexes.

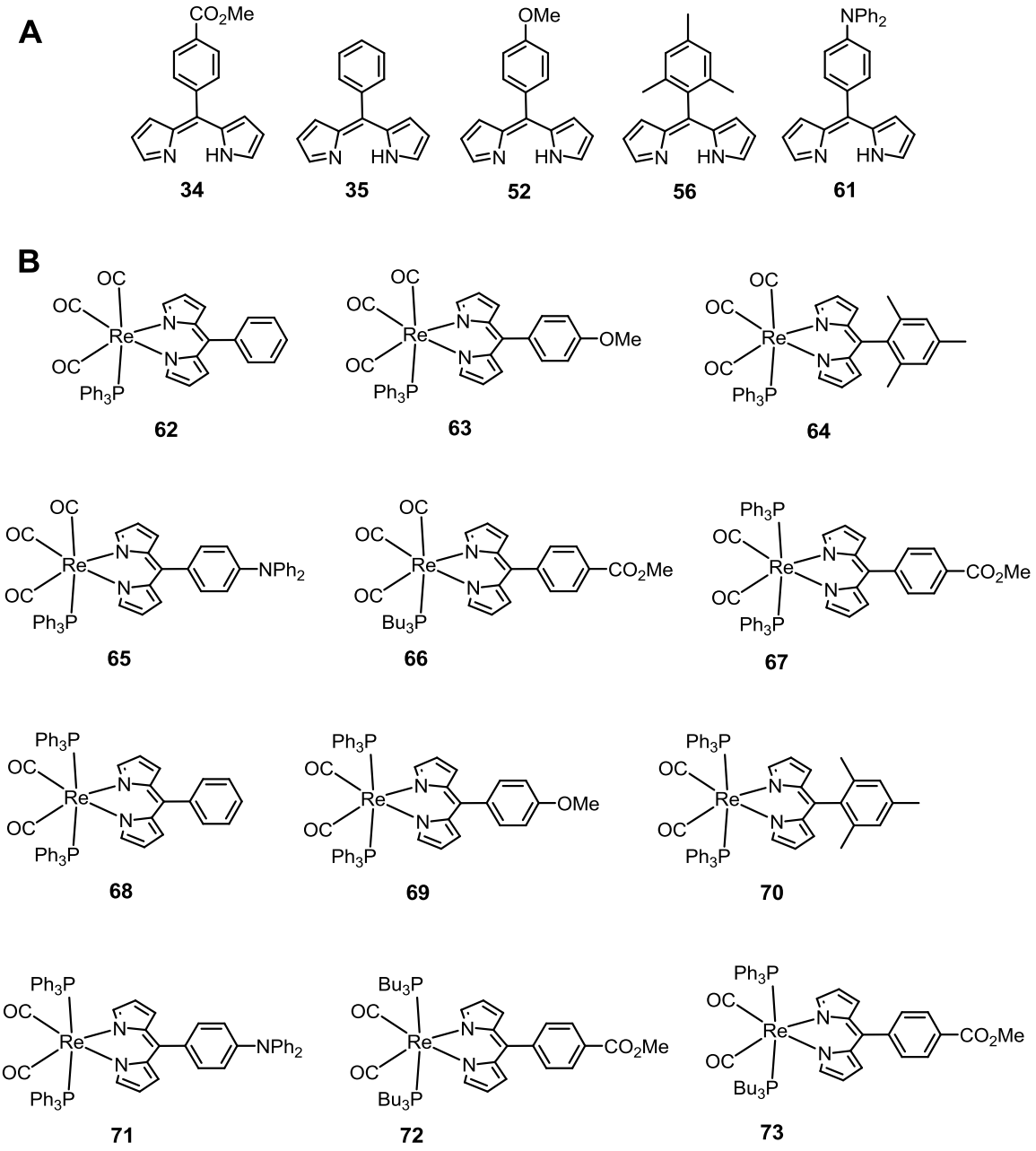

Figure 5.4. (A) Structure of the dipyrrin ligands (**L**H) employed in this chapter and (B) target Re(I)-dipyrrinato complexes. The ligand is deprotonated to give L^- before coordination to the Re(I) centre.

5.3 Experimental details

5.3.1 Computational procedures

All calculations were performed using Gaussian *03*[232] or Gaussian *09*.[145] Calculations were carried out by using density functional theory (DFT), with the B3LYP exchange-correlation functional. The SDD basis set was used for all calculations. Self-consistent

reaction field methods, more specifically the polarisable continuum model (C-PCM) of Barone,[151] were used to model solvent effects. All calculations were carried out using the C-PCM model. Attempts were made to optimise the full structure of **60** and **65**, using a SDD basis set with the C-PCM model.[151] However, the calculations failed to converge for complexes **60**. This is most likely due to the phenyl rings on the triphenyl phosphine rotating and preventing the calculation from finding the minimum on the potential energy surface or there are a number of equivalent minima. There is good agreement between bond lengths and angles of the calculated structure and the crystal structure of **60** therefore it is sufficient to use the crystal structure in place of the optimised geometry calculation. Following this, the optimised geometry of **60** and the crystal structure geometry of **65**[32] was used to perform time-dependent DFT calculations. All further calculations were carried out using the C-PCM solvent model. Excited-state energies and oscillator strengths were calculated using time-dependent methods with the basis set described above. Electron density difference maps were generated by subtracting the ground-state one-particle total density from the one-particle densities for selected excited-states using the Cubeman utility in Gaussian *03*.

5.3.2 Experimental procedures

5.3.2.1 Synthesis of dipyrrin ligands

The synthesis and purification of the ligands, **34**-**35** and **52** and **56** are outlined in the relevant sections of chapter 2 and 4. The synthesis of ligand **61** is outlined in the literature.[32]

*5.3.2.2 Synthesis of fac-[Re**L**(CO)$_3$Cl][NEt$_3$H], **59** and fac-[Re**L**(CO)$_3$PR$_3$] **60** and **62**-**66***

The synthesis (via conventional heating) and purification of **59**, **60** and **64** were established by previous members of the group and are outlined in the literature.[32] These characterisation data have been included here for comparison purposes. Both conventional and microwave heating methods (as outlined below) have been developed in the synthesis of **60** and **62**-**66** (Figure 5.5).

Conventional method (method A)

$Re(CO)_5Cl$ (0.70 mmol) and **L**H (1 equiv.) were dissolved in dry toluene (15 mL) and heated to 100 °C under argon. Dry NEt_3 (~2 equiv.) was added via a syringe and heating continued for 1 h. PR_3 (PPh_3 or n-PBu_3) (1 equiv.) was then added and heating continued for a further 1 h. All volatiles were removed under reduced pressure before the product was obtained as an orange crystalline solid by chromatography on neutral deactivated alumina.

Microwave method (method B)

$Re(CO)_5Cl$ (0.354 mmol) and **L**H (1.25 equiv.) were dissolved in dry toluene (5 mL). Dry NEt_3 (~2 equiv.) was added and the reaction was heated to 100 °C for 15 mins in a microwave synthesizer (open vessel mode) under argon. PR_3 (PPh_3 or n-PBu_3) (1 equiv.) was then added and heating continued for a further 15 mins. All volatiles were removed under reduced pressure before the product was obtained as an orange crystalline solid by chromatography on neutral deactivated alumina.

*Synthesis of **59***

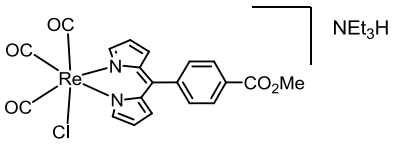

Yield: 75%. ^{1}H NMR (400 MHz, $CDCl_3$, 25 °C): δ (ppm) 1.26 (t, *J* = 7.20 Hz, 9H), 2.93 (q, *J* = 7.20 Hz, 6H), 3.97 (s, 3H), 6.35 (dd, *J* = 4.20, 1.60 Hz, 2H), 6.45 (dd, *J* = 4.20, 1.60 Hz, 2H), 7.44 (dd, *J* = 7.80, 1.60 Hz, 1H), 7.59 (dd, *J* = 7.80, 1.60 Hz, 1H), 8.05 (m, 3H), 8.09 (dd, *J* = 7.80, 1.60 Hz, 1H); ^{13}C NMR (100 MHz, $CDCl_3$, 25 °C): δ (ppm) 8.66, 46.22, 52.29, 117.86, 128.18, 128.49, 129.83, 130.08, 130.72, 130.82, 136.24, 143.75, 146.45, 154.02, 166.87, 193.48, 198.89; Anal. Calcd for [**59**] $C_{26}H_{29}ClN_3O_5Re$: C, 45.58; H, 4.27; N, 6.13. Found C, 45.77; H, 4.38; N, 6.12; UV-Vis (DMSO): λ_{max} / nm (ε / L mol^{-1} cm^{-1}): 487 (33 800), 308 (10 100); ESI-MS (-ve mode): *m/z* 583.7 ([M$^-$]); IR (cm^{-1}): 729 (m), 762 (m), 829 (w), 897 (w), 995 (m), 1030 (s), 1242 (m), 1279 (m), 1340 (m), 1377 (m), 1551 (m), 1716 (m), 1863 (s), 1888 (s), 2004 (s).

*Synthesis of **60***, via Method A

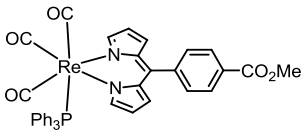

Purification was achieved by chromatography on neutral deactivated alumina, eluting with CH_2Cl_2/hexane (1/7). Yield: 87%. ^{1}H NMR (500 MHz, $CDCl_3$, 25 °C): δ (ppm) 3.96 (s, 3H), 6.38 (m, 2H), 6.42 (m, 2H), 6.78 (dd, *J* = 7.9, 1.4 Hz, 1H), 7.01 (m, 6H), 7.37 (m, 6H), 7.48 (m, 3H), 7.52 (dd, *J* = 7.9, 1.4 Hz, 1H), 7.78 (d, *J* = 1.4 Hz, 2H), 8.01 (dd, *J* = 7.9, 1.4 Hz, 1H), 8.09 (dd, *J* = 7.9, 1.4 Hz, 1H); ^{13}C NMR (100 MHz, $CDCl_3$): δ (ppm) 52.24, 119.16, 128.14, 128.36, 128.45, 129.80, 129.83, 129.99, 130.01, 130.42, 130.83, 131.58, 133.42, 133.53, 136.10, 143.14, 146.39, 154.63, 166.94, 189.53, 196.4; ^{31}P NMR (161.9 MHz, $CDCl_3$): δ (ppm) 11.26; Anal. Calcd for [**60**] $C_{38}H_{28}N_2O_5PRe$: C, 56.36; H, 3.49; N, 3.46. Found C, 56.62; H, 3.70; N, 3.47; UV-Vis (CH_2Cl_2) λ_{max}/nm (ε / L mol^{-1} cm^{-1}): 491 (36 600), 302 (sh, 11 100), 262 (sh, 18 100); MALDI-MS: *m/z* = 809.2 ([M$^+$]); IR (cm^{-1}): 723 (m), 750 (m), 829 (m), 893 (w), 993 (s), 1036 (s), 1099 (w), 1240 (m), 1277 (m), 1342 (m), 1381 (m), 1541 (m), 1727 (m), 1880 (s), 1913 (s), 2015 (s).

*Synthesis of **62***, via Method B

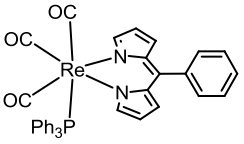

Purification for this complex was achieved by dissolving the crude product in minimal hexane/CH_2Cl_2 (1/2) and loading onto neutral deactivated alumina and eluting with CH_2Cl_2/hexane (1/7). The gradient was gradually increased to CH_2Cl_2/hexane (1/5). Further purification was achieved by recrystallisation from hot hexane and CH_2Cl_2. Yield: 37%. ^{1}H NMR (500 MHz, $CDCl_3$, 25 °C): δ (ppm) 6.29 (d, *J* = 4.4 Hz, 2H), 6.40 (d, *J* = 4.4 Hz, 2H), 6.53 (d, *J* = 7.6 Hz, 1H), 6.93 (m, 6H), 7.24 (m, 7H), 7.36 (m, 6H), 7.68 (m, 2H); ^{13}C NMR (125 MHz, $CDCl_3$): δ (ppm) 118.59, 126.69, 127.06, 128.00, 128.32, 128.39, 129.70, 129.91, 130.24, 130.56, 130.88, 131.87, 133.45, 133.54, 136.68, 138.54, 147.84, 154.21 196.51; ^{31}P NMR (161.9 MHz, $CDCl_3$): δ (ppm) 19.80; Anal. Calcd for [**62**] ($C_{36}H_{26}N_2O_3PRe$): C, 57.51; H, 3.49; N, 3.73. Found: C, 57.22; H, 3.45; N, 3.70; UV-Vis (CH_2Cl_2) λ_{max} (ε / L mol^{-1} cm^{-1}): 489 (38 100), 316 (sh, 7 400), 270 (sh, 13 900); ESI-MS (+ve mode): 753.8 *m/z* ([M + H]); IR (cm^{-1}): 697 (m), 722 (m), 744 (s), 773 (w), 837 (w), 872 (w), 885 (w), 993 (s), 1030 (s), 1091 (w), 1193 (w), 1206 (w), 1240 (m), 1341 (m), 1379 (m), 1407 (w), 1435 (w), 1544 (s), 1890 (s), 1909 (s), 2010 (s).

*Synthesis of **63***, via Method A

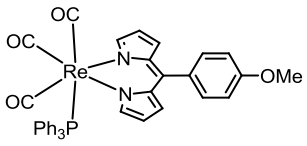

Purification for this complex was achieved by dissolving the crude product in CH_2Cl_2 and adsorbing to neutral deactivated alumina and eluting with CH_2Cl_2/hexane (1/7). The gradient was gradually increased to CH_2Cl_2/hexane (1/5). Further purification was achieved by recrystallisation from hot hexane and CH_2Cl_2. Yield: 49%. ^{1}H NMR (500 MHz, $CDCl_3$, -10 °C): δ (ppm) 3.86 (s, 3H), 6.30 (dd, *J* = 1.5, 4.4 Hz, 2H), 6.36 (dd, *J* = 2.4, 8.4 Hz, 1H), 6.46 (dt, *J* = 1.5, 4.4 Hz, 2H), 6.79 (dd, *J* = 2.4, 8.4 Hz, 1H), 6.89 (m, 7H), 7.23 (td, *J* = 2.2, 8.0 Hz, 6H), 7.30 (dd, *J* = 2.4, 8.4 Hz, 1H), 7.35 (m, 3H), 7.69 (d, *J* = 1.5 Hz, 2H); ^{13}C NMR (125 MHz, $CDCl_3$): δ (ppm) 55.32, 112.32, 118.46, 128.30, 128.37, 128.88, 128.89, 130.57, 130.90, 131.02, 131.84, 133.45, 133.54, 137.00, 147.90, 154.03, 159.54, 196.51; ^{31}P NMR (161.9 MHz, $CDCl_3$): δ (ppm) 11.31; Anal. Calcd for [**63**] ($C_{37}H_{28}N_2O_4PRe$) · $0.25C_6H_{14}$: C, 57.56; H, 3.95; N, 3.49. Found: C, 57.32; H, 3.66; N, 3.64; UV-Vis (CH_2Cl_2) λ_{max} / nm (ε / L mol^{-1} cm^{-1}): 488 (37 700), 357 (5 700), 274 (13 700); ESI-MS (+ve mode): 783.7 *m/z* ([M + H]); IR (cm^{-1}): 694 (m), 729 (m), 750 (m), 769 (m), 820 (m), 888 (w), 993 (s), 1034 (s), 1092 (w), 1175 (m), 1239 (s), 1290 (w), 1340 (m), 1379 (m), 1410 (w), 1434 (w), 1537 (m), 1883 (s), 1910 (s), 2013 (s).

*Synthesis of **64***, via Method A

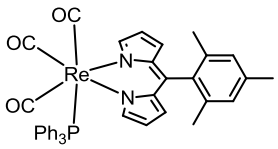

Yield: 93%. ^{1}H NMR (500 MHz, $CDCl_3$, 25 °C): δ (ppm) 1.63 (s, 3H), 1.94 (s, 3H), 2.33 (s, 3H), 6.18 (dd, *J* = 1.5, 4.4 Hz, 2H), 6.37 (dt, *J* = 1.5, 4.4 Hz, 2H), 6.82 (s, 1H), 6.86 (s, 1H), 7.04 (m, 6H), 7.23 (tt, *J* = 2.0, 6.5 Hz, 6H), 7.33 (m, 3H), 7.47 (d, *J* = 1.5 Hz, 2H); ^{13}C NMR (125 MHz, $CDCl_3$): δ (ppm) 19.40, 19.57, 21.08, 118.73, 127.30, 127.66, 128.29, 128.37, 129.96, 130.15, 130.74, 131.07, 133.64, 133.72, 135.23, 135.73, 136.03, 137.01, 137.06, 146.98, 153.96; ^{31}P NMR (161.9 MHz, $CDCl_3$): δ (ppm) 12.97; Anal. Calcd for [**64**] ($C_{39}H_{32}N_2O_3PRe$): C, 59.00; H, 4.06; N, 3.49. Found: C, 59.28; H, 4.20; N, 3.53; UV-Vis (CH_2Cl_2) λ_{max} (ε / L mol^{-1} cm^{-1}): 490 (42 100), 280 (11 600); ESI-MS (+ve mode): 833.7 *m/z* ([M + K]); IR (cm^{-1}): 695 (m), 723 (m), 729 (m), 746 (m), 772 (m), 836 (m), 864 (w), 887 (w), 993 (s), 1031 (s), 1092 (w), 1194 (w), 1244 (m), 1342 (m), 1378 (m), 1409 (w), 1436 (w), 1548 (s), 1885 (s), 1916 (s), 2012 (s).

*Synthesis of **65**,* via Method A

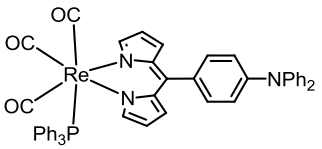

Purification for this complex was achieved by dissolving the crude product in CH_2Cl_2 and adsorbing to neutral deactivated alumina and then eluting with CH_2Cl_2/hexane (1/7). Further purification was achieved by recrystallisation from hot hexane and CH_2Cl_2. Yield: 36%. ^{1}H NMR (500 MHz, $CDCl_3$, -10 °C): δ (ppm) 6.26 (dd, *J* = 2.0, 8.30 Hz, 1H), 6.34 (dd, *J* = 1.50, 4.40 Hz, 2H), 6.56 (dt, *J* = 1.50, 4.40 Hz, 2H), 6.84 (m, 6H), 6.91 (dd, *J* = 2.0, 8.30 Hz, 1H), 7.03 (dd, *J* = 2.0, 8.30 Hz, 1H), 7.08 (t, *J* = 7.3 Hz, 2H), 7.16 (m, 4H), 7.22 (m, 7H), 7.32 (m, 7H), 7.69 (d, *J* = 1.5 Hz, 2H); ^{13}C NMR (125 MHz, $CDCl_3$): δ (ppm) 118.43, 123.34, 124.86, 128.28, 128.36, 129.41 129.88, 129.89, 130.55, 130.88, 131.78, 132.19, 133.44, 133.53, 136.82, 147.51, 147.83, 148.01, 153.98, 196.43; ^{31}P NMR (161.9 MHz, $CDCl_3$): δ (ppm) 11.35; Anal. Calcd for [**65**] ($C_{48}H_{35}N_3O_3PRe$) · $0.33C_6H_{14}$: C, 63.55; H, 3.92; N, 4.66. Found: C, 63.36; H, 4.22; N, 4.44; UV-Vis (CH_2Cl_2) λ_{max} (ε / L mol^{-1} cm^{-1}): 490 (40 500), 302 (34 800); ESI-MS (+ve mode): 920.7 *m/z* ([M + H]); IR (cm^{-1}): 697 (s), 717 (m), 733 (m), 758 (m), 821 (m), 889 (w), 994 (s), 1035 (s), 1092 (w), 1192 (m), 1239 (m), 1282 (w), 1331 (m), 1341 (m), 1379 (m), 1409 (m), 1435 (w), 1486 (m), 1533 (m), 1590 (m), 1881 (s), 1912 (s), 2011 (s).

*Synthesis of **66**,* via Method B

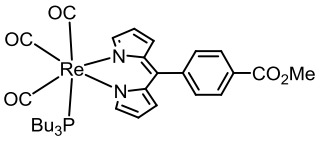

Purification for this complex was achieved by dissolving the crude product in CH_2Cl_2/hexane (1/4) and loading onto neutral deactivated alumina and eluting with CH_2Cl_2/hexane (1/7). The gradient was gradually increased to CH_2Cl_2/hexane (1/3). Further purification was achieved by recrystallisation from hot hexane and CH_2Cl_2. Yield: 78%. ^{1}H NMR (500 MHz, $CDCl_3$, 25 °C): δ (ppm) 0.83 (t, *J* = 7.1 Hz, 9H), 1.12 (m, 12H), 1.43 (m, 6H) 3.97 (s, 3H), 6.40 (dd, *J* = 1.4, 4.4 Hz, 2H), 6.50 (d, *J* = 1.1, 4.4 Hz, 2H), 7.37 (d, *J* = 7.9 Hz, 1H), 7.55 (d, *J* = 7.9 Hz, 1H), 7.96 (q, *J* = 1.4 Hz , 2H), 8.10 (m, 2H); ^{13}C NMR (125 MHz, $CDCl_3$): δ (ppm) 13.59, 23.47, 23.66, 24.43, 24.53, 25.09, 25.11, 52.32, 118.68, 128.40, 128.63, 129.68, 130.11, 130.65, 131.38, 136.12, 143.30, 146.05, 154.66, 166.75, 196.69; ^{31}P NMR (161.9 MHz, $CDCl_3$): δ (ppm) -7.60; Anal. Calcd for [**66**] ($C_{32}H_{40}N_2O_5PRe$): C, 51.26; H, 5.38; N, 3.74. Found: C, 51.37; H, 5.37; N, 3.74; UV-Vis (CH_2Cl_2) λ_{max} (ε / L mol^{-1} cm^{-1}): 485 (36 400), 303 (8 700); ESI-MS (+ve

mode): 789.8 *m/z* ([M+K]); IR (cm^{-1}): 727 (m), 759 (w), 781 (w), 832 (w), 893 (w), 966 (w), 986 (m), 994 (m), 1034 (s), 1112 (w), 1194 (w), 1241 (m), 1282 (m), 1343 (m), 1378 (m), 1410 (m), 1436 (w), 1539 (m), 1569 (m), 1609 (w), 1723 (m), 1881 (s), 1910 (s), 2010 (s), 2873 (w), 2934 (w), 2960 (w).

*5.3.2.3 Synthesis of [Re**L**$(CO)_2(PR_3)$ (PR'_3)], **67-73***

Both conventional and microwave heating methods (as outlined below) have been developed in the synthesis of **67-73** (Figure 5.5). The synthesis and purification of **70** was established by previous members of the group and is outlined in the literature.[32] These characterisation data have been included here for comparison purposes.

Conventional method (method C)

[Re**L**$(CO)_3PR_3$] (0.027 mmol) and PR_3 (PPh_3 or n-PBu_3) (~2.5 equiv.) were combined in dry toluene (11 mL). The reaction was heated to 100 °C for ~48 hours. The reaction was monitored by TLC to check for the disappearance of [Re**L**$(CO)_3PR_3$]. All volatiles were removed under reduced pressure and the crude product was obtained as a red or brown solid by chromatography on deactivated neutral alumina.

Microwave method (method D)

[Re**L**$(CO)_3PR_3$] (0.185 mmol) and PR_3 (PPh_3 or n-PBu_3) (~5.5 equivalents) were combined in dry toluene (5 mL). The reaction was heated to 130 °C for 45 mins in a microwave synthesizer (closed vessel mode, power = 200 W, pressure = 250 psi). All volatiles were removed under reduced pressure and the crude product was obtained as a red or brown solid by chromatography on deactivated neutral alumina.

*Synthesis of **67**,* via Method C

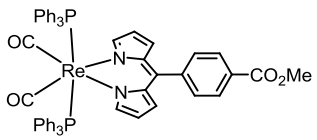

Purification for this complex was achieved by dissolving the crude product in CH_2Cl_2 and adsorbing to neutral deactivated alumina and then eluting with CH_2Cl_2/hexane (1/7). Further purification was achieved by recrystallisation from hot hexane and CH_2Cl_2. Yield: 49%. ^{1}H NMR (500 MHz, $CDCl_3$, 25 °C): δ (ppm) 3.97 (s, 3H), 5.84 (dd, *J* = 1.3, 4.3

Hz, 2H), 6.07 (dd, *J* = 1.3, 4.3 Hz, 2H), 6.93 (d, *J* = 8.3 Hz, 2H), 7.09 (m, 14H), 7.17 (t, *J* = 7.4 Hz, 12H), 7.25 (t, *J* = 7.4 Hz, 6H), 7.98 (d, *J* = 8.3 Hz, 2H); ^{13}C NMR (125 MHz, $CDCl_3$): δ (ppm) 52.30, 118.77, 127.77, 127.81, 127.84, 128.17, 129.01, 129.43, 129.90, 130.40, 133.10, 133.22, 133.44, 133.58, 133.61, 133.66, 135.22, 144.04, 144.46, 153.87, 166.93, 203.90; ^{31}P NMR (161.9 MHz, $CDCl_3$): δ (ppm) 19.79; Anal. Calcd for [**67**] ($C_{55}H_{43}N_2O_4P_2Re$): C, 63.27; H, 4.15; N, 2.68. Found: C, 63.24; H, 4.19; N, 2.54; UV-Vis (CH_2Cl_2) λ_{max} / nm (ε / L mol^{-1} cm^{-1}): 480 (25 500), 307 (16 300); ESI-MS(+ve mode): 1045.7 *m/z* ([M + H]); IR (cm^{-1}): 693 (s), 723 (m), 746 (m), 827 (m), 893 (w), 990 (s), 1032 (s), 1092 (m), 1193 (w), 1243 (s), 1274 (m), 1343 (m), 1378 (m), 1410 (w), 1433 (m), 1482 (w), 1550 (m), 1724 (m), 1836 (s), 1912 (s).

*Synthesis of **68***, via Method D

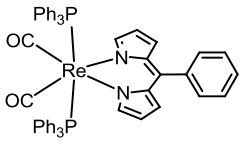

Purification for this complex was achieved by dissolving the crude product in hexane/CH_2Cl_2 (1/2) and loading onto neutral deactivated alumina and eluting with CH_2Cl_2/hexane (1/7). The gradient was gradually increased to CH_2Cl_2/hexane (1/3). Further purification was achieved by recrystallization from hot hexane and CH_2Cl_2. Yield: 80%. ^{1}H NMR (500 MHz, $CDCl_3$, 25 °C): δ (ppm) 5.81 (d, *J* = 4.2 Hz, 2H), 6.13 (d, *J* = 4.2 Hz, 2H), 6.89 (d, *J* = 7.8 Hz, 2H), 7.03 (s, 2H), 7.10 (m, 12H), 7.16 (t, *J* = 7.8 Hz, 12H), 7.23 (m, 6H), 7.30 (m, 2H), 7.35 (m, 1H); ^{13}C NMR (125 MHz, $CDCl_3$): δ (ppm) 118.36, 126.75, 127.56, 127.73, 127.76, 127.80, 128.92, 129.84, 130.72, 133.19, 133.36, 133.53, 133.60, 133.64, 133.68, 135.80, 139.34, 145.82, 153.47; ^{31}P NMR (161.9 MHz, $CDCl_3$): δ (ppm) 19.86; Anal. Calcd for [**68**] ($C_{53}H_{41}N_2O_2P_2Re$) · $3H_2O$: C, 61.20; H, 4.55; N, 2.69. Found: C, 61.16; H, 4.28; N, 4.66; UV-Vis (CH_2Cl_2) λ_{max} (ε / L mol^{-1} cm^{-1}): 481 (27 300), 312 (14 600); ESI-MS (+ve mode): 986.8 *m/z* ([M$^+$]); IR (cm^{-1}): 695 (s), 721 (m), 743 (m), 771 (w), 836 (w), 993 (m), 1031 (s), 1093 (w), 1195 (w), 1244 (m), 1282 (w), 1343 (m), 1378 (m), 1410 (w), 1432 (w), 1481 (w), 1552 (m), 1827 (s), 1906 (s).

*Synthesis of **69***, via Method D

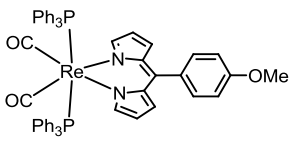

Purification for this complex was achieved by dissolving the crude product in CH_2Cl_2 and adsorbing to neutral deactivated alumina and then eluting with CH_2Cl_2/hexane (1/7). Further purification was achieved by recrystallisation from hot hexane and CH_2Cl_2. The

gradient was gradually increased to CH_2Cl_2/hexane (1/4). Yield: 86%. ^{1}H NMR (500 MHz, $CDCl_3$, 25 °C): δ (ppm) 3.87 (s, 3H), 5.83 (dd, *J* = 1.3, 4.2 Hz, 2H), 6.20 (d, *J* = 4.2 Hz, 2H), 6.83 (m, 4H), 7.04 (s, 2H), 7.09 (m, 12H), 7.16 (t, *J* = 7.4 Hz, 12H), 7.23 (t, *J* = 7.4 Hz, 6H); ^{13}C NMR (125 MHz, $CDCl_3$): δ (ppm) 55.32, 112.21, 118.24, 127.71, 127.75, 127.78, 128.91, 130.71, 131.71, 131.85, 133.21, 133.38, 133.55, 133.61, 133.65, 133.69, 136.16, 145.87, 153.41, 159.28, 204.03; ^{31}P NMR (161.9 MHz, $CDCl_3$): δ (ppm) 19.76; Anal. Calcd for [**69**] ($C_{54}H_{43}N_2O_3P_2Re$) · $3H_2O$: C, 60.65; H, 4.44; N, 2.57. Found: C, 60.61; H, 4.62; N, 2.62. UV-Vis (CH_2Cl_2) λ_{max} (ε / L mol^{-1} cm^{-1}): 481 (25 400), 321 (12 200); ESI-MS (+ve mode) 1016.6 *m/z* ([M$^+$]); IR (cm^{-1}): 695 (s), 727 (m), 771 (w), 803 (m), 813 (m), 887 (w), 899 (w), 994 (m), 1030 (m), 1093 (m), 1172 (w), 1248 (m), 1292 (w), 1343 (m), 1377 (m), 1410 (w), 1432 (w), 1481 (w), 1554 (m), 1610 (w), 1822 (s), 1904(s).

*Synthesis of **70***, via Method C

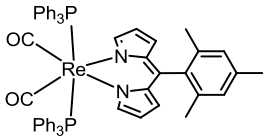

Yield: 95% ^{1}H NMR (500 MHz, $CDCl_3$, 25 °C): δ (ppm) 1.57 (s, 6H), 2.30 (s, 3H), 5.87 (d, *J* = 5.0 Hz, 2H), 6.14 (d, *J* = 5.0 Hz, 2H), 6.78 (s, 2H), 6.99 (t, *J* = 5.0 Hz, 2H), 7.06 (m, 12H), 7.15 (t, *J* = 10.0 Hz, 12H), 7.22 (t, *J* = 10.0 Hz, 6H); ^{13}C NMR (125 MHz, $CDCl_3$): δ (ppm) 19.64, 21.01, 29.71, 118.88, 127.41, 127.74, 127.78, 128.95, 133.16, 133.33, 133.85, 133.89, 133.93, 135.00, 135.83, 136.60, 153.42, 194.83; ^{31}P NMR (161.9 MHz, $CDCl_3$): δ (ppm) 18.89; Anal. Calcd for [**70**] ($C_{56}H_{47}N_2O_2P_2Re$) · $0.25CH_2Cl_2$ · $0.33C_6H_{14}$: C, 64.89; H, 4.87; N, 2.60. Found: C, 64.63; H, 5.05; N, 2.53; UV-Vis (CH_2Cl_2) λ_{max} (ε / L mol^{-1} cm^{-1}): 487 (27 600), 315 (12 600); ESI-MS (+ve mode): 1067.7 *m/z* ([M + K]); IR (cm^{-1}): 696 (s), 741 (m), 774 (w), 834 (m), 864 (w), 885 (w), 985 (m), 1030 (m), 1090 (w), 1193 (w), 1242 (m), 1343 (m), 1376 (m), 1410 (w), 1433 (w), 1481 (w), 1550 (m), 1834 (s), 1909 (m).

*Synthesis of **71***, via Method D

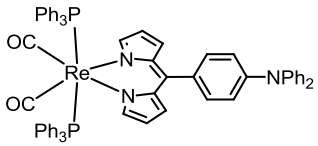

Purification for this complex was achieved by dissolving the crude product in CH_2Cl_2 and adsorbing to neutral deactivated alumina and then eluting with CH_2Cl_2/hexane (1/7). Further purification was achieved by recrystallisation from hot hexane and CH_2Cl_2. Yield: 59%. ^{1}H NMR (500 MHz, $CDCl_3$, 25 °C): δ (ppm) 5.88 (dd, *J* = 1.4, 4.3 Hz, 2H), 6.32

(d, *J* = 4.3 Hz, 2H), 6.78 (d, *J* = 6.6 Hz, 2H), 7.01 (d, J = 8.6 Hz, 2H), 7.07 (m, 2H), 7.10 (m, 14H), 7.17 (t, *J* = 7.4 Hz, 16H), 7.24 (t, *J* = 7.7 Hz, 6H), 7.32 (m, 4H); ^{13}C NMR (125 MHz, $CDCl_3$): δ (ppm) 118.21, 121.40, 123.17, 124.70, 127.73, 127.77, 127.80, 128.94, 129.40, 130.67, 130.96, 133.20, 133.25, 133.54, 133.62 133.66, 133.70, 135.96, 145.94, 147.39, 147.67, 153.34; ^{31}P NMR (161.9 MHz, $CDCl_3$): δ (ppm) 19.80; Anal. Calcd for [**71**] ($C_{65}H_{50}N_3O_2P_2Re$): C, 67.69; H, 4.37; N, 3.64. Found: C, 67.55; H, 4.42; N, 3.73; UV-Vis (CH_2Cl_2) λ_{max} (ε / L mol^{-1} cm^{-1}): 481 (27 200), 303 (39 500); IR (cm^{-1}): 695 (s), 722 (m), 808 (m), 889 (w), 986 (s), 1023 (s), 1091 (w), 1180 (w), 1194 (w), 1245 (m), 1282 (w), 1342 (m), 1379 (m), 1410 (w), 1432 (w), 1485 (w), 1543 (m), 1589 (w), 1832 (s), 1907 (m).

*Synthesis of **72***, via Method D

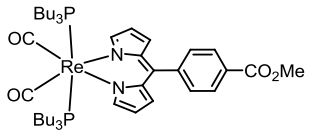

Purification for this complex was achieved by dissolving the crude product in minimal hexane/CH_2Cl_2 (2/1) and loading onto neutral deactivated alumina and eluting with CH_2Cl_2/hexane (1/7). Yield: 92%. ^{1}H NMR (500 MHz, $CDCl_3$, 25 °C): δ (ppm) 0.82 (t, *J* = 7.1 Hz, 18H), 1.19 (m, 24H), 1.45 (m, 12H) 3.96 (s, 3H), 6.35 (dd, *J* = 1.3, 4.4 Hz, 2H), 6.43 (dd, *J* = 1.3, 4.3 Hz, 2H), 7.39 (d, *J* = 8.2 Hz, 2H), 7.95 (t, *J* = 1.3 Hz, 2H), 8.08 (d, *J* = 8.2 Hz, 2H); ^{13}C NMR (125 MHz, $CDCl_3$): δ (ppm) 13.71, 24.51, 24.55, 24.60, 25.00, 25.11, 25.15, 25.20, 52.26, 118.18, 128.42, 129.77, 130.06, 130.37, 135.88, 144.08, 144.62, 153.59, 166.84, 204.32; ^{31}P NMR (161.9 MHz, $CDCl_3$): δ (ppm) -5.87; Anal. Calcd for [**72**] ($C_{43}H_{67}N_2O_4P_2Re$): C, 55.88; H, 7.31; N, 3.03. Found: C, 56.16; H, 7.57; N, 2.87; UV-Vis (CH_2Cl_2) λ_{max} (ε / L mol^{-1} cm^{-1}): 474 (40 900), 300 (9 500); MALDI-MS: 924.51 *m/z* ([M$^+$]); IR (cm^{-1}): 723 (m), 760 (m), 774 (w), 826 (w), 873 (w), 893 (w), 985 (m), 1027 (s), 1097 (w), 1111 (w), 1191 (w), 1209 (w), 1240 (m), 1275 (m), 1340 (m), 1376 (m), 1407 (w), 1436 (w), 1544 (m), 1569 (w), 1610 (w), 1729 (m), 1825 (s), 1903 (s), 2871 (w), 2932 (w), 2957 (w).

*Synthesis of **73***, via Method D

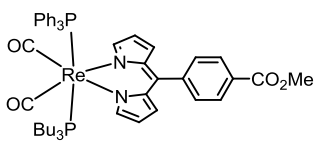

Purification for this complex was achieved by dissolving the crude product in ethyl acetate/hexane (1/1) and loading onto neutral deactivated alumina then eluting with ethyl acetate/hexane (1/40). Further purification was achieved by recrystallisation from hot

methanol and H_2O. Yield: 47%. ^{1}H NMR (500 MHz, $CDCl_3$, 25 °C): δ (ppm) 0.83 (t, *J* = 6.7 Hz, 9H), 1.21 (m, 12H), 1.52 (m, 6H), 4.00 (s, 3H), 6.14 (dd, *J* = 1.3, 4.4 Hz, 2H), 6.28 (dd, *J* = 1.3, 4.4 Hz, 2H), 7.03 (dd, *J* = 1.8, 7.9 Hz, 1H), 7.12 (m, 6H), 7.21 (m, 6H), 7.26 (m, 3H), 7.35 (dd, *J* = 1.8, 7.9 Hz, 1H), 7.54 (t, *J* = 1.3 Hz, 2H), 8.06 (m, 2H); ^{13}C NMR (125 MHz, $CDCl_3$): δ (ppm) 13.66, 24.46, 24.55, 24.88, 25.09, 52.26, 118.48, 127.73, 127.80, 128.29, 128.33, 128.86, 129.61, 129.80, 130.14, 130.40, 130.49, 133.57, 133.89, 135.56, 144.03, 144.51, 153.76; ^{31}P NMR (161.9 MHz, $CDCl_3$): δ (ppm) 21.46, 20.19, -4.70, -5.92; Anal. Calcd for [**73**] ($C_{49}H_{55}N_2O_4P_2Re$): C, 59.80; H, 5.63; N, 2.85. Found: C, 59.79; H, 5.60; N, 2.86; UV-Vis (CH_2Cl_2) λ_{max} (ε / L mol^{-1} cm^{-1}): 474 (32 200), 301 (14 000); MALDI-MS: 984.4 *m/z* ([M+]); IR (cm^{-1}): 723 (m), 760 (m), 774 (w), 826 (w), 873 (w), 893 (w), 985 (m), 1027 (s), 1097 (w), 1111 (w), 1191 (w), 1209 (w), 1240 (m), 1275 (m), 1340 (m), 1376 (m), 1407 (w), 1436 (w), 1544 (m), 1569 (w), 1610 (w), 1729 (m), 1825 (s), 1903 (s), 2871 (w), 2932 (w), 2957 (w).

*5.3.2.4 Photochemical synthesis of [Re**L**(CO)$_2$(PPh$_3$)(CD$_3$CN)],* **74**

60 (~ 0.0070 g, ~ 8.6 μmol) was dissolved (with sonication) in CD_3CN (~ 0.8 mL). The sample was irradiated (with stirring) using 355 nm excitation from a Quantel Brilliant B Nd:YAG pulsed laser (10 ns pulses) with a power output of 40-45 mW for 2-2.5 hours. The sample was half wrapped in aluminium foil to improve the efficiency of the reaction. The progress of the reaction was monitored by ^{1}H NMR, UV-Vis and IR spectroscopy. After 2.5 hours ~ 95% conversion was observed by NMR. Exhaustive attempts to isolate the product for a full characterisation were made, however the product is unstable. ^{1}H NMR (500 MHz, CD_3CN, 25 °C): δ (ppm) 3.92 (s, 3H), 6.15 (dd, *J* = 1.3, 4.1 Hz, 2H), 6.22 (dd, *J* = 0.9, 4.4 Hz, 2H), 7.07 (m, 6H), 7.10 (d, *J* = 7.1 Hz, 1H), 7.22 (td, *J* = 1.6, 7.2 Hz, 6H), 7.28 (tq, *J* = 1.3, 7.1 Hz, 3H), 7.44 (dd, *J* = 2.0, 8.8 Hz, 1H), 7.62 (s, 2H), 8.02 (d, *J* = 8.4 Hz, 2H); ^{13}C NMR (125 MHz, CD_3CN): δ (ppm) 51.89, 118.32, 127.81, 127.89, 128.06, 128.13, 129.18, 129.86, 130.13, 130.27, 130.56, 131.66, 131.74, 133.06, 133.13, 134.72, 135.10, 135.71, 143.66, 145.68, 153.83, 159.68, 166.52, 203.13; ^{31}P NMR (161.9 MHz, CD_3CN_3): δ (ppm) 29.92; UV-Vis (CD_3CN) λ_{max}: 472, 300; IR (cm^{-1}) (C≡O only): 1833 (s), 1913 (s).

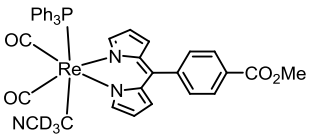

5.3.3 General procedures

5.3.3.1 Resonance Raman solutions

The weak fluorescence of the Re(I)-dipyrrinato complexes did not prevent resonance Raman measurements. Solutions of the Re(I)-dipyrrinato complexes were prepared in dichloromethane with concentrations ranging between 367 – 778 μM for resonant Raman measurements at excitation wavelengths of 458 nm, 488 nm, and 514.5 nm. Only 458 nm and 488 nm wavelengths are presented in this thesis.

5.3.3.2 Fluorescence protocol

All samples were subjected to 3-4 freeze pump thaw (FPT) cycles to removed dissolved oxygen before the emission spectrum was recorded. Fluorescence cells were dried, fitted with a septum, and purged with argon, before the sample was introduced. For complexes **59**-**60** and **62**-**65** an excitation wavelength of 485 nm was used with slit widths of 7 nm. For complexes **66** and **70**, an excitation wavelength of 480 nm was used with slit widths of 10 nm.

5.3.3.3 Relative quantum yield measurements

With an emission maximum of ~640 nm cresyl violet perchlorate is an ideal standard for emission in the red region of the spectrum. The absolute quantum yield of cresyl violet was reported at room temperature, in a variety of solvents, using multiple techniques with an average quantum yield of 0.54 ± 0.03.[288, 289] This value is reported to be insensitive to oxygen.[288]

Relative quantum yields were determined in dichloromethane relative to cresyl violet in methanol (Φ_F = 0.54 ± 0.03, excitation 540 nm)[288], using equation 1.10:

$$\Phi_{F(X)} = \left(\frac{A_S}{A_X}\right)\left(\frac{F_X}{F_S}\right)\left(\frac{n_X}{n_S}\right)^2 \Phi_{F(S)} \qquad (1.10)$$

where Φ_F is the emission quantum yield, *A* is the absorbance at the excitation wavelength, *F* is the area under the emission curve, and *n* is the refractive index of the solvents used. The subscripts s and x refer to the standard and the unknown, respectively.

A solution of cresyl violet (2 mg) was prepared in methanol (500 mL). This solution was diluted 10-fold and the absorbance value at the excitation wavelength (540 nm) was typically recorded as ~ 0.037, followed by a further dilution (4 mL into 100 mL) to give a typical absorbance value of ~ 0.0015. This solution was used for quantum yield measurements. The relatively large slit widths required for a respectable emission spectrum of the Re(I)-dipyrrinato complexes proved problematic when measuring the emission spectrum of the standard. To avoid saturating the detector on the fluorimeter, the absorbance of the cresyl violet had to be significantly below the ideal 0.04 – 0.05 absorbance units.

Typically, the ideal absorbance for fluorescence measurements is between 0.04 – 0.05. This absorbance is best achieved by obtaining a solution around 0.5 absorbance units followed by a careful 10-fold dilution.[143] However, owing to the extremely low emission intensity from the Re(I)-dipyrrinato complexes the optimum absorbance was determined to be around 0.1 ± 0.02 after FPT cycles. At these absorbance values we can possibly expect that the emission intensity is no longer proportional to the concentration of the sample. This can result in lower emission intensities as a result of self-absorption. [Self-absorption occurs at higher concentrations where the analyte can absorb some of the emission]. The Re(I)-dipyrrinato samples were all prepared in dichloromethane for the relative quantum yield measurements.

The emission quantum yields could not be measured using the integrating sphere attachment of the fluorimeter due to the very weak emission intensity of these complexes combined with the number of reflections which take place in an integrating sphere before the photons reach the detector.

5.3.3.4 Quenching studies

After recording the emission spectra of **60** and **62-65** 2 mL of air was pumped into each sample using a syringe and needle, and the emission spectrum was re-recorded.

A solution of methyl viologen (49 mg, 0.19 mmol, Sigma) was prepared in methanol (25 mL). Each Re(I)-dipyrrinato complex was prepared in methanol and the dissolved oxygen removed by FPT cycles. 3 mL of each sample was injected into the argon-filled fluorescence cell (fitted with a septum). Using Beer's Law (A = 0.1 ± 0.02), the concentration of each complex was determined (after FPT cycles) and therefore the number of moles of the complex were determined. After recording the emission spectra

of **60** and **62-65** in methanol, methyl viologen was titrated into the sample using a 25 μL syringe. After each titration, the sample was mixed via gentle shaking and the emission spectrum re-recorded. Titrations were continued until the emission was quenched.

From the fluorescence intensity and using (5.1):[290, 291]

$$\frac{\phi^0}{\phi} = 1 + K_{SV}[Q] \qquad (5.1)$$

the Stern-Volmer quenching constant, K_{SV}, could be obtained from the Stern-Volmer plots ($\frac{\phi^0}{\phi}$-1as a function of [Q]), where ϕ^0 is the quantum yield in the absence of methyl viologen and ϕ is the quantum yield in the presence of methyl viologen, and [Q] is the concentration of the methyl viologen.

5.3.3.5 Photochemical ligand substitution (PLS) reactions

A ModuLaser Stellar-Pro argon laser (458 nm, 488 nm, and 514.5 nm excitation), a Quantel Brilliant B Nd:YAG pulsed laser (355 nm excitation) and a mercury arc lamp (200 nm and 250 nm excitation) were all used as irradiation sources in the photochemical ligand substitution reactions of the Re(I)-dipyrrinato complexes. These sources typically provided 40-50mW of power at the sample.

5.4 Results and Discussion

5.4.1 Synthesis

The general synthetic routes to the three families of complexes ([$HNEt_3$][Re**L**$(CO)_3Cl$], [Re**L**$(CO)_3PR_3$], and [Re**L**$(CO)_2(PR_3)(PR'_3)$] where R and R' are either phenyl or n-butyl) are given in Figure 5.5. Each complex was obtained in moderate to excellent yields. Conducting these reactions using microwave irradiation rather than conventional heating shortened the reaction times and generally led to improved yields.

The reaction between [$Re(CO)_5Cl$], a dipyrrin ligand (**L**H), and triethylamine in hot toluene yields *fac*-[Re**L**$(CO)_3Cl$][$HNEt_3$] as a deeply coloured orange crystalline solid (Figure 5.5). This complex is formed by the displacement of two CO ligands from [$Re(CO)_5Cl$]. The dipyrrinato ligand coordinates in the *cis* position relative to the chloride ligand. These complexes show a tendency to decompose over a few weeks at

room temperature; therefore, these complexes were not isolated for each dipyrrin ligand. Rather, the *in situ* displacement of the chloride ligand in *fac*-[Re**L**$(CO)_3$Cl] [$HNEt_3$] by PR_3 (R = phenyl, n-butyl) in hot toluene was found to reliably produce *fac*-[Re**L**$(CO)_3PR_3$] complexes (Figure 5.5). These complexes can be isolated as orange/green dichroic crystals, which are stable at room temperature when stored in the dark. The addition of further PR'_3 (R' = phenyl, n-butyl) in hot toluene results in the displacement of the CO ligand *trans* to the coordinated phosphine ligand to produce [Re**L**$(CO)_2(PR_3)(PR'_3)$] (Figure 5.5) as crystalline red or brown solids. Typically, PR_3 = PR'_3; however, mixed phosphine complexes such as **73** can be prepared.

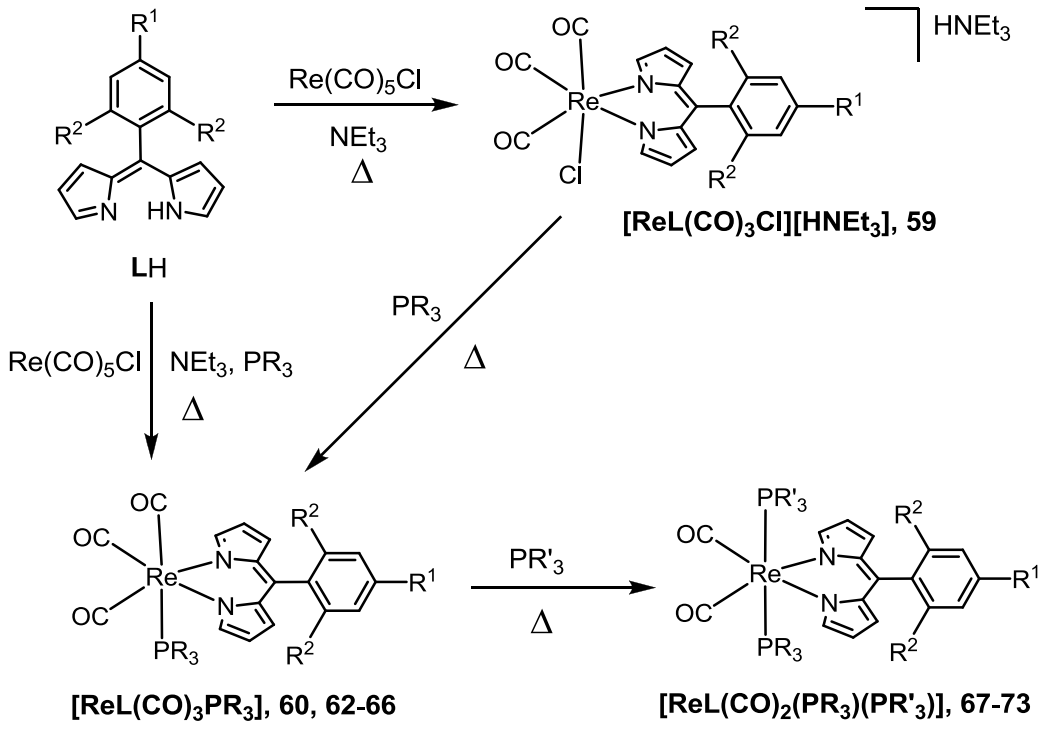

Figure 5.5. The synthetic routes to Re(I)-dipyrrinato complexes **59**-**60** and **62**-**73**.

The synthetic methodology that we have established for the Re(I)-dipyrrinato complexes shares similarities with Re(I)-bipyridine chemistry.[266, 292] For example, the reaction between [$Re(CO)_5Cl$] and bipyridine in hot toluene yields *fac*-[Re(bipy)$(CO)_3$Cl] and further reaction with a phosphine ligand (PR_3) furnishes *fac*-[Re(bipy)$(CO)_3PR_3]^+$. In the latter step Ag(I) salts are typically employed to assist in the displacement of the chloride ligand from [Re(bipy)$(CO)_3$Cl];[274, 280, 293] however, this is not required for the above Re(I)-dipyrrinato complexes. Synthetic routes to

$[Re(bipy)(CO)_2(PR_3)_2]^+$ complexes are highly varied, and both thermal and photochemical pathways have been employed from $[Re(bipy)(CO)_3Cl]$.[269, 272, 294-296] A two-step procedure employing both photochemical and thermal synthesis has been employed to efficiently obtain mixed phosphine products, $[Re(bipy)(CO)_2(PR_3)(PR'_3)]^+$.[269]

5.4.2 NMR spectroscopy

The structure of the *fac*-[Re**L**$(CO)_3PR_3$] complexes was determined in solution by ^{1}H NMR spectroscopy in $CDCl_3$. The ^{1}H NMR and ^{31}P NMR spectra of all the *fac*-[Re**L**$(CO)_3PR_3$] complexes are consistent with the anticipated C_s symmetry of these complexes.

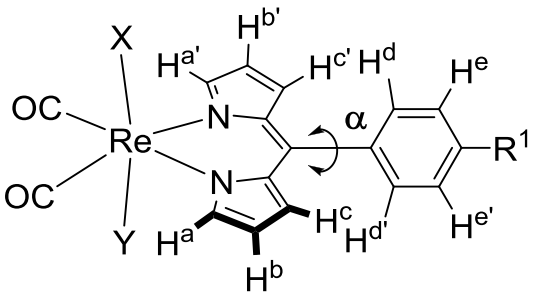

Figure 5.6. Labelling scheme adopted in the discussion of the ^{1}H NMR spectra of the Re(I)-dipyrrinato complexes. For complexes **60** and **62-66**, X = CO, Y = PR_3 and complexes **67-73**, X = PR_3 and Y = PR'_3. Note that protons $H^{d/d'}$ are replaced by methyl groups in **64** and **70**.

The average C_s symmetry is reflected by the magnetic equivalence of the H^{a-c} and $H^{a'-c'}$ protons (Figure 5.6). In all cases the six pyrrolic protons are observed as three sets of peaks; two peaks corresponding to four protons ($H^b/H^{b'}$ and $H^c/H^{c'}$) are found between 6.18 – 6.50 ppm and a third peak, corresponding to two protons ($H^a/H^{a'}$), is shifted downfield in the range 7.47 – 7.96 ppm. However, the chemical shifts of the phenyl ring protons of the dipyrrinato ligand are rather varied and distinctive for each complex. Rapid rotation of the phenyl ring (and hence magnetic equivalence of $H^d/H^{d'}$ and $H^e/H^{e'}$) is not observed in the NMR spectra for most of the complexes at room temperature (25 °C). This indicates that the transannular torsion angle (α) averages 90°, however, the phenyl ring most likely rocks about this angle. In the NMR spectra of **63** and **65**, the

phenyl ring resonances are broad and unresolved, which indicates that the phenyl ring rotation occurs on the NMR timescale in these cases. The rotation of the phenyl ring can be frozen out using low temperature NMR (-10 °C) to give four distinct peaks (Figure 5.7 and Figure E1). One of the phenyl ring protons ($H^{d'}$) of **60**, **62**-**63** and **65** experiences a significant upfield shift (to ~ 6.26 − 6.78 ppm) compared to the corresponding resonances in **59** and **66**. This is a consequence of its proximity to the π clouds of the PPh_3 ligand.

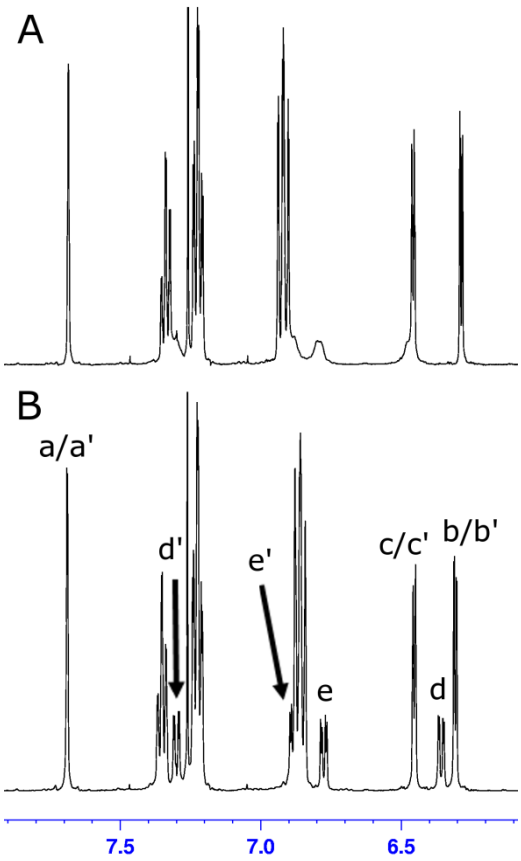

Figure 5.7. The aromatic region of the ^{1}H NMR spectrum of **63** in $CDCl_3$ at (A) room temperature (25 °C); and (B) low temperature (-10 °C). Labelling scheme is given in Figure 5.6. The unlabelled peaks correspond to the PPh_3 resonances.

The ^{1}H NMR and ^{31}P NMR spectra of the [Re**L**$(CO)_2(PR_3)(PR'_3)$] complexes (**67**-**73**) are consistent with their expected C_{2h} point group symmetry (Figure E2 for a representative example). With the exception of **73**, these complexes have two-fold rotational symmetry and therefore $H^{a-c}/H^{a'-c'}$ and $H^{d-e}/H^{d'-e'}$ are magnetically equivalent.

The symmetry in **73** is broken by the coordination of two different phosphine (PPh_3 and n-PBu_3) ligands. Therefore its ^{1}H NMR spectrum resembles the spectra of **60** and **62-66** (discussed above) where the protons $H^{a-c}/H^{a'-c'}$ are magnetically equivalent and protons $H^{d-e}/H^{d'-e'}$ give rise to four distinct peaks.

5.4.3 Electronic and vibrational spectroscopy and TD-DFT calculations

All complexes were further characterised in the solid state by IR spectroscopy (Table 5.1). Three strong bands are observed in the IR spectrum in the range 1880–2012 cm^{-1}, for **59-60** and **62-66** which is consistent with the facial disposition of the carbonyl ligands about a pseudo-octahedral metal centre.[297] These vibrations are assigned as a totally symmetric in-phase vibration, A′(1), an out-of-phase totally symmetric vibration, A′(2), and an out-of-phase anti-symmetric vibration A″ (Figure 5.8A).[298] For complexes **67-73**, two strong bands are observed between 1822–1912 cm^{-1} which parallels $[Re(bipy)(CO)_2(PPh_3)_2]^+$ and $[Re(bipy)(CO)_2(PR_3)_2]^+$ type complexes.[272, 294] These vibrations are assigned as an out-of-phase totally symmetric vibration, A′(2) and an out-of-phase anti-symmetric vibration A″ (Figure 5.8B). By comparison with related complexes,[43] all of the prominent peaks in the 1727 − 995 cm^{-1} region are attributable to vibrational modes of the dipyrrinato ligands and their functional groups.

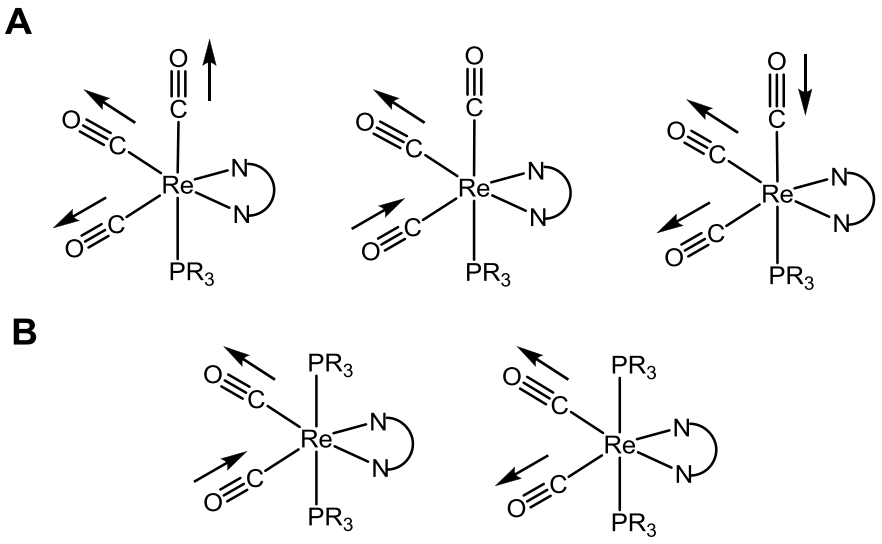

Figure 5.8. Vibrational modes of the carbonyl ligands in (A) [Re**L**$(CO)_3PR_3$] and (B) [Re**L**$(CO)_2(PR_3)_2$] complexes.

The electronic absorption spectra of **59**, **60**, and **67** are presented in Figure 5.9 as a representative selection of the complexes in each family. All complexes display an intense band centred between 480 – 491 nm (Table 5.1) which may be ascribed to an intraligand π–π* transition ($S_0 \rightarrow S_1$) on the dipyrrinato ligand but also involves some orbital contribution from the phenyl ring (refer to chapter 2 and chapter 4).[53, 92] The position of the π–π* absorption bands are similar to those observed for other dipyrrinato complexes and are relatively insensitive to the identity of the metal ion (refer to chapters 3 and 4).[24, 26, 42, 43, 48, 50, 88, 91] Exciton coupling[88] is not observed in these complexes since the complexes only contain a single dipyrrinato ligand. Some vibronic structure is apparent on the high energy side of the π–π* band, particularly for the complexes **59**-**60** and **62**-**66**. Vibronic structure is commonly observed as a shoulder on the high energy side of the dominant absorption feature for many other dipyrrinato complexes[26, 31, 88, 90] as well as BODIPY type complexes.[58]

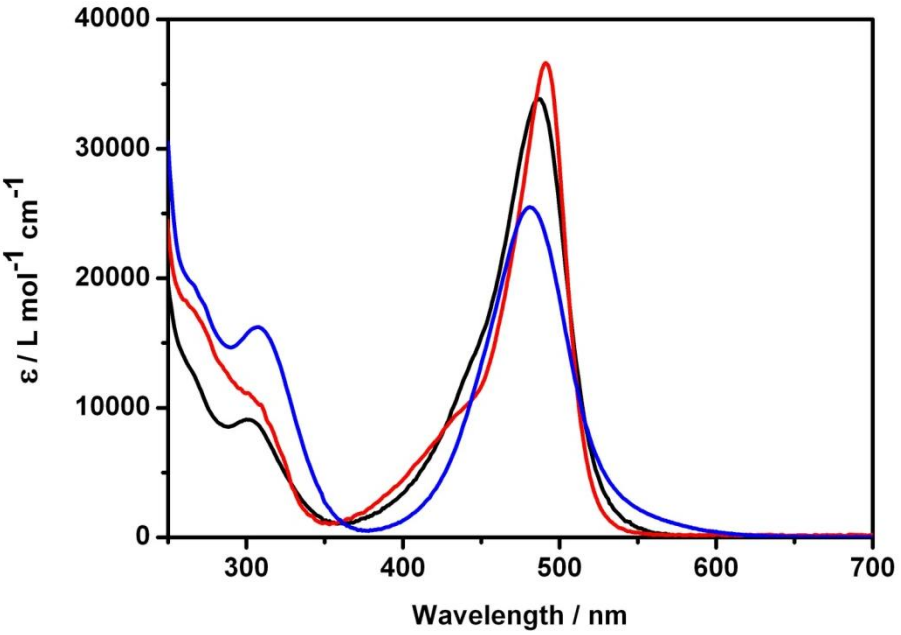

Figure 5.9. Representative absorbance spectra of each family of Re(I)-dipyrrinato complexes recorded in CH_2Cl_2; [Re**L**$(CO)_3$Cl][NEt_3H] (**59**, black), [Re**L**$(CO)_3PPh_3$] (**60**, red), and [Re**L**$(CO)_2(PPh_3)_2$] (**67**, blue).

There are subtle differences between the absorption spectra of [Re**L**$(CO)_3PR_3$] and [Re**L**$(CO)_2(PR_3)(PR'_3)$] complexes: the absorption band for the π–π* transition is broadened, slightly blue-shifted, and has a reduced intensity for [Re**L**$(CO)_2(PR_3)(PR'_3)$] complexes. There is also a clear trend in the absorption spectra of the complexes that

possess PBu_3 ligands (**66**, **72**, and **73**) where the π–π* transition is slightly blue-shifted with respect to their PPh_3 counterparts. The absorption spectrum of **66** parallels that of other [Re**L**$(CO)_3PR_3$] complexes in terms of peak intensity although the vibronic structure is less prominent in this case (Figure E3).

Minor peaks (or shoulders) are observed in the absorption spectra of the complexes around 300 nm. Similar spectral features have been observed for Ir(III)-dipyrrinato and certain BODIPYs complexes[50, 188] (including diphenylamino-substituted BODIPYs[299]) where this has been ascribed to a dipyrrin-centred $S_0 \rightarrow S_2$ transition. This assignment can be made for the Re(I)-dipyrrinato complexes on the basis of the excitation spectra (see later). The intensity of this $S_0 \rightarrow S_2$ transition is attributed to the rotation of the phenyl substituent where hindering the rotation of the phenyl ring reduces the probability of the transition.[188] However, only a minor peak or a shoulder is observed in the absorption spectra of all Re(I)-dipyrrinato complexes even in complexes **62** and **68**, where the rotation of the phenyl ring would be completely unhindered (Figure E4). Therefore this trend does not appear to exist for the Re(I)-dipyrrinato complexes.

The exception to this is the diphenylamino-substituted dipyrrinato complexes (**65** and **71**) which both display a prominent peak at 302 nm in the absorption spectra (Figure 5.10). The intensity of this peak has a similar magnitude to the dipyrrin-centred π–π* ($S_0 \rightarrow S_1$) transition. In addition to higher order π–π* transitions ($S_0 \rightarrow S_2$), the lone pair of electrons on the nitrogen atom of the diphenylamino ligands enable the possibility of a $n \rightarrow \pi^*$ transition for these Re(I)-dipyrrinato complexes.[138] $n \rightarrow \pi^*$ transitions occur when the electron is promoted from the non-bonding orbital of N, O, and S atoms to an antibonding π orbital.[139, 300] Each transition is characterised by remarkably different properties.[139] $n \rightarrow \pi^*$ transitions typically have low oscillator strengths and can be hidden by the intensity of the π–π* transition.[138] A charge transfer transition should also be possible for complexes **65** and **71** since resonance forms of the diphenylamino complexes exist (Figure 5.11).

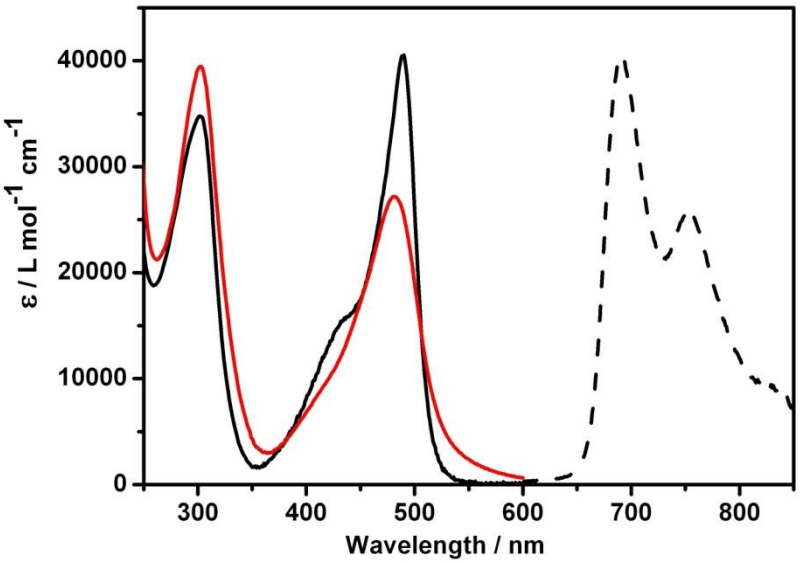

Figure 5.10. Absorption spectra of **65** (black solid line) and **71** (red solid line) and emission spectra of **65** (black dotted line, λ_{ex} = 485 nm) in CH_2Cl_2.

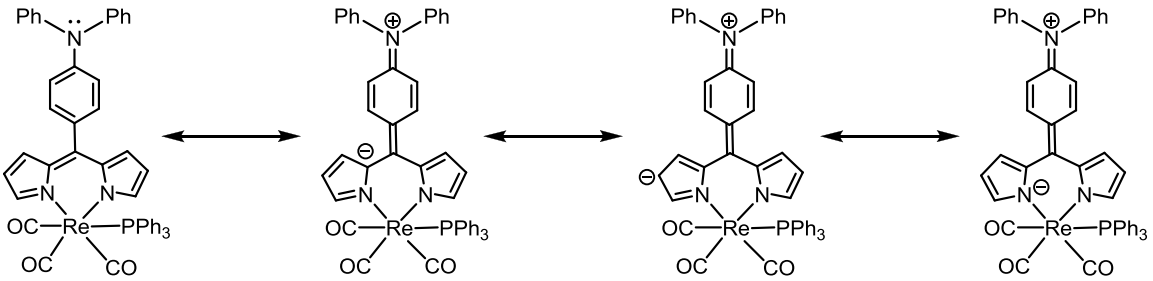

Figure 5.11. Illustration of the resonance forms of diphenylamino substituted Re(I)-dipyrrinato complex **65**.

The electronic absorption spectra of literature examples containing diphenylamino substituted ligands show absorption bands in the region of 300-400 nm. Intense absorption bands in this region have been assigned to π–π* transitions[301, 302] while the weaker absorption band is assigned as a n → π* transition.[302] The intensity of the transition centred at 302 nm in these complexes suggests that the origin of the transition is not n → π* transition,[138] however, a weaker n → π* transition coincident with this strong transition cannot be eliminated.

Resonance Raman spectroscopy with excitation wavelengths of 458 and 488 nm were used to confirm that the dominant transition in the visible region of the absorption spectra is localised on the dipyrrinato ligand. Resonance Raman spectra for **60** and **67** are presented as representative examples for all the complexes in Figures 5.12 and 5.13, respectively. All other resonance Raman spectra are present in the Appendix E (Figures

E5-E15). These spectra closely resemble the resonance Raman spectra of ligand (chapter 2) and related complexes (at these wavelengths) already presented. Table E1 displays the Raman shifts of complexes **60** and **67** against the Raman shifts of Ru(II)-dipyrrinato complex **46** and dipyrrin ligand **34**. All of the prominent peaks in the region 400 – 1620 cm^{-1} are attributable to vibrational modes of the dipyrrinato ligand[42, 53] (also refer to chapter 2), while in the region 1620 – 2200 cm^{-1} weak overtones and combinations are present.

Table 5.1. Summary of optical properties (in CH_2Cl_2) and IR bands of Re(I)-dipyrrinato complexes.

	Absorption		Emission			IR
Complex	Abs. max. (nm)	λ_{max} (L mol^{-1} cm^{-1})	Em. Max [a] (nm)	Φ_{em}	Stokes shift [b] (cm^{-1})	CO modes (cm^{-1})
59	487[c]	33 800	708[d]	<0.001[e]	6410	1863, 1888, 2004
60	491	36 600	706, 762	0.0014	6202	1880, 1913, 2015
62	489	38 100	694, 755	0.0026	6041	1890, 1909, 2010
63	488	37 700	694, 751	0.0060	6083	1883, 1910, 2013
64	490	42 100	688, 754	0.0051	5873	1885, 1916, 2012
65	490	40 500	691, 751	0.0099	5936	1881, 1912, 2011
66	485	36 400	711, 764	<0.001[e]	6554	1881, 1910, 2010
67	480	25 500	no emission			1836, 1912
68	481	27 300	no emission			1827, 1906
69	481	25 400	no emission			1822, 1904
70	487	27 600	706[d]	< 0.001[e]	6370	1834, 1909
71	481	27 200	no emission			1832, 1907
72	474	40 900	no emission			1825, 1903
73	474	32 200	no emission			1825, 1903
74	472	-	not measured			1834, 1914

[a] The excitation wavelength was 485 nm for **59**-**60** and **62**-**65** and 480 nm for **66** and **70**.
[b] The Stokes shifts are calculated using the absorption maximum and the high energy emission peak.
[c] Recorded in DMSO.
[d] Emission is very weak and the long wavelength emission peak is not visible.
[e] Emission was too weak to allow a more accurate estimation of the quantum yield.

Table E1 shows that most of the peaks that appear in the resonant Raman spectra of the Ru(II)-dipyrrinato complex (**46**) (and dipyrrin ligand **34**) also appear in the resonant Raman spectra of all the Re(I)-dipyrrinato complexes. Substantial structural reorganisation of the phenyl ring occurs in the π–π* excited state for the uncoordinated dipyrrin ligand **34** (chapter 2) and Ru(II)-dipyrrinato complex **46** (chapter 4). This indicates that the same vibrational modes of the dipyrrinato ligand are involved in transforming the Re(I)-dipyrrinato complexes from the ground state geometry to its excited state geometry. The intensity patterns observed in the resonant Raman spectra of the Re(I)- and Ru(II)-dipyrrinato complexes are significantly different. For example, the modes at 872 and 898 cm^{-1}, which can be assigned (by comparison to the assignments given in chapters 2 and 4) as dipyrrin (including the phenyl group) deformations, are significantly enhanced for the Re(I)-dipyrrinato complexes relative to the Ru(II)-dipyrrinato complexes. The different intensity patterns indicate that the dipyrrin π–π* transitions in the Ru(II)- and Re(I)-dipyrrinato complexes do result in slightly different excited state dipyrrin geometries.

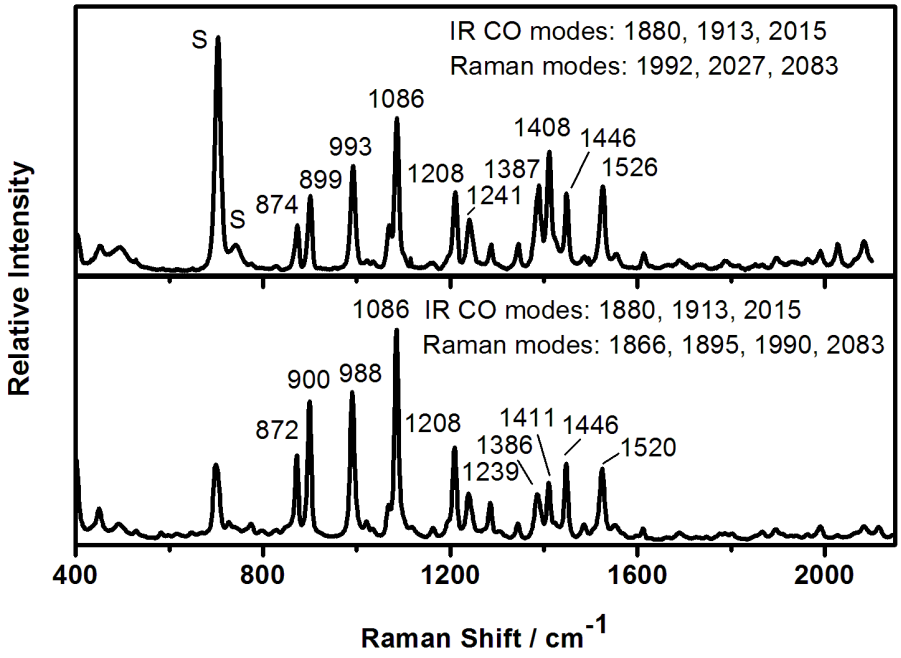

Figure 5.12. Resonance Raman spectra of **60** in CH_2Cl_2. λ_{exc} = 458 nm (top), 488 nm (bottom).

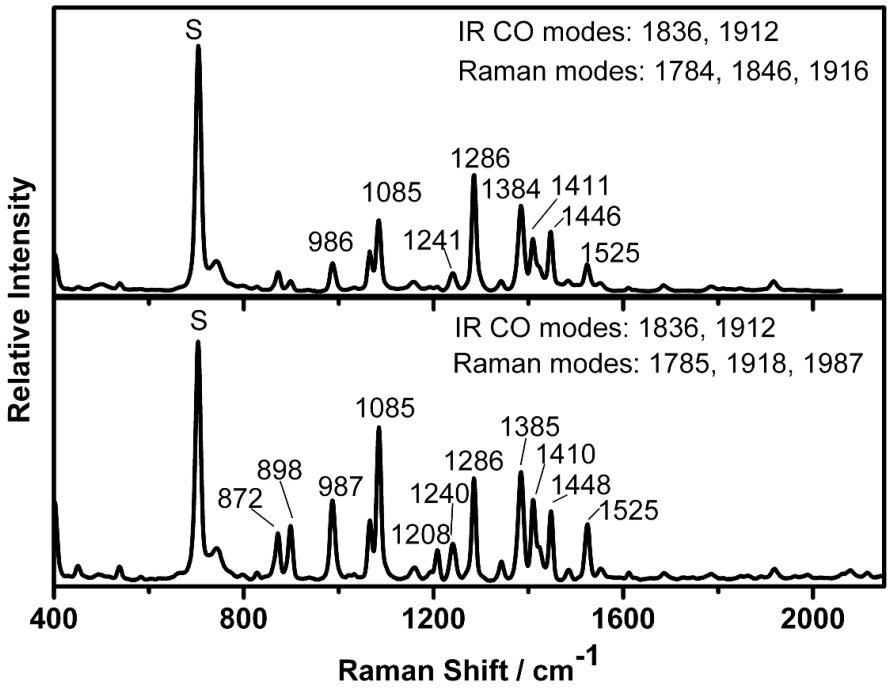

Figure 5.13. Resonance Raman spectra of **67** in CH_2Cl_2. λ_{exc} = 458 nm (top), 488 nm (bottom).

Re(I)-dipyrrin MLCT electronic transitions may be expected to be accessible in these complexes. For MLCT transitions, the enhancement of the CO vibrational modes via π backbonding to the Re(I) centre[303] can typically be observed in the resonance Raman spectra. However, strong enhancement of the CO vibrational modes is not observed in the resonance Raman spectra (Figures 5.12/5.13 and E5-15) and therefore this would seem to rule out the coincidence of any such transitions with the π–π* transition.

TD-DFT calculations provide further insight. The results of TD-DFT calculations of **60** are presented as representative examples for all complexes (except complexes **65** and **71**). Table 5.2 shows that multiple configurations contribute to the electronic transitions. The molecular orbitals (Figure E16) are similar to the dipyrrinato complexes already presented in this thesis, where the occupied orbitals have amplitude centred only on the dipyrrin core and the unoccupied orbitals have amplitude on the dipyrrin core and extending out onto the phenyl ring. The multiple configurations make a simple interpretation difficult and therefore the electron density difference (EDD) plots are used to simplify the analysis.

The large oscillator strength (412 nm, f = 0.340) transition confirms the nature of the transition assigned as π–π* in the experimental absorption spectrum (491 nm). This

transition has contributions from the HOMO-2, HOMO, and LUMO orbitals. In particular, the HOMO-2 orbital has mixed Re(I), CO, dipyrrinato ligand character. The EDD plots for this transition (Figure 5.14) shows the electron density shifts away from the dipyrrin core (green) out towards the phenyl ring (blue). There is also some change in electron density at the Re centre indicating a significant degree of MLCT character. Metal contribution is also observed in the π–π* transition of **46** (chapter 4) and in the Re(I)-azadipyrrinato complex.[85]

The calculations predict closely spaced transitions at 444 nm (f = 0.039) and 435 nm (f = 0.088). Electron density centred on the d orbitals of the Re centre (green) shifts predominantly onto the π orbitals of dipyrrin core with minimal density on the phenyl ring and functional group (blue), strongly suggesting MLCT character (Figure 5.14). If the MLCT transition is coincident with the π–π transition of the dipyrrin enhancement of the CO modes is expected.[303] The absence of the CO vibrational modes in the resonance Raman spectra can be rationalised as follows. Resonance Raman intensities are related to the square of the transition dipole moment and the calculations predict the oscillator strengths of the MLCT transitions to be significantly lower than the nearby dipyrrin centred π–π* transition. Enhancements of the CO vibrational modes are unlikely to be observed in the resonance Raman spectra over the dominant vibrations associated with the dipyrrin core. Therefore resonance Raman spectroscopy is inconclusive in determining the position and relative contribution of the MLCT transition.

The calculations also reveal an intraligand charge transfer (ILCT) transition localised entirely on the dipyrrinato ligand (360 nm, f = 0.043) (Figure 5.14). This transition may contribute to the observed shoulder generally attributed to vibronic effects, on the high-energy side of the π–π* band in the absorption spectrum.

Table 5.2. Calculated and experimental absorption parameters for **60**.

Calculated				Experimental	
λ (nm)	Configuration (% contribution)	Oscillator strength[a]	Assignment	λ (nm)	ε (M^{-1} cm^{-1})
444	HOMO-2→LUMO (63), HOMO-1→LUMO (-18), HOMO→LUMO (13)	0.039	MLCT (Re-dipyrrin)		
435	HOMO-2→LUMO (11), HOMO-1→LUMO (75)	0.088	MLCT (Re-dipyrrin)		
412	HOMO-2→LUMO (-21), HOMO→LUMO (56)	0.340	π-π*	491	36 000
360	HOMO→LUMO+1 (96)	0.043	ILCT		

[a] Only calculated oscillator strengths of greater than 0.03 are reported.

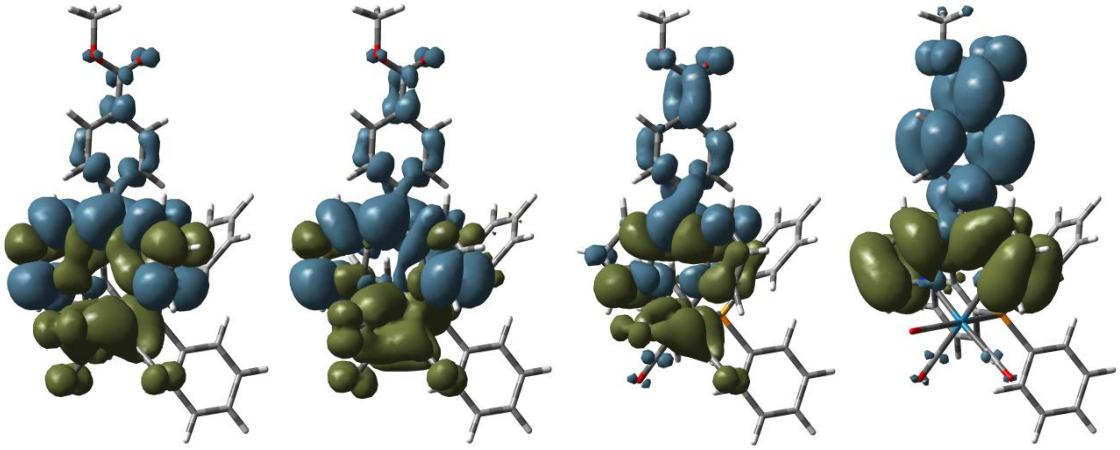

Figure 5.14. Electron density difference plots for the strongest transitions of **60**. Green represents depletion of electron density and blue represents accumulation of electron density.

TD-DFT calculations were investigated to gain insight into the transitions expected for the diphenylamino substituted complexes **65** and **71**. The results of the calculations of **65** (Table E2 and Figures E17-18) are discussed here as a representation of both diphenylamino substituted complexes (**65** and **71**). Again the multiple configurations make for a difficult analysis which is further complicated by the diphenylamino substituent. The large oscillator strength (396 nm, f = 0.362) transition correlates with the dominant band in the experimental absorption spectrum (490 nm) and is consistent with the previous assignment of a π–π* transition centred on the dipyrrinato ligand. However, this transition appears to be slightly different from the other dipyrrin centred π–π* transitions already presented in this thesis, in that the electron density is

reorganised on the dipyrrin core and there is minimal accumulation of electron density on the phenyl ring. The EDD plots also indicate some MLCT character is expected for this transition. Two closely spaced MLCT transitions are also predicted at 444 nm (f = 0.031) and 440 nm (f = 0.077).

The intensity of the transition (302 nm) in the absorption spectra of **65** and **71** suggests that the transition cannot be n → π* transition. An n → π* transition is characterised by electron density shifting from the lone pair of electrons on the nitrogen of the diphenylamino substituent. However, the calculations show no evidence of such a transition. The EDD plots for **65** show high energy transitions with significant oscillator strengths (288 nm, f = 0.139; 284 nm, f = 0.050; and to some extent 285 nm, f = 0.192) have movement of electron density (green) from the diphenylamino substituent is accumulating on the dipyrrin (blue) during the transitions (Figure E18). These transitions can all be described as π–π* in nature, or more specifically as intraligand charge transfer transitions. A combination of these three transitions is probably responsible for the prominent peak observed at 302 nm in the experimental absorption spectrum of **65** and **71**.

The emission properties of all the complexes in CH_2Cl_2 were also studied and the data are summarised in Table 5.1. Figure 5.10 displays the emission spectrum of **65** and Figure E19 displays the excitation spectrum of **64** as a representative example. Other fluorescence spectra are presented in Appendix E (Figures E20-E25). Upon excitation into the dipyrrinato π–π* absorption band (λ_{ex} = 485) nm a vibronically structured[48, 50] doublet emission profile was observed for all the [Re**L**$(CO)_3PR_3$] complexes, with the first intense emission peak centred between 688 – 711 nm and the second weaker emission peak observed between 751 – 762 nm. This equates to a large Stokes shift in the vicinity of 6000 cm^{-1}. All of the [Re**L**$(CO)_2(PR_3)(PR'_3)$] complexes were non-emissive, except for **70**, which exhibited very weak emission. The excitation spectrum of **64** (λ_{em} = 700 nm, Figure E19) displays two prominent peaks at 490 nm and 299 nm. Assuming that the emission is from the dipyrrinato ligand, the peak at 490 nm (in the excitation spectrum) coincides with the transition (at 490 nm) assigned as a dipyrrin centred π–π* transition in the absorption spectrum. The peak at 299 nm can probably be attributed to the dipyrrinato $S_0 \rightarrow S_2$ transition. The excitation spectrum in the region of 250-300 nm is vastly different from the same region of the absorption spectrum. This indicates that the higher energy electronic transitions are not emissive.

These transitions may be localised on regions of the complex that are electronically insulated from the dipyrrinato ligand.

The relative emission quantum yields of all the [Re**L**$(CO)_3PR_3$] complexes were determined to be between 0.0014 and 0.0099 at room temperature in deoxygenated CH_2Cl_2 solution. As established by many groups (including ours), one key non-radiative pathway for the relaxation of dipyrrin-centred excited states involves the rotation of the *meso*-phenyl substituent.[41, 48, 53, 90, 231] Enhanced emission is observed where this motion is hindered, for example in mesityl dipyrrinato complexes[41, 48, 50, 90, 91] or BODIPY complexes with substituents in the α or β positions.[231] The relatively high emission quantum yield observed for **64** complements these earlier studies. The quantum yields of the [Re**L**$(CO)_3PR_3$] complexes are similar to other dipyrrinato complexes[48] but significantly lower than others.[40, 41, 49, 50, 90, 91, 304] Re(I)-bipyridine complexes, where emission is from a ^{3}MLCT state rather than a $^3\pi-\pi^*$, also typically have higher quantum yields.[269, 274, 305]

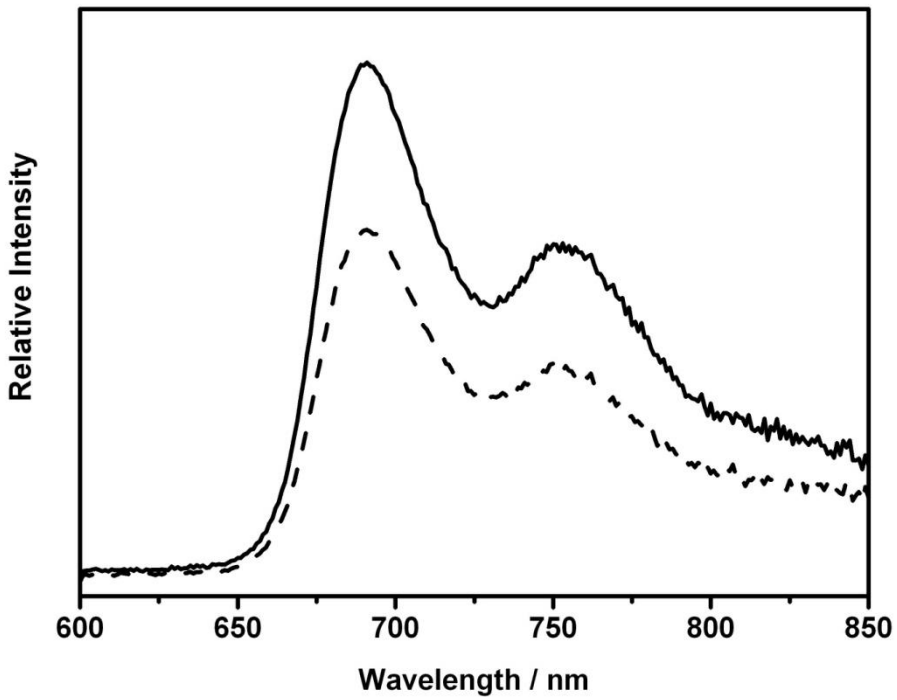

Figure 5.15. Emission spectra of **65** in CH_2Cl_2 (λ_{ex} = 485 nm). The solid curve was measured following rigorous deoxygenation of the solvent, while the dotted curve after 2 mL of air was bubbled through the sample.

The large Stokes shift is immediately suggestive of emission from a triplet excited electronic state where intersystem crossing from an initially formed singlet state is likely to be promoted by the heavy atom effect.[306] This has previously been observed in both dipyrrinato complexes and BODIPYs.[48, 50, 307-309] Emission from a triplet state is further supported by the dependence of the emission intensity on presence of both dissolved oxygen[140] and methyl viologen (MV^{2+}). Emission intensity was greatest for rigorously degassed samples of **60** and **62-65**; however it was significantly reduced when air was bubbled through the solution (Figure 5.15). Titrations of methyl viologen (MV^{2+}) into **65** (Figure 5.16A) revealed that Stern-Volmer kinetics (Figure 5.16B) are obeyed for this quencher. Other spectra are given in Figures E20-25. The two peaks in the emission spectrum are quenched at the same rate by MV^{2+}, which strongly implies that the emission is arising from the same excited state. MV^{2+} acts as a quencher by oxidizing the excited state of complexes **60** and **62-65**. This is an exciting observation in the context of employing these complexes as photocatalysts for the reduction of CO_2 or as dyes in dye-sensitised solar cells. However, reductive quenching of the excited state of **60** and **62-65** by triethanolamine (TEOA) was not observed.

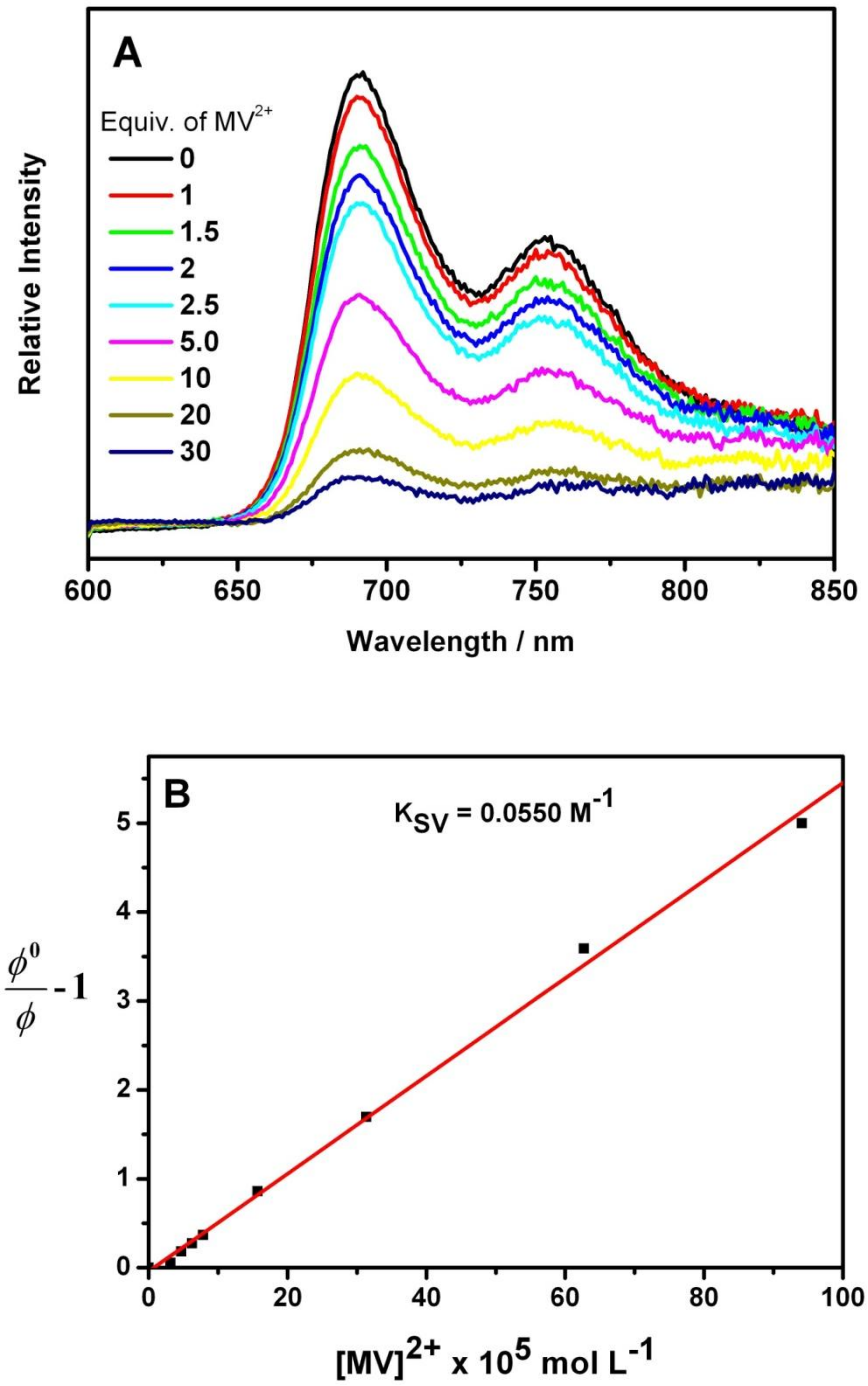

Figure 5.16. (A) Emission spectra of **65** in CH_2Cl_2 (λ_{ex} = 485 nm) as a function of added methyl viologen (MV^{2+}, 1-30 molar equivalents). (B) Stern-Volmer plot showing the quenching of emission from **65** by MV^{2+}. ϕ^o is the quantum yield in the absence of MV^{2+} and ϕ is the quantum yield in the presence of MV^{2+}.

5.4.4 Photochemical ligand substitution (PLS) reactions

Photochemical ligand substitution (PLS) reactions of many transition metal complexes, including Re(I)-polypyridyl complexes, are well known in the literature.[106, 257-261, 287] When a ligand such as bipyridine is coordinated to the Re centre the CO ligand *trans* to the axial PR_3 ligand is labilised presumably via a metal-centred triplet excited state (^{3}MC). This state can be populated by internal conversion from the MLCT excited states (refer to Figure 5.2).[283]

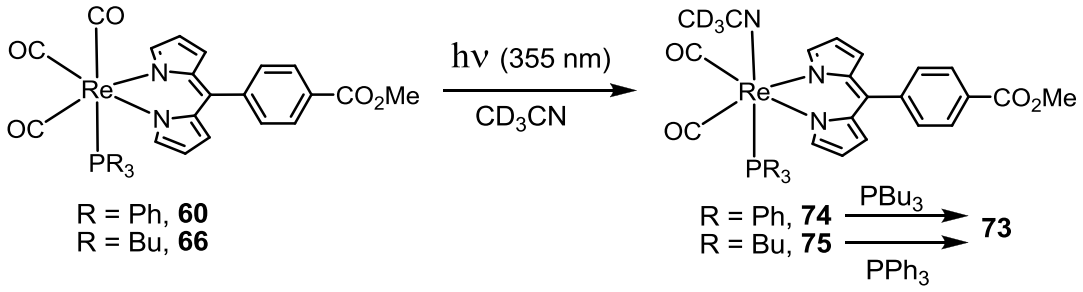

Figure 5.17. The proposed photoproducts from the photochemical ligand substitution reactions of **60** and **66**. Irradiation of **60** and **66** with 355 nm excitation is proposed to generate complexes **74** and **75**, respectively. Further reactions of **74** with PBu_3 and **75** with PPh_3 produce complex **73**.

The PLS reactions of Re(I)-dipyrrinato complexes were briefly investigated using visible radiation (458 nm, 488 nm and 514.5 nm), a mercury arc lamp (200 nm and 250 nm), and a pulse laser (355 nm, 40-45 mW average power). No reaction was observed using visible excitation and the reaction was very slow using the mercury arc lamp. The proposed reaction is given in Figure 5.17 to give the products where the CD_3CN is *trans* to the phosphine ligand. During the irradiation of a (deuterated) acetonitrile solution of **60** significant changes were observed in the ^{1}H NMR and ^{31}P NMR spectrum (Figure 5.18, Figure E26-27). A laser-induced thermal (rather than photochemical) reaction can probably be ruled out on the basis of the low power input (40-45 mW) into the sample. The temperature of the sample, recorded during the reaction, did not rise above 30 °C during the photolysis reaction.

After ~2.5 hours, approximately 95% of the starting material was consumed and a new set of peaks corresponding to a new complex were evident (Figure 5.18B). Trace quantities of **67** are also observed by NMR. A ^{13}C NMR spectrum collected

immediately after the reaction shows that initially only one product is formed. Exhaustive attempts to isolate and purify the product were made; however the product is unstable and decomposes rapidly over a period of ~24 hours to give **60** (starting material), **67** and at least one other (unidentifiable) product on the basis of ^{1}H NMR (Figure E28) and ^{31}P NMR spectroscopy (Figure E27). Presumably the starting material (**60**) is reformed by a thermal reaction of **74** with dissolved CO. Free PPh_3 probably arises from the decomposition of **74**, which provides a source of PPh_3, to form **67** (and a source of dissolved CO).

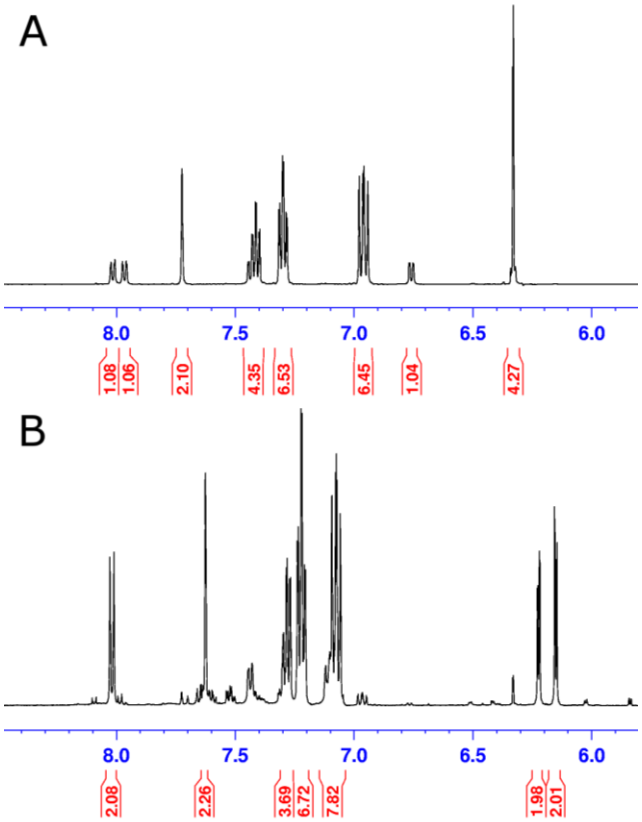

Figure 5.18. Aromatic region of the ^{1}H NMR spectrum of **60** (A) before and (B) after two hours irradiation with 355 nm laser light in CD_3CN to give the proposed product **74**.

The structure of the photolysis product is proposed to be **74** (Figure 5.17). ^{1}H NMR (Figure 5.18), ^{31}P NMR (Figure E27) and 2D-COSY NMR (Figure E29) spectra support this conclusion by indicating that the PPh_3 ligand remains coordinated and the dipyrrin core retains its mirror symmetry. Although mass spectrometry proved fruitless, this

conclusion is further supported by IR spectroscopy (Figure 5.19). The peaks corresponding to **60** disappear, while peaks at 1840 cm^{-1} and 1920 cm^{-1} gradually grow into the spectrum. These are assigned as the out-of-phase totally symmetric and anti-symmetric vibrational modes expected for *cis* coordinated CO ligands (Figure 5.8B), as expected for **74**. Modest changes are also evident in the electronic absorption spectrum (Figure 5.20). The vibronic structure of the π–π* absorption band of **60** disappears, and this band broadens and shifts slightly blue shifted.

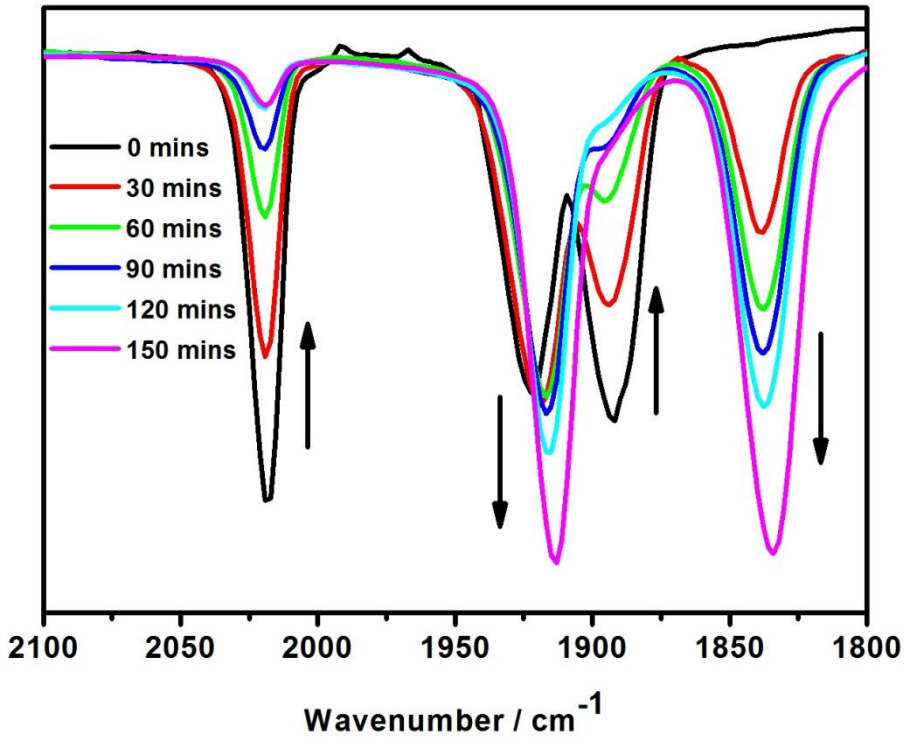

Figure 5.19. The photochemical conversion of **60** to **74** monitored by IR spectroscopy over a period of 150 minutes.

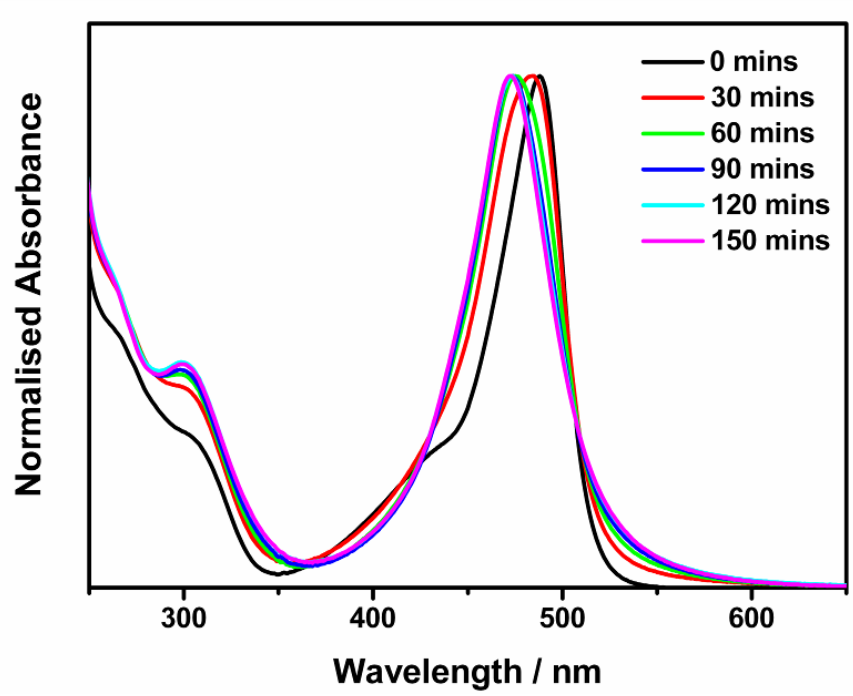

Figure 5.20. The photochemical conversion of **60** to **74** in CD_3CN monitored by absorption spectroscopy over the period of 150 minutes. Note that the spectra have been normalized.

The PLS reaction of **60** was repeated in the presence of free PBu_3. In this case, **74** was anticipated to form as an intermediate; and that it would subsequently react with PBu_3 to yield complex **73** (Figure 5.17). This reaction proceeds smoothly, and the characterisation of **73** produced in this manner was aided by comparison with the spectral data of thermally prepared material. A PLS reaction also occurs if complex **66** is irradiated in CD_3CN, and it is assumed that this yields **75** (Figure 5.17). **73** is formed when this PLS reaction is conducted in the presence of PPh_3. A PLS reaction also takes place when **60** was irradiated in deuterated acetone which eventuated in the formation of **67**. It is proposed that the CO ligand *trans* to the PPh_3 ligand in **60** is initially labilised and [Re**L**$(CO)_2(PPh_3)((CD_3)_2CO)$] is formed as an intermediate species. Since the $(CD_3)_2CO$ is likely to be weakly bound, this complex may decompose to liberate free PPh_3, which subsequently reacts with further [Re**L**$(CO)_2(PPh_3)((CD_3)_2CO)$] to produce **67** (Figure E30).

For Re(I)-dipyrrinato complexes such as **60** and **66**, suitable triplet excited states from which internal conversion to ^{3}MC excited states could occur include the dipyrrinato centred $^3\pi$–π^*, the assumed ^{3}MLCT (Re(I)-dipyrrin) state, and higher energy dipyrrinato centred states. Unfortunately, the precise energy of these states is unknown. The $^3\pi$–π^* state that is responsible for the observed emission from the [Re**L**$(CO)_3PR_3$] complexes is probably too low in energy for internal conversion to a ^{3}MC state to occur. This is supported by no observed PLS reaction using visible wavelength excitation into the π–π^* transition. An alternative possibility is the direct population of the ^{3}MC states, albeit with limited efficiency given the typically low oscillator strengths of d-d transitions. In the case of PLS reactions described here there is only very limited absorption at 355 nm (Figure 5.9, ε = 1000 M^{-1} cm^{-1} for **60**). The use of a pulse laser as an intense light source may compensate for the low efficiency of light absorption.

5.5 Summary

The synthesis and characterisation of the first Re(I)-dipyrrinato complexes have been achieved. Complexes with the general formulae *fac*-[Re**L**$(CO)_3$Cl][NEt_3], *fac*-[Re**L**$(CO)_3PR_3$], and [Re**L**$(CO)_2(PR_3)(PR'_3)$] have been prepared with a series of *meso*-substituted aryl dipyrrin ligands. The complexes have prominent bands in the visible region of their absorption spectra which are ascribed to a π–π^* transition centred on the dipyrrinato ligand. TD-DFT calculations indicate there may be a Re(I)-dipyrrinato MLCT transition coincident with the π–π^* transition centred on the dipyrrinato ligand. However, resonance Raman spectroscopy is dominated by vibrational modes associated with the dipyrrinato ligand and is inconclusive in determining the position of the MLCT transition. TD-DFT calculations of the diphenylamino substituted dipyrrinato complex suggests that the intense high energy peak in the experimental absorption spectrum is an ILCT transition where the electron density shifts from the diphenylamino substituent to the dipyrrin core. The calculations confirm there is no evidence of an n $\rightarrow$ π^* transition on the diphenylamino substituent.

Excitation into the π–π^* band of the [Re**L**$(CO)_3(PR_3)$] complexes results in weak emission (quantum yields < 0.01) centred around 700 nm, and the large Stokes shift (~6000 cm^{-1}) indicates emission from a triplet excited state. Emission from these complexes is quenched by dissolved oxygen and methyl viologen (obeying Stern-Volmer kinetics). The ability of these complexes to harvest visible light and the

oxidation potential of their excited states (as estimated by quenching studies with methyl viologen) indicates that Re(I)-dipyrrinato complexes warrant further investigation as photocatalysts for the photochemical reduction of CO_2 and water and as dyes for dye-sensitized solar cells.

5.6 Future work

The quenching of the emission of the Re(I)-dipyrrinato complexes by methyl viologen is an exciting observation. This suggests that the reduction potential of the excited state is more negative than the reduction potential of methyl viologen. Establishing the redox potential of these Re(I)-dipyrrinato complexes is an important step in confirming that these complexes are suitable candidates for catalysts in the reduction of CO_2. The redox potentials of the ground-state can be determined using electrochemical methods. The redox potentials of the ground state together with the excited-state energy, which can be determined spectroscopically by extrapolation from the electronic absorption spectrum or as an output from the resonance Raman intensity analysis (RRIA), the excited-state redox potentials can then be estimated. Furthermore, the redox process must be reversible to be efficient photocatalysts, but this can only be established by examining the products of the photoinduced redox processes.

The nature of the electronic excited states and photophysical properties of these Re(I)-dipyrrinato complexes are important in the application of these complexes for solar energy conversion applications. To further probe the electronic structure of the Re(I)-dipyrrinato complexes a detailed analysis of the absorption spectra, quantitative analysis of the resonance Raman (RRIA) in combination with a detailed computational chemistry analysis is underway.

Acknowledgements

I wish to thank the following people for their assistance in this chapter: Serena Smalley for establishing the synthetic protocol for **61** and Janice Moody for establishing the synthetic protocol Re(I)-dipyrrinato complexes (**59**, **60**, **64**, **70**). I wish also to acknowledge Professor Osamu Ishitani (Tokyo Institute of Technology) for valuable discussions on the photochemical ligand substitution reactions of Re(I)-bipyridine complexes on his visit to Massey University in 2010.

References

1. Nocera, D. G., Living healthy on a dying planet. *Chem. Soc. Rev.*, **2009**, 38, 13-15.
2. Sanderson, K., Chemistry: The photon trap. *Nature*, **2008**, 452, 400-402.
3. Lubitz, W., Reijerse, E. J., Messinger, J., Solar water-splitting into H_2 and O_2: design principles of photosystem II and hydrogenases. *Energy Environ. Sci.*, **2008**, 1, 15-31.
4. Balzani, V., Credi, A., Venturi, M., Photochemical conversion of solar energy. *ChemSusChem*, **2008**, 1, 26-58.
5. Lewis, N. S., Toward cost-effective solar energy use. *Science*, **2007**, 315, 798-801.
6. Armaroli, N., Balzani, V., The future of energy supply: challenges and opportunities. *Angew. Chem., Int. Edit.*, **2007**, 46, 52-66.
7. Lewis, N. S., Nocera, D. G., Powering the planet: chemical challenges in solar energy utilization. *Proc. Natl. Acad. Sci. U. S. A.*, **2006**, 103, 15729-15735.
8. Barber, J., Photosynthetic energy conversion: natural and artificial. *Chem. Soc. Rev.*, **2009**, 38, 185-196.
9. Eisenberg, R., Rethinking water splitting. *Science*, **2009**, 324, 44-45.
10. Balzani, V., Moggi, L., Manfrin, M. F., Bolletta, F., Gleria, M., Solar energy conversion by water photodissociation. *Science*, **1975**, 189, 852-856.
11. Dempsey, J. L., Esswein, A. J., Manke, D. R., Rosenthal, J., Soper, J. D., Nocera, D. G., Molecular chemistry of consequence to renewable energy. *Inorg. Chem.*, **2005**, 44, 6879-6892.
12. Penner, S. S., Steps toward the hydrogen economy. *Energy*, **2006**, 31, 33-43.
13. Lubitz, W., Tumas, W., Hydrogen: an overview. *Chem. Rev.*, **2007**, 107, 3900-3903.
14. Alstrum-Acevedo, J. H., Brennaman, M. K., Meyer, T. J., Chemical approaches to artificial photosynthesis 2. *Inorg. Chem.*, **2005**, 44, 6802-6827.
15. Kohl, S. W., Weiner, L., Schwartsburd, L., Konstantinovski, L., Shimon, L. J. W., Ben-David, Y., Iron, M. A., Milstein, D., Consecutive thermal H_2 and light-induced O_2 evolution from water promoted by a metal complex. *Science*, **2009**, 324, 74-77.
16. Kanan, M. W., Surendranath, Y., Nocera, D. G., Cobalt-phosphate oxygen-evolving compound. *Chem. Soc. Rev.*, **2009**, 38, 109-114.
17. O'Regan, B., Grätzel, M., A low-cost, high-efficiency solar-cell based on dye-sensitized colloidal TiO_2 films. *Nature*, **1991**, 353, 737-740.
18. Lenzmann, F. O., Kroon, J. M., Recent advances in dye-sensitized solar cells. *Adv. OptoElectr.*, **2007**, 1-10.
19. Bessho, T., Yoneda, E., Yum, J., Guglielmi, M., Tavernelli, I., Imai, H., Rothlisberger, U., Nazeeruddin, M. K., Grätzel, M., New paradigm in molecular engineering of sensitizers for solar cell applications. *J. Am. Chem. Soc.*, **2009**, 131, 5930-5934.
20. Grätzel, M., Dye-sensitized solar cells. *J. Photochem. Photobio. C.*, **2003**, 4, 145-153.
21. Robertson, N., Optimizing dyes for dye-sensitized solar cells. *Angew. Chem. Int. Ed.*, **2006**, 45, 2338-2345.

22. Grätzel, M., Recent advances in sensitized mesoscopic solar cells. *Acc. Chem. Res.*, **2009**, 42, 1788-1798.
23. Fischer, H., Orth, H., *Die Chemie des Pyrrols*. **1937**, Leipzig: Akademische Verlagsgesellschaft.
24. Wood, T. E., Thompson, A., Advances in the chemistry of dipyrrins and their complexes. *Chem. Rev.*, **2007**, 107, 1831-1861.
25. Loudet, A., Burgess, K., BODIPY dyes and their derivatives: syntheses and spectroscopic properties. *Chem. Rev.*, **2007**, 107, 4891-4932.
26. Brückner, C., Karunaratne, V., Rettig, S. J., Dolphin, D., Synthesis of meso-phenyl-4,6-dipyrrins, preparation of their Cu(II), Ni(II), and Zn(II) chelates, and structural characterization of bis[meso-phenyl-4,6-dipyrrinato]Ni(II). *Can. J. Chem.*, **1996**, 74, 2182-2193.
27. Laha, J. K., Dhanalekshmi, S., Taniguchi, M., Ambroise, A., Lindsey, J. S., A scalable synthesis of meso-substituted dipyrromethanes. *Org. Process Res. Dev*, **2003**, 7, 799-812.
28. Rohand, T., Dolusic, E., Ngo, T. H., Maes, W., Dehaen, W., Efficient synthesis of aryldipyrromethanes in water and their application in the synthesis of corroles and dipyrromethenes. *Arkivoc*, **2007**, 307-324.
29. Brückner, C., Zhang, Y., Rettig, S. J., Dolphin, D., Synthesis, derivatization and structural characterization of octahedral tris(5-phenyl-4,6-dipyrrinato) complexes of cobalt(III) and iron(III). *Inorg. Chim. Acta* **1997**, 263, 279-286.
30. Garibay, S. J., Stork, J. R., Wang, Z. Q., Cohen, S. M., Telfer, S. G., Enantiopure vs. racemic metalloligands: impact on metal-organic framework structure and synthesis. *Chem. Commun.*, **2007**, 4881-4883.
31. Yu, L., Muthukumaran, K., Sazanovich, I. V., Kirmaier, C., Hindin, E., Diers, J. R., Boyle, P. D., Bocian, D. F., Holten, D., Lindsey, J. S., Excited-state energy-transfer dynamics in self-assembled triads composed of two porphyrins and an intervening bis(dipyrrinato)metal complex. *Inorg. Chem.*, **2003**, 42, 6629-6647.
32. McLean, T. M., Moody, J. L., Waterland, M. R., Telfer, S. G., Luminescent Re(I)-dipyrrinato complexes. *Inorg. Chem.*, **2012**, 51, 446-455.
33. Ikeda, C., Ueda, S., Nabeshima, T., Aluminium complexes of N_2O_2-type dipyrrins: the first hetero-multinuclear complexes of metallo-dipyrrins with high fluorescence quantum yields. *Chem. Commun.*, **2009**, 2544-2546.
34. Murakami, Y., Matsuda, Y., Iiyama, K., Transition metal complexes of pyrrole pigments: synthesis and characterization of acetatobis (3,3',5,5'-tetramethyldipyrromethenato) chromium(III). *Chem. Lett.*, **1972**, 1069-1072.
35. Halper, S. R., Stork, J. R., Cohen, S. M., Preparation and characterization of asymmetric alpha-alkoxy dipyrrin ligands and their metal complexes. *Dalton Trans.*, **2007**, 1067-1074.
36. Do, L., Halper, S. R., Cohen, S. M., Helical coordination polymers and cyclic dimers formed from heteroleptic thioether-dipyrrinato copper(II) complexes. *Chem. Commun.*, **2004**, 2662-2663.
37. Halper, S. R., Cohen, S. M., Self-assembly of heteroleptic [Cu(dipyrrinato)(hfacac)] complexes directed by fluorine-fluorine interactions. *Inorg. Chem.*, **2005**, 44, 4139-4141.
38. Heinze, K., Reinhart, A., Heteroleptic Cu(II) dipyrromethene complexes linked via hydrogen bonds, coordinative bonds, and covalent bonds: probing the coordination environment by electron paramagnetic resonance spectroscopy. *Inorg. Chem.*, **2006**, 45, 2695-2703.

39. Amiri, A., Comeau, I. M., Thompson, A., Heteroleptic zinc dipyrromethene complexes. *J. Heterocycl. Chem.*, **2006**, 43, 431-435.
40. Filatov, M. A., Lebedev, A. Y., Mukhin, S. N., Vinogradov, S. A., Cheprakov, A. V., π-extended dipyrrins capable of highly fluorogenic complexation with metal ions. *J. Am. Chem. Soc.*, **2010**, 132, 9552-9554.
41. Sutton, J. M., Rogerson, E., Wilson, C. J., Sparke, A. E., Archibald, S. J., Boyle, R. W., Synthesis and structural characterisation of novel bimetallic dipyrromethene complexes: rotational locking of the 5-aryl group. *Chem. Commun.*, **2004**, 1328-1329.
42. Smalley, S. J., Waterland, M. R., Telfer, S. G., Heteroleptic dipyrrin/bipyridine complexes of ruthenium(II). *Inorg. Chem.*, **2009**, 48, 13-15.
43. Hall, J. D., McLean, T. M., Smalley, S. J., Waterland, M. R., Telfer, S. G., Chromophoric dipyrrin complexes capable of binding to TiO_2: synthesis, structure and spectroscopy. *Dalton Trans.*, **2010**, 39, 437-445.
44. Yadav, M., Singh, A. K., Maiti, B., Pandey, D. S., Heteroleptic arene ruthenium complexes based on meso-substituted dipyrrins: synthesis, structure, reactivity, and electrochemical studies. *Inorg. Chem.*, **2009**, 48, 7593-7603.
45. Roomi, M. W., New rhodium complexes of dipyrromethenes. *Tetrahedron Lett.*, **1974**, 1131-1132.
46. Yadav, M., Singh, A. K., Pandey, D. S., First examples of heteroleptic dipyrrin/η^5-pentamethylcyclopentadienyl rhodium/iridium(III) complexes and their catalytic activity. *Organometallics*, **2009**, 28, 4713-4723.
47. Porter, C. R., The stereochemistry of metallic derivatives of pyrromethenes. *J. Chem. Soc.*, **1938**, 368-372.
48. Bronner, C., Baudron, S. A., Hosseini, M. W., Strassert, C. A., Guenet, A., De Cola, L., Dipyrrin based luminescent cyclometallated palladium and platinum complexes. *Dalton Trans.*, **2010**, 39, 180-184.
49. Kobayashi, J., Kushida, T., Kawashima, T., Synthesis and reversible control of the fluorescent properties of a divalent tin dipyrromethene. *J. Am. Chem. Soc.*, **2009**, 131, 10836-10837.
50. Hanson, K., Tamayo, A., Diev, V. V., Whited, M. T., Djurovich, P. I., Thompson, M. E., Efficient dipyrrin-centered phosphorescence at room temperature from bis-cyclometalated iridium(III) dipyrrinato complexes. *Inorg. Chem.*, **2010**, 49, 6077-6084.
51. Halper, S. R., Cohen, S. M., Synthesis, structure, and spectroscopy of phenylacetylenylene rods incorporating meso-substituted dipyrrin ligands. *Chem. Eur. J.*, **2003**, 9, 4661-4669.
52. Halper, S. R., Malachowski, M. R., Delaney, H. M., Cohen, S. M., Heteroleptic copper dipyrromethene complexes: synthesis, structure, and coordination polymers. *Inorg. Chem.*, **2004**, 43, 1242-1249.
53. McLean, T. M., Cleland, D. M., Lind, S. J., Gordon, K. C., Telfer, S. G., Waterland, M. R., Strongly absorbing π–π* states in heteroleptic dipyrrin/2,2'-bipyridine ruthenium complexes: excited-state dynamics from resonance Raman spectroscopy. *Chem.-Asian J.*, **2010**, 5, 2036-2046.
54. Halper, S. R., Cohen, S. M., Self-assembly of two distinct supramolecular motifs in a single crystalline framework. *Angew. Chem. Int. Ed.* , **2004**, 43, 2385-2388.
55. Treibs, A., Kreuzer, F. H., Difluorboryl-komplexe von di- und tri-pyrrylmethenen. *Liebigs Ann. Chem.*, **1968**, 718, 208-223.

56. Yee, M., Fas, S. C., Stohlmeyer, M. M., Wandless, T. J., Cimprich, K. A., A cell-permeable, activity-based probe for protein and lipid kinases. *J. Biol. Chem.*, **2005**, 280, 29053-29059.
57. Bergstrom, F., Hagglof, P., Karolin, J., Ny, T., Johansson, L. B. A., The use of site-directed fluorophore labeling and donor-donor energy migration to investigate solution structure and dynamics in proteins. *Proc. Natl. Acad. Sci. U. S. A.*, **1999**, 96, 12477-12481.
58. Arbeloa, T. L., Arbeloa, F. L., Arbeloa, I. L., García-Moreno, I., Costela, A., Sastre, R., Amat-Guerri, F., Correlations between photophysics and lasing properties of dipyrromethene-BF_2 dyes in solution. *Chem. Phys. Lett.*, **1999**, 299, 315-321.
59. Boyer, J. H., Haag, A. M., Sathyamoorthi, G., Soong, M. L., Thangaraj, K., Pavlopoulos, T. G., Pyrromethene-BF_2 complexes as laser dyes: 2. *Heteroatom Chem.*, **1993**, 4, 39-49.
60. Shah, M., Thangaraj, K., Soong, M. L., Wolford, L. T., Boyer, J. H., Politzer, I. R., Pavlopoulos, T. G., Pyrromethene-BF_2 complexes as laser dyes:1. *Heteroatom Chem.*, **1990**, 1, 389-399.
61. Trieflinger, C., Rurack, K., Daub, M., "Turn ON/OFF your LOV light": boron-dipyrromethene-flavin dyads as biomimetic switches derived from the LOV domain. *Angew. Chem. Int. Ed.*, **2005**, 44, 2288-2291.
62. Golovkova, T. A., Kozlov, D. V., Neckers, D. C., Synthesis and properties of novel fluorescent switches. *J. Org. Chem.*, **2005**, 70, 5545-5549.
63. Turfan, B., Akkaya, E. U., Modulation of boradiazaindacene emission by cation-mediated oxidative PET. *Org. Lett.*, **2002**, 4, 2857-2859.
64. Rurack, K., Kollmannsberger, M., Daub, J., Molecular switching in the near infrared (NIR) with a functionalized boron - dipyrromethene dye. *Angew. Chem. Int. Ed.*, **2001**, 40, 385-387.
65. Baki, C. N., Akkaya, E. U., Boradiazaindacene-appended calix[4]arene: fluorescence sensing of pH near neutrality. *J. Org. Chem.*, **2001**, 66, 1512-1513.
66. Cha, N. R., Moon, S. Y., Chang, S. K., New ON-OFF type Ca^{2+}-selective fluoroionophore having boron-dipyrromethene fluorophores. *Tetrahedron Lett.*, **2003**, 44, 8265-8268.
67. Wu, Y. K., Peng, X. J., Guo, B. C., Fan, J. L., Zhang, Z. C., Wang, J. Y., Cui, A. J., Gao, Y. L., Boron dipyrromethene fluorophore based fluorescence sensor for the selective imaging of Zn(II) in living cells. *Org. Biomol. Chem.*, **2005**, 3, 1387-1392.
68. Ziessel, R., Ulrich, G., Harriman, A., The chemistry of Bodipy: a new El Dorado for fluorescence tools. *New J. Chem.*, **2007**, 31, 496-501.
69. Bura, T., Ziessel, R., Design, synthesis and redox properties of a fluorene platform linking two different Bodipy dyes. *Tetrahedron Lett.*, **2010**, 51, 2875-2879.
70. Rachford, A. A., Ziessel, R., Bura, T., Retailleau, P., Castellano, F. N., Boron dipyrromethene (Bodipy) phosphorescence revealed in $[Ir(ppy)_2(bpy\text{-}C{\equiv}C\text{-}Bodipy]^+$. *Inorg. Chem.*, **2010**, 49, 3730-3736.
71. Rogers, M. A. T., Tetra-arylazadipyrromethines - a new class of synthetic colouring matter. *Nature*, **1943**, 151, 504-504.
72. Rogers, M. A. T., 2,4-diarylpyrroles. I. Synthesis of 2,4-diarylpyrroles and 2,2',4,4'-tetra-arylazadipyrromethines. *J. Chem. Soc.*, **1943**, 590-596.

73. Davies, W. H., Rogers, M. A. T., 2,4-diarylpyrroles. IV. Formation of acylated 5-amino-2,4-diphenylpyrroles from β-benzoyl-α-phenylpropionitrile and some notes on the Leuckart reaction. *J. Chem. Soc.*, **1944**, 126-131.
74. Knott, E. B., β-Cycloylpropionitriles: conversion into bis-2-(5-cyclylpyrrole)azamethin salts. *J. Chem. Soc.*, **1947**, 1196-1201.
75. Rio, Y., Rodriguez-Morgade, M. S., Torres, T., Modulating the electronic properties of porphyrinoids: a voyage from the violet to the infrared regions of the electromagnetic spectrum. *Org. Biomol. Chem.*, **2008**, 6, 1877-1894.
76. Mack, J., Kobayashi, N., Low symmetry phthalocyanines and their analogues. *Chem. Rev.*, **2011**, 111, 281-321.
77. Hall, M. J., McDonnell, S. O., Killoran, J., O'Shea, D. F., A modular synthesis of unsymmetrical tetraarylazadipyrromethenes. *J. Org. Chem.*, **2005**, 70, 5571-5578.
78. Palma, A., Gallagher, J. F., Muller-Bunz, H., Wolowska, J., McInnes, E. J. L., O'Shea, D. F., Co(II), Ni(II), Cu(II) and Zn(II) complexes of tetraphenylazadipyrromethene. *Dalton Trans.*, **2009**, 273-279.
79. Gorman, A., Killoran, J., O'Shea, C., Kenna, T., Gallagher, W. M., O'Shea, D. F., In vitro demonstration of the heavy-atom effect for photodynamic therapy. *J. Am. Chem. Soc.*, **2004**, 126, 10619-10631.
80. Hall, M. J., Allen, L. T., O'Shea, D. F., PET modulated fluorescent sensing from the BF_2 chelated azadipyrromethene platform. *Org. Biomol. Chem.*, **2006**, 4, 776-780.
81. Byrne, A. T., O'Connor, A. E., Hall, M., Murtagh, J., O'Neill, K., Curran, K. M., Mongrain, K., Rousseau, J. A., Lecomte, R., McGee, S., Callanan, J. J., O'Shea, D. F., Gallagher, W. M., Vascular-targeted photodynamic therapy with BF_2-chelated tetraaryl-azadipyrromethene agents: a multi-modality molecular imaging approach to therapeutic assessment. *Br. J. Cancer*, **2009**, 101, 1565-1573.
82. Coskun, A., Yilmaz, M. D., Akkaya, E. U., Bis(2-pyridyl)-substituted boratriazaindacene as an NIR-emitting chemosensor for Hg(II). *Org. Lett.*, **2007**, 9, 607-609.
83. Teets, T. S., Partyka, D. V., Esswein, A. J., Updegraff, J. B., Zeller, M., Hunter, A. D., Gray, T. G., Luminescent, three-coordinate azadipyrromethene complexes of d^{10} copper, silver, and gold. *Inorg. Chem.*, **2007**, 46, 6218-6220.
84. Teets, T. S., Updegraff, J. B., Esswein, A. J., Gray, T. G., Three-coordinate, phosphine-ligated azadipyrromethene complexes of univalent group 11 metals. *Inorg. Chem.*, **2009**, 48, 8134-8144.
85. Partyka, D. V., Deligonul, N., Washington, M. P., Gray, T. G., *fac*-tricarbonyl rhenium(I) azadipyrromethene complexes. *Organometallics*, **2009**, 28, 5837-5840.
86. Teets, T. S., Partyka, D. V., Updegraff, J. B., Gray, T. G., Homoleptic, four-coordinate azadipyrromethene complexes of d^{10} zinc and mercury. *Inorg. Chem.*, **2008**, 47, 2338-2346.
87. Telfer, S. G., Wuest, J. D., Metallotectons: using enantiopure tris(dipyrrinato) cobalt(III) complexes to build chiral molecular materials. *Chem. Commun.*, **2007**, , 3166-3168.
88. Telfer, S. G., McLean, T. M., Waterland, M. R., Exciton coupling in coordination compounds. *Dalton Trans.*, **2011**, 40, 3097-3108.
89. Kasha, M., Rawls, H. R., Ashraf El-Bayoumi, M., The exciton model in molecular spectroscopy. *Pure Appl. Chem.*, **1965**, 11, 371-392.

90. Sazanovich, I. V., Kirmaier, C., Hindin, E., Yu, L. H., Bocian, D. F., Lindsey, J. S., Holten, D., Structural control of the excited-state dynamics of bis(dipyrrinato)zinc complexes: self-assembling chromophores for light-harvesting architectures. *J. Am. Chem. Soc.*, **2004**, 126, 2664-2665.
91. Thoi, V. S., Stork, J. R., Magde, D., Cohen, S. M., Luminescent dipyrrinato complexes of trivalent group 13 metal ions. *Inorg. Chem.*, **2006**, 45, 10688-10697.
92. McLean, T. M., Cleland, D. M., Gordon, K. C., Telfer, S. G., Waterland, M. R., Raman spectroscopy of dipyrrins: non-resonant, resonant, and surface-enhanced cross-sections and enhancement factors. *J. Raman Spectrosc.*, **2011**, 42, 2154-2164
93. Yadav, M., Kumar, P., Pandey, D. S., Heteroleptic rhodium complexes containing both the dipyrrin/cyclooctadiene ligands and application of [(η^4-C_8H_{12})Rh(4-pyrdpm)] in the construction of homo-/hetero-bimetallic complexes. *Polyhedron*, **2010**, 29, 791-800.
94. Maeda, H., Hashimoto, T., Nanoscale metal coordination macrocycles fabricated by using "dimeric" dipyrrins. *Chem. Eur. J.*, **2007**, 13, 7900-7907.
95. Salazar-Mendoza, D., Baudron, S. A., Hosseini, M. W., Many faces of dipyrrins: from hydrogen-bonded networks to homo- and heteronuclear metallamacrocycles. *Inorg. Chem.*, **2008**, 47, 766-768.
96. Baudron, S. A., Dipyrrin based homo- and hetero-metallic infinite architectures. *CrystEngComm*, **2010**, 12, 2288-2295.
97. Bronner, C., Baudron, S. A., Hosseini, M. W., Carboxylic acid appended dipyrrin for the formation of a hexanuclear iridium/copper paddlewheel complex. *Inorg. Chem.*, **2010**, 49, 8659-8661.
98. King, E. R., Betley, T. A., C-H Bond amination from a ferrous dipyrromethene complex. *Inorg. Chem.*, **2009**, 48, 2361-2363.
99. Scharf, A. B., Betley, T. A., Electronic perturbations of iron dipyrrinato complexes via ligand β-halogenation and *meso*-fluoroarylation. *Inorg. Chem.*, **2011**, 50, 6837-6845.
100. King, E. R., Hennessy, E. T., Betley, T. A., Catalytic C-H bond amination from high-spin iron imido complexes. *J. Am. Chem. Soc.*, **2011**, 133, 4917-4923.
101. Ma, L., Shin, J.-Y., Patrick, B. O., Dolphin, D., Metal complexes of dipyrromethenes linked by rigid spacer arms. *CrystEngComm*, **2008**, 10, 1531-1533.
102. Crawford, S. M., Al-Sheikh Ali, A., Cameron, T. S., Thompson, A., Synthesis and characterization of fluorescent pyrrolyldipyrrinato Sn(IV) complexes. *Inorg. Chem.*, **2011**, 50, 8207-8213.
103. Ali, A. A., Cipot-Wechsler, J., Crawford, S. M., Selim, O., Stoddard, R. L., Cameron, T. S., Thompson, A., The first series of alkali dipyrrinato complexes. *Can. J. Chem.*, **2010**, 88, 725-735.
104. Kirgan, R. A., Sullivan, B. P., Rillema, D. P., *Photochemistry and photophysics of coordination compounds: rhenium*, in *Photochemistry and photophysics of coordination compounds II*2007. p. 45-100.
105. Goud, T. V., Tutar, A., Biellmann, J.-F., Synthesis of 8-heteroatom-substituted 4,4-difluoro-4-bora-3a,4a-diaza-s-indacene dyes (BODIPY). *Tetrahedron*, **2006**, 62, 5084-5091.
106. Clezy, P. S., Smythe, G. A., Chemistry of pyrrolic compounds: dipyrrylthiones. *Aust. J. Chem.*, **1969**, 22, 239-&.

107. Pena-Cabrera, E., Aguilar-Aguilar, A., Gonzalez-Dominguez, M., Lager, E., Zamudio-Vazquez, R., Godoy-Vargas, J., Villanueva-Garcia, F., Simple, general, and efficient synthesis of meso-substituted borondipyrromethenes from a single platform. *Org. Lett.*, **2007**, 9, 3985-3988.
108. Smekal, A., The quantum theory of dispersion. *Naturwissenschaften*, **1923**, 11, 873-875.
109. Raman, C. V., Krishnan, K. S., A new type of secondary radiation. *Nature*, **1928**, 121, 501-502.
110. *The nobel prize winners: physics*. **1989**, Pasadena: Salem Press Inc.
111. Smith, E., Dent, G., *Modern Raman spectrosopy: a practical approach*. **2005**, England: John Wiley and Sons Ltd.
112. Petry, R., Schmitt, M., Popp, J., Raman spectroscopy – a prospective tool in the life sciences. *ChemPhysChem*, **2003**, 4, 14-30.
113. McCreery, R. L., *Raman spectroscopy for chemical analysis*. **2000**, New York: Wiley Interscience.
114. Placzek, G., *Handbuch der radiologie*. **1934**, Leipzig: Academische Verlag.
115. Skoog, D. A., Holler, F. J., Crouch, S. R., *Principles of Instrumental Analysis*. **2007**, Belmont: Thomson Brooks/Cole.
116. Kneipp, J., Kneipp, H., Kneipp, K., SERS - a single-molecule and nanoscale tool for bioanalytics. *Chem. Soc. Rev.*, **2008**, 37, 1052-1060.
117. Haynes, C. L., McFarland, A. D., Van Duyne, R. P., Surface-enhanced Raman spectroscopy. *Anal. Chem.*, **2005**, 77, 338A-346A.
118. Schrader, B. *Infrared and Raman spectroscopy: methods and application*. **1995**, Weinheim: VCH.
119. Long, D. A., *The Raman effect: a unified treatment of the theory of Raman scattering by molecules*. **2002**, London: John Wiley & Sons Inc.
120. Long, D. A., *Raman spectroscopy*. **1977**, Great Britain: McGraw-Hill Inc.
121. Baena, J. R., Lendl, B., Raman spectroscopy in chemical bioanalysis. *Curr. Opin. Chem. Biol.*, **2004**, 8, 534–539.
122. Fleischmann, M., Hendra, P. J., McQuillan, A. J., Raman spectra of pyridine adsorbed at a silver electrode. *Chem. Phys. Lett.*, **1974**, 26, 163-6.
123. Doering, W. E., Nie, S. M., Single-molecule and single-nanoparticle SERS: examining the roles of surface active sites and chemical enhancement. *J. Phys. Chem. B*, **2002**, 106, 311-317.
124. Haynes, C. L., Van Duyne, R. P., Plasmon-sampled surface-enhanced Raman excitation spectroscopy. *J. Phys. Chem. B*, **2003**, 107, 7426-7433.
125. Willets, K. A., Van Duyne, R. P., Localized surface plasmon resonance spectroscopy and sensing. *Annu. Rev. Phys. Chem.*, **2007**, 58, 267-297.
126. Lombardi, J. R., Birke, R. L., A unified view of surface-enhanced Raman scattering. *Acc. Chem. Res.*, **2009**, 42, 734-742.
127. Le Ru, E. C., Blackie, E., Meyer, M., Etchegoin, P. G., Surface enhanced Raman scattering enhancement factors: a comprehensive study. *J. Chem. Phys. C*, **2007**, 111, 13794-13803.
128. Kneipp, K., Wang, Y., Kneipp, H., Itzkan, I., Dasari, R. R., Feld, M. S., Population pumping of excited vibrational states by spontaneous surface-enhanced Raman scattering. *Phys. Rev. Lett.*, **1996**, 76, 2444-2447.
129. Michaels, A. M., Nirmal, M., Brus, L. E., Surface enhanced Raman spectroscopy of individual rhodamine 6G molecules on large Ag nanocrystals. *J. Am. Chem. Soc.*, **1999**, 121, 9932-9939.

130. Talley, C. E., Jackson, J. B., Oubre, C., Grady, N. K., Hollars, C. W., Lane, S. M., Huser, T. R., Nordlander, P., Halas, N. J., Surface-enhanced Raman scattering from individual Au nanoparticles and nanoparticle dimer substrates. *Nano Lett.*, **2005**, 5, 1569-1574.
131. Kneipp, K., Wang, Y., Kneipp, H., Perelman, L. T., Itzkan, I., Dasari, R. R., Feld, M. S., Single molecule detection using surface-enhanced Raman scattering (SERS). *Phys. Rev. Lett.*, **1997**, 78, 1667-1670.
132. Nie, S., Emory, S. R., Probing single molecules and single nanoparticles by surface-enhanced Raman scattering. *Science*, **1997**, 275, 1102-1106.
133. Otter, C. A., Patty, P. J., Williams, M. A. K., Waterland, M. R., Telfer, S. G., Mechanically interlocked gold and silver nanoparticles using metallosupramolecular catenane chemistry. *Nanoscale*, **2011**, 3, 941-944.
134. Clark, B. J., Frost, T., Russell, M. A., eds. *UV spectroscopy - techniques, instrumentation, data handling*. Techniques in visible and ultraviolet spectometry Vol. 4. 1993, Chapman & Hall: London.
135. Perkampus, H.-H., *UV-Vis spectroscopy and its applications*. **1992**, Berlin: Springer-Verlag.
136. Shriver, D. F., Atkins, P. W., *Inorganic Chemistry*. **1999**, Oxford: Oxford University Press.
137. Housecroft, C. E., Sharpe, A. G., *Inorganic chemistry*. **2005**, New Jersey: Pearson Prentice Hall.
138. Klessinger, M., Michl, J., *Excited states and photochemistry of organic molecules*. **1995**, New York: VCH Publishers.
139. Kasha, M., Characterization of electronic transitions in complex molecules. *Discuss. Faraday Soc.*, **1950**, 14-19.
140. Lakowicz, J. R., *Principles of fluorescence spectroscopy*. **2006**, New York: Springer.
141. Cato, M. A., ed. *Focus on organometallic chemistry research*. 2005, Nova Science Publishers, Inc.: New York.
142. Kawaoka, K., Khan, A. U., Kearns, D. R., Role of singlet excited states of molecular oxygen in the quenching of organic triplet states. *J. Chem. Phys.*, **1967**, 46, 1842-1853.
143. Fery-Forgues, S., Lavabre, D., Are fluorescence quantum yields so tricky to measure? A demonstration using familiar stationery products. *J. Chem. Educ.*, **1999**, 76, 1260-1264.
144. Le Ru, E. C., Etchegoin, P. G., *Principles of surface-enhanced Raman spectroscopy and related plasmonic effects*. **2009**, Great Britain: Elsevier.
145. Frisch, M. J., Trucks, G. W., Schlegel, H. B., Scuseria, G. E., Robb, M. A., Cheeseman, J. R., Scalmani, G., Barone, V., Mennucci, B., Petersson, G. A., Nakatsuji, H., Caricato, M., Li, X., Hratchian, H. P., Izmaylov, A. F., Bloino, J., Zheng, G., Sonnenberg, J. L., Hada, M., Ehara, M., Toyota, K., Fukuda, R., Hasegawa, J., Ishida, M., Nakajima, T., Honda, Y., Kitao, O., Nakai, H., Vreven, T., Montgomery, J., J. A., Peralta, J. E., Ogliaro, F., Bearpark, M., Heyd, J. J., Brothers, E., Kudin, K. N., Starverov, V. N., Kobayashi, R., Normand, J., Raghavachari, K., Rendell, A., Burant, J. C., Iyengar, S. S., Tomasi, J., Cossi, M., Rega, N., Millam, J. M., Klene, M., Knox, J. E., Cross, J. B., Bakken, V., Adamo, C., Jaramillo, J., Gomperts, R., Stratmann, R. E., Yazyev, O., Austin, A. J., Cammi, R., Pomelli, C., Ochterski, J. W., Martin, R. L., Morokuma, K., Zakrzewski, V. G., Voth, G. A., Salvador, P., Dannenberg, J.

J., Dapprich, S., Daniels, A. D., Farkas, O., Foresman, J. B., Ortiz, J. V., Cioslowski, J., Fox, D. J., *Gaussian 09*. **2009**, Wallingford CT: Gaussian, Inc.
146. Becke, A. D., Density-functional thermochemistry. II. The effect of the Perdew-Wang generalized-gradient correlation correction. *J. Chem. Phys.*, **1992**, 97, 9173.
147. Lee, C., Yang, W., Parr, R. G., Development of the Colle-Salvetti correlation-energy formula into a functional of the electron density. *Phys. Rev. B*, **1988**, 37, 785.
148. Hoe, W.-M., Cohen, A. J., Handy, N. C., Assessment of a new local exchange functional OPTX. *Chem. Phys. Lett.*, **2001**, 341, 319-328.
149. Handy, N. C., Cohen, A. J., Left-right correlation energy. *Mol. Phys.*, **2001**, 99, 403-412.
150. Zhao, Y., Truhlar, D. G., The M06 suite of density functionals for main group thermochemistry, thermochemical kinetics, noncovalent interactions, excited states, and transition elements: two new functionals and systematic testing of four M06-class functionals and 12 other functionals. *Theor. Chem. Acc.*, **2008**, 120, 215-241.
151. Cossi, M., Rega, N., Scalmani, G., Barone, V., Energies, structures, and electronic properties of molecules in solution with the C-PCM solvation model. *J. Comput. Chem.*, **2003**, 24, 669-681.
152. O'Boyle, N. M., Tenderholt, A. L., Langner, K. M., A library for package-independent computational chemistry algorithms. *J. Comput. Chem.* , **2007**, 29, 839-845.
153. Andersson, M. P., Uvdal, P., New scale factors for harmonic vibrational frequencies using the B3LYP density functional method with the triple-ξ basis set 6-311+G(d,p). *J. Phys. Chem. A*, **2005**, 109, 2937-2941.
154. Tantirungrotechai, Y., Phanasant, K., Roddecha, S., Surawatanawong, P., Sutthikhum, V., Limtrakul, J., Scaling factors for vibrational frequencies and zero-point vibrational energies of some recently developed exchange-correlation functionals. *Theochem-J. Mol. Struct.*, **2006**, 760, 189-192.
155. Alecu, I. M., Zheng, J. J., Zhao, Y., Truhlar, D. G., Computational thermochemistry: scale factor databases and scale factors for vibrational frequencies obtained from electronic model chemistries. *J. Chem. Theory Comput.*, **2010**, 6, 2872-2887.
156. Lee, P. C., Meisel, D., Adsorption and surface-enhanced Raman of dyes on silver and gold sols. *J. Phys. Chem.*, **1982**, 86, 3391-3395.
157. Le Ru, E. C., Meyer, M., Etchegoin, P. G., Proof of single-molecule sensitivity in surface enhanced Raman scattering (SERS) by means of a two-analyte technique. *J. Chem. Phys. B*, **2006**, 110, 1944-1948.
158. Moran, A. M., Delbecque, C., Kelley, A. M., Solvent effects on ground and excited electronic state structures of the push-pull chromophore julolidinyl-n-N,N'-diethylthiobarbituric acid. *J. Phys. Chem. A*, **2001**, 105, 10208-10219.
159. Trulson, M. O., Mathies, R. A., Raman cross-section measurements in the visible and ultraviolet using an integrating cavity: application to benzene, cyclohexane, and cacodylate. *J. Chem. Phys.*, **1986**, 84, 2068-2074.
160. Egolf, D. S., Waterland, M. R., Kelley, A. M., Resonance Raman intensity analysis of the carbazole/tetracyanoethylene charge-transfer complex: mode-specific reorganization energies for a hole-transport molecule. *J. Phys. Chem. B*, **2000**, 104, 10727-10737.

161. Myers, A. B., *Laser techniques in chemistry*. **1995**, New York: John WIley & Sons Inc.
162. Zhao, J., Jensen, L., Sung, J. H., Zou, S. L., Schatz, G. C., Van Duyne, R. P., Interaction of plasmon and molecular resonances for rhodamine 6G adsorbed on silver nanoparticles. *J. Am. Chem. Soc.*, **2007**, 129, 7647-7656.
163. Walters, V. A., Depaula, J. C., Babcock, G. T., Leroi, G. E., Resonance Raman spectrum of the lowest triplet state of zinc(II) tetraphenylporphyrin. *J. Am. Chem. Soc.*, **1989**, 111, 8300-8302.
164. Li, X. Y., Czernuszewicz, R. S., Kincaid, J. R., Su, Y. O., Spiro, T. G., Consistent porphyrin force-field. 1. Normal-mode analysis for nickel porphine and nickel tetraphenylporphine from resonance Raman and infrared spectra and isotope shifts. *J. Phys. Chem.*, **1990**, 94, 31-47.
165. Walsh, P. J., Gordon, K. C., Wagner, P., Officer, D. L., Resonance Raman studies of β-substituted porphyrin systems with unusual electronic absorption properties. *ChemPhysChem*, **2006**, 7, 2358-2365.
166. Zhao, X. H., Burt, J. A., McHale, J. L., Resonance Raman analysis of nonlinear solvent dynamics: Betaine-30 in ethanol. *J. Chem. Phys.*, **2004**, 121, 11195-11201.
167. Biswas, N., Umapathy, S., Resonance Raman study of the solvent dynamics for ultrafast charge transfer transition in 4-nitro-4'-dimethylamino-azobenzene. *J. Chem. Phys.*, **2003**, 118, 5526-5536.
168. Shoute, L. C. T., Loppnow, G. R., Excited-state metal-to-ligand charge transfer dynamics of a ruthenium(II) dye in solution and adsorbed on TiO_2 nanoparticles from resonance Raman spectroscopy. *J. Am. Chem. Soc.*, **2003**, 125, 15636-15646.
169. Pristinski, D., Tan, S., Erol, M., Du, H., Sukhishvili, S., In situ SERS study of rhodamine 6G adsorbed on individually immobilized Ag nanoparticles. *J. Raman Spectrosc.*, **2006**, 37, 762–770.
170. Albrecht, A. C., Theory of Raman intensities. *J. Chem. Phys.*, **1961**, 34, 1476-1484.
171. Nordlander, P., Prodan, E., Plasmon hybridization in nanoparticles near metallic surfaces. *Nano Lett.*, **2004**, 4, 2209-2213.
172. Vogel, N., Fischer, J., Mohammadi, R., Retsch, M., Butt, H. J., Landfester, K., Weiss, C. K., Kreiter, M., Plasmon hybridization in stacked double crescents arrays fabricated by colloidal lithography. *Nano Lett.*, **2011**, 11, 446-454.
173. Cathcart, N., Frank, A. J., Kitaev, V., Silver nanoparticles with planar twinned defects: effect of halides for precise tuning of plasmon resonance maxima from 400 to > 900 nm. *Chem. Commun.*, **2009**, 7170-7172.
174. Bergstrom, F., Mikhalyov, I., Hagglof, P., Wortmann, R., Ny, T., Johansson, L. B.-A., Dimers of dipyrrometheneboron difluoride (BODIPY) with light spectroscopic applications in chemistry and biology. *J. Am. Chem. Soc.*, **2002**, 124, 196-204.
175. Mikhalyov, l., Gretskaya, N., Bergstrom, F., Johansson, L. B.-A., Electronic ground and excited state properties of dipyrrometheneboron difluoride (BODIPY): dimers with application to biosciences. *Phys. Chem. Chem. Phys.*, **2002**, 4, 5663-5670.
176. Sasai, R., Fujita, T., Iyi, N., Itoh, H., Takagi, K., Aggregated structures of rhodamine 6G intercalated in a fluor-taeniolite thin film. *Langmuir*, **2002**, 18, 6578-6583.

177. Li, R., Ren, J., de Queiroz, T. B., de Camargo, A. S. S., Eckert, H., Fluorescent $AlPO_4$ gels and glasses doped with rhodamine 6G: preparation, structural and optical characterization. *J. Non-Cryst. Solids*, **2010**, 356, 2089-2096.
178. Jackson, J. D., *Classical electrodynamics*. **1999**, New York: John Wiley & Sons Ltd.
179. Telfer, S. G., Tajima, N., Kuroda, R., Cantuel, M., Piguet, C., CD spectra of d-f heterobimetallic helicates with segmental di-imine ligands. *Inorg. Chem.*, **2004**, 43, 5302-5310.
180. Seibt, J., Marquetand, P., Engel, V., Chen, Z., Dehrn, V., Wurthner, F., On the geometry dependence of molecular dimer spectra with an application to aggregates of perylene bisimide. *Chem. Phys.*, **2006**, 328, 354-362.
181. Palmer, G., Esposti, M. D., Application of exciton coupling theory to the structure of mitochondrial cytochrome b. *Biochem.*, **1994**, 33, 176-185.
182. Ziegler, M., von Zelewsky, A., Charge-transfer excited state properties of chiral transition metal coordination compounds studied by chiroptical spectroscopy. *Coord. Chem. Rev.*, **1998**, 177, 257-300.
183. Rodger, A., Norden, B., *Circular dichroism and linear dichroism*. **1997**, Oxford: Oxford University Press.
184. Bosnich, B., Application of exciton theory to determination of absolute configurations of inorganic complexes. *Acc. Chem. Res.*, **1969**, 2, 266-273.
185. Scholes, G. D., Quantum-coherent electronic energy transfer: did nature think of it first? *J. Phys. Chem. Lett.*, **2010**, 1, 2-8.
186. Gromilov, S. A., Baidina, I. A., Stabnikov, P. A., Romanenko, G. V., Crystal structure of copper(II) bis-hexafluoroacetylacetonate. *J. Struct. Chem.*, **2004**, 45, 476-481.
187. Fergusson, J. E., March, F. C., Couch, D. A., Emerson, K., Robinson, W. T., Dipyrromethene complexes of transition metals: stereochemistry of complexes of cobalt(II), nickel(II), copper(II), zinc(II), cadmium(II), mercury(II), and palladium(II), and crystal structure analysis of palladium complex. *J. Chem. Soc. A*, **1971**, 440-448.
188. Kee, H. L., Kirmaier, C., Yu, L., Thamyongkit, P., Youngblood, W. J., Calder, M. E., Ramos, L., Noll, B. C., Bocian, D. F., Scheidt, W. R., Birge, R. R., Lindsey, J. S., Holten, D., Structural control of the photodynamics of boron-dipyrrin complexes. *J. Phys. Chem. B*, **2005**, 109, 20433-20443.
189. Cotton, F. A., DeBoer, B. G., Pipal, J. R., Crystal and molecular structure of bis(3,3',5,5'-tetramethyldipyrromethenato)nickel(II). *Inorg. Chem.*, **1970**, 9, 783-788.
190. Morgan, O., Wang, S., Bae, S. A., Morgan, R. J., Baker, A. D., Strekas, T. C., Engel, R., Two complete stereochemical sets of dinuclear ruthenium complexes. *J. Chem. Soc.-Dalton Trans.*, **1997**, 3773-3776.
191. Campagna, S., Puntoriero, F., Nastasi, F., Bergamini, G., Balzani, V., Photochemistry and photophysics of coordination compounds: ruthenium, in *Topics in current chemistry: photochemistry and photophysics of coordination compounds I*, **2007**, Springer-Verlag Berlin: Berlin.
192. Juris, A., Balzani, V., Barigelletti, F., Campagna, S., Belser, P., Vonzelewsky, A., Ru(II) polypyridine complexes - photophysics, photochemistry, electrochemistry, and chemiluminescence. *Coord. Chem. Rev.*, **1988**, 84, 85-277.
193. Hagfeldt, A., Grätzel, M., Molecular photovoltaics. *Acc. Chem. Res.*, **2000**, 33, 269-277.

194. Hagfeldt, A., Boschloo, G., Sun, L. C., Kloo, L., Pettersson, H., Dye-sensitized solar cells. *Chem. Rev.*, **2010**, 110, 6595-6663.
195. Li, L., Duan, L. L., Xu, Y. H., Gorlov, M., Hagfeldt, A., Sun, L. C., A photoelectrochemical device for visible light driven water splitting by a molecular ruthenium catalyst assembled on dye-sensitized nanostructured TiO_2. *Chem. Commun.*, **2010**, 46, 7307-7309.
196. Piers, W. E., Future trends in organometallic chemistry: organometallic approaches to water splitting. *Organometallics*, **2011**, 30, 13-16.
197. Livanov, K., Madhu, V., Balaraman, E., Shimon, L. J. W., Diskin-Posner, Y., Neumann, R., Photocatalytic splitting of CS_2 to S_8 and a carbon-sulfur polymer catalyzed by a bimetallic ruthenium(II) compound with a tertiary amine binding site: toward photocatalytic splitting of CO_2? *Inorg. Chem.*, **2011**, 50, 11273-11275.
198. Takeda, H., Ishitani, O., Development of efficient photocatalytic systems for CO_2 reduction using mononuclear and multinuclear metal complexes based on mechanistic studies. *Coord. Chem. Rev.*, **2010**, 254, 346-354.
199. Koike, K., Naito, S., Sato, S., Tamaki, Y., Ishitani, O., Architecture of supramolecular metal complexes for photocatalytic CO_2 reduction III: effects of length of alkyl chain connecting photosensitizer to catalyst. *J. Photochem. Photobiol. A-Chem.*, **2009**, 207, 109-114.
200. Ghosh, A., Das, P., Gill, M. R., Kar, P., Walker, M. G., Thomas, J. A., Das, A., Photoactive Ru(II)-polypyridyl complexes that display sequence selectivity and high-affinity binding to duplex DNA through groove binding. *Chem. Eur. J.*, **2011**, 17, 2089-2098.
201. Morgan, J. L., Spillane, C. B., Smith, J. A., Buck, D. P., Collins, J. G., Keene, R., Dinuclear ruthenium(II) complexes with flexible bridges as non-duplex DNA binding agents. *Dalton Trans.*, **2007**, 4333-4342.
202. Smith, J. A., Collins, J. G., Patterson, B. T., Keene, F. R., Total enantioselectivity in the DNA binding of the dinuclear ruthenium(II) complex $[\{Ru(Me_2bpy)_2\}_2(\mu\text{-bpm})]^{4+}$ {bpm = 2,2'-bipyrimidine; Me_2bpy = 4,4'-dimethyl-2,2'-bipyridine}. *Dalton Trans.*, **2004**, 1277-1283.
203. Spillane, C. B., Morgan, J. L., Fletcher, N. C., Collins, J. G., Keene, F. R., Inert benzothiazole functionalised ruthenium(II) complexes; potential DNA hairpin binding agents. *Dalton Trans.*, **2006**, 3122-3133.
204. Spillane, C. B., Smith, J. A., Morgan, J. L., Keene, F. R., DNA affinity binding studies using a fluorescent dye displacement technique: the dichotomy of the binding site. *J. Biol. Inorg. Chem.*, **2007**, 12, 819-824.
205. Gonzalez, V., Wilson, T., Kurihara, I., Imai, A., Thomas, J. A., Otsuki, J., A dinuclear ruthenium(II) complex that functions as a label-free colorimetric sensor for DNA. *Chem. Commun.*, **2008**, 1868-1870.
206. Pascu, G. I., Hotze, A. C. G., Sanchez-Cano, C., Kariuki, B. M., Hannon, M. J., Dinuclear ruthenium(II) triple-stranded helicates: luminescent supramolecular cylinders that bind and coil DNA and exhibit activity against cancer cell lines. *Angew. Chem., Int. Edit.*, **2007**, 46, 4374-4378.
207. Ghosh, A., Mandoli, A., Kumar, D. K., Yadav, N. S., Ghosh, T., Jha, B., Thomas, J. A., Das, A., DNA binding and cleavage properties of a newly synthesised Ru(II)-polypyridyl complex. *Dalton Trans.*, **2009**, 9312-9321.
208. Liu, Y.-J., Zeng, C.-H., Synthesis and DNA interaction studies of ruthenium(II) complexes with isatino[1,2-b]-1,4,8,9-tetraazatriphenylene as an intercalative ligand. *Transit. Met. Chem.*, **2009**, 34, 455-462.

209. Suss-Fink, G., Arene ruthenium complexes as anticancer agents. *Dalton Trans.*, **2010**, 39, 1673-1688.
210. Fricker, S. P., Metal based drugs: from serendipity to design. *Dalton Trans.*, **2007**, 4903-4917.
211. Rose, M. J., Mascharak, P. K., Photoactive ruthenium nitrosyls: effects of light and potential application as NO donors. *Coord. Chem. Rev.*, **2008**, 252, 2093-2114.
212. Fry, N. L., Mascharak, P. K., Photoactive ruthenium nitrosyls as NO donors: how to sensitize them toward visible light. *Acc. Chem. Res.*, **2011**, 44, 289-298.
213. Smestad, G. P., *Optoelectronics of solar cells*. **2002**, Bellingham: SPIE.
214. Grätzel, M., Photovoltaic and photoelectrochemical conversion of solar energy. *Philos. Trans. R. Soc. A-Math. Phys. Eng. Sci.*, **2007**, 365, 993-1005.
215. Ardo, S., Meyer, G. J., Photodriven heterogeneous charge transfer with transition-metal compounds anchored to TiO_2 semiconductor surfaces. *Chem. Soc. Rev.*, **2009**, 38, 115-164.
216. Nazeeruddin, M. K., Kay, A., Rodicio, I., Humphrybaker, R., Muller, E., Liska, P., Vlachopoulos, N., Grätzel, M., Conversion of light to electricity by *cis*-X_2bis(2,2'-bipyridyl-4,4'-dicarboxylate)ruthenium(II) charge-transfer sensitizers (X = Cl^-, Br^-, I^-, CN^-, and SCN^-) on nanocrystalline TiO_2 electrodes. *J. Am. Chem. Soc.*, **1993**, 115, 6382-6390.
217. Nazeeruddin, M. K., Zakeeruddin, S. M., Humphry-Baker, R., Jirousek, M., Liska, P., Vlachopoulos, N., Shklover, V., Fischer, C. H., Grätzel, M., Acid-base equilibria of (2,2'-bipyridyl-4,4'-dicarboxylic acid)ruthenium(II) complexes and the effect of protonation on charge-transfer sensitization of nanocrystalline titania. *Inorg. Chem.*, **1999**, 38, 6298-6305.
218. Nazeeruddin, M. K., Pechy, P., Grätzel, M., Efficient panchromatic sensitization of nanocrystalline TiO_2 films by a black dye based on a trithiocyanato-ruthenium complex. *Chem. Commun.*, **1997**, 1705-1706.
219. Wang, P., Zakeeruddin, S. M., Humphry-Baker, R., Moser, J. E., Grätzel, M., Molecular-scale interface engineering of TiO_2 nanocrystals: improving the efficiency and stability of dye-sensitized solar cells. *Adv. Mater.*, **2003**, 15, 2101-2104.
220. Fujishima, A., Honda, K., Electrochemical photolysis of water at a semiconductor electrode. *Nature*, **1972**, 238, 37-40.
221. Poverenov, E., Efremenko, I., Frenkel, A. I., Ben-David, Y., Shimon, L. J. W., Leitus, G., Konstantinovski, L., Martin, J. M. L., Milstein, D., Evidence for a terminal Pt(IV)-oxo complex exhibiting diverse reactivity. *Nature*, **2008**, 455, 1093-1096.
222. Walter, M. G., Warren, E. L., McKone, J. R., Boettcher, S. W., Mi, Q. X., Santori, E. A., Lewis, N. S., Solar water splitting cells. *Chem. Rev.*, **2010**, 110, 6446-6473.
223. Esswein, M. J., Nocera, D. G., Hydrogen production by molecular photocatalysis. *Chem. Rev.*, **2007**, 107, 4022-4047.
224. Kanan, M. W., Nocera, D. G., In situ formation of an oxygen-evolving catalyst in neutral water containing phosphate and Co^{2+}. *Science*, **2008**, 321, 1072-1075.
225. Service, R. F., New trick for splitting water with sunlight. *Science*, **2009**, 325, 1200-1201.
226. Benko, G., Kallioinen, J., Korppi-Tommola, J. E. I., Yartsev, A. P., Sundstrom, V., Photoinduced ultrafast dye-to-semiconductor electron injection from

nonthermalized and thermalized donor states. *J. Am. Chem. Soc.*, **2002**, 124, 489-493.
227. Meyer, G. J., The 2010 millennium technology grand prize: dye-sensitized solar cells. *ACS Nano*, **2010**, 4, 4337-4343.
228. Galoppini, E., Guo, W. Z., Zhang, W., Hoertz, P. G., Qu, P., Meyer, G. J., Long-range electron transfer across molecule-nanocrystalline semiconductor interfaces using tripodal sensitizers. *J. Am. Chem. Soc.*, **2002**, 124, 7801-7811.
229. Meyer, G. J., Molecular approaches to solar energy conversion with coordination compounds anchored to semiconductor surfaces. *Inorg. Chem.*, **2005**, 44, 6852-6864.
230. Kleverlaan, C. J., Indelli, M. T., Bignozzi, C. A., Pavanin, L., Scandola, F., Hasselman, G. M., Meyer, G. J., Stepwise charge separation in heterotriads. Binuclear Ru(II)-Rh(III) complexes on nanocrystalline titanium dioxide. *J. Am. Chem. Soc.*, **2000**, 122, 2840-2849.
231. Hedley, G. J., Ruseckas, A., Harriman, A., Samuel, I. D. W., Conformational effects on the dynamics of internal conversion in boron dipyrromethene dyes in solution. *Angew. Chem., Int. Edit.*, **2011**, 50, 6634-6637.
232. Frisch, M. J., Trucks, G. W., Schlegel, H. B., Scuseria, G. E., Robb, M. A., Cheeseman, J. R., Montgomery, J., J. A.; , Vreven, T., Kudin, K. N., Burant, J. C., Millam, J. M., Iyengar, S. S., Tomasi, J., Barone, V., Mennucci, B., Cossi, M., Scalmani, G., Rega, N., Petersson, G. A., Nakatsuji, H., Hada, M., Ehara, M., Toyota, K., Fukuda, R., Hasegawa, J., Ishida, M., Nakajima, T., Honda, Y., Kitao, O., Nakai, H., Klene, M., Li, X., Knox, J. E., Hratchian, H. P., Cross, J. B., Bakken, V., Adamo, C., Jaramillo, J., Gomperts, R., Stratmann, R. E., Yazyev, O., Austin, A. J., Cammi, R., Pomelli, C., Ochterski, J. W., Ayala, P. Y., Morokuma, K., Voth, G. A., Salvador, P., Dannenberg, J. J., Zakrzewski, V. G., Dapprich, S., Daniels, A. D., Strain, M. C., Farkas, O., Malick, D. K., Rabuck, A. D., Raghavachari, K., Foresman, J. B., Ortiz, J. V., Cui, Q., Baboul, A. G., Clifford, S., Cioslowski, J., Stefanov, B. B., Liu, G., Liashenko, A., Piskorz, P., Komaromi, I., Martin, R. L., Fox, D. J., Keith, T., Al-Laham, M. A., Peng, C. Y., Nanayakkara, A., Challacombe, M., Gill, P. M. W., Johnson, B., Chen, W., Wong, M. W., Gonzalez, C., Pople, J. A., *Gaussian 03*. **2004**, Wallingford, CT: Gaussian, Inc.
233. Sierraalta, A., Martorell, G., Ehrmann, E., Anez, R., Improvement of scale factors for harmonic vibrational frequency calculations using new polarisation functions. *Int. J. Quantum Chem.*, **2008**, 108, 1036-1043.
234. Ambroise, A., Wagner, R. W., Rao, P. D., Riggs, J. A., Hascoat, P., Diers, J. R., Seth, J., Lammi, R. K., Bocian, D. F., Holten, D., Lindsey, J. S., Design and synthesis of porphyrin-based optoelectronic gates. *Chem. Mat.*, **2001**, 13, 1023-1034.
235. Sun, Y. L., Machala, M. L., Castellano, F. N., Controlled microwave synthesis of Ru(II) synthons and chromophores relevant to solar energy conversion. *Inorg. Chim. Acta*, **2010**, 363, 283-287.
236. Schwalbe, M., Schafer, B., Gorls, H., Rau, S., Tschierlei, S., Schmitt, M., Popp, J., Vaughan, G., Henry, W., Vos, J. G., Synthesis and characterisation of poly(bipyridine)ruthenium complexes as building blocks for heterosupramolecular arrays. *Eur. J. Inorg. Chem.*, **2008**, 3310-3319.
237. Wiederholt, K., McLaughlin, L. W., A 2,2'-bipyridine ligand for incorporation into oligodeoxynucleotides: synthesis, stability and fluorescence properties of ruthenium-DNA complexes. *Nucleic Acids Res.*, **1999**, 27, 2487-2493.

238. Hua, X., Lappin, A. G., Preparation and characterisation of cis-Λ–$[Ru(bpy)_2(py)(O)]^{2+}$. *Inorg. Chem.*, **1995**, 34, 992-994.
239. Takahashi, Y., Arakawa, H., Sugihara, H., Hara, K., Islam, A., Katoh, R., Tachibana, Y., Yanagida, M., Highly efficient polypyridyl-ruthenium(II) photosensitizers with chelating oxygen donor ligands: β-diketonato-bis(dicarboxybipyridine)ruthenium. *Inorg. Chim. Acta*, **2000**, 310, 169-174.
240. Caspar, R., Cordier, C., Waern, J. B., Guyard-Duhayon, C., Gruselle, M., Le Floch, P., Amouri, H., A new family of mono- and dicarboxylic ruthenium complexes $[Ru(DIP)_2L_2]^{2+}$ (DIP=4,7-diphenyl-1,10-phenanthroline): synthesis, solution behavior, and x-ray molecular structure of *trans*-$[Ru(DIP)_2(MeOH)_2][OTf]_2$. *Inorg. Chem.*, **2006**, 45, 4071-4078.
241. Mabrouk, P. A., Wrighton, M. S., Resonance Raman spectroscopy of the lowest excited state of derivatives of tris(2,2'-bipyridine)ruthenium(II): substituent effects on electron localization in mixed-ligand complexes. *Inorg. Chem.*, **1986**, 25, 526-531.
242. Dreuw, A., Head-Gordon, M., Failure of time-dependent density functional theory for long-range charge-transfer excited states: the zincbacteriochlorin−bacteriochlorin and bacteriochlorophyll−spheroidene complexes. *J. Am. Chem. Soc.*, **2004**, 126, 4007-4016.
243. Dreuw, A., Head-Gordon, M., Single-reference ab initio methods for the calculation of excited states of large molecules. *Chem. Rev.*, **2005**, 105, 4009-4037.
244. Goerigk, L., Grimme, S., Quantum chemical investigation of exciton coupling: super-molecular calculations of a merocyanine dimer aggregate. *ChemPhysChem*, **2008**, 9, 2467-2470.
245. Li, F. R., Yang, S. I., Ciringh, Y. Z., Seth, J., Martin, C. H., Singh, D. L., Kim, D. H., Birge, R. R., Bocian, D. F., Holten, D., Lindsey, J. S., Design, synthesis, and photodynamics of light-harvesting arrays comprised of a porphyrin and one, two, or eight boron-dipyrrin accessory pigments. *J. Am. Chem. Soc.*, **1998**, 120, 10001-10017.
246. Webb, M. A., Knorr, F. J., McHale, J. L., Resonance Raman spectrum of $[Ru(bipyridine)_3]^{2+}$ in water, acetonitrile and their deuterated derivatives: the possible role of solvent in excited-state charge localization. *J. Raman Spectrosc.*, **2001**, 32, 481-485.
247. Howell, S. L., Gordon, K. C., Waterland, M. R., Leung, K. H., Phillips, D. L., Resonance Raman excitation profile of a ruthenium(II) complex of dipyrido 2,3-*a*:3′,2′-*c* phenazine. *J. Phys. Chem. A*, **2006**, 110, 11194-11199.
248. Lind, S. J., Gordon, K. C., Waterland, M. R., Ultrafast dynamics in Cu(I)bisdiimine complexes from resonance Raman intensities. *J. Raman Spectrosc.*, **2008**, 39, 1556-1567.
249. Shoute, L. C. T., Loppnow, G. R., Excited-state dynamics of alizarin-sensitized TiO_2 nanoparticles from resonance Raman spectroscopy. *J. Chem. Phys.*, **2002**, 117, 842-850.
250. Fischer, J., Hall, J. D., Patty, P. J., Williams, M. A. K., Waterland, M. R., Telfer, S. G., Stereoselective aggregation of chiral complexes with threefold-symmetric pendant carboxyl groups: an example of "perfect" self-assembly not seen in the crystalline state? *Dalton Trans.*, **2011**, submitted.
251. Bond, A. M., *Broadening electrochemical horizons: principles and illustration of voltammetric and related techniques*. **2002**, New York: Oxford University Press.

252. Pavlishchuk, V. V., Addison, A. W., Conversion constants for redox potentials measured versus different reference electrodes in acetonitrile solutions at 25°C. *Inorg. Chim. Acta*, **2000**, 298, 97-102.
253. Kovala-Demertzi, D., Hadjikakou, S. K., Demertzis, M. A., Deligiannakis, Y., Metal ion-drug interactions. Preparation and properties of manganese (II), cobalt (II) and nickel (II) complexes of diclofenac with potentially interesting anti-inflammatory activity: behavior in the oxidation of 3,5-di-*tert*-butyl-*o*-catechol *J. Inorg. Biochem.*, **1998**, 69, 223-229.
254. Kulkarni, A. P., Tonzola, C. J., Babel, A., Jenekhe, S. A., Electron transport materials for organic light-emitting diodes. *Chem. Mat.*, **2004**, 16, 4556-4573.
255. Dwayne Miller, R. J., McLendon, G. L., Nozik, A. J., Schmickler, W., Willig, F., *Surface electron transfer processes*. **1995**, New York: VCH Publishers.
256. Clifford, J. N., Palomares, E., Nazeeruddin, M. K., Grätzel, M., Nelson, J., Li, X., Long, N. J., Durrant, J. R., Molecular control of recombination dynamics in dye-sensitized nanocrystalline TiO_2 films: free energy vs distance dependence. *J. Am. Chem. Soc.*, **2004**, 126, 5225-5233.
257. Haque, S. A., Palomares, E., Cho, B. M., Green, A. N. M., Hirata, N., Klug, D. R., Durrant, J. R., Charge separation versus recombination in dye-sensitized nanocrystalline solar cells: the minimization of kinetic redundancy. *J. Am. Chem. Soc.*, **2005**, 127, 3456-3462.
258. Tachibana, Y., Moser, J. E., Gratzel, M., Klug, D. R., Durrant, J. R., Subpicosecond interfacial charge separation in dye-sensitized nanocrystalline titanium dioxide films. *J. Phys. Chem.*, **1996**, 100, 20056-20062.
259. Palomares, E., Martinez-Diaz, M. V., Haque, S. A., Torres, T., Durrant, J. R., State selective electron injection in non-aggregated titanium phthalocyanine sensitised nanocrystalline TiO_2 films. *Chem. Commun.*, **2004**, 2112-2113.
260. Cid, J.-J., Yum, J.-H., Jang, S.-R., Nazeeruddin, M. K., Martínez-Ferrero, E., Palomares, E., Ko, J., Grätzel, M., Torres, T., Molecular cosensitization for efficient panchromatic dye-sensitized solar cells. *Angew. Chem., Int. Edit.*, **2007**, 46, 8358-8362.
261. Lynn, P. A., *Electricity from sunlight - an introduction to photovoltaics*. **2010**, Chichester: John Wiley & Sons Ltd.
262. Wang, P., Zakeeruddin, S. M., Exnar, I., Grätzel, M., High efficiency dye-sensitized nanocrystalline solar cells based on ionic liquid polymer gel electrolyte. *Chem. Commun.*, **2002**, 2972-2973.
263. Robertson, N., Catching the rainbow: Light harvesting in dye-sensitized solar cells. *Angew. Chem., Int. Edit.*, **2008**, 47, 1012-1014.
264. Reddy, P. Y., Giribabu, L., Lyness, C., Snaith, H. J., Vijaykumar, C., Chandrasekharam, M., Lakshmikantam, M., Yum, J.-H., Kalyanasundaram, K., Grätzel, M., Nazeeruddin, M. K., Efficient sensitization of nanocrystalline TiO_2 films by a near-IR-absorbing unsymmetrical zinc phthalocyanine. *Angew. Chem., Int. Edit.*, **2007**, 46, 373-376.
265. Burke, A., Schmidt-Mende, L., Ito, S., Grätzel, M., A novel blue dye for near-IR 'dye-sensitised' solar cell applications. *Chem. Commun.*, **2007**, 234-236.
266. Worl, L. A., Duesing, R., Chen, P. Y., Dellaciana, L., Meyer, T. J., Photophysical properties of polypyridyl carbonyl complexes of rhenium(I). *J. Chem. Soc.-Dalton Trans.*, **1991**, 849-858.
267. Sato, S., Morimoto, T., Ishitani, O., Photochemical synthesis of *mer*-$[Re(bpy)(CO)_3Cl]$. *Inorg. Chem.*, **2007**, 46, 9051-9053.

268. Sato, S., Sekine, A., Ohashi, Y., Ishitani, O., Blanco-Rodriguez, A. M., Vicek, A., Unno, T., Koike, K., Photochemical ligand substitution reactions of *fac*-[Re(bpy)$(CO)_3$Cl] and derivatives. *Inorg. Chem.*, **2007**, 46, 3531-3540.
269. Koike, K., Tanabe, J., Toyama, S., Tsubaki, H., Sakamoto, K., Westwell, J. R., Johnson, F. P. A., Hori, H., Saitoh, H., Ishitani, O., New synthetic routes to biscarbonylbipyridinerhenium(I) complexes *cis,trans*-[Re$(X_2$bpy$)(CO)_2(PR_3)(Y)]^{n+}$ (X_2bpy = 4,4'-X_2-2,2'-bipyridine) via photochemical ligand substitution reactions, and their photophysical and electrochemical properties. *Inorg. Chem.*, **2000**, 39, 2777-2783.
270. Koike, K., Okoshi, N., Hori, H., Takeuchi, K., Ishitani, O., Tsubaki, H., Clark, I. P., George, M. W., Johnson, F. P. A., Turner, J. J., Mechanism of the photochemical ligand substitution reactions of *fac*-[Re(bpy)$(CO)_3(PR_3)]^+$ complexes and the properties of their triplet ligand-field excited states. *J. Am. Chem. Soc.*, **2002**, 124, 11448-11455.
271. Kumar, A., Sun, S. S., Lees, A. J., Photophysics and photochemistry of organometallic rhenium diimine complexes, in *Topics in organometallic chemistry*, **2010**, Springer-Verlag: Berlin.
272. Smithback, J. L., Helms, J. B., Schutte, E., Woessner, S. M., Sullivan, B. P., Preparative routes to luminescent mixed-ligand rhenium(I) dicarbonyl complexes. *Inorg. Chem.*, **2006**, 45, 2163-2174.
273. Wrighton, M., Morse, D. L., Nature of lowest excited-state in tricarbonylchloro-1,10-phenanthroline rhenium(I) and related complexes. *J. Am. Chem. Soc.*, **1974**, 96, 998-1003.
274. Hori, H., Koike, K., Ishizuka, M., Takeuchi, K., Ibusuki, T., Ishitani, O., Preparation and characterization of [Re(bpy)$(CO)_3$L][SbF_6] (L=phosphine, phosphite). *J. Organomet. Chem.*, **1997**, 530, 169-176.
275. Giordano, P. J., Wrighton, M. S., Nature of the lowest excited-state in *fac*-tricarbonylhalobis(4-phenylpyridine) rhenium(I) and *fac*-tricarbonylhalobis(4-4'-bipyridine) rhenium(I): emissive organometallic complexes in fluid solution. *J. Am. Chem. Soc.*, **1979**, 101, 2888-2897.
276. Lo, K. K.-W., Zhang, K. Y., Li, S. P.-Y., Recent exploitation of luminescent rhenium(I) tricarbonyl polypyridine complexes as biomolecular and cellular probes. *Eur. J. Inorg. Chem.*, **2011**, 2011, 3551-3568.
277. Mak, C. S. K., Wong, H. L., Leung, Q. Y., Tam, W. Y., Chan, W. K., Djurisic, A. B., The use of sublimable chlorotricarbonyl bis(phenylimino)acenaphthene rhenium(I) complexes as photosensitizers in bulk-heterojunction photovoltaic devices. *J. Organomet. Chem.*, **2009**, 694, 2770-2776.
278. Hawecker, J., Lehn, J. M., Ziessel, R., Photochemical and electrochemical reduction of carbon dioxide to carbon monoxide mediated by (2,2'-bipyridine)tricarbonylchlororhenium(I) and related complexes as homogeneous catalysts. *Helv. Chim. Acta*, **1986**, 69, 1990-2012.
279. Takeda, H., Koike, K., Inoue, H., Ishitani, O., Development of an efficient photocatalytic system for CO_2 reduction using rhenium(l) complexes based on mechanistic studies. *J. Am. Chem. Soc.*, **2008**, 130, 2023-2031.
280. Hori, H., Johnson, F. P. A., Koike, K., Ishitani, O., Ibusuki, T., Efficient photocatalytic CO_2 reduction using [Re(bpy)$(CO)_3${$P(OEt)_3$}]$^+$. *J. Photochem. Photobiol. A-Chem.*, **1996**, 96, 171-174.
281. Gholamkhass, B., Mametsuka, H., Koike, K., Tanabe, T., Furue, M., Ishitani, O., Architecture of supramolecular metal complexes for photocatalytic CO_2

reduction: ruthenium-rhenium bi- and tetranuclear complexes. *Inorg. Chem.*, **2005**, 44, 2326-2336.
282. Sato, S., Koike, K., Inoue, H., Ishitani, O., Highly efficient supramolecular photocatalysts for CO_2 reduction using visible light. *Photochem. Photobiol. Sci.*, **2007**, 6, 454-461.
283. Vlček, A., Mechanistic roles of metal-to-ligand charge-transfer excited states in organometallic photochemistry. *Coord. Chem. Rev.*, **1998**, 177, 219-256.
284. Anderson, N. A., Lian, T., Ultrafast electron injection from metal polypyridyl complexes to metal-oxide nanocrystalline thin films. *Coord. Chem. Rev.*, **2004**, 248, 1231-1246.
285. Wong, H. L., Lam, L. S. M., Cheng, K. W., Man, K. Y. K., Chan, W. K., Kwong, C. Y., Djurisic, A. B., Low-band-gap, sublimable rhenium(I) diimine complex for efficient bulk heterojunction photovoltaic devices. *Appl. Phys. Lett.*, **2004**, 84, 2557-2559.
286. Wong, H. L., Mak, C. S. K., Chan, W. K., Djurisic, A. B., Efficient photovoltaic cells with wide photosensitization range fabricated from rhenium benzathiazole complexes. *Appl. Phys. Lett.*, **2007**, 90,
287. Clifford, J. N., Yahioglu, G., Milgrom, L. R., Durrant, J. R., Molecular control of recombination dynamics in dye-sensitised nanocrystalline TiO_2 films. *Chem. Commun.*, **2002**, 1260-1261.
288. Magde, D., Brannon, J. H., Cremers, T. L., Olmsted, J., Absolute luminescence yield of cresyl violet - standard for the red. *J. Phys. Chem.*, **1979**, 83, 696-699.
289. Du, H., Fuh, R. C. A., Li, J. Z., Corkan, L. A., Lindsey, J. S., PhotochemCAD: a computer-aided design and research tool in photochemistry. *Photochem. Photobio.*, **1998**, 68, 141-142.
290. Demas, J. N., Luminescence spectroscopy and bimolecular quenching: a physical chemistry experiment. *J. Chem. Educ.*, **1975**, 52, 677-679.
291. Demas, J. N., Photophysical pathways in metal complexes. *J. Chem. Educ.*, **1983**, 60, 803-808.
292. Caspar, J. V., Meyer, T. J., Application of the energy-gap law to non-radiative, excited-state decay. *J. Phys. Chem.*, **1983**, 87, 952-957.
293. Tsubaki, H., Tohyama, S., Koike, K., Saitoh, H., Ishitani, O., Effect of intramolecular π–π and CH-π interactions between ligands on structure, electrochemical and spectroscopic properties of fac-$[Re(bpy)(CO)_3(PR_3)]^+$ (bpy = 2,2'-bipyridine; PR_3 = trialkyl or triarylphosphines). *Dalton Trans.*, **2005**, 385-395.
294. Caspar, J. V., Sullivan, B. P., Meyer, T. J., Synthetic routes to luminescent 2,2'-bipyridyl complexes of rhenium - preparation and spectral and redox properties of mono(bipyridyl) complexes of Re(III) and Re(I). *Inorg. Chem.*, **1984**, 23, 2104-2109.
295. Schutte, E., Helms, J. B., Woessner, S. M., Bowen, J., Sullivan, B. P., A new class of luminescent polypyridine complexes of rhenium(I) containing *cis*-carbonyl ligands. *Inorg. Chem.*, **1998**, 37, 2618-2619.
296. Pac, C. J., Kaseda, S., Ishii, K., Yanagida, S., A novel type of photosubstitution of *fac*-$[Re(bpy)(CO)_3Br]$ (bpy = 2,2'-bipyridine) with $P(OR)_3$ in the presence of triethylamine - efiicient formation of $[Re(bpy)(CO)_2\{P(OR)_3\}_2]^+$ *Br. J. Chem. Soc.-Chem. Commun.*, **1991**, 787-788.
297. Sullivan, B. P., Meyer, T. J., Photoinduced irreversible insertion of CO_2 into a metal-hydrid bond. *J. Chem. Soc.-Chem. Commun.*, **1984**, 1244-1245.

298. Vlček, A., Ultrafast excited-state processes in Re(I) carbonyl-diimine complexes: from excitation to photochemistry, in *Photophysics of organometallics*, **2010**, Springer-Verlag: Berlin.
299. Lager, E., Liu, J., Aguilar-Aguilar, A., Tang, B. Z., Pena-Cabrera, E., Novel meso-polyarylamine-BODIPY hybrids: synthesis and study of their optical properties. *J. Org. Chem.*, **2009**, 74, 2053-2058.
300. Kasha, M., Rawls, H. R., Correlation of orbital classification of molecular electronic transitions with transition mechanism - aromatic amines. *Photochem. Photobio.*, **1968**, 7, 561-569.
301. Chen, H. F., Wong, K. T., Liu, Y. H., Wang, Y., Cheng, Y. M., Chung, M. W., Chou, P. T., Su, H. C., Bis(diphenylamino)-9,9'-spirobifluorene functionalized Ir(III) complex: a conceptual design en route to a three-in-one system possessing emitting core and electron and hole transport peripherals. *J. Mat. Chem.*, **2011**, 21, 768-774.
302. Qiu, D. F., Zhao, Q. A., Bao, X. Y., Liu, K. C., Wang, H. W., Guo, Y. C., Zhang, L. F., Zeng, J. L., Wang, H. A., Electropolymerization and characterization of an alternatively conjugated donor-acceptor metallopolymer: Poly-[Ru(4'-(4-(diphenylamino) phenyl)-2,2':6',2''-terpyridine)$_2$]$^{2+}$. *Inorg. Chem. Commun.*, **2011**, 14, 296-299.
303. Waterland, M. R., Simpson, T. J., Gordon, K. C., Burrell, A. K., Spectroelectrochemical studies and excited-state resonance Raman spectroscopy of some mononuclear rhenium(I) polypyridyl bridging ligand complexes. Crystal structure determination of tricarbonylchloro[2,3-di(2-pyridyl)quinoxaline]rhenium(I). *J. Chem. Soc.-Dalton Trans.*, **1998**, 185-192.
304. Sakamoto, N., Ikeda, C., Yamamura, M., Nabeshima, T., Structural interconversion and regulation of optical properties of stable hypercoordinate dipyrrin-silicon complexes. *J. Am. Chem. Soc.*, **2011**, 133, 4726-4729.
305. Tsubaki, H., Sekine, A., Ohashi, Y., Koike, K., Takeda, H., Ishitani, O., Control of photochemical, photophysical, electrochemical, and photocatalytic properties of rhenium(I) complexes using intramolecular weak interactions between ligands. *J. Am. Chem. Soc.*, **2005**, 127, 15544-15555.
306. McGlynn, S. P., Azumi, T., Kinoshita, M., *Molecular spectroscopy of the triplet state*. **1969**, Englewood Cliffs, NJ: Prentice-Hall.
307. Sabatini, R. P., McCormick, T. M., Lazarides, T., Wilson, K. C., Eisenberg, R., McCamant, D. W., Intersystem crossing in halogenated Bodipy chromophores used for solar hydrogen production. *J. Phys. Chem. Lett.*, **2011**, 2, 223-227.
308. Nastasi, F., Puntoriero, F., Campagna, S., Diring, S., Ziessel, R., Photoinduced intercomponent processes in multichromophoric species made of Pt(II)-terpyridine-acetylide and dipyrromethene-BF_2 subunits. *Phys. Chem. Chem. Phys.*, **2008**, 10, 3982-3986.
309. Harriman, A., Rostron, J. P., Cesario, M., Ulrich, G., Ziessel, R., Electron transfer in self-assembled orthogonal structures. *J. Phys. Chem. A*, **2006**, 110, 7994-8002.
310. Lee, S. Y., Heller, E. J., Time-dependent theory of Raman scattering. *J. Chem. Phys.*, **1979**, 71, 4777-4788.
311. Myers, A. B., Hochstrasser, R. M., Resonance Raman depolarisation ratios as a probe of excited state dephasing times. *J. Chem. Phys.*, **1987**, 87, 2116-2121.
312. Myers, A. B., Resonance Raman intensity analysis of excited state dynamics. *Acc. Chem. Res.*, **1997**, 30, 519-527.

313. Lilichenko, M., Tittelbach-Helmrich, D., Verhoeven, J. W., Gould, I. R., Myers, A. B., Resonance Raman intensity analysis of a dicyanovinyl-azaadamantane: mode-specific reorganization energies for charge-transfer and locally-excited states. *J. Chem. Phys.*, **1998**, 109, 10958-10969.
314. Li, B. L., Johnson, A. E., Mukamel, S., Myers, A. B., The Browian oscillator model for solvation effects in spontaneous light emission and their relationship to electron transfer. *J. Am. Chem. Soc.*, **1994**, 116, 11039-11047.
315. Lombardi, J. R., Birke, R. L., A unified approach to surface-enhanced Raman spectroscopy. *J. Phys. Chem. C*, **2008**, 112, 5605-5617.
316. Kelley, A. M., Frequency-dependent first hyperpolarisabilities from linear absorption spectra. *J. Opt. Soc. Am. B.*, **2002**, 1890-1900.
317. Atkins, P., Friedman, R., Molecular Quantum Mechanics (4^{th} edition). 2005. Oxford University Press: New York.

Appendix A

(Chapter 1)

A1 Resonance Raman theory

A1.1 Albrecht theory of resonance Raman

Resonance Raman spectroscopy can only be understood by examining the coupling between the ground and electronic excited states, and consequently, is more closely related to absorption or fluorescence spectroscopy than to IR spectroscopy. The formal theory underlying resonance Raman spectroscopy was developed by Albrecht.[170] The following section is a summary from Long.[119] For the resonance Raman case, the transition polarisability is given by:

$$(\alpha_{\rho\sigma})_{e^g v^f : e^g v^i} = A + B + C + D \tag{A1}$$

where

$$A = \frac{1}{\hbar}(p_\rho)^0_{e^g e^r}(p_\sigma)^0_{e^r e^g}\sum_{v_k^r}\frac{\left\langle v_k^{f(g)}\middle|v_k^{r(r)}\right\rangle\left\langle v_k^{r(r)}\middle|v_k^{i(g)}\right\rangle}{\omega_{e^r v_k^r : e^g v_k^i} - \omega_1 - i\Gamma_{e^r v_k^r}} \tag{A2}$$

$$\begin{aligned} B = {} & \frac{1}{\hbar^2}(p_\rho)^0_{e^g e^s}\frac{h^k_{e^s e^r}}{\omega_{e^r} - \omega_{e^s}}(p_\sigma)^0_{e^r e^g}\sum_{v_k^r}\frac{\left\langle v_k^{f(g)}\middle|Q_k\middle|v_k^{r(r)}\right\rangle\left\langle v_k^{r(r)}\middle|v_k^{i(g)}\right\rangle}{\omega_{e^r v_k^r : e^g v_k^i} - \omega_1 - i\Gamma_{e^r v_k^r}} \\ & + \frac{1}{\hbar^2}(p_\rho)^0_{e^g e^r}\frac{h^k_{e^r e^s}}{\omega_{e^r} - \omega_{e^s}}(p_\sigma)^0_{e^s e^g}\sum_{v_k^r}\frac{\left\langle v_k^{f(g)}\middle|v_k^{r(r)}\right\rangle\left\langle v_k^{r(r)}\middle|Q_k\middle|v_k^{i(g)}\right\rangle}{\omega_{e^r v_k^r : e^g v_k^i} - \omega_1 - i\Gamma_{e^r v_k^r}} \end{aligned} \tag{A3}$$

$$\begin{aligned} C = {} & \frac{1}{\hbar^2}\frac{h^k_{e^g e^t}}{\omega_{e^g} - \omega_{e^t}}(p_\rho)^0_{e^t e^r}(p_\sigma)^0_{e^r e^g}\sum_{v_k^r}\frac{\left\langle v_k^{f(g)}\middle|Q_k\middle|v_k^{r(r)}\right\rangle\left\langle v_k^{r(r)}\middle|v_k^{i(g)}\right\rangle}{\omega_{e^r v_k^r : e^g v_k^i} - \omega_1 - i\Gamma_{e^r v_k^r}} \\ & + \frac{1}{\hbar^2}(p_\rho)^0_{e^g e^r}(p_\sigma)^0_{e^r e^t}\frac{h^k_{e^t e^g}}{\omega_{e^g} - \omega_{e^t}}(p_\sigma)^0_{e^s e^g}\sum_{v_k^r}\frac{\left\langle v_k^{f(g)}\middle|v_k^{r(r)}\right\rangle\left\langle v_k^{r(r)}\middle|Q_k\middle|v_k^{i(g)}\right\rangle}{\omega_{e^r v_k^r : e^g v_k^g} - \omega_1 - i\Gamma_{e^r v_k^r}} \end{aligned} \tag{A4}$$

$$D = \frac{1}{\hbar^3}(p_\rho)^0_{e^g e^s}\frac{h^k_{e^s e^r}h^k_{e^r e^{s'}}}{(\omega_{e^r} - \omega_{e^s})(\omega_{e^r} - \omega_{e^{s'}})}(p_\sigma)^0_{e^{s'} e^g}\sum_{v_k^r, v_{k'}^r}\frac{\left\langle v_k^{f(g)}\middle|Q_k\middle|v_k^{r(r)}\right\rangle\left\langle v_{k'}^{r(r)}\middle|Q_{k'}\middle|v_{k'}^{r(r)}\right\rangle}{\omega_{e^r v_k^r : e^g v_k^i} - \omega_1 - i\Gamma_{e^r v_k^r}} \tag{A5}$$

The A term (given in A2 and sometimes called the Condon term) is non-zero, when two conditions are met. The transition dipole moments, $(p_\rho)^0_{e^g e^r}$ and $(p_\sigma)^0_{e^r e^g}$ must be non-

zero. This condition requires the resonant electronic transition, $\left|e^g\right\rangle \rightarrow \left|e^r\right\rangle$, to be electric-dipole allowed. To observe strong scattering, the transition dipole moments should have considerable magnitudes. For example, excitation into a charge transfer or a π-π* transition would result in a strong scattering, whereas excitation into a weak band such as a d-d transition would have a small A term and therefore negligible scattering (as a result of the A term). The second condition requires the vibrational overlap integrals, $\left\langle \nu_k^{f(g)} \middle| \nu_k^{r(r)} \right\rangle \left\langle \nu_k^{r(r)} \middle| \nu_k^{i(g)} \right\rangle$, to be non-zero for at least one value of $\nu_k^{r(r)}$. There will be no contribution from the A term if the electronic states $\left|e^g\right\rangle$ and $\left|e^r\right\rangle$ are identical and therefore the vibrational overlap integrals are orthogonal and will be zero unless $\nu_k^{f(g)} = \nu_k^{r(r)}$ and $\nu_k^{r(r)} = \nu_k^{i(g)}$. Non-orthogonality arises when the vibrational frequency is different in the electronic states $\left|e^g\right\rangle$ and $\left|e^r\right\rangle$, so that $\omega_k^r \neq \omega_k^g$ or when there is a displacement along the normal coordinate, Q_k of the potential energy minimum between the electronic states $\left|e^g\right\rangle$ and $\left|e^r\right\rangle$. This means that either the shape of the potential energy surface is different in the two electronic states or there is a displacement of ΔQ_k along the normal coordinate. If $\omega_k^r = \omega_k^g$ and $\Delta Q_k \neq 0$ then for transitions which $\nu_k^{f(g)} = \nu_k^{i(g)} + 1$ are allowed, then the A term contributes to Raman scattering of the fundamental frequencies. However, resonance Raman can also be complicated by overtones and combinations. If the magnitude of ΔQ_k is adequate, then the product of the vibrational overlap integrals may have magnitudes significant enough to observe transitions from $\nu_k^{i(g)} = 0$ to $\nu_k^{f(g)} = 2, 3, 4....$ Only totally symmetric modes result from the A term when $\Delta Q_k \neq 0$ and as a result of the molecular symmetry in the ground and excited states. Further details on this can be found in the literature.[119]

The B term (given in A3 and sometimes called the Herzberg-Teller term) involves the vibronic coupling of the resonant excited state $\left|e^r\right\rangle$ to one other excited state $\left|e^s\right\rangle$. The B term is usually much smaller than the A term but it plays an important role in resonance Raman scattering when the A term is zero. The B term can be non-zero for both totally symmetric and non-totally symmetric fundamental modes. For symmetric modes the excited states $\left|e^r\right\rangle$ and $\left|e^s\right\rangle$ must have the same symmetry. But it is rare for electronic states of the same symmetry to be close together in energy and therefore the B term is usually irrelevant for totally symmetric modes. To observe a non-totally symmetric normal coordinate (Q_k), then the vibronic coupling term $h^k_{e^s e^r}$ must be effective in coupling the resonant excited state $\left|e^r\right\rangle$ to a second excited state $\left|e^s\right\rangle$. The

B term only contributes to Raman scattering of the fundamental frequencies and the particulars of this is detailed in the literature.[119]

The C term (given in A4) relates to vibronic coupling of the ground electronic state $\left|e^{g}\right\rangle$ to an excited electronic state $\left|e^{t}\right\rangle$ and D term (given in A5) relates to vibronic coupling of the excited electronic state $\left|e^{r}\right\rangle$ to two other excited electronic states $\left|e^{s}\right\rangle$ and $\left|e^{s'}\right\rangle$. Both terms are likely to be negligible and are not discussed further.

A1.2 Resonance Raman Intensity Analysis (RRIA)

Resonance Raman is probably the most powerful technique for probing the first 0-100 femtosecond nuclear dynamics of a molecule and therefore determining changes in the nuclear geometry following the excitation. Consequently useful information about the nuclear dynamics can be gained from resonance Raman intensity analysis (RRIA). The time-dependent formulation (as developed by Lee and Heller[310]) has been employed (as summarized) by Myers and others[161, 311-313] to simulate both absorption and resonance Raman intensities. The central points of these works have been concisely condensed in the literature[248] and are as follows.

The Raman amplitude between the initial and final vibrational states for a single resonant electronic state, α_{if}, is calculated from equation A6 as the half-Fourier transform of the time-dependent overlap of a wavepacket propagating on the resonant electronic excited and the v'' = 1 ground electronic state vibrational wavefunction:

$$\alpha_{if}\left(\omega_L,\delta\right)=\frac{1}{\hbar}\int_0^\infty dt\left\langle\chi_f\left|\chi_i\left(t\right)\right\rangle\exp\left[i\left(\omega_L-\omega-\delta+\omega_i\right)t-g\left(t\right)\right]\right. \qquad \text{(A6)}$$

where ω_L is the incident laser frequency, $\hbar\omega_i$ is the energy of the initial vibrational level. This is set to zero as it is assumed that scattering from all modes in the simulation occurs from the ground vibrational level. ω is the zero-zero (0-0) electronic transition frequency, δ is the electronic zero-zero frequency shift due to inhomogeneous broadening. $\left\langle\chi_f\right|=\left\langle f\right|\mu_0$ and $\left\langle\chi_i\right|=\left\langle i\right|\mu_0$ are the multidimensional ground state vibrational wavefunctions multiplied by the transition dipole moment and $\left|\chi_i\left(t\right)\right\rangle=\exp\left(-iHt/\hbar\right)\left|\chi_i\right\rangle$ is the initial vibrational wavefunction propagated for a time, *t*, on the electronic excited state surface, by the excited state vibrational Hamiltonian. *g(t)* is the solvent broadening function, modelled as an overdamped Brownian

oscillator.[314] Separable harmonic oscillators, with frequencies taken from the ground state Raman modes were used in the model for the potential energy surfaces. The ground and excited state normal modes are assumed to have the same form (so Dushinsky rotation is not considered), and non-Condon effects were not included.

The differential Raman cross-section (the experimental observable), is calculated as (equation A7):

$$\left(\frac{d\sigma}{d\Omega}\right)_{\square+\perp} = \sum_i B_i \sum_f \int d\omega_s \left(\frac{\omega_S^3 \omega_L}{c^4} \int_{-\infty}^{+\infty} d\delta G(\delta) \left| \alpha_{if}(\omega_L, \delta) \right|^2 \right) L_{if}(\omega_L - \omega_S) \qquad \text{(A7)}$$

where B_i is the Boltzmann population of the initial vibrational state (assumed to be unity here) and $L_{if}(\omega_L - \omega_S)$ is a Raman line-shape function. $G(\delta)$ is a normalized inhomogeneous broadening function which is taken to be Gaussian.

The absorption cross-section is calculated using the following (equation A8) where the real part of the Fourier transform is taken and n is the refractive index of the solvent.

$$\sigma_A(\omega_L) = \frac{4\pi |\mu|^2 \omega_L}{3n\hbar c} \sum_i B_i \int_{-\infty}^{+\infty} d\delta G(\delta) \,\mathrm{Re} \int_{-\infty}^{+\infty} dt \langle \chi_i | \chi_i(t) \rangle \exp\left[i(\omega_L - \omega - \delta + \omega_i)t - g(t) \right] \qquad \text{(A8)}$$

In the case of two resonant electronic states the Raman amplitude is calculated for each excited state surface and then summed before taking the modulus square to obtain the Raman intensity.[313] The absorption cross-section is a simple sum. The angle between the transition dipole moments of the electronic transitions can usually be obtained from DFT calculations or crystal structures. It is possible for vibrational modes to have displacements of opposite signs in each electronic state, although only the relative sign carries any significance.

A2 Albrecht theory applied to SERS

Recently, a theoretical description of surface-enhanced Raman using Albrecht's approach (for resonant Raman scattering) has been proposed and summarised below.[126, 315] This approach provides a lucid and unified expression to describe the SERS enhancement which considers all three enhancement mechanisms. The expression for the polarisability (α) is analogous to the Albrecht term; however, the expression is extended to consider the coupling of the molecule-metal system and to include the filled and unfilled levels of the conduction band of the metal.

Away from any (molecule-to-metal) charge transfer or molecular resonance (e.g. $\pi-\pi^*$ transition or MLCT), then the A term vanishes and the B and C term are responsible for SERS intensities. On resonance (with a charge transfer or molecular resonance), the A term becomes quite large and therefore totally symmetric Raman modes are observed, yet the A term does not contribute to SERS intensities when only resonant with the plasmon resonance of the metal surface. In this situation the B and C terms are important and make substantial contributions to the observed SERS (and SE(R)RS) intensities via charge-transfer transitions between the molecule and metal nanoparticle.

The size of the enhancement, the relative contribution from each of the resonances, and the relative intensities in the Raman spectrum depend critically on the choice of the excitation wavelength, the size, shape, and Fermi level of the nanoparticle, and the position, width, and oscillator strength of the molecular resonance. The three resonances which contribute to the SERS intensities cannot be considered separately. The plasmon resonance and the charge transfer are closely coupled to one another because the charge transfer transition is coupled with electric field of the plasmon resonance and therefore knowledge of the orientation of the molecule on the metal surface is required. This means that these two components are not separable. The charge transfer resonance and the molecular resonance are linked by the molecular transition dipole moment because they both refer to the same excited state. This means that these two components are not separable. The vibronic coupling constant links the charge transfer and the observed Raman modes observed. To determine the contribution from each resonance, a complete description of each transition (in terms of the position, width, and oscillator strength) involved is required.

The SERS spectrum of a molecule is often somewhat different to the non-resonant or resonant Raman spectrum. Relative to non-resonant or resonant Raman spectrum, the frequencies of the modes are usually similar; however, the relative intensities are usually altered. Totally symmetric modes dominate the spectrum far from charge transfer or molecular resonances while non-totally symmetric modes become prominent in the region of charge transfer or molecular resonances.

Appendix B

(Chapter 2)

B1 Basis sets and frequency calculations

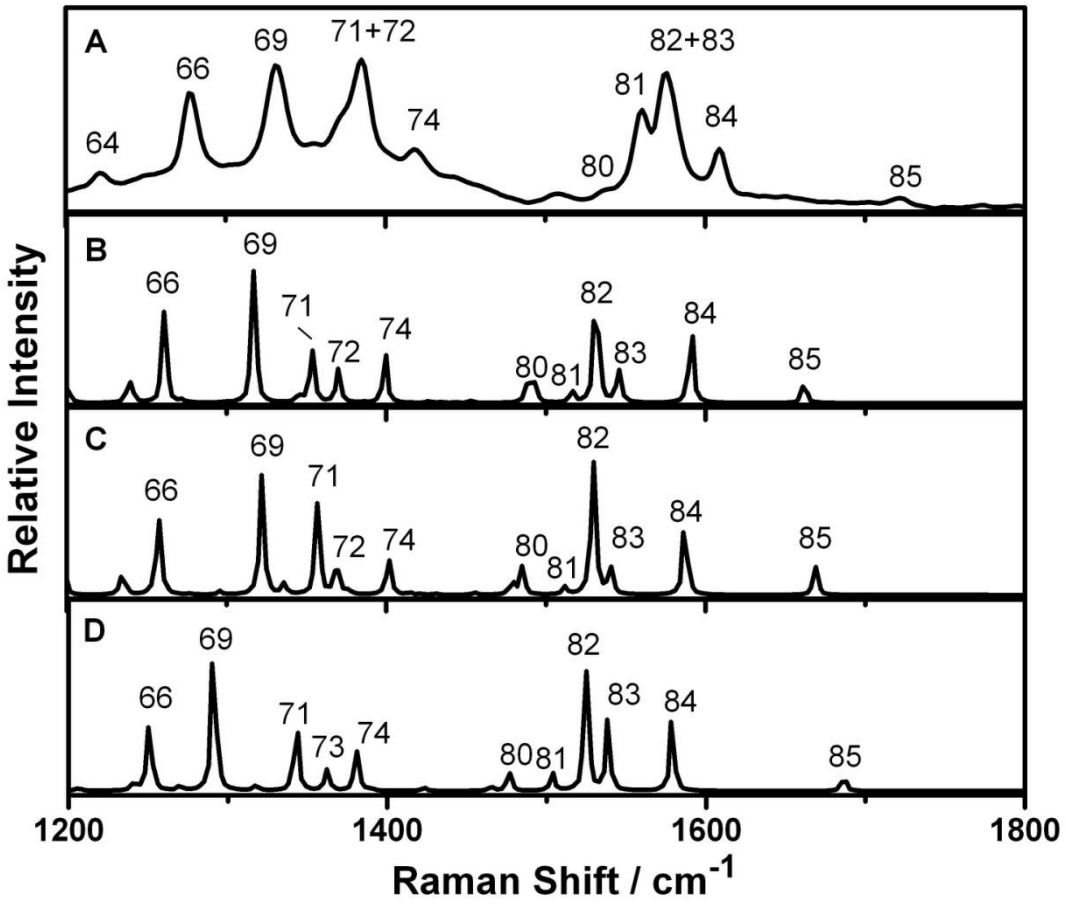

Figure B1. Experimental and calculated Raman spectra using different basis sets for **34**. (A) Experimental spectrum in methanol; (B) DFT/B3LYP 6-311+G (2d,2p) and frequencies scaled by 0.9679,[153] (C) DFT/O3LYP 6-311+G (2d,2p) and frequencies scaled by 0.9678,[154] (D) DFT/M06 6-311+G (2d,2p) and frequencies scaled by 0.950.[155]

Table B1. Experimental and calculated Raman frequencies and cross-sections for **34**.

Mode	**Experimental**		**Calculated**[b]								
	Frequency	$\frac{d\sigma_{nRRS}}{d\Omega}$ [a]	DFT/B3LYP 6-311+G (2d,2p) Frequency	$\frac{d\sigma_{nRRS}}{d\Omega}$ [c]	MAD[d]	DFT/O3LYP 6-311+G (2d,2p) Frequency	$\frac{d\sigma_{nRRS}}{d\Omega}$ [c]	MAD[d]	DFT/M06 6-311+G (2d,2p) Frequency	$\frac{d\sigma_{nRRS}}{d\Omega}$ [c]	MAD[d]
	[cm^{-1}]	[10^{-28} cm^2 sr^{-1}]	[cm^{-1}]	[10^{-28} cm^2 sr^{-1}]		[cm^{-1}]	[10^{-28} cm^2 sr^{-1}]		[cm^{-1}]	[10^{-28} cm^2 sr^{-1}]	
66	1279	0.0850	1260	0.0801	19	1256	0.0653	23	1249	0.0736	30
69	1331	0.1007	1316	0.1080	15	1321	0.0755	10	1290	0.1807	41
71+72	1385	0.1094	1352+1368	0.0802	33 17	1356+1368	0.0773	29 17	1341+1361	0.0827	44 24
74	1418	0.0418	1398	0.0364	20	1400	0.0248	18	1379	0.0060	39
81	1560	0.0372	1515	0.0076	45	1511	0.0040	49	1502	0.0152	58
82+83	1576	0.1125	1530+1544	0.1083	46 32	1528+1539	0.0888	48 37	1523+1537	0.1644	53 39
84	1609	0.0261	1590	0.0478	19	1586	0.0361	23	1577	0.0570	32
Average					**27**			**28**			**40**

[a] Experimental Raman cross-sections were calculated using equation 1.9

[b] Calculated frequencies are scaled by the appropriate scaling factor [B3LYP – 0.9679, O3LYP – 0.9678, M06 – 0.950]

[c] Calculated Raman cross-sections were calculated using equation 2.1 with the local field correction factor applied

[d] MAD = Mean Average Deviation = |Experimental Freq. – Calculated Freq|

[e] NB: for the M06 mode 72 is actually mode 73 for this basis set

B2 Conversion of molar absorptivity (ε) to oscillator strength (*f*)

The raw data from the spectrometer is given as absorbance versus wavelength (nm). To find the oscillator strength the absorbance axis must first be converted to molar absorptivity (ε, L mol^{-1} cm^{-1}) using Beer's Law and the wavelength (nm) axis must be converted to wavenumber (ω, cm^{-1}). The next step is to plot molar absorptivity (ε, L mol^{-1} cm^{-1}) divided by wavenumber (ω, cm^{-1}) to give molar absorptivity ((ε(ω), L mol^{-1}) on the y-axis and wavenumber (ω, cm^{-1}) on the x-axis. Integrating to find the area under the absorption band ($\int \frac{\varepsilon(\varpi)}{\varpi} d\varpi$) gives the square of the transition dipole moment ($|\mu_{ge}|^2$, in D^2) using the following equation:[316]

$$\left|\mu_{ge}\right|^2 = 9.185 \times 10^{-3} n \int \frac{\varepsilon(\varpi)}{\varpi} d\varpi \qquad \text{(B1)}$$

where n is the refractive index of the solvent and 9.185 x 10^{-3} [D^2] is the numerical value of constants from a similar equation given in reference 317. Equation B1 is the simpler of the two equations and therefore was used in preference.

From the transition dipole moment (μ_{ge}), it is a straightforward task to obtain the oscillator strength (f) using the following equation:[317]

$$f = \left(\frac{4\pi m_e c \nu_{ge}}{3e^2\hbar} \right) \left|\mu_{ge}\right|^2 \qquad \text{(B2)}$$

where m_e ≡ mass of an electron = 9.11 x 10^{-31} kg, c ≡ speed of light = 3.00 x 10^8 cm s^{-1}, ν_{ge} = centre of the absorption band (cm^{-1}), e ≡ elementary charge = 1.602 x 10^{-19} C, and $\hbar$ ≡h bar = 1.055 x 10^{-34} J s. It is important to note that the square of the transition dipole moment obtained in equation B1 has units of $D^{2.}$ This needs to be converted from units of D^2 to units of C^2 cm^2 (where 1 D = 3.33 x 10^{-30} C m and 1 m = 100 cm) before using equation B2.

B3 TD-DFT studies of 34

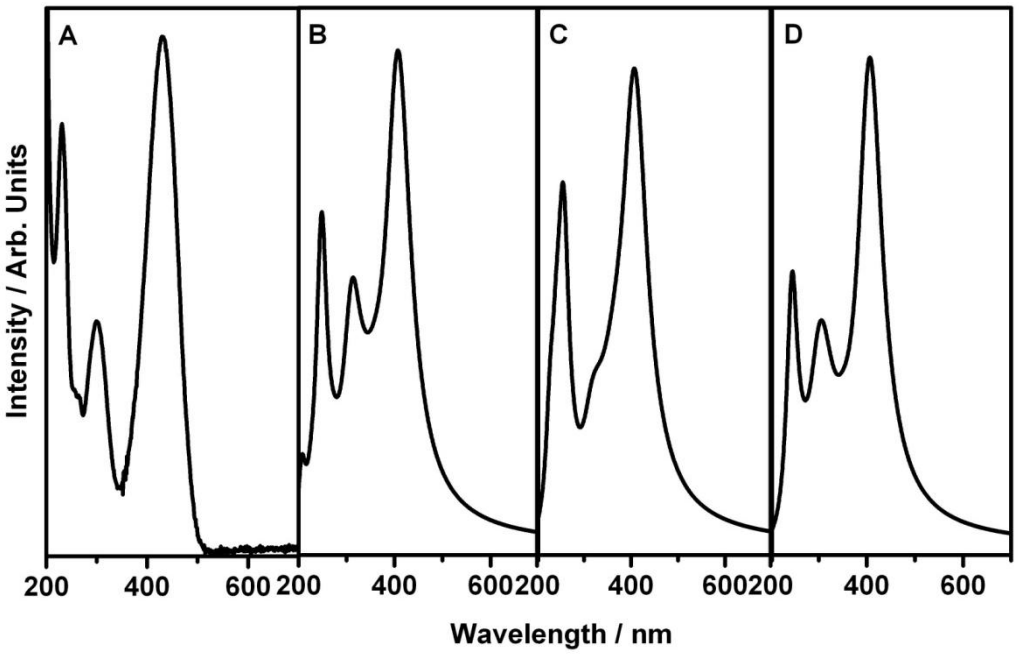

Figure B2. Experimental and calculated absorption spectra for **34** with the C-PCM solvent model applied. (A) Experimental in methanol; (B) DFT/B3LYP 6-311+G (2d,2p); (C) DFT/O3LYP 6-311+G (2d,2p); and (D) DFT/M06 6-311+G (2d,2p).

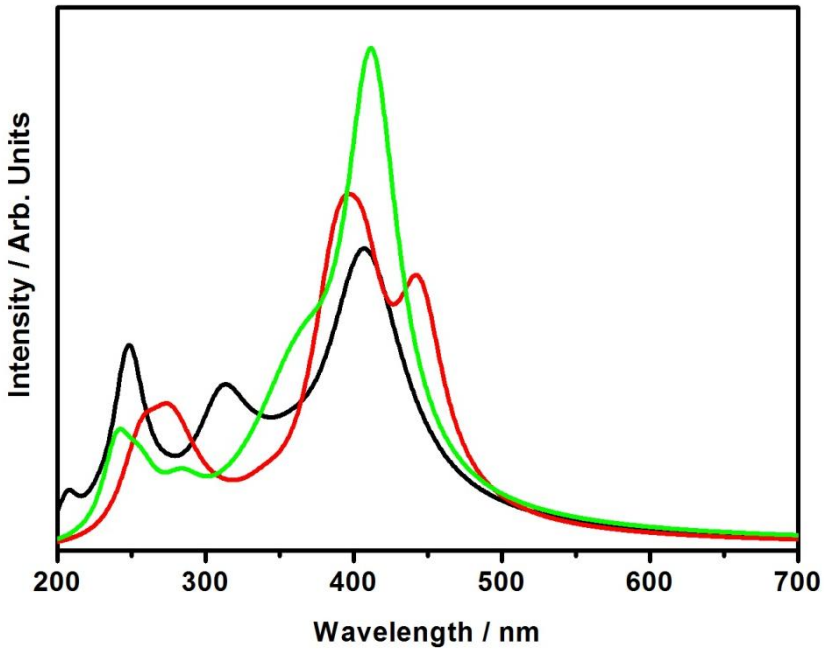

Figure B3. Calculated absorption spectrum of **34** using B3LYP/6-311+G(2d,2p) including C-PCM solvent model. Neutral ligand (black), protonated ligand (red), deprotonated ligand (green).

Table B2. Experimental and calculated absorption parameters for **34** for all basis sets.

Experimental	**Calculated**					
	DFT/B3LYP 6-311+G (2d,2p)		DFT/O3LYP 6-311+G (2d,2p)		DFT/M06 6-311+G (2d,2p)	
λ / nm	λ / nm	Configuration (% contribution)	λ / nm	Configuration (% contribution)	λ / nm	Configuration (% contribution)
432	408	HOMO→LUMO (95)	408	HOMO→LUMO (88)	407	HOMO→LUMO (98)
300	339	HOMO→LUMO+1 (95)	365	HOMO-1→LUMO (14), HOMO→LUMO (-10), HOMO→LUMO+1 (75)	320	HOMO→LUMO+1 (97)
231	313	HOMO-3→LUMO (97)	315	HOMO-4→LUMO (76), HOMO-2→LUMO (13)	305	HOMO-2→LUMO (92)
	311	HOMO-5→LUMO (-23), HOMO-2→LUMO (71)	257	HOMO-4→LUMO+1 (71), HOMO-3→LUMO+2 (13)	246	HOMO-4→LUMO+1 (46), HOMO-3→LUMO+1 (16), HOMO-1→LUMO+1 (19)
	248	HOMO-7→LUMO (50), HOMO-3→LUMO+1 (-32), HOMO-2→LUMO+1 (-11)	256	HOMO-7→LUMO (55), HOMO-4→LUMO+1 (12), HOMO-3→LUMO+1 (18)	245	HOMO-7→LUMO (-42), HOMO-2→LUMO+1 (45)
			243	HOMO-1→LUMO+2 (96)		
			241	HOMO-7→LUMO (22), HOMO-3→LUMO+1 (54)		
			228	HOMO-7→LUMO+1 (89)		

Table B3. Calculated and experimental absorption parameters for protonated and deprotonated **34**.

	Experimental			Calculated		
	λ / nm	ε / L mol^{-1} cm^{-1}	Oscillator strength (f)	λ / nm	Configuration (% contribution)	Oscillator strength (f)
Protonated ligand	479	47 900	0.605	412	HOMO→LUMO (99)	0.566
				369	HOMO-2→LUMO (96)	0.013
	351	12 300	0.297	363	HOMO-1→LUMO (97)	0.463
				330	HOMO-4→LUMO (97)	0.020
	276	3 100		284	HOMO→LUMO+1 (99)	0.080
				256	HOMO-7→LUMO (82), HOMO-1→LUMO+1 (12),	0.103
				234	HOMO-7→LUMO (75), HOMO-1→LUMO+2 (10),	0.200
Deprotonated ligand				445	HOMO→LUMO (76), HOMO→LUMO+1 (-22)	0.206
				407	HOMO-2→LUMO (-21), HOMO-1→LUMO (-34), HOMO→LUMO+1 (38)	0.123
				390	HOMO-2→LUMO (16), HOMO-1→LUMO (26), HOMO→LUMO (18), HOMO→LUMO+1 (39)	0.412
				340	HOMO-3→LUMO (93)	0.023
				323	HOMO→LUMO+2 (99)	0.028
				280	HOMO-4→LUMO (79)	0.230

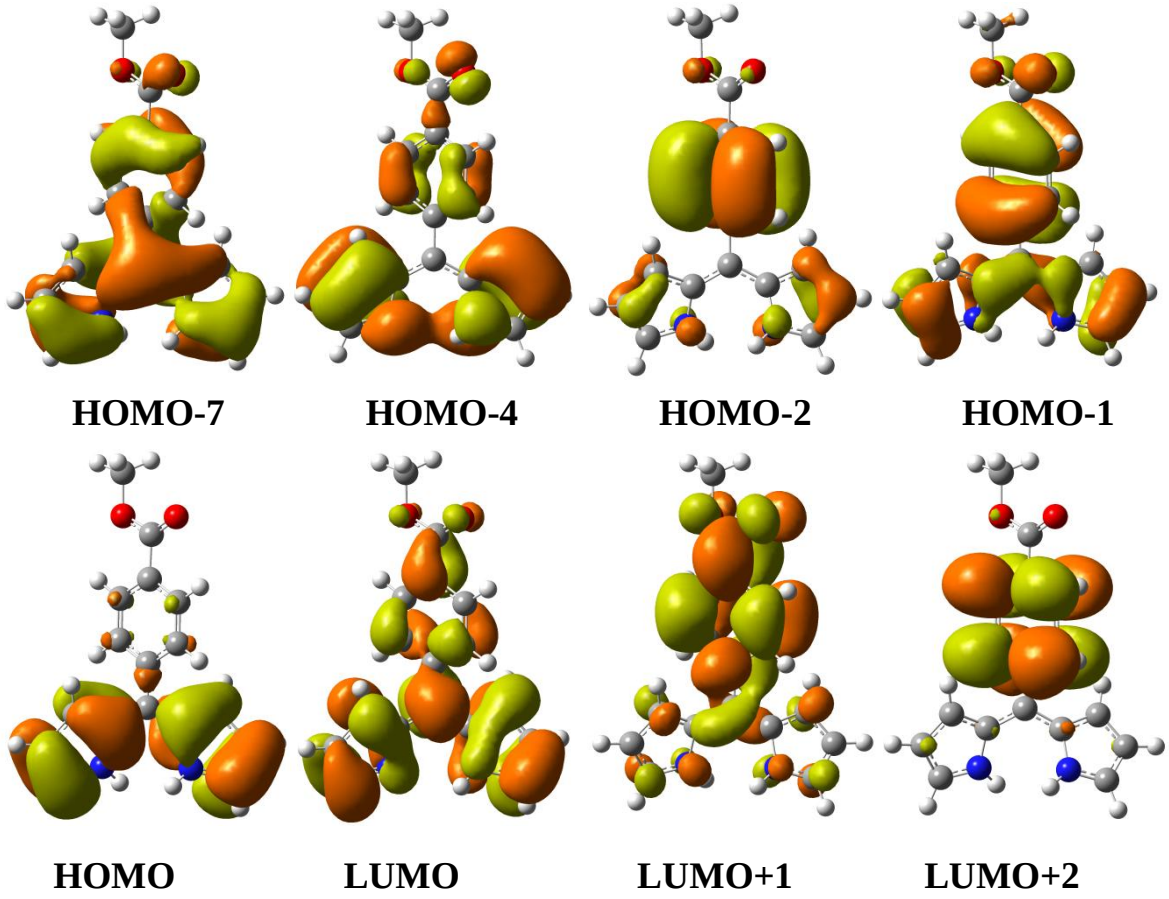

Figure B4. Selected molecular orbitals involved in the absorption spectrum of **34** when protonated.

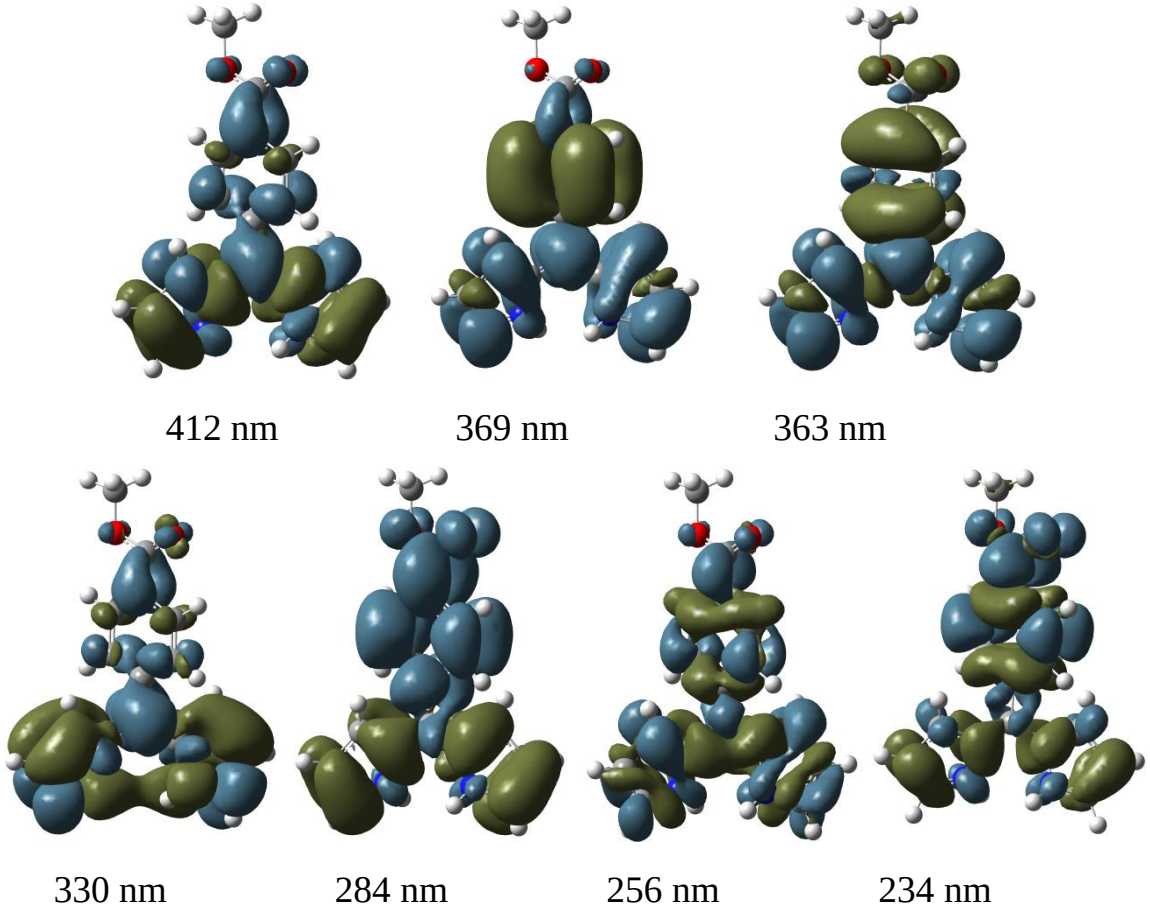

Figure B5. Electron density difference plots for **34** when protonated. Green represents depletion of electron density and blue represents accumulation of electron density.

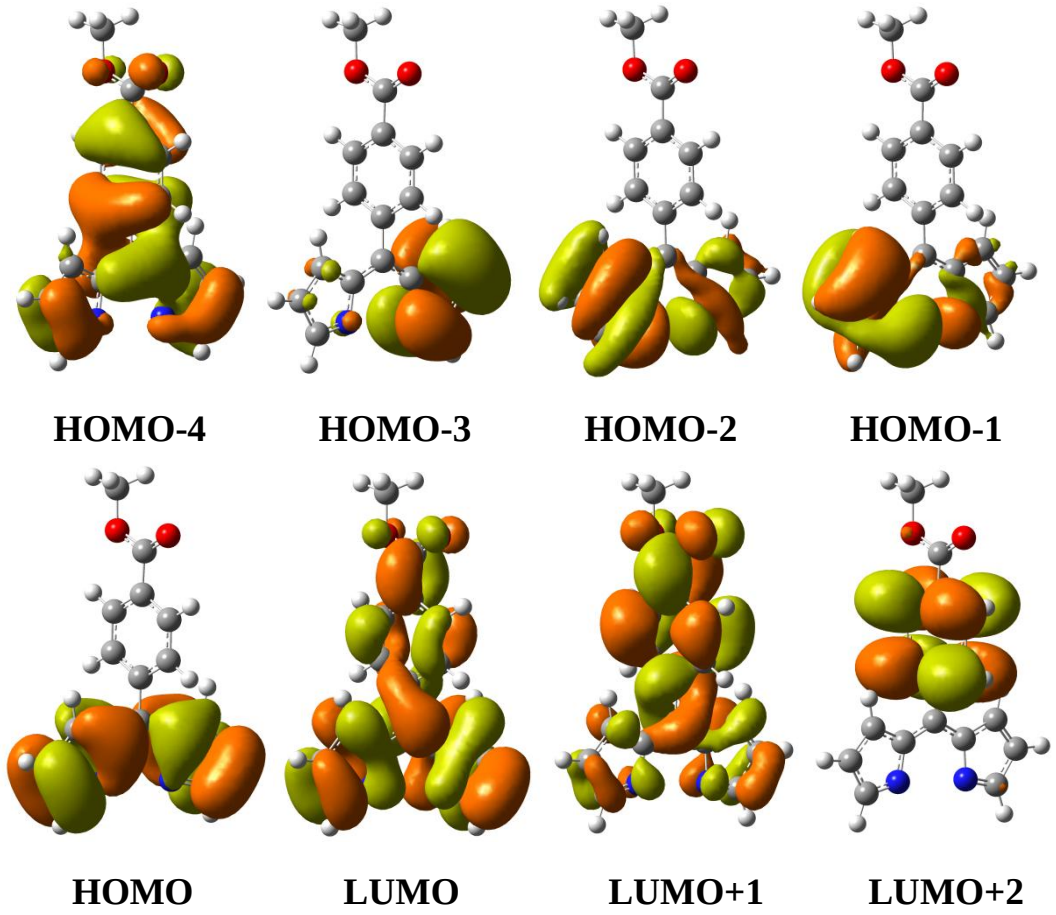

Figure B6. Selected molecular orbitals involved in the absorption spectrum of **34** when deprotonated.

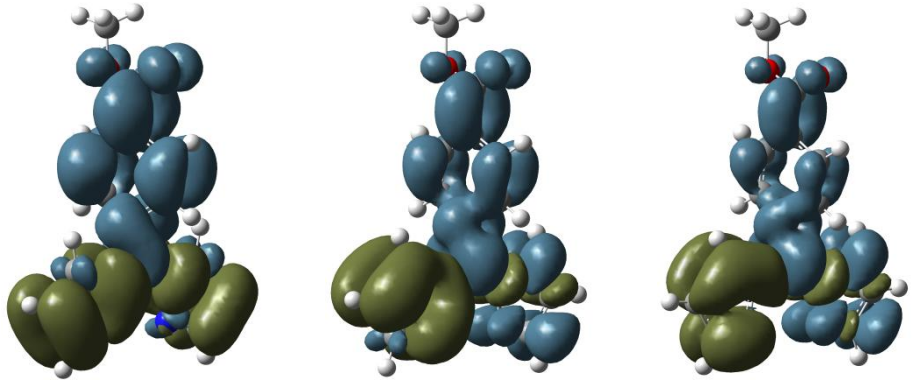

445 nm 381 nm 358 nm

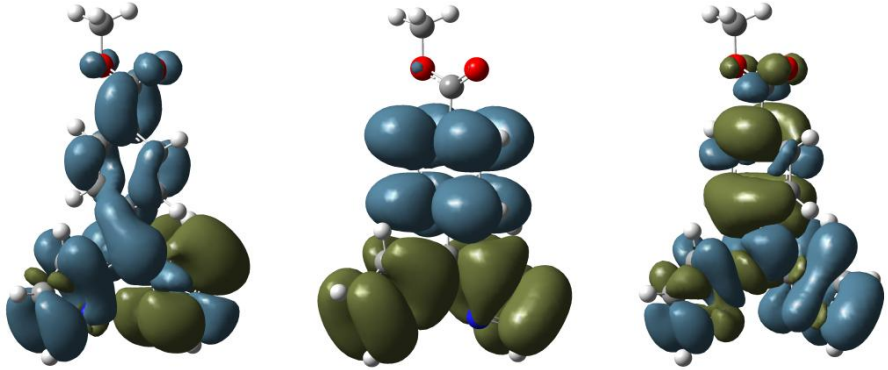

351 nm 337 nm 331 nm

Figure B7. Electron density difference plots for **34** when deprotonated. Green represents depletion of electron density and blue represents accumulation of electron density.

Appendix C

(Chapter 3)

C1 Resonance Raman of 43

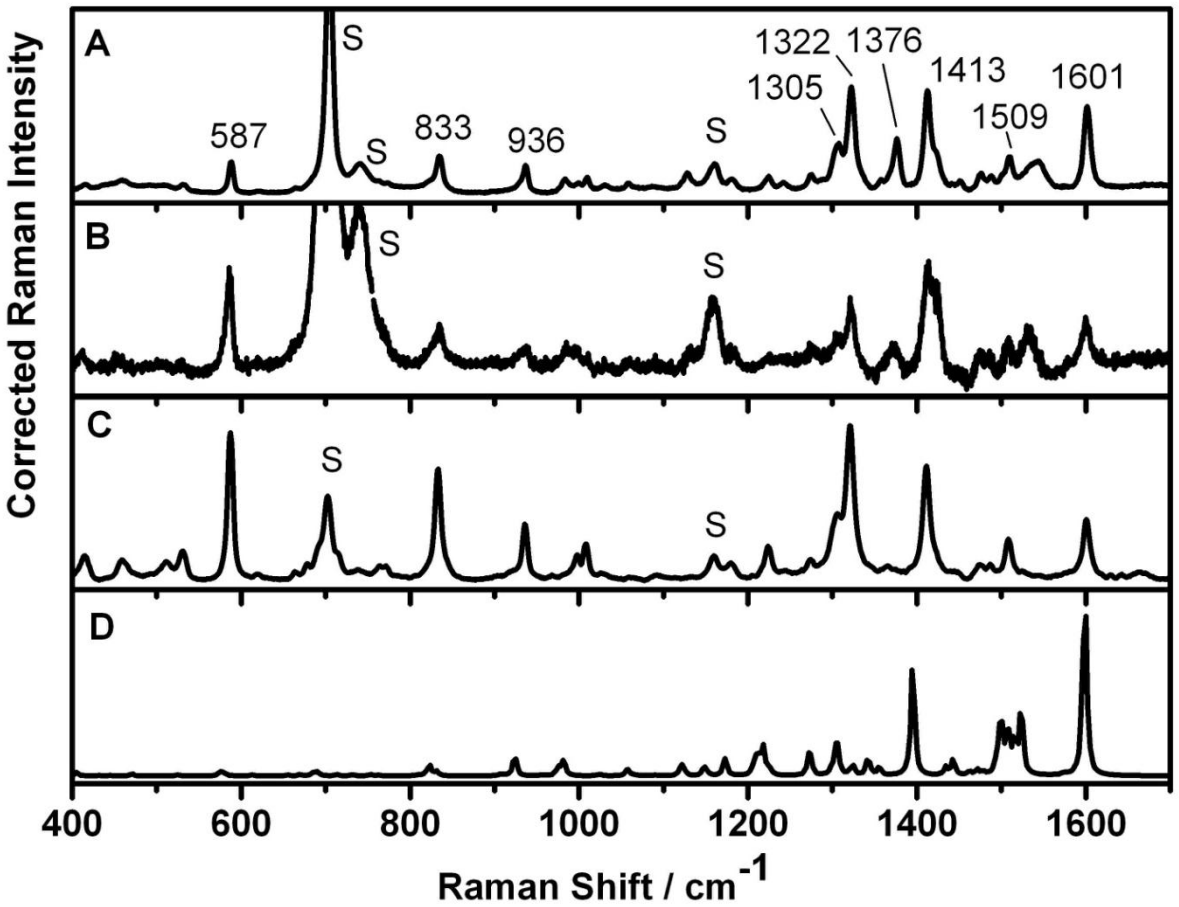

Figure C1. Experimental resonant Raman spectra in CH_2Cl_2 and calculated Raman spectra of **43** (A) 514.5 nm, (B) 568 nm, (C), 633 nm, and (D) calculated (DFT/B3LYP 6-311+G (d, p) on the Cu(II) and the dipyrrin core atoms and 6-31G(d) on the phenyl ring atoms) with C-PCM solvent model included. [S denotes solvent peaks (CH_2Cl_2)]. Note that not all wavelengths are shown.

Appendix D

(Chapter 4)

D1 Electrochemistry methods

Solution state (staircase) cyclic voltammetry (CV) measurements were performed using a three electrode system comprised of a macro platinum working electrode, a macro platinum auxiliary (counter) electrode and a silver wire (Ag wire) as a pseudo-reference electrode. CV measurements were performed on 0.5-1 mM solutions using 0.1 M tetra-*n*-butylammonium tetrafluoroborate ($TBABF_4$) as the supporting electrolyte. A reference CV of ferrocene in 0.1 M $TBABF_4$ was acquired. Values are reported against NHE using literature values (relative to the Fc/Fc^+ redox couple) after the addition of Fc/Fc^+ in 0.1 M $TBABF_4$ as a standard. Values for the Fc/Fc^+ couple relative to NHE are +0.63 V (vs NHE) in MeCN[252] and +0.40 V (vs NHE) in DMF.[253]

To calculate electronic bandgaps for each molecule the HOMO potential was calculated from the cyclic voltammograms (with respect to Fc/Fc^+). To convert the E_{onset}^{ox} values into a HOMO potential, the following relationship was used (D1):[254, 255]

$$\text{Ionisation Potential (HOMO)} = E_{onset}^{ox} \text{ (vs } Fc/Fc^+) + 4.5588 \text{ eV} \qquad \text{(D1)}$$

The bandgap was estimated from onset wavelength (λ_{onset}) of the lowest energy band in the absorption spectra. To calculate the bandgap, the UV-Vis onset wavelength was converted to energy (in eV) using Planck's equation $E = h\upsilon$ (where 1243 is the conversion factor to energy in eV) (D2):

$$\text{Band gap (eV)} = \frac{1243}{\lambda_{onset}\,(nm)} \qquad \text{(D2)}$$

This allowed a retrospective calculation of the LUMO potential of each dye.

D2 Cyclic voltammetry

D2.1 Cyclic voltammograms of Ru(II)-dipyrrinato and Rh(III)-dipyrrinato complexes

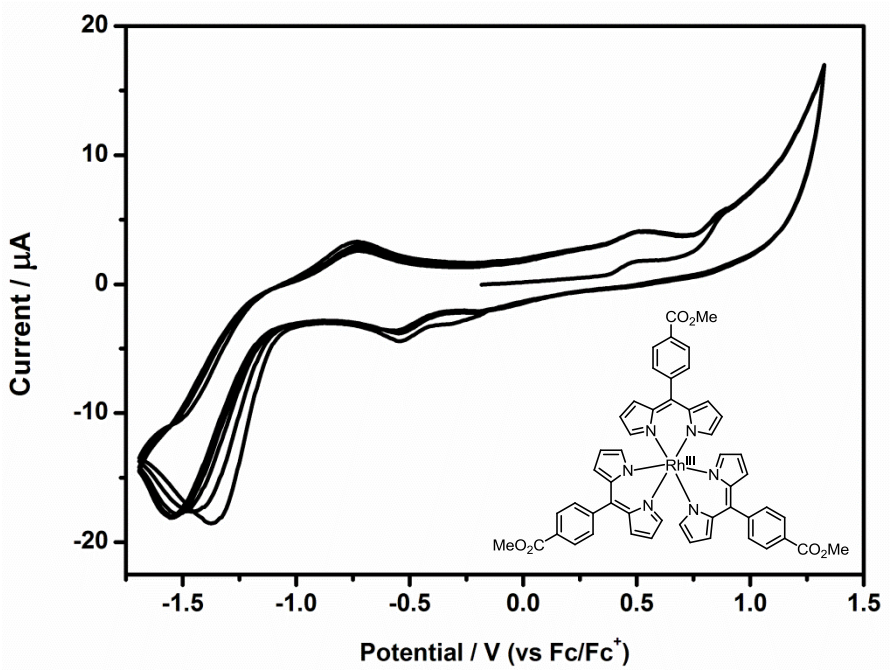

Figure D1. Cyclic voltammogram of **42** in MeCN.

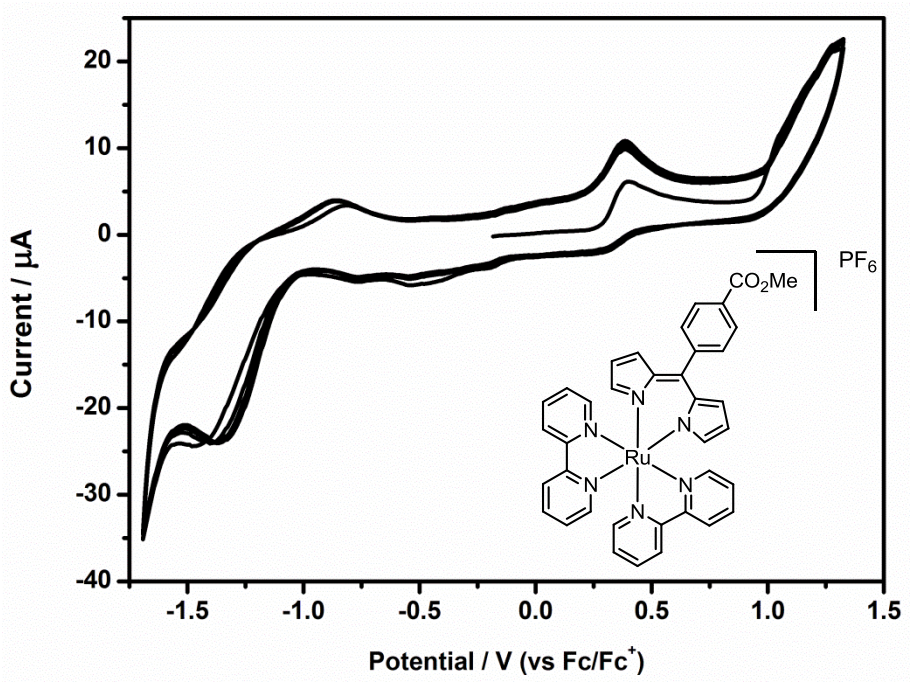

Figure D2. Cyclic voltammogram of **46b** in MeCN.

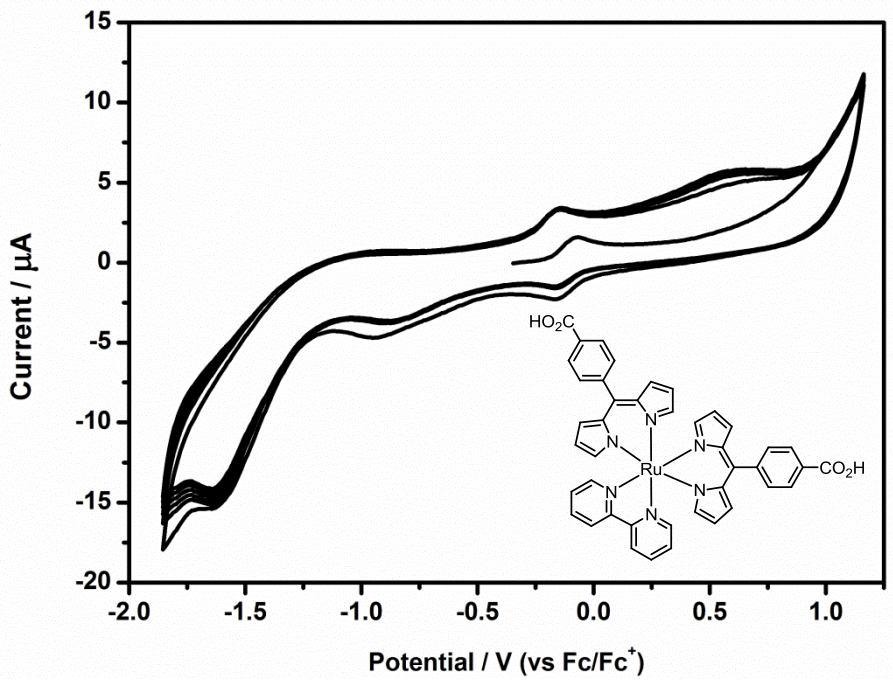

Figure D3. Cyclic voltammogram of **47** in DMF.

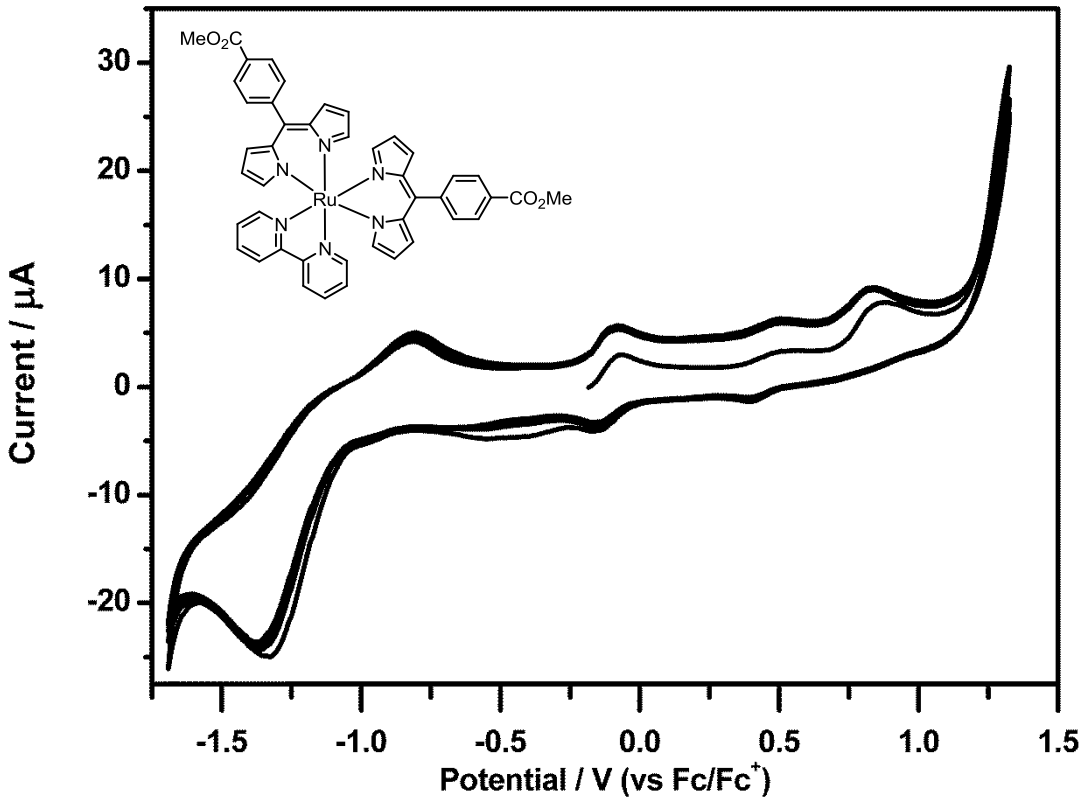

Figure D4. Cyclic voltammogram of **47a** in MeCN.

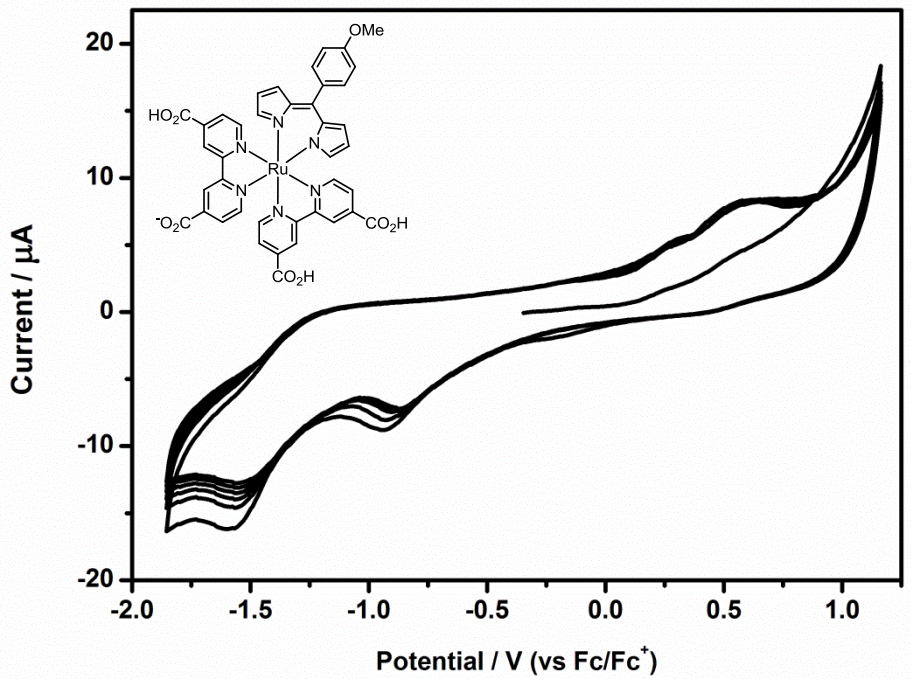

Figure D5. Cyclic voltammogram of **49** in DMF.

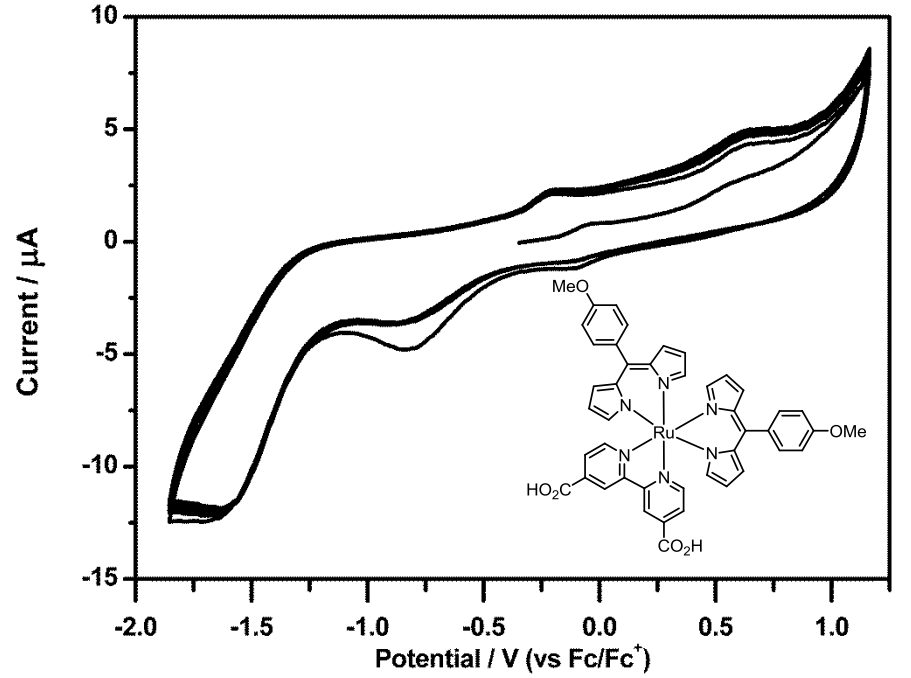

Figure D6. Cyclic voltammogram of **50** in DMF.

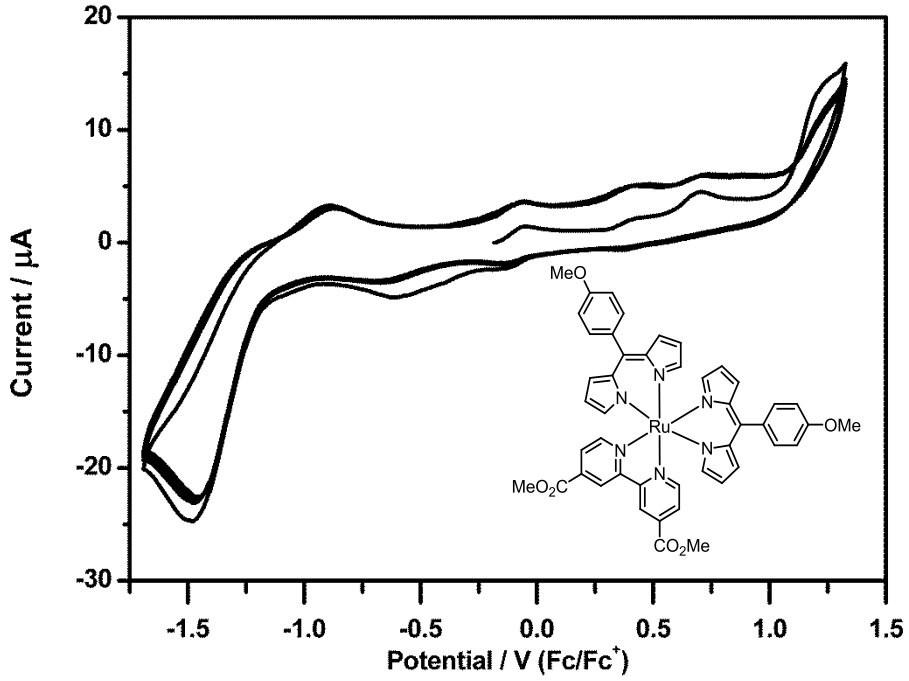

Figure D7. Cyclic voltammogram of **50a** in MeCN.

D2.2 Cyclic voltammograms of dipyrrin ligands

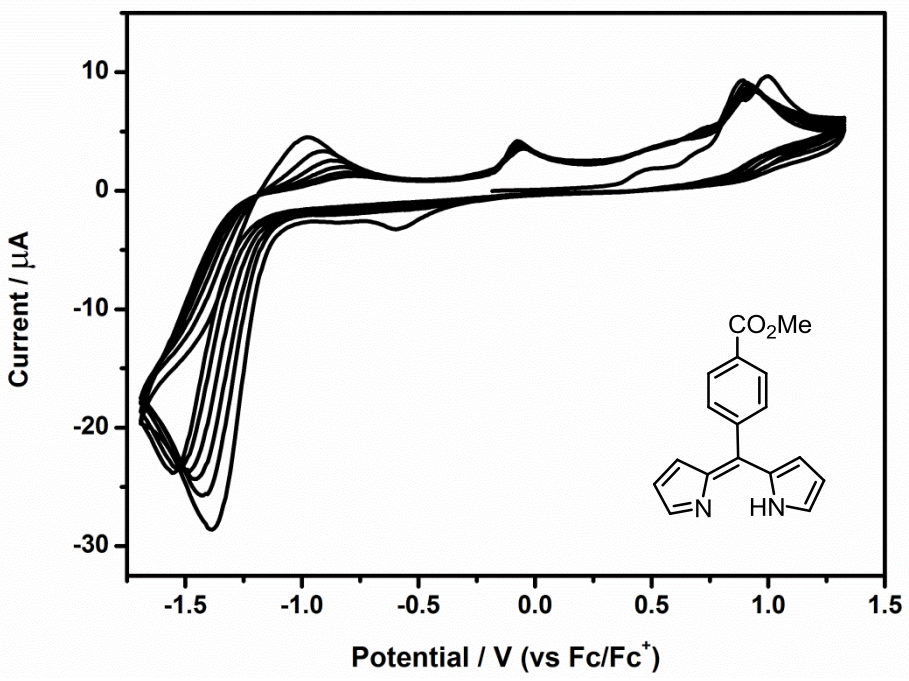

Figure D8. Cyclic voltammogram of **34** in MeCN.

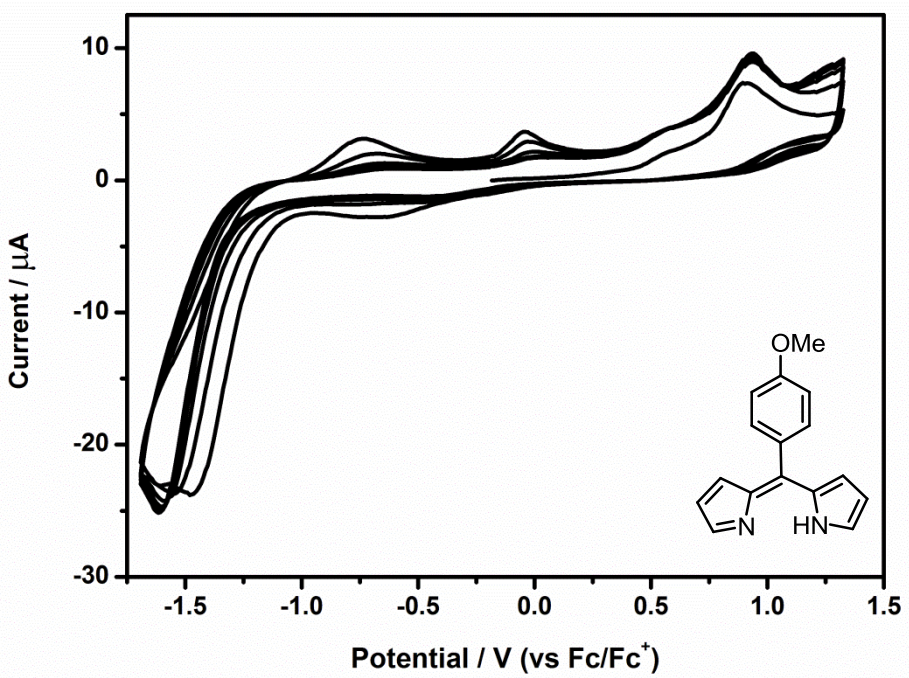

Figure D9. Cyclic voltammogram of **52** in MeCN.

D3 Solid state absorption spectroscopy

Solid state absorption spectra were acquired from sensitised TiO_2 or NiO films deposited on to fluorinated-tin oxide electrodes.

D4 Solar cell device fabrication

An FTO-glass substrate was cut into 6.0 x 4.0 cm strip and then cleaned using the supercritical CO_2 snow cleaner and 18 mins illumination in the UV-ozone cleaner. Transparent TiO_2 paste from Solaronix (Nanoxide-T) was then deposited onto this cleaned substrate using the technique of doctor-blading with two scotch tape masking layers. This layer was allowed to dry for approximately one hour, before a scattering layer consisting of Solaronix Nanoxide-R paste was deposited using a single two scotch tape masking layer. This layer was allowed to dry for 24 hours. The final film thickness was ~9 μm.

The film was then sintered with the programmable hotplate using Temperature Program 1 (five step ramp to a maximum temperature of 500 °C). Once sintering was complete, the substrate was removed from the furnace and cut into 1.5 x 1.7 cm pieces. A clean FTO-glass off-cut was used to scrape the film away from the edge of each substrate to

produce a film area of ~0.5 cm x ~0.5 cm. Care was taken to place the TiO_2 film towards a corner of the substrate, with 3 mm clearances towards two edges.

The surface area of the films was accurately measured by scanning the substrates and using a digital image program (Image J) to calculate the TiO_2 area with reference to a known standard. ITO-glass with a platinum layer sputter coated onto the conductive side was used for the counter electrodes. Holes were drilled into the counter electrodes in a position that would overlap with the TiO_2 films (approximately 3 mm x 3 mm in from one corner). Each film was then resintered using a fast ramp to 450°C to remove any adsorbed moisture or organic contaminants. These prepared TiO_2 films were then immersed in 2 x 10^{-4} M THF solutions of the dyes of interest and allowed to sensitise for a period of ~18 hours.

The counter electrodes were cleaned using two successive 5 minute sonications in water, followed by five minutes of sonication in 0.1 M hydrochloric acid (prepared by a 10-fold dilution from 1 M stock), and then one more sonication in water. These counter electrodes were then placed in the oven and held at 120°C for ~30 minutes to remove any adsorbed moisture.

Devices were prepared from the sensitised films by sealing the clean counter electrodes to the films using a 25 μm Himalin (surlyn) gasket pre-cut with a CO_2 laser. The sealing was performed with a particular orientation, such that the hole in the counter electrode was placed directly over the sealed space and close to the TiO_2 film. The final arrangement formed an L-shape as shown in Figure D10.

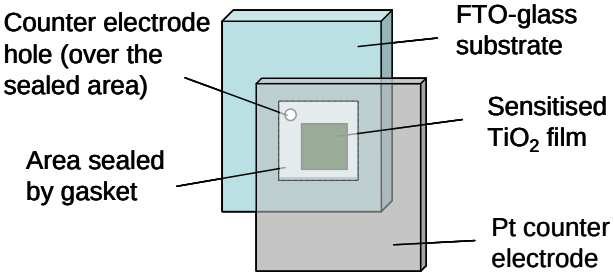

Figure D10. Orientation of the electrodes once sealed together with a polymer gasket.

After sealing the two electrodes together, an iodide/triiodide (I^-/I_3^-) redox electrolyte was introduced into the sensitised cell through the hole in the counter electrode. The mediator was composed of 0.6 M 1,2-dimethyl-3-propylimidazolium iodide, (DMPII);

0.5 M tertiary butyl-pyridine, (HtBP); 0.1 M lithium iodide, (LiI); and 0.05 M iodine, (I_2) in an 85:15 mixture of acetonitrile to valeronitrile. Electrolyte was placed on the electrode surface and a vacuum system was used to fill the sealed space of the cell with electrolyte.

Following this procedure the counter electrode hole was sealed by placing a surlyn gasket over the hole and sealing it under a No. 5 (19 mm) microscope cover slide. The exposed edges (those not overlapping each other) of the conducting sides of both electrodes were then coated with solder in order to provide a good connection for characterisation. The current-voltage curves for these devices were then measured on the solar simulator using a silicon diode to calibrate the light intensity of the instrument.

The NiO films were prepared by screen printing and sintering for 30 minutes at 400 ºC, then for 10 minutes at 550 ºC, followed by dyed overnight (18 hours) in 0.2mM dye solution. The redox electrolyte is composed of 0.5 M LiI, and 0.05 M I_2 in propylene carbonate.

Similar experimental protocol was followed in the testing of complex **49** at the Energy Materials Lab, Hanyang University.

D5 Current-voltage curves

D5.1 Current-voltage curves on TiO_2

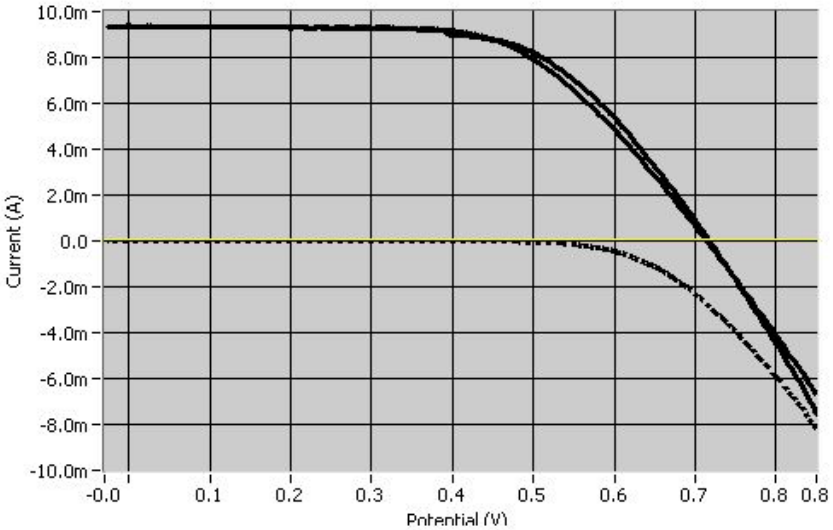

	100.0%	100.0%
Voltage o/c	720.01 mV	715.00 mV
Current s/c	15.56 mA/cm2	15.62 mA/cm2
Fill Factor	0.61	0.60
Max Power	6.84 mW/cm2	6.66 mW/cm2
V pmax	495.00 mV	480.00 mV
Efficiency	6.84 %	6.66 %

Current Compliance	100.00 mA
Settling Time	40.00 ms
Voltage Step	5.03 mV
Cell Size	0.60 cm2

Figure D11. Current-voltage curve for the reference dye (**N719**) adsorbed to TiO_2.

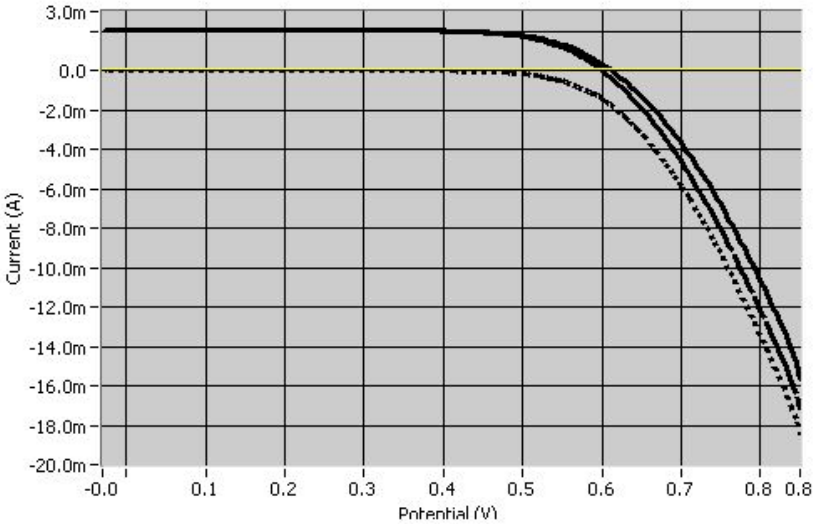

	100.0%	100.0%
Voltage o/c	615.00 mV	605.00 mV
Current s/c	3.25 mA/cm2	3.27 mA/cm2
Fill Factor	0.70	0.70
Max Power	1.40 mW/cm2	1.39 mW/cm2
V pmax	475.00 mV	475.00 mV
Efficiency	1.40 %	1.39 %

Current Compliance	100.00 mA
Settling Time	40.00 ms
Voltage Step	5.03 mV
Cell Size	0.64 cm2

Figure D12. Current-voltage curve for reference dye (**395**) adsorbed to TiO_2.

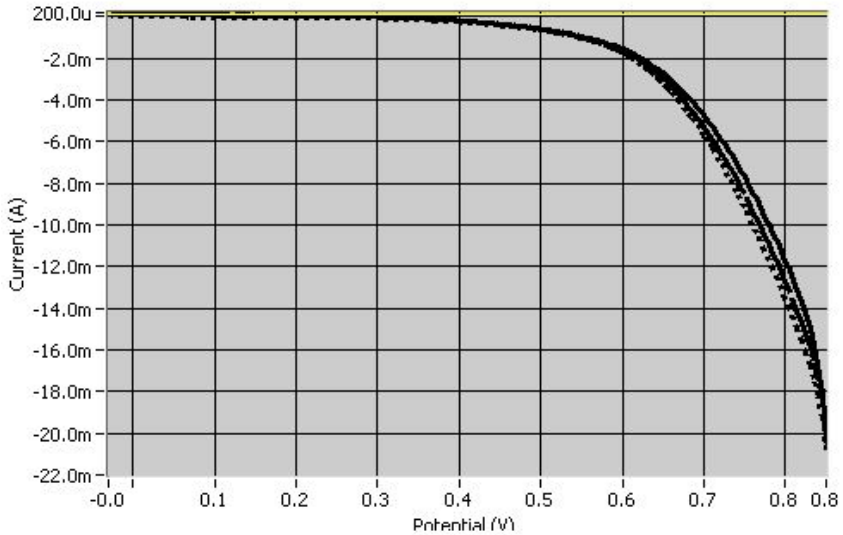

	100.0%	100.0%
Voltage o/c	300.00 mV	310.00 mV
Current s/c	139.48 uA/cm2	153.76 uA/cm2
Fill Factor	0.42	0.41
Max Power	17.39 uW/cm2	19.48 uW/cm2
V pmax	190.00 mV	215.00 mV
Efficiency	0.02 %	0.02 %

Current Compliance	100.00 mA
Settling Time	40.00 ms
Voltage Step	5.03 mV
Cell Size	0.64 cm2

Figure D13. Current-voltage curve for **46** adsorbed to TiO_2.

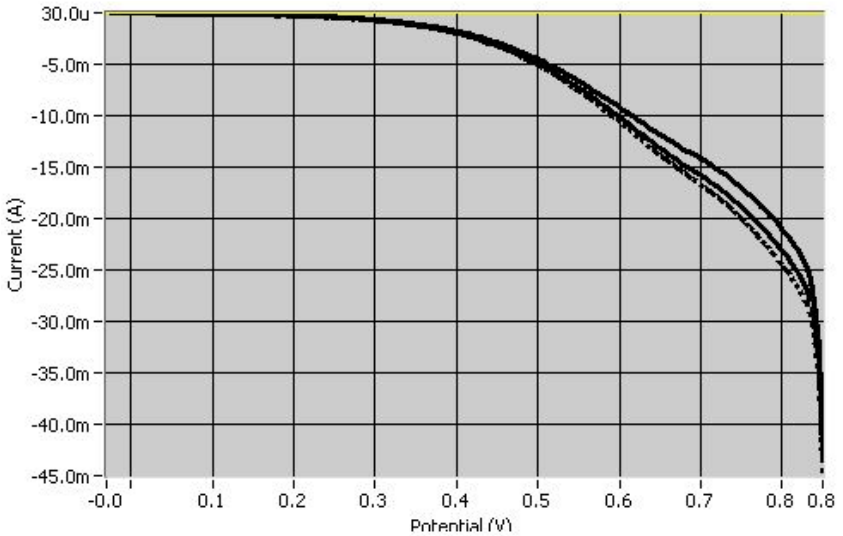

	100.0%	100.0%
Voltage o/c	0.00 V	0.00 V
Current s/c	0.00 A/cm2	0.00 A/cm2
Fill Factor	0.26	0.30
Max Power	174.90 nW/cm2	152.82 nW/cm2
V pmax	0.00 V	0.00 V
Efficiency	0.00 %	0.00 %

Current Compliance	100.00 mA
Settling Time	40.00 ms
Voltage Step	5.03 mV
Cell Size	0.64 cm2

Figure D14. Current-voltage curve for **47** adsorbed to TiO_2.

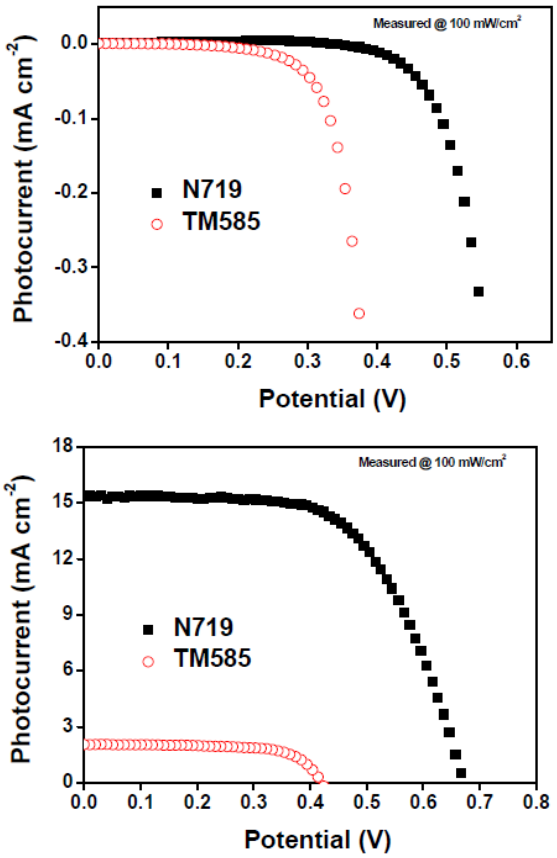

Figure D15. Current-voltage curves for **49** adsorbed to TiO_2.

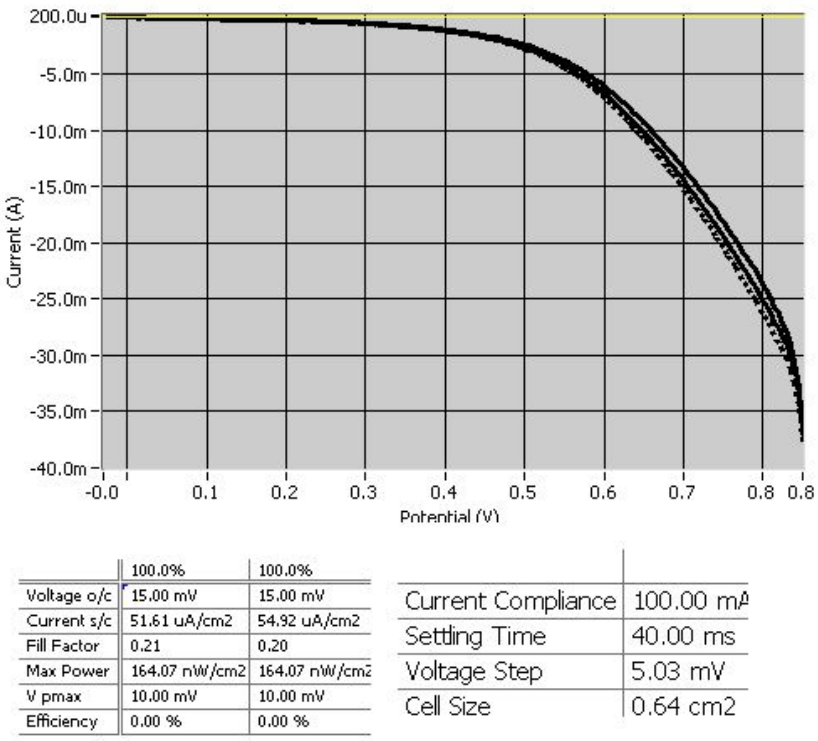

	100.0%	100.0%
Voltage o/c	15.00 mV	15.00 mV
Current s/c	51.61 uA/cm2	54.92 uA/cm2
Fill Factor	0.21	0.20
Max Power	164.07 nW/cm2	164.07 nW/cm2
V pmax	10.00 mV	10.00 mV
Efficiency	0.00 %	0.00 %

Current Compliance	100.00 mA
Settling Time	40.00 ms
Voltage Step	5.03 mV
Cell Size	0.64 cm2

Figure D16. Current-voltage curve for **50** adsorbed to TiO_2.

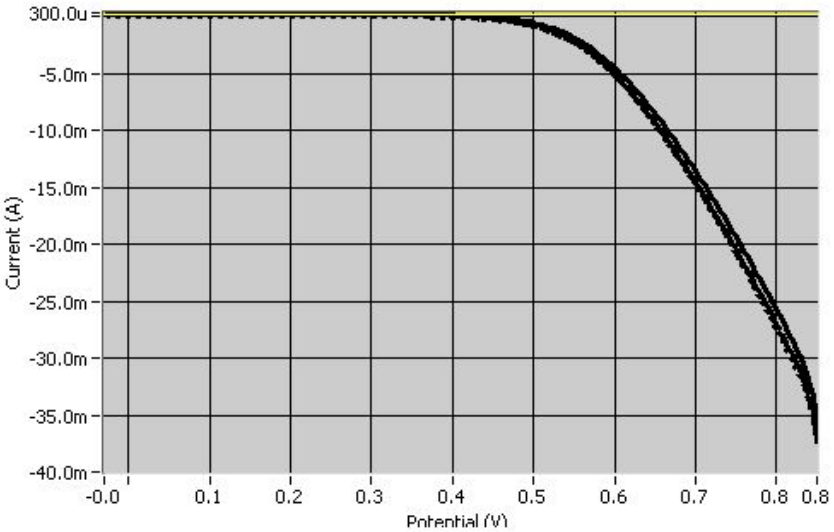

	100.0%	100.0%
Voltage o/c	430.00 mV	425.00 mV
Current s/c	372.10 uA/cm2	377.26 uA/cm2
Fill Factor	0.55	0.55
Max Power	88.44 uW/cm2	88.96 uW/cm2
V pmax	320.00 mV	315.00 mV
Efficiency	0.09 %	0.09 %

Current Compliance	100.00 mA
Settling Time	40.00 ms
Voltage Step	5.03 mV
Cell Size	0.64 cm2

Figure D17. Current-voltage curve for **51** adsorbed to TiO_2.

D5.2 Current-voltage curves on NiO

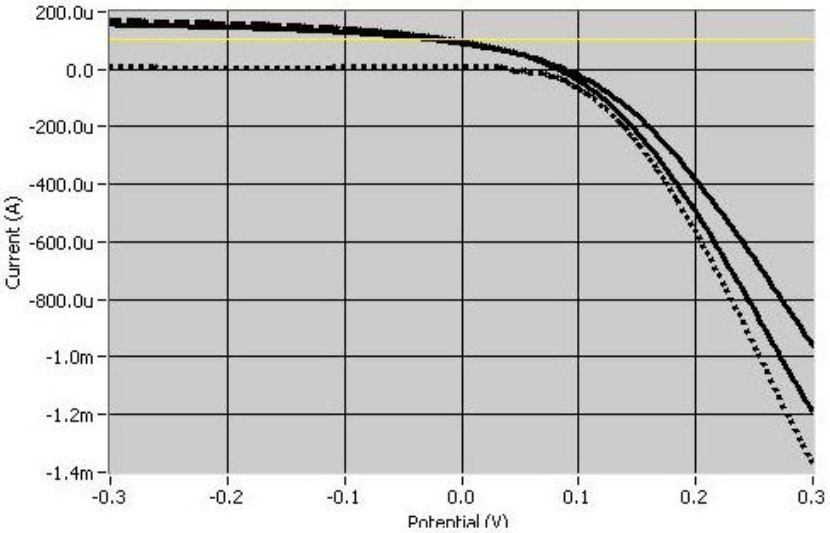

	100.0%	100.0%
Voltage o/c	90.86 mV	84.00 mV
Current s/c	563.31 uA/cm2	611.71 uA/cm2
Fill Factor	0.32	0.32
Max Power	16.36 uW/cm2	16.67 uW/cm2
V pmax	49.72 mV	46.28 mV
Efficiency	0.02 %	0.02 %

Current Compliance	100.00 mA
Settling Time	40.00 ms
Voltage Step	3.43 mV
Cell Size	0.16 cm2

Figure D18. Current-voltage curve for reference dye (**395**) adsorbed to NiO.

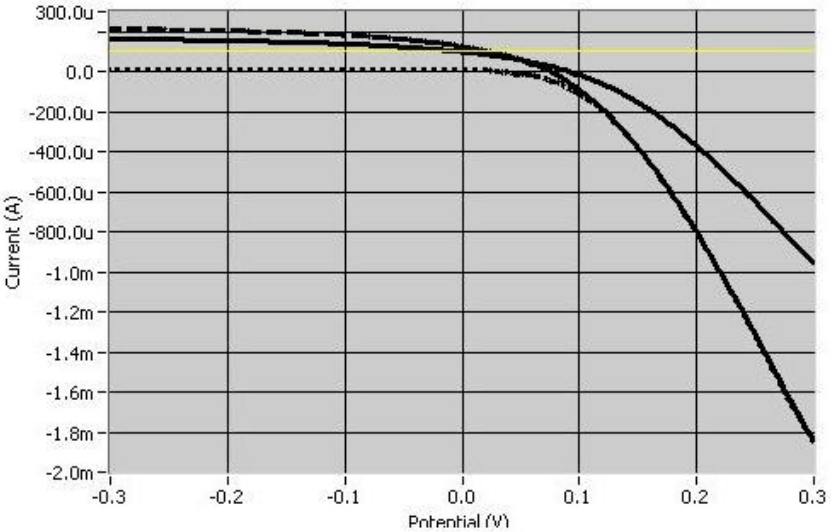

	100.0%	100.0%
Voltage o/c	94.29 mV	77.15 mV
Current s/c	623.44 uA/cm2	791.92 uA/cm2
Fill Factor	0.32	0.32
Max Power	18.69 uW/cm2	19.66 uW/cm2
V pmax	53.14 mV	42.85 mV
Efficiency	0.02 %	0.02 %

Current Compliance	100.00 mA
Settling Time	40.00 ms
Voltage Step	3.43 mV
Cell Size	0.16 cm2

Figure D19. Current-voltage curve for reference dye (**395**) adsorbed to NiO.

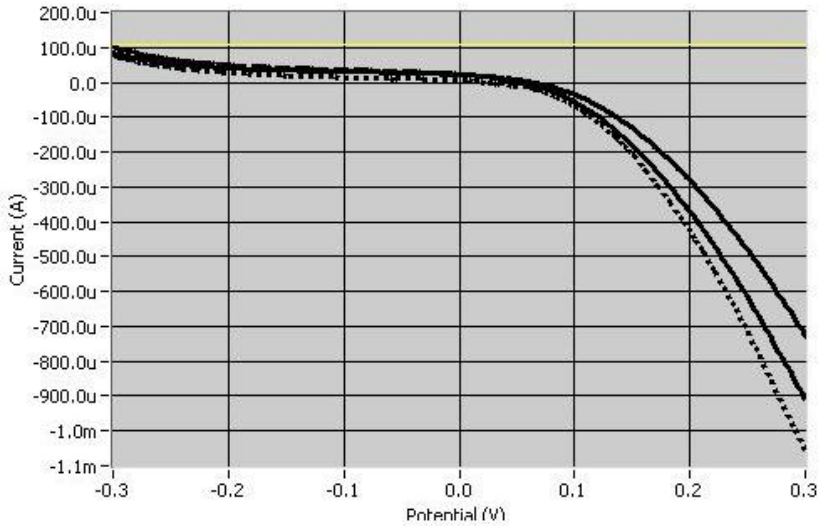

	100.0%	100.0%
Voltage o/c	63.43 mV	53.15 mV
Current s/c	136.55 uA/cm2	144.96 uA/cm2
Fill Factor	0.32	0.32
Max Power	2.81 uW/cm2	2.47 uW/cm2
V pmax	42.85 mV	39.43 mV
Efficiency	0.00 %	0.00 %

Current Compliance	100.00 mA
Settling Time	40.00 ms
Voltage Step	3.43 mV
Cell Size	0.16 cm2

Figure D19. Current-voltage curve for **46** adsorbed to NiO.

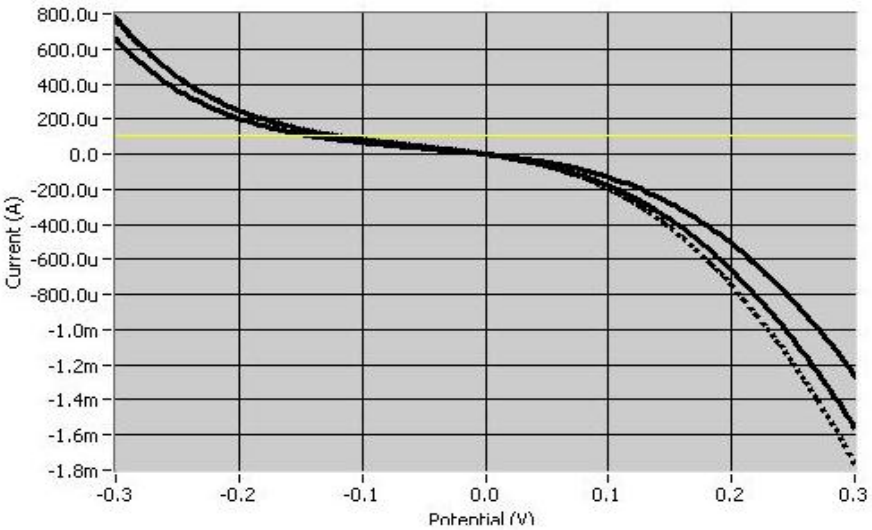

	100.0%	100.0%
Voltage o/c	1.72 mV	1.72 mV
Current s/c	0.00 A/cm2	0.00 A/cm2
Fill Factor	0.00	0.00
Max Power	0.00 W/cm2	0.00 W/cm2
V pmax	0.00 V	0.00 V
Efficiency	0.00 %	0.00 %

Current Compliance	100.00 mA
Settling Time	40.00 ms
Voltage Step	3.43 mV
Cell Size	0.16 cm2

Figure D20. Current-voltage curve for **46** adsorbed to NiO.

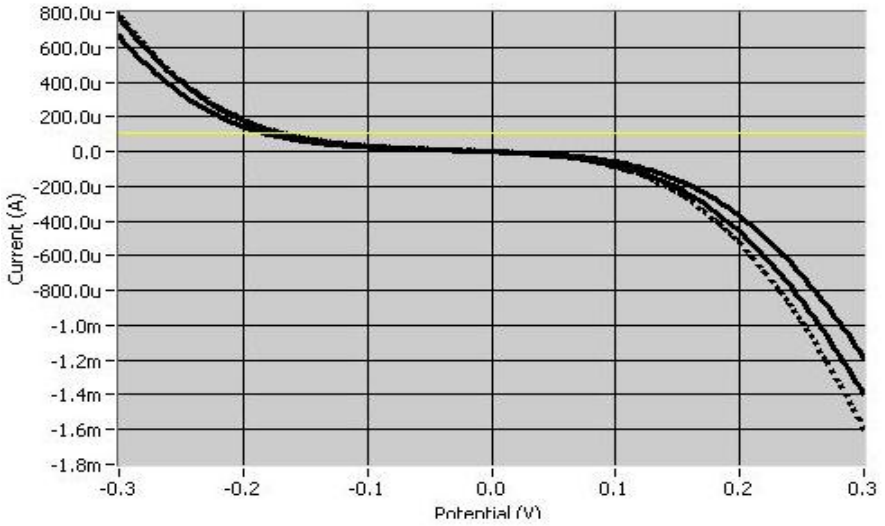

	100.0%	100.0%
Voltage o/c	0.00 V	0.00 V
Current s/c	0.00 A/cm2	0.00 A/cm2
Fill Factor	0.56	0.38
Max Power	30.64 nW/cm2	18.91 nW/cm2
V pmax	0.00 V	0.00 V
Efficiency	0.00 %	0.00 %

Current Compliance	100.00 mA
Settling Time	40.00 ms
Voltage Step	3.43 mV
Cell Size	0.16 cm2

Figure D21. Current-voltage curve for **50** adsorbed to NiO.

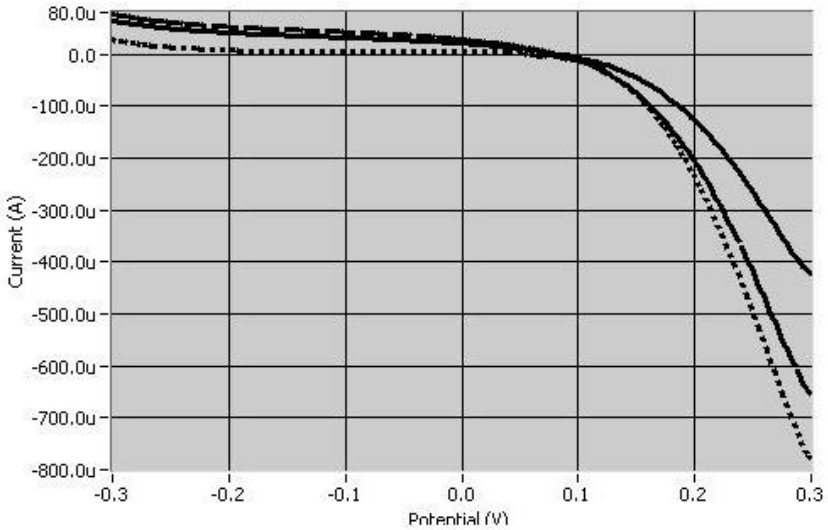

	100.0%	100.0%
Voltage o/c	80.57 mV	80.57 mV
Current s/c	128.88 uA/cm2	174.69 uA/cm2
Fill Factor	0.33	0.31
Max Power	3.46 uW/cm2	4.41 uW/cm2
V pmax	53.14 mV	46.28 mV
Efficiency	0.00 %	0.00 %

Current Compliance	100.00 mA
Settling Time	40.00 ms
Voltage Step	3.43 mV
Cell Size	0.16 cm2

Figure D22. Current-voltage curve for **51** adsorbed to NiO.

D6 Structure of the references dyes

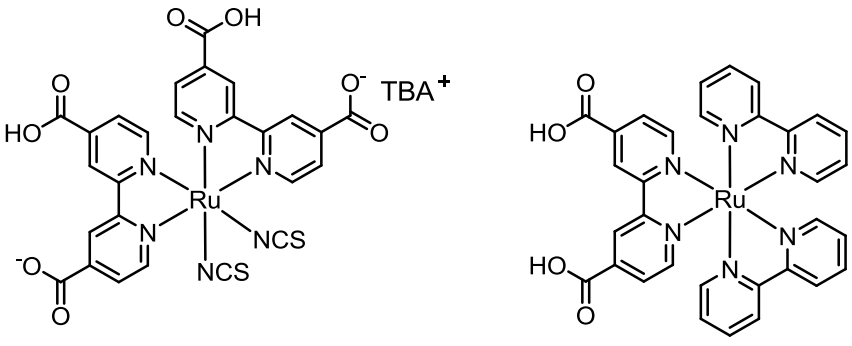

N719 **395**

Figure D23. Structure of the references dyes **N719** and **395** employed in solar cell testing.

Appendix E

(Chapter 5)

E1 ^{1}H NMR spectra

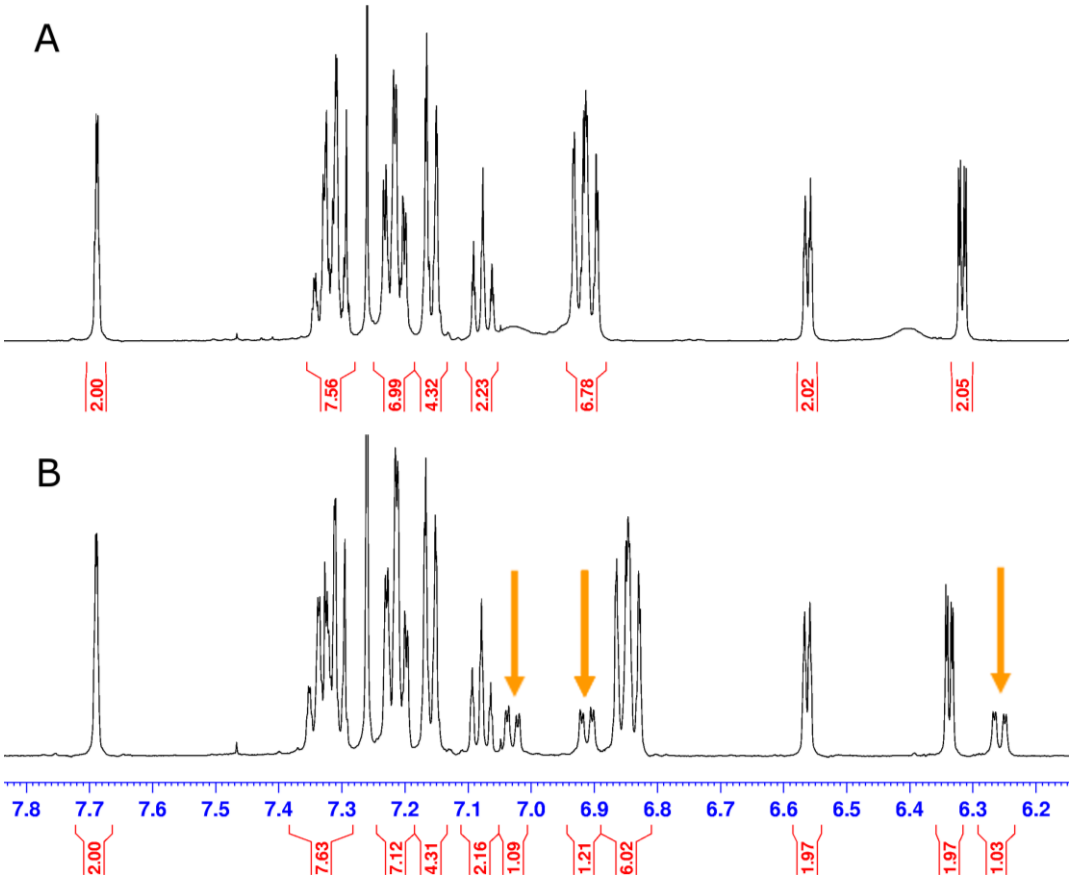

Figure E1. The aromatic region of the ^{1}H NMR spectrum of **65** in $CDCl_3$ at (A) room temperature (25 °C); and (B) low temperature (-10 °C). Orange arrows indicate the resonance for three of the four phenyl ring protons.

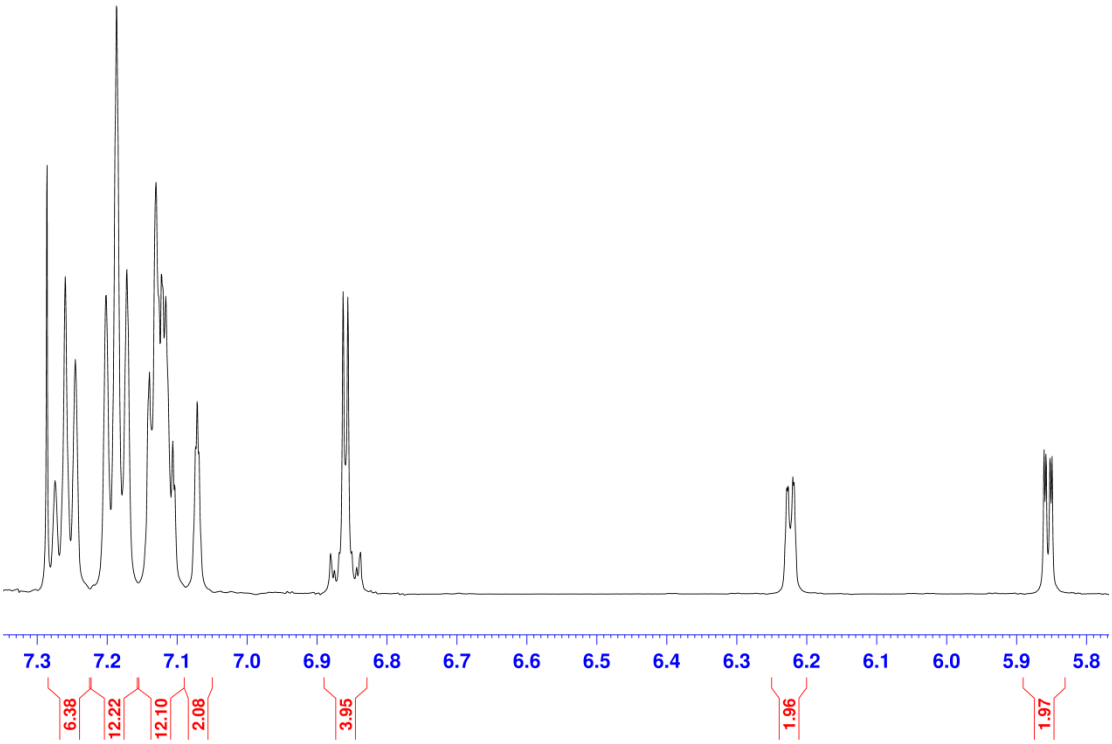

Figure E2. The aromatic region of the ^{1}H NMR spectrum of **69** in $CDCl_3$ at room temperature (25 °C).

E2 Absorption spectra

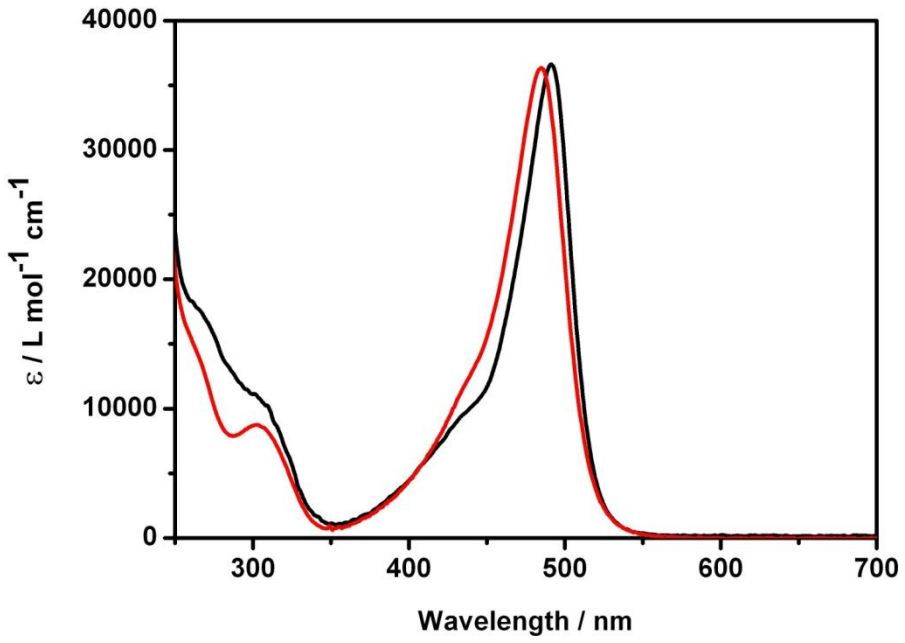

Figure E3. Absorbance spectra of **60** (black) and **66** (red) recorded in CH_2Cl_2.

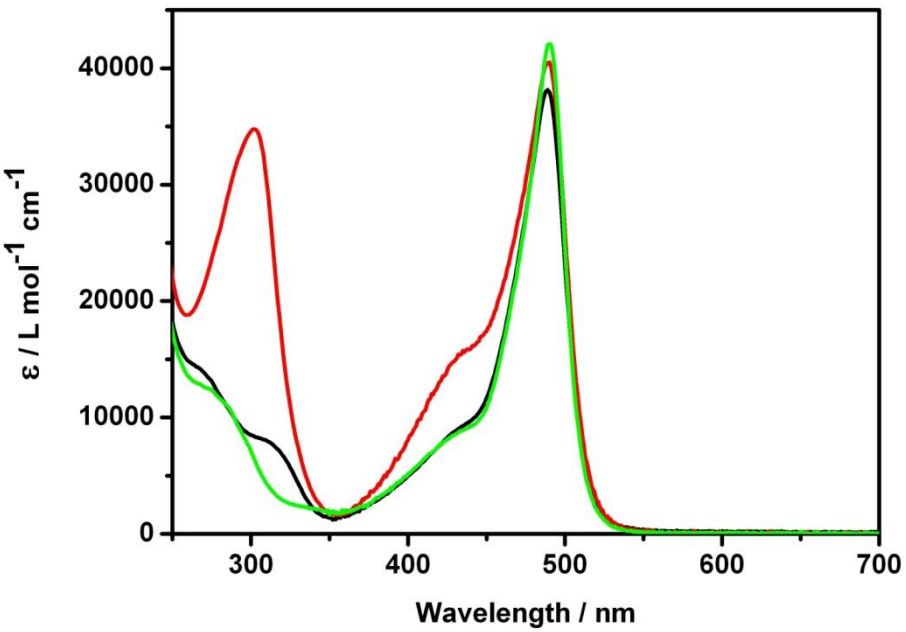

Figure E4. Absorbance spectra of **62** (black), **64** (green), and **65** (red) recorded in CH_2Cl_2.

E3 Resonance Raman spectroscopy

Table E1. Comparison of the observed resonance Raman shifts for Re(I)-dipyrrinato complexes (**60**, **67**) and Ru(II)-dipyrrinato complex (**46**) and dipyrrin ligand (**34**) (in CH_2Cl_2). Excitation wavelengths into the absorption band ascribed as a dipyrrin centred $\pi-\pi^*$ transition.

60[a]	**67**[a]	**46**[b]	**34**[a]
		409 (vs)	
872	872	874	870 (w)
900	898	900 (w)	895 (w)
988	987	990	989
1021(w)		1018 (w)	1007*
1033 (w)		1033 (w)	1047*
	1066	1058 (w)*	1074*
1086	1085	1081	1099 (w)*
			1123 (w)
1161 (w)	1161 (w)	1175 (w)*	1178 (w)*
1208	1208	1203 (w)	1222(w)*
1239	1240	1245 (w)	1255 (w)*
1285	1286	1287	1275
			1329
1344	1344 (w)		1355
1386	1385	1380	1390
1411	1410	1409 (w)	1410 (w)
1446	1448	1447	
1483 (w)	1485 (w)	1486 (w)	
1520	1525	1519 (w)	1518 (w)
			1538 (w)
1552 (w)	1552 (w)	1555 (w)	1561*
			1580
1611 (w)	1612 (w)	1603 (w)	1612 (w)

[a] 488 nm
[b] 458 nm
* possibly the same vibrational modes
(w) denotes the intensity of the peak is weak
(vs) denotes the intensity of the peak is very strong

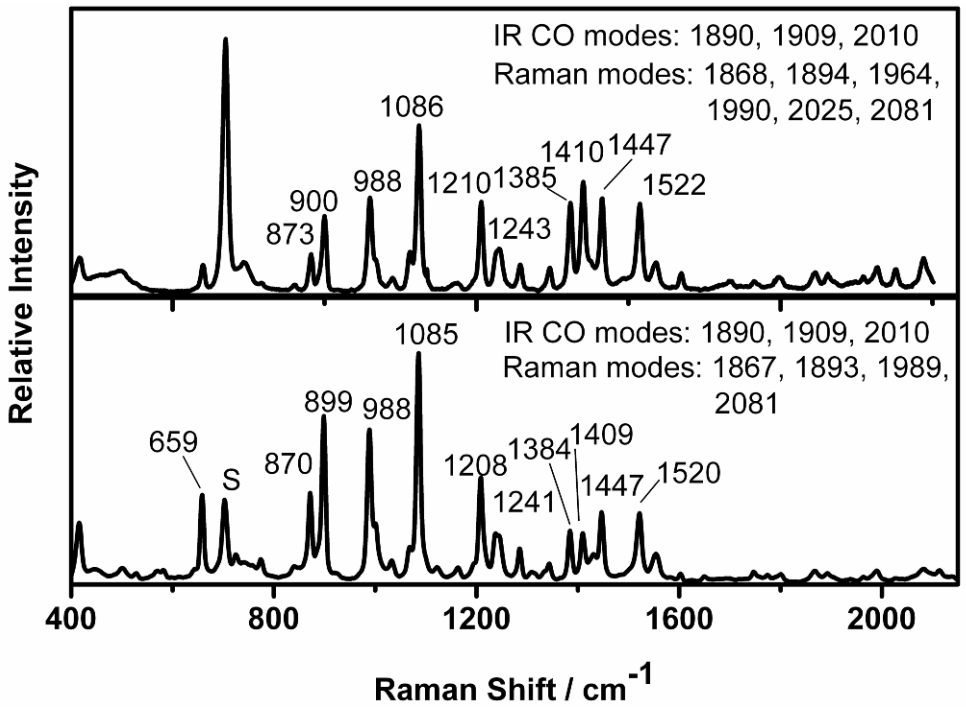

Figure E5. Resonance Raman spectrum of **62** in CH_2Cl_2. λ_{exc} = 458 nm (top), 488 nm (bottom).

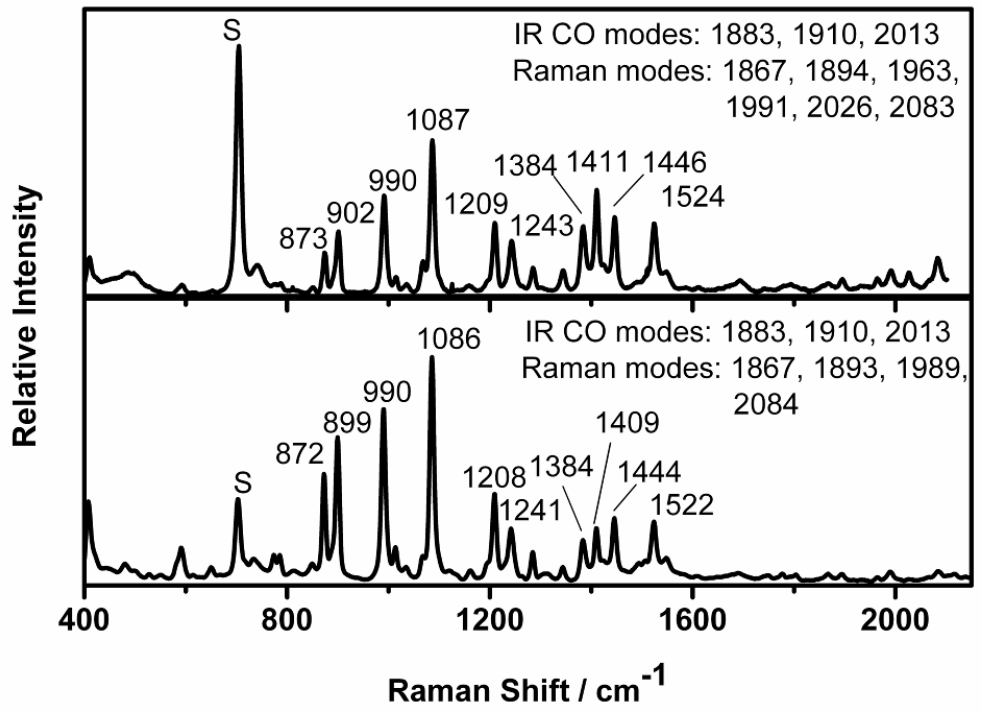

Figure E6. Resonance Raman spectrum of **63** in CH_2Cl_2. λ_{exc} = 458 nm (top), 488 nm (bottom).

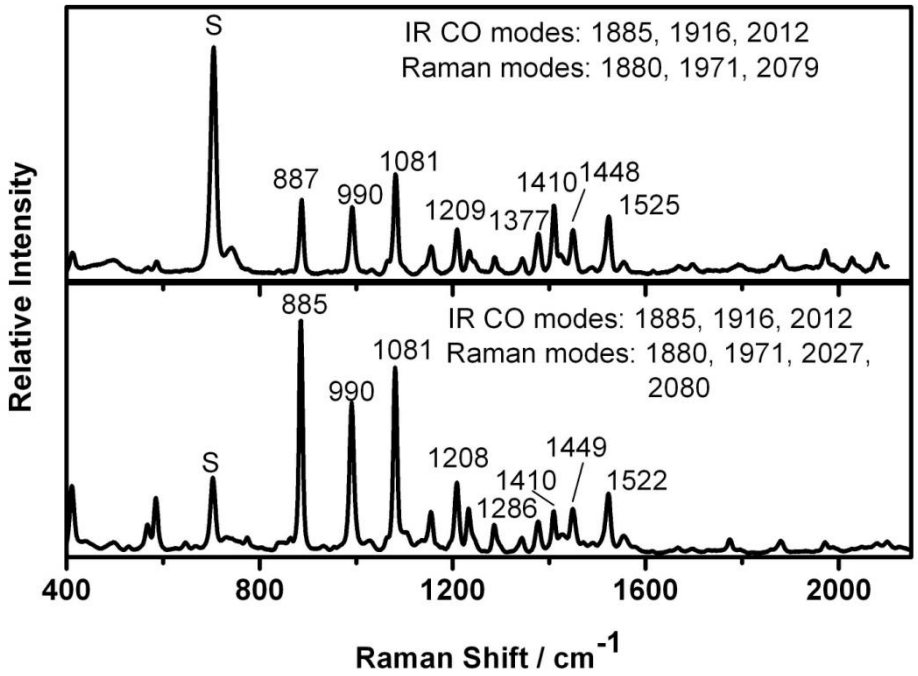

Figure E7. Resonance Raman spectrum of **64** in CH_2Cl_2. λ_{exc} = 458 nm (top), 488 nm (bottom).

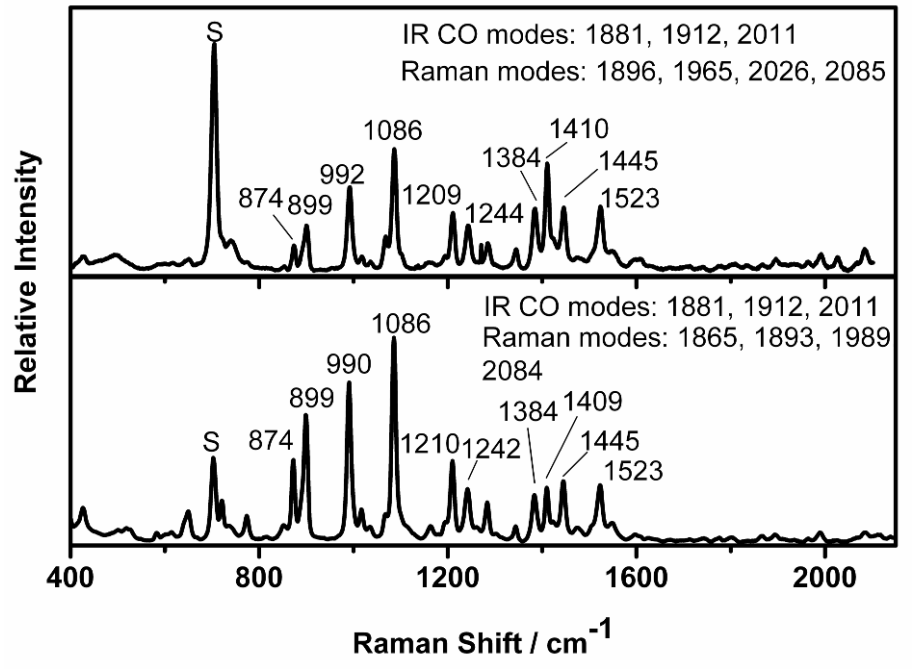

Figure E8. Resonance Raman spectrum of **65** in CH_2Cl_2. λ_{exc} = 458 nm (top), 488 nm (bottom).

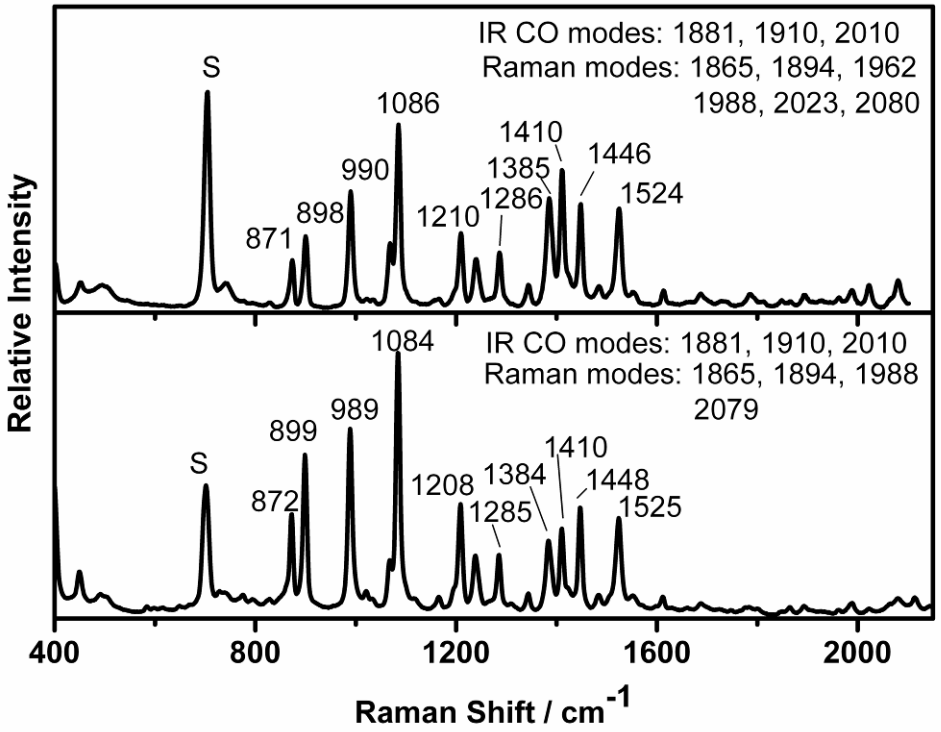

Figure E9. Resonance Raman spectrum of **66** in CH_2Cl_2. λ_{exc} = 458 nm (top), 488 nm (bottom).

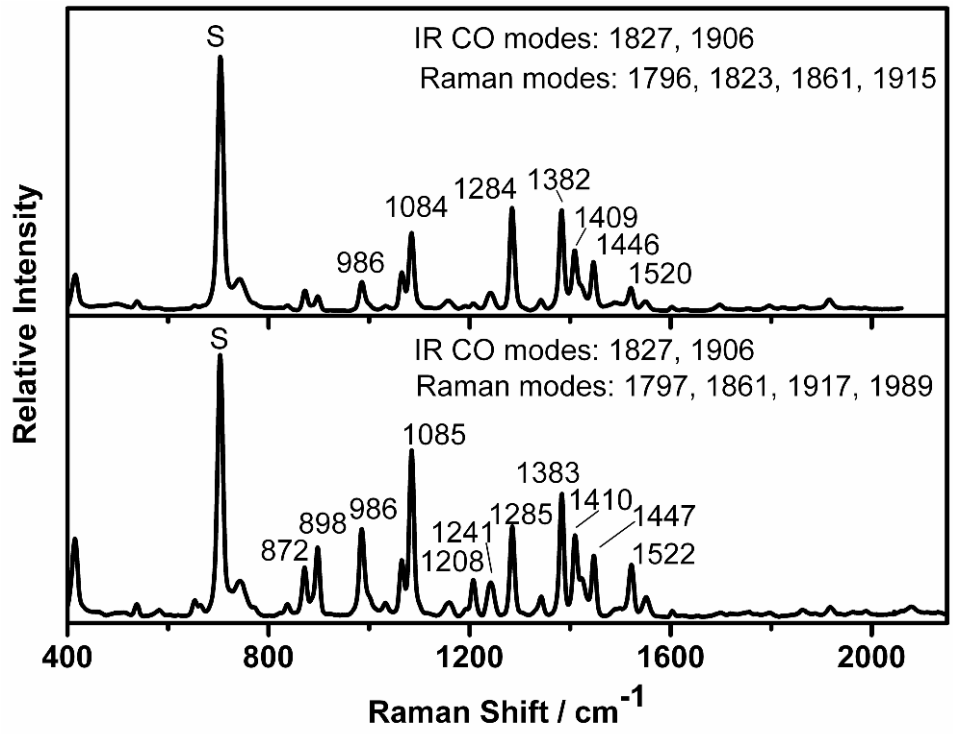

Figure E10. Resonance Raman spectrum of **68** in CH_2Cl_2. λ_{exc} = 458 nm (top), 488 nm (bottom).

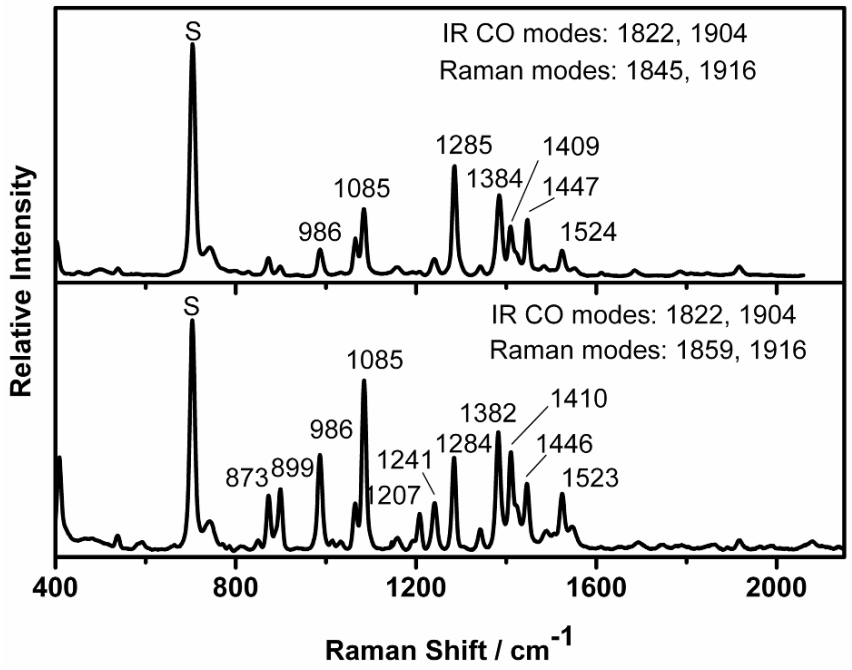

Figure E11. Resonance Raman spectrum of **69** in CH_2Cl_2. λ_{exc} = 458 nm (top), 488 nm (bottom).

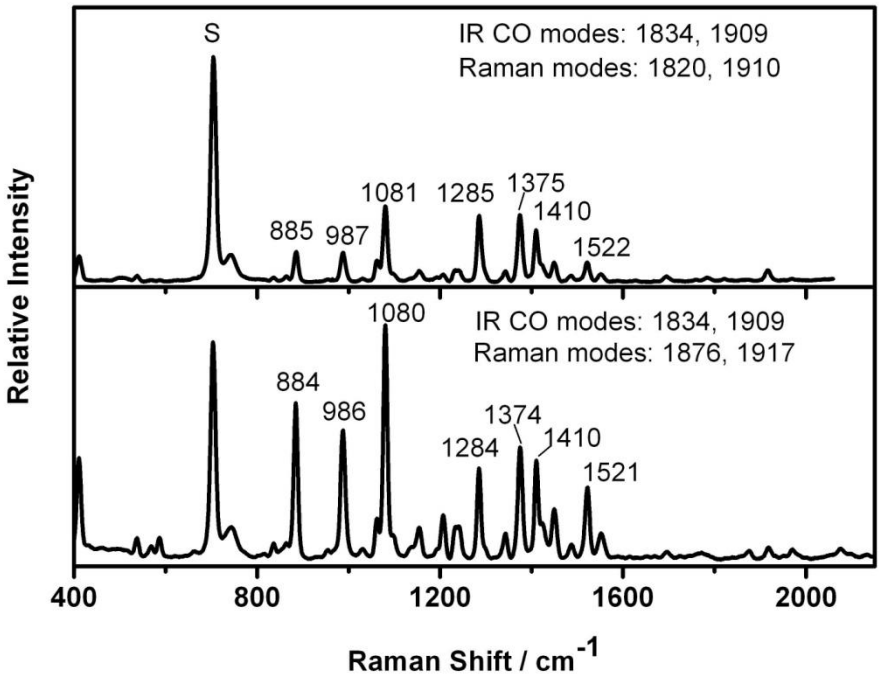

Figure E12. Resonance Raman spectrum of **70** in CH_2Cl_2. λ_{exc} = 458 nm (top), 488 nm (bottom).

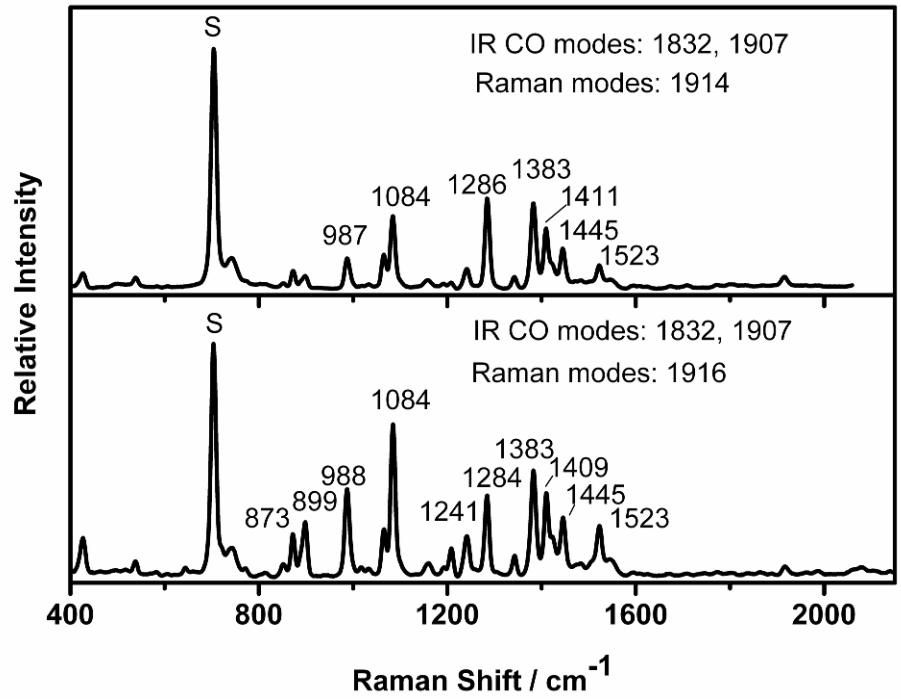

Figure E13. Resonance Raman spectrum of **71** in CH_2Cl_2. λ_{exc} = 458 nm (top), 488 nm (bottom).

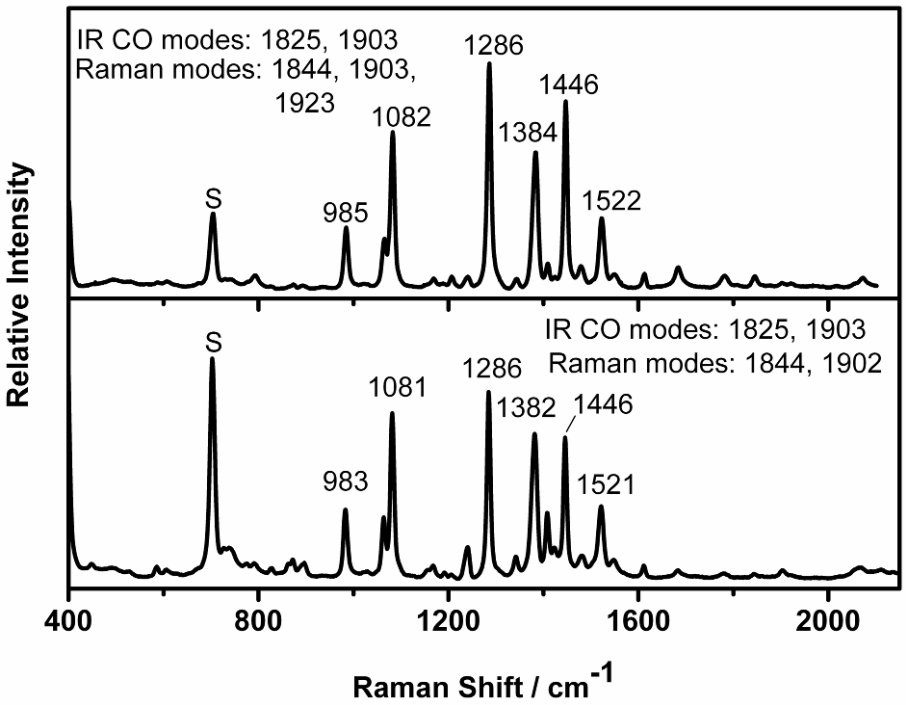

Figure E14. Resonance Raman spectrum of **72** in CH_2Cl_2. λ_{exc} = 458 nm (top), 488 nm (bottom).

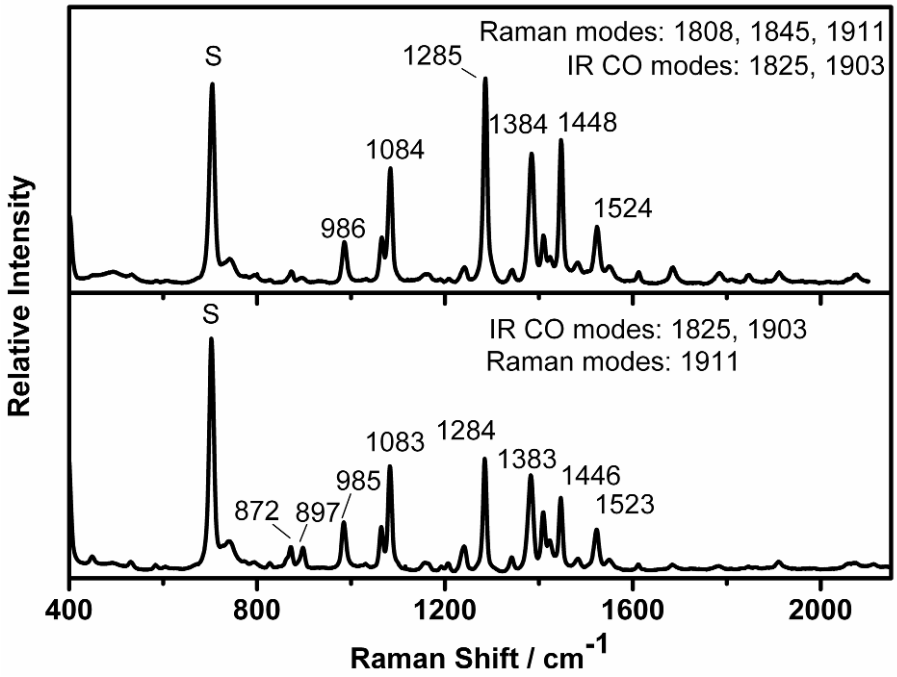

Figure E15. Resonance Raman spectrum of **73** in CH_2Cl_2. λ_{exc} = 458 nm (top), 488 nm (bottom).

E4 Time dependent DFT studies

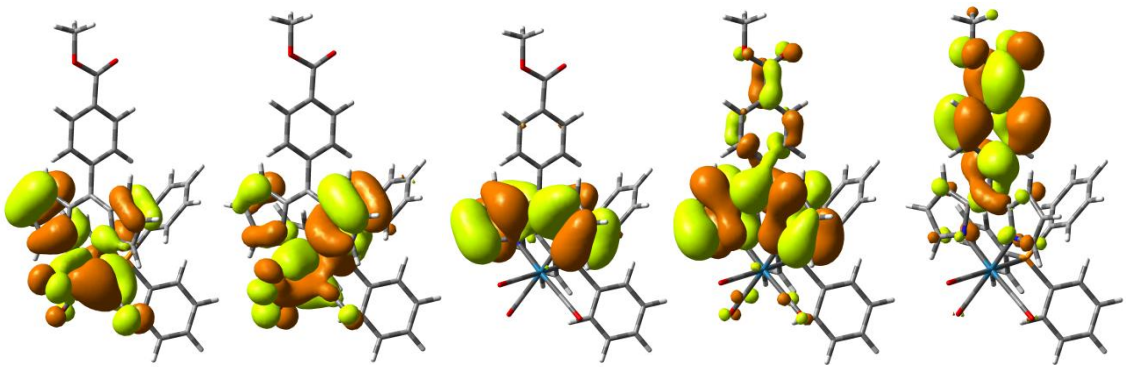

Figure E16. Selected molecular orbitals involved in the absorption spectrum of **60**.

Table E2. Calculated and experimental absorption parameters for **65**.

Calculated				Experimental	
λ (nm)	Configuration (% contribution)	Oscillator strength[a]	Assignment	λ (nm)	ε (L mol^{-1} cm^{-1})
529	HOMO→LUMO (97)	0.093			
444	HOMO-3→LUMO (22), HOMO-2→LUMO (71)	0.031	Re-dipyrrin (MLCT)		
440	HOMO-3→LUMO (55), HOMO-2→LUMO (-10), HOMO-1→LUMO (27)	0.077	Re-dipyrrin (MLCT)		
396	HOMO-3→LUMO (-18), HOMO-2→LUMO (11), HOMO-1→LUMO (48)	0.362	π–π*	490	40 500
321	HOMO→LUMO+4 (79)	0.049			
302	HOMO-8→LUMO (33), HOMO-6→LUMO (-33), HOMO→LUMO+8 (-19)	0.048			
301	HOMO-6→LUMO (-15), HOMO→LUMO+8 (64)	0.059			
288	HOMO→LUMO+9 (72), HOMO→LUMO+11 (15)	0.139	ILCT (π–π*)[b]	302	34 800
286	HOMO-2→LUMO+2 (32), HOMO-1→LUMO+3 (11)	0.047			
285	HOMO-11→LUMO (-15), HOMO→LUMO+11 (44)	0.192	ILCT (π–π*)[b]		
284	HOMO-11→LUMO (21), HOMO-10→LUMO (10), HOMO-9→LUMO (18), HOMO→LUMO+11 (16)	0.050	ILCT (π–π*)[b]		

[a] Only calculated oscillator strengths of greater than 0.03 are reported.
[b] A combination of these three transitions is probably responsible for the prominent peak observed at 302 nm in the experimental absorption spectrum.

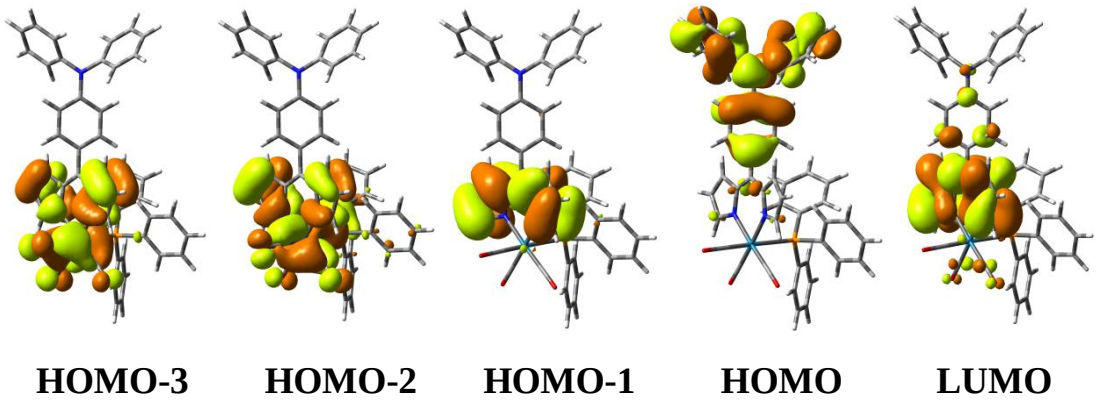

Figure E17. Selected molecular orbitals involved in the absorption spectrum of **65**.

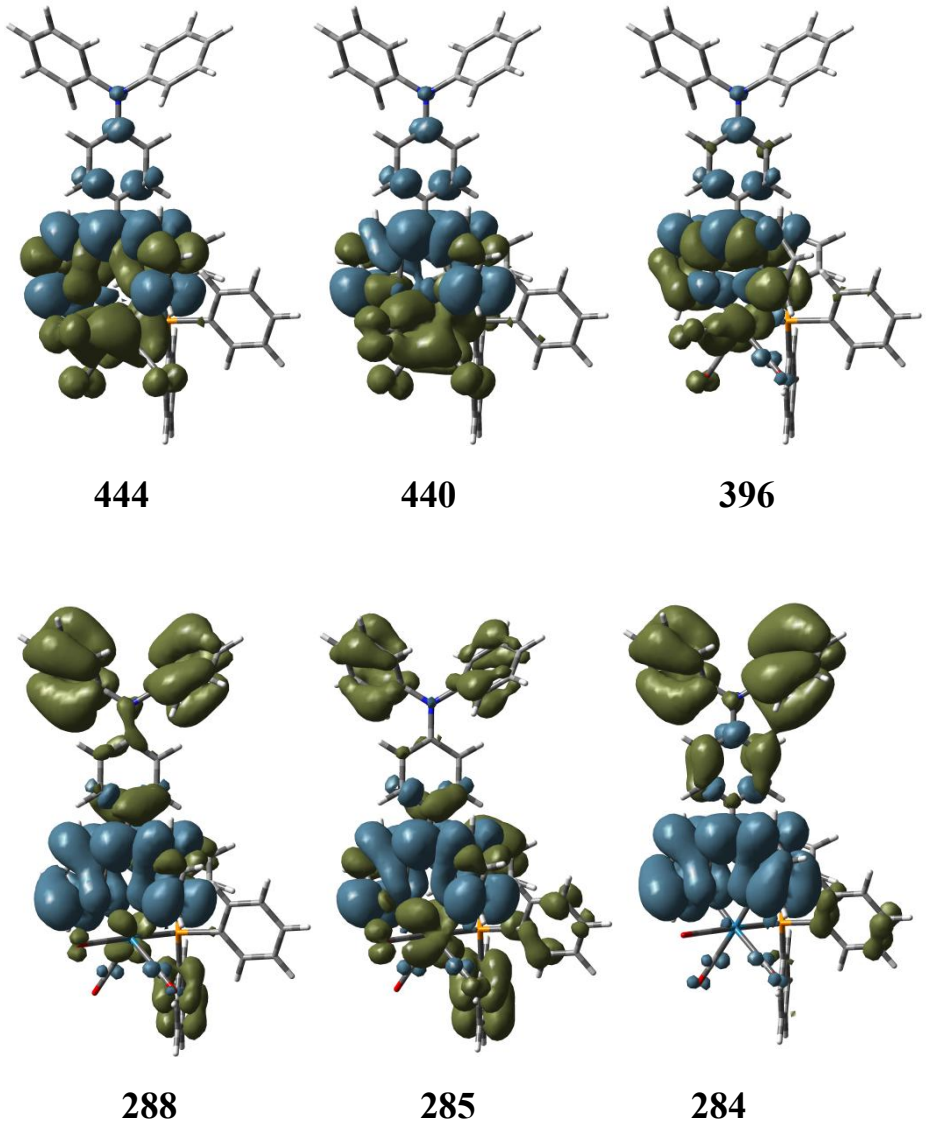

Figure E18. Electron density difference plots for **65**. Green represents depletion of electron density and blue represents accumulation of electron density.

E5 Excitation and emission spectra

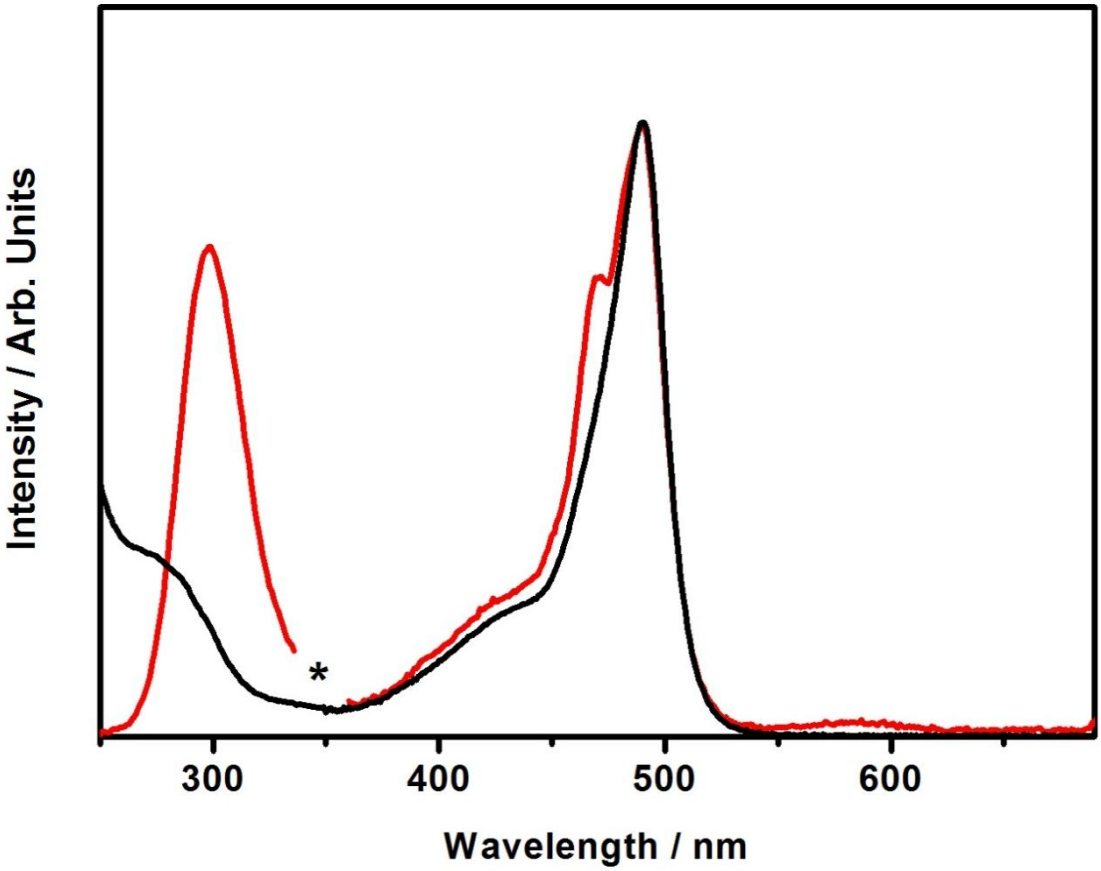

Figure E19. Excitation (red, λ_{em} = 700 nm) and absorption (black) spectra of **64** in CH_2Cl_2. The excitation spectra has been normalised to the absorption spectra at 490 nm. The * denotes where an artefact peak was removed.

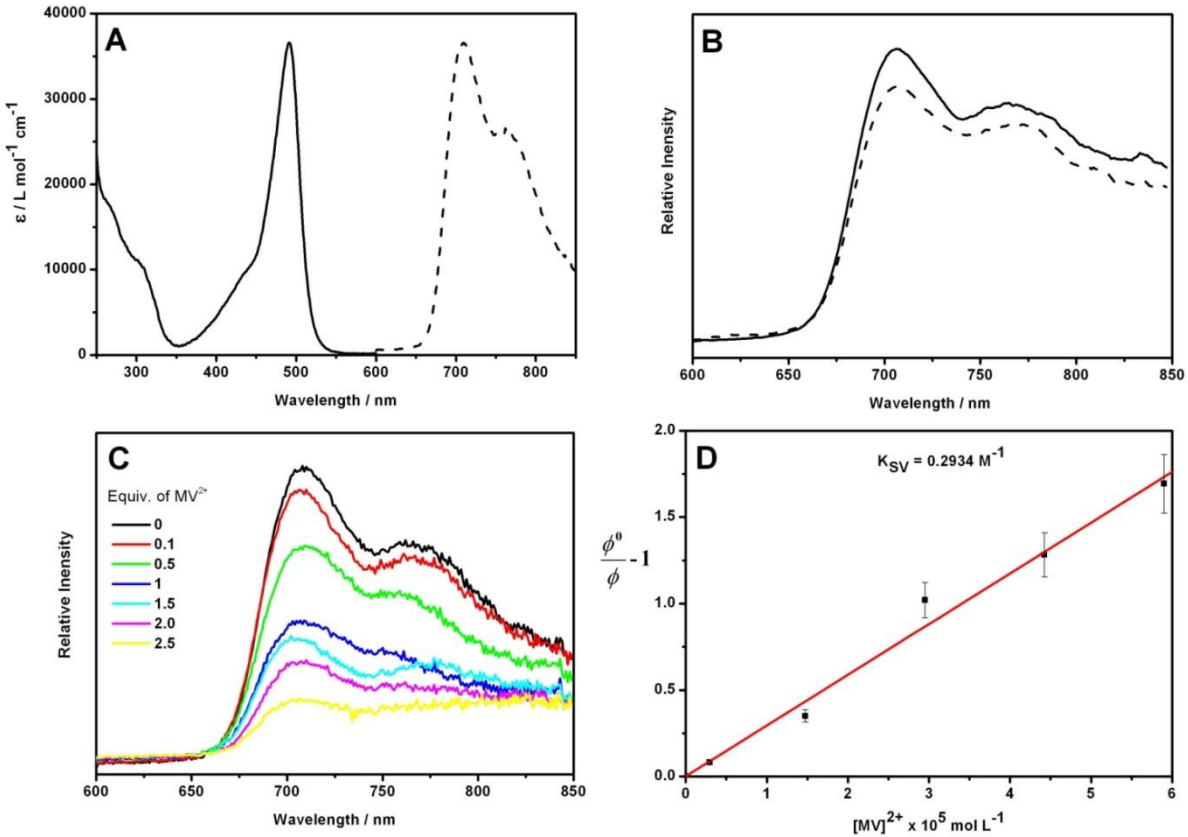

Figure E20. Absorption and emission spectra (λ_{ex} = 485 nm) of **60** in CH_2Cl_2 (A) absorption spectra (black solid line) and emission spectra (black dotted line, λ_{ex} = 485 nm) in CH_2Cl_2. (B) Emission spectra (λ_{ex} = 485 nm) after rigorous deoxygenation of the solvent (solid black line) and after bubbling air (2 mL) through the sample (black dotted line). (C) Emission spectra (λ_{ex} = 485 nm) as a function of added methyl viologen (MV^{2+}, 1-30 molar equivalents). (D) Stern-Volmer plot showing the quenching of emission by MV^{2+}. ϕ^0 is the quantum yield in the absence of MV^{2+} and ϕ is the quantum yield in the presence of MV^{2+}.

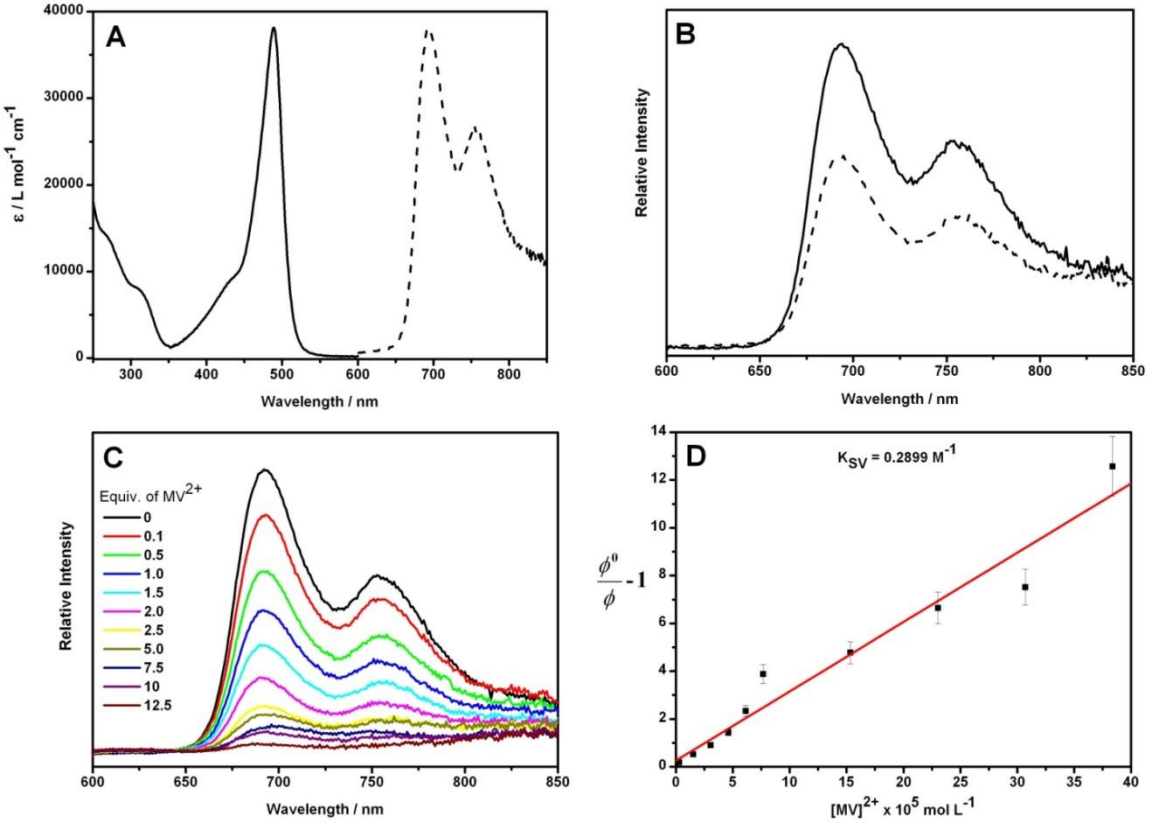

Figure E21. Absorption and emission spectra (λ_{ex} = 485 nm) of **62** in CH_2Cl_2 (A) absorption spectra (black solid line) and emission spectra (black dotted line, λ_{ex} = 485 nm) in CH_2Cl_2. (B) Emission spectra (λ_{ex} = 485 nm) after rigorous deoxygenation of the solvent (solid black line) and after bubbling air (2 mL) through the sample (black dotted line). (C) Emission spectra (λ_{ex} = 485 nm) as a function of added methyl viologen (MV^{2+}, 1-30 molar equivalents). (D) Stern-Volmer plot showing the quenching of emission by MV^{2+}. ϕ^0 is the quantum yield in the absence of MV^{2+} and ϕ is the quantum yield in the presence of MV^{2+}.

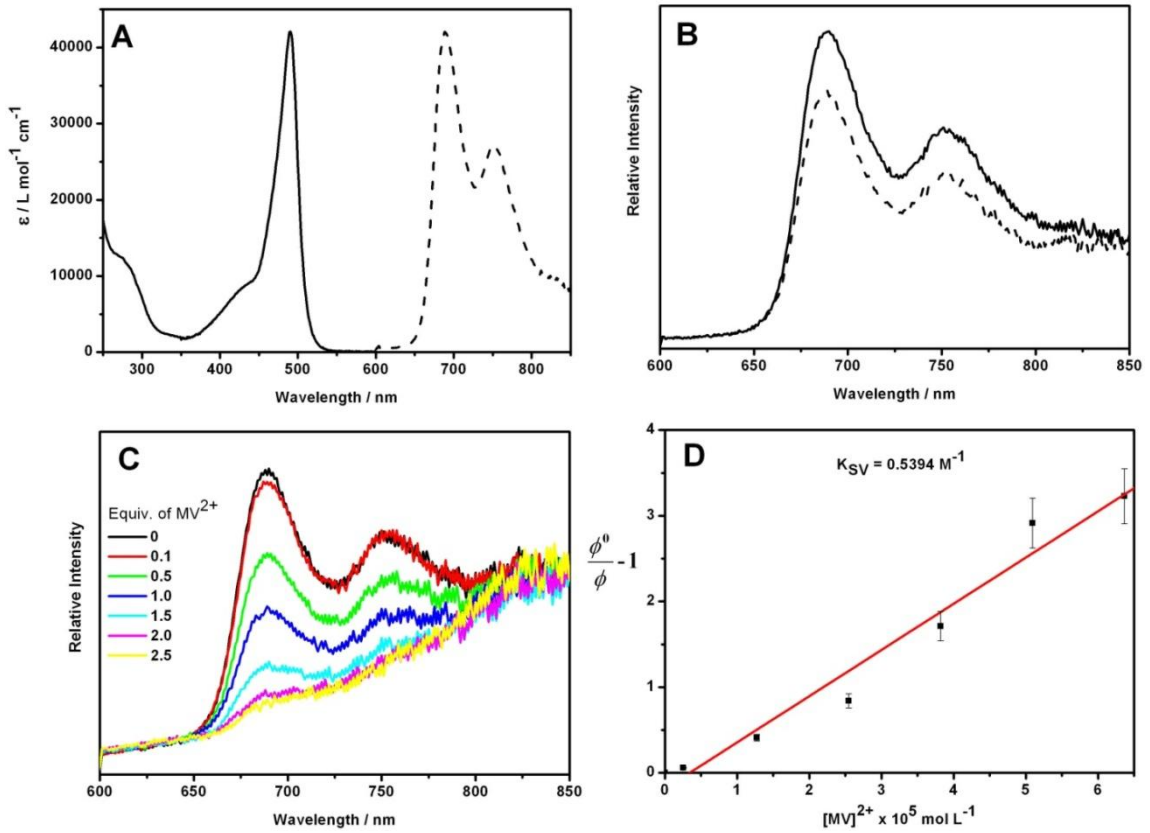

Figure E22. Absorption and emission spectra (λ_{ex} = 485 nm) of **63** in CH_2Cl_2 (A) absorption spectra (black solid line) and emission spectra (black dotted line, λ_{ex} = 485 nm) in CH_2Cl_2. (B) Emission spectra (λ_{ex} = 485 nm) after rigorous deoxygenation of the solvent (solid black line) and after bubbling air (2 mL) through the sample (black dotted line). (C) Emission spectra (λ_{ex} = 485 nm) as a function of added methyl viologen (MV^{2+}, 1-30 molar equivalents). (D) Stern-Volmer plot showing the quenching of emission by MV^{2+}. ϕ^0 is the quantum yield in the absence of MV^{2+} and ϕ is the quantum yield in the presence of MV^{2+}.

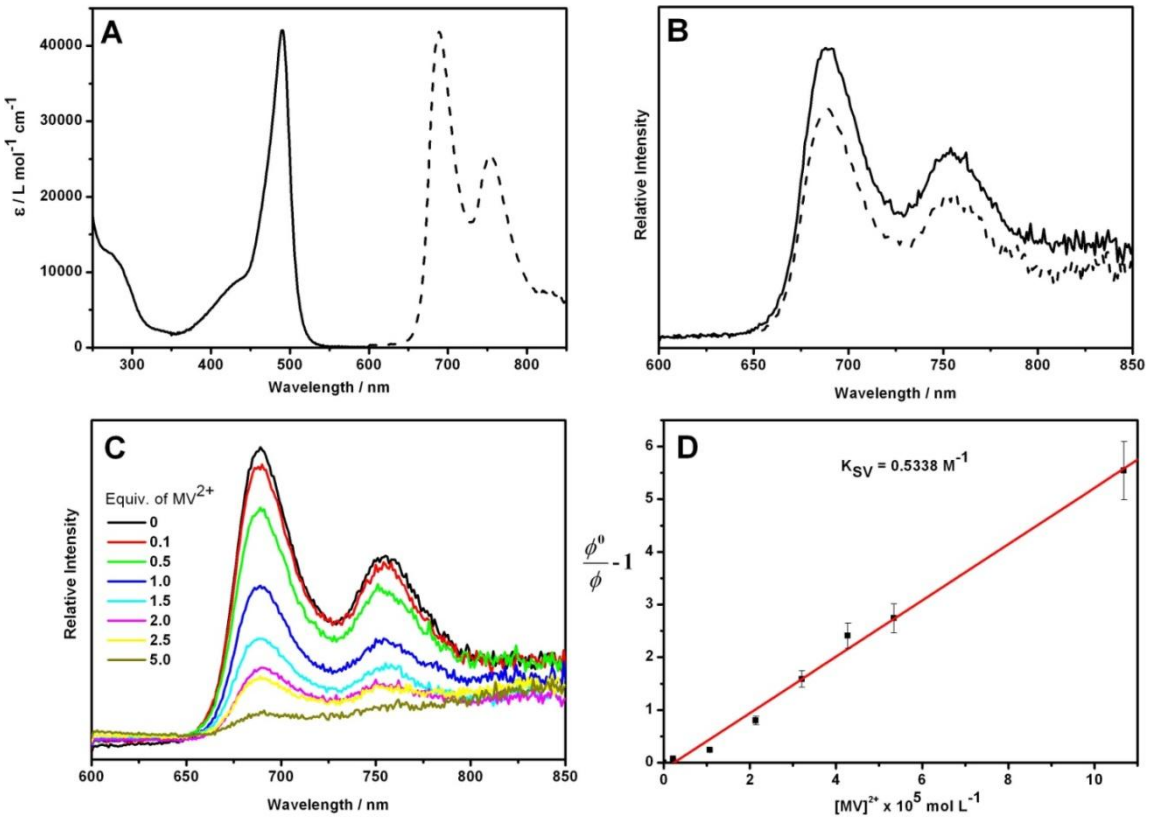

Figure E23. Absorption and emission spectra (λ_{ex} = 485 nm) of **64** in CH_2Cl_2 (A) absorption spectra (black solid line) and emission spectra (black dotted line, λ_{ex} = 485 nm) in CH_2Cl_2. (B) Emission spectra (λ_{ex} = 485 nm) after rigorous deoxygenation of the solvent (solid black line) and after bubbling air (2 mL) through the sample (black dotted line). (C) Emission spectra (λ_{ex} = 485 nm) as a function of added methyl viologen (MV^{2+}, 1-30 molar equivalents). (D) Stern-Volmer plot showing the quenching of emission by MV^{2+}. ϕ^0 is the quantum yield in the absence of MV^{2+} and ϕ is the quantum yield in the presence of MV^{2+}.

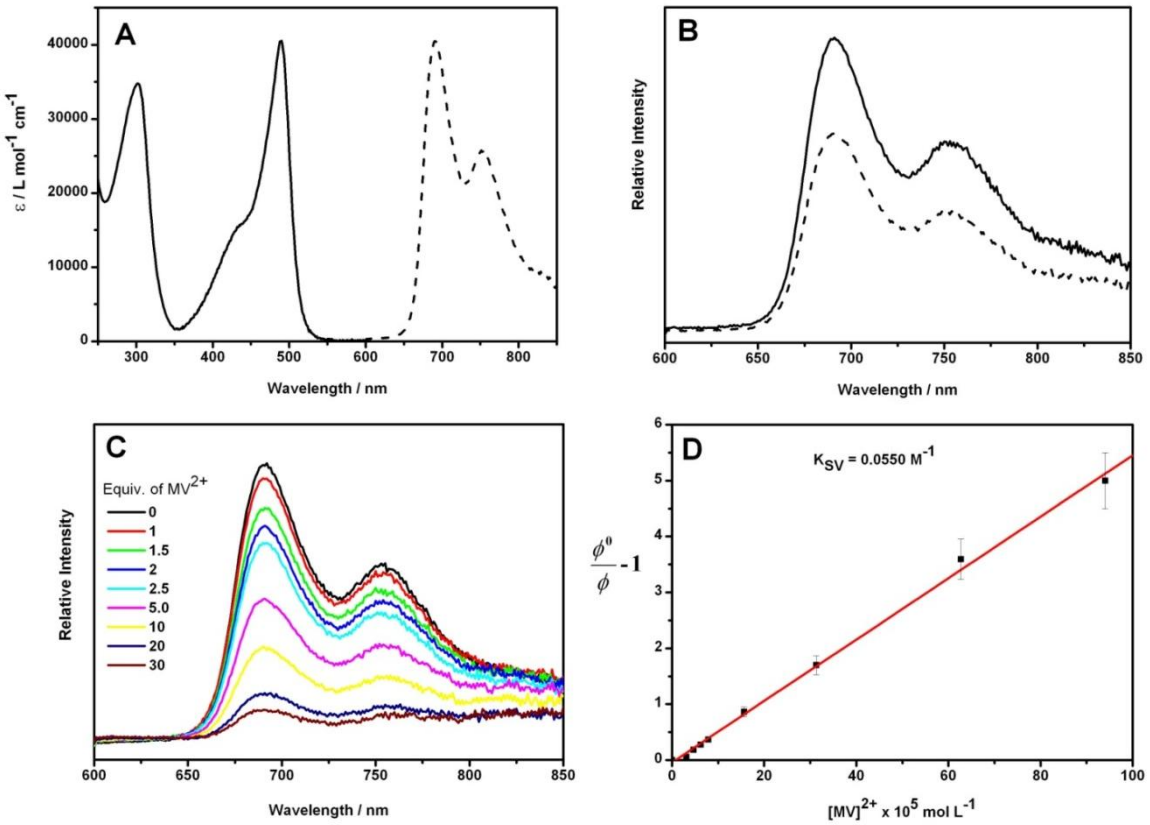

Figure E24. Absorption and emission spectra (λ_{ex} = 485 nm) of **65** in CH_2Cl_2 (A) absorption spectra (black solid line) and emission spectra (black dotted line, λ_{ex} = 485 nm) in CH_2Cl_2. (B) Emission spectra (λ_{ex} = 485 nm) after rigorous deoxygenation of the solvent (solid black line) and after bubbling air (2 mL) through the sample (black dotted line). (C) Emission spectra (λ_{ex} = 485 nm) as a function of added methyl viologen (MV^{2+}, 1-30 molar equivalents). (D) Stern-Volmer plot showing the quenching of emission by MV^{2+}. ϕ^0 is the quantum yield in the absence of MV^{2+} and ϕ is the quantum yield in the presence of MV^{2+}.

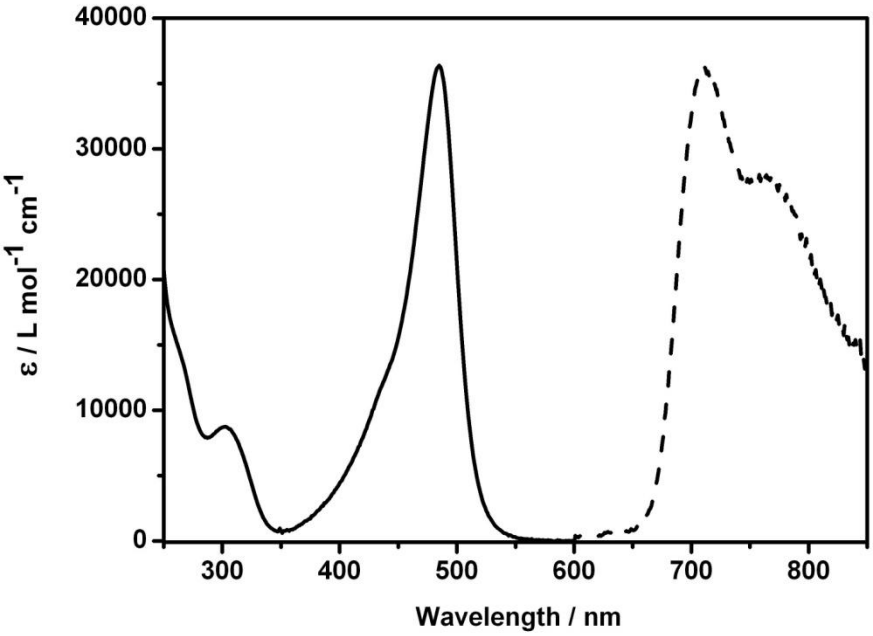

Figure E25. Absorption and emission spectra of **66** in CH_2Cl_2. Absorption spectra (black solid line) and emission spectra (black dotted line, λ_{ex} = 480 nm)

E6 Photochemical ligand substitution of 60

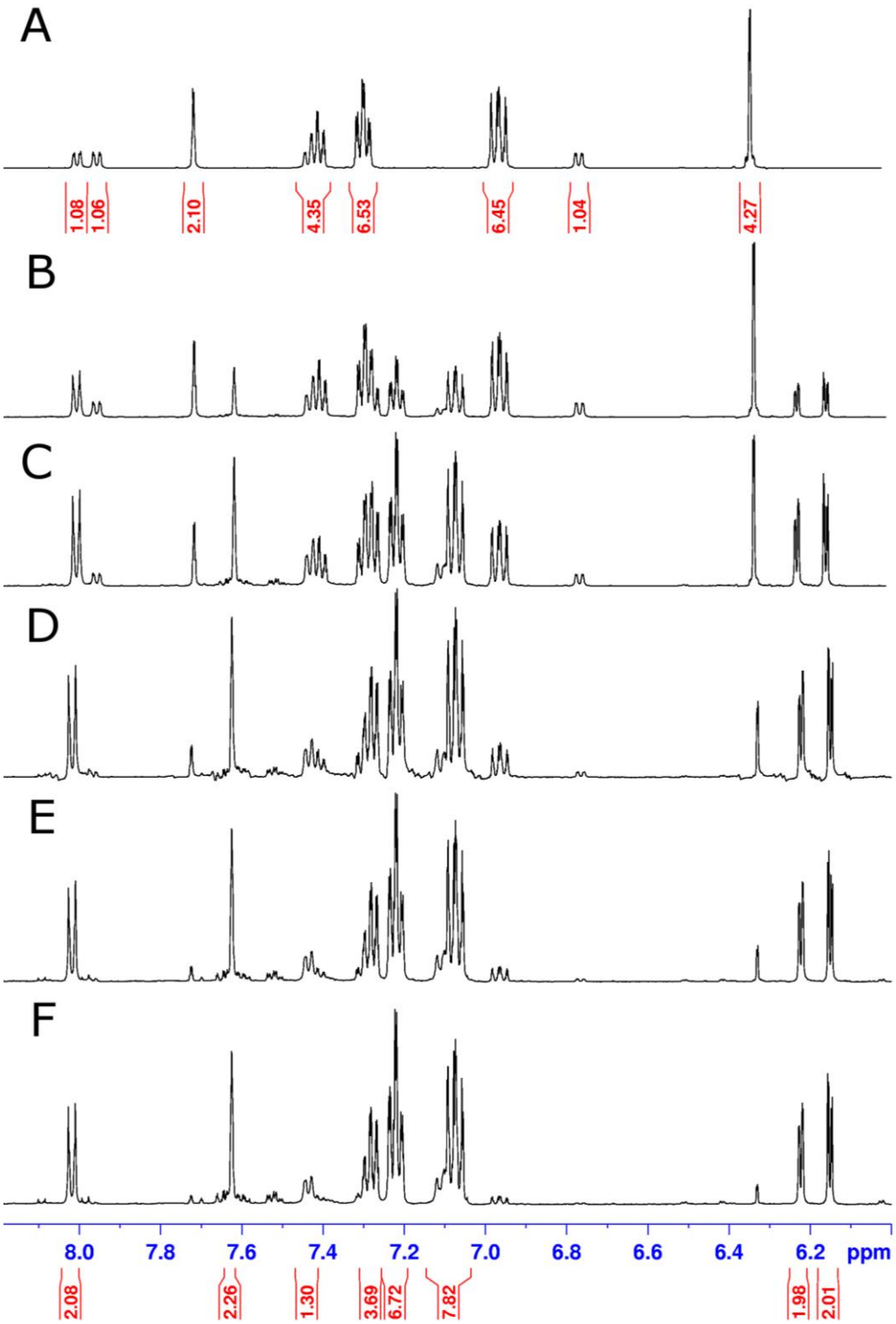

Figure E26. Aromatic region of the ^{1}H NMR spectrum (CD_3CN) of the PLS reaction of **60**. (A) Starting material, **60**; (B) after 30 mins irradiation, (C) after 60 mins irradiation, (D) after 90 mins irradiation, (E) after 120 mins irradiation, and (f) after 150 mins irradiation (proposed complex, **74**).

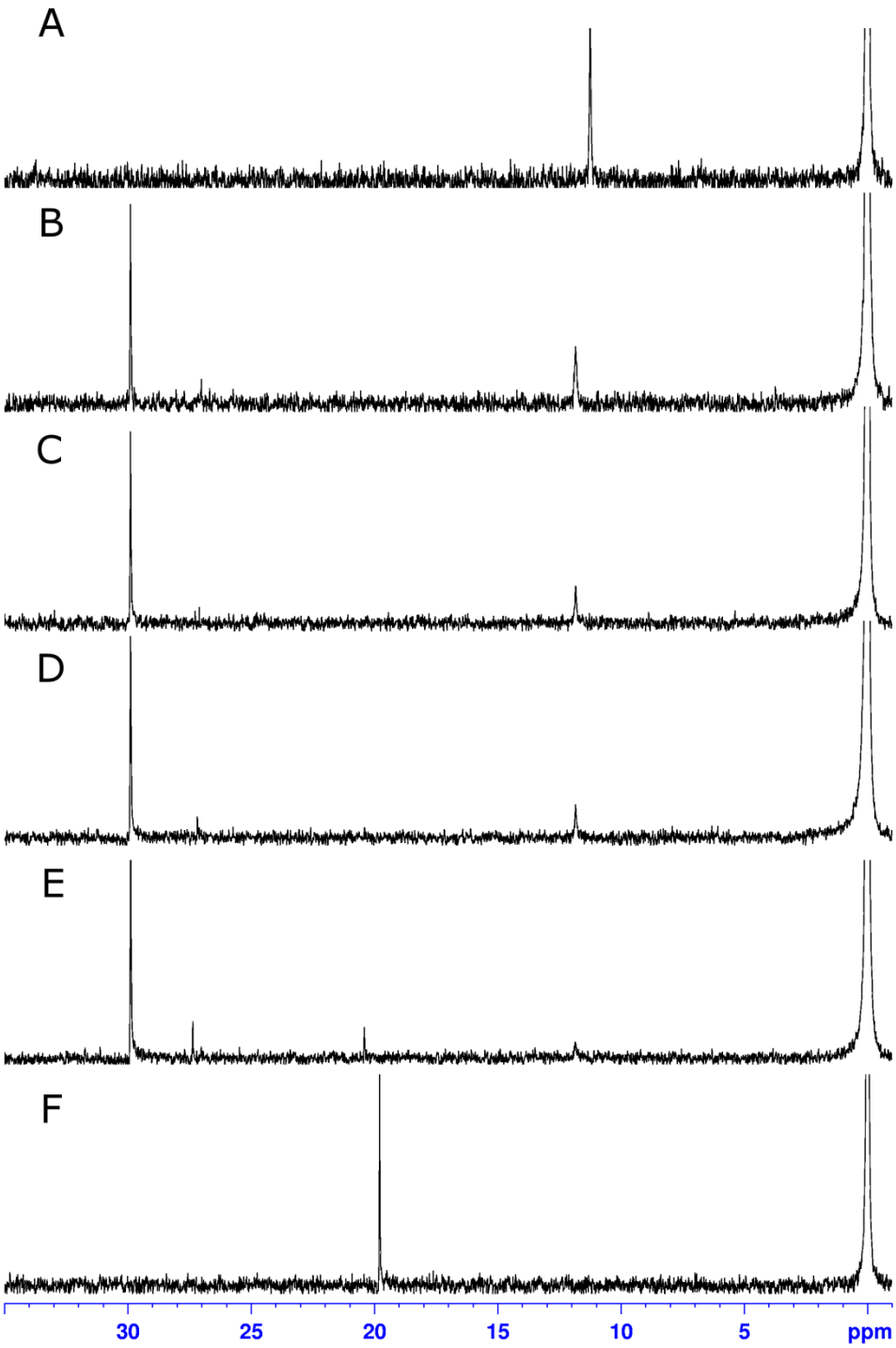

Figure E27. The PLS reaction of **60** was monitored by ^{31}P NMR spectroscopy. (A) Starting material, **60** (in $CDCl_3$), (B) after 60 mins irradiation, (C) after 90 mins irradiation in CD_3CN, (D) after 120 mins irradiation in CD_3CN, (E) after 150 mins irradiation in CD_3CN. (F) For comparison, the spectrum of **67** in $CDCl_3$ is shown. The peak at 0 ppm is the internal reference (H_3PO_4).

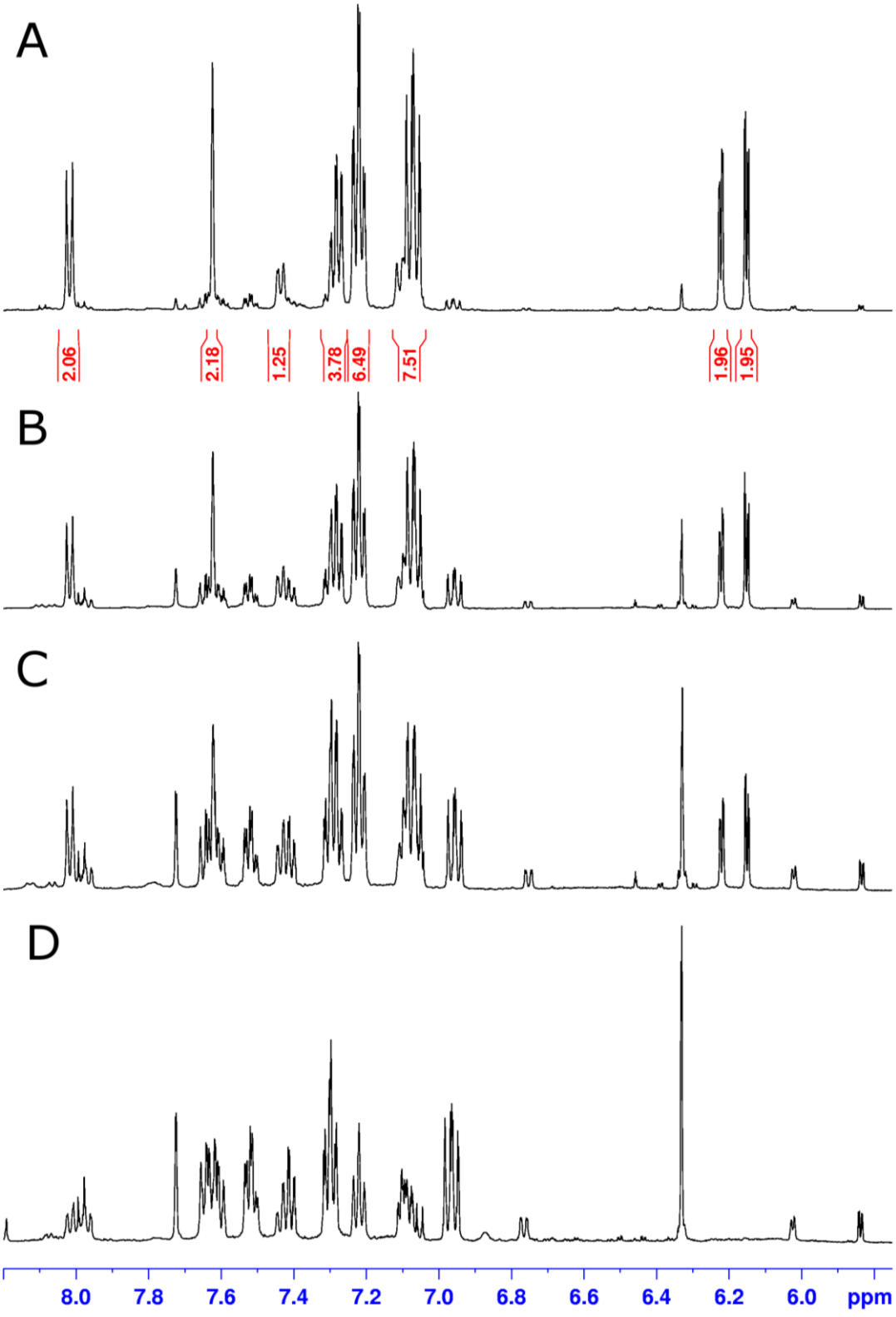

Figure E28. ^{1}H NMR evidence (CD_3CN, 25 °C) of the decomposition of **74** following its generation by the PLS reaction of **60**. (A) Proposed complex **74** (B) 1 day after the reaction; (C) 2 days after the reaction; (D) 13 days after the reaction.

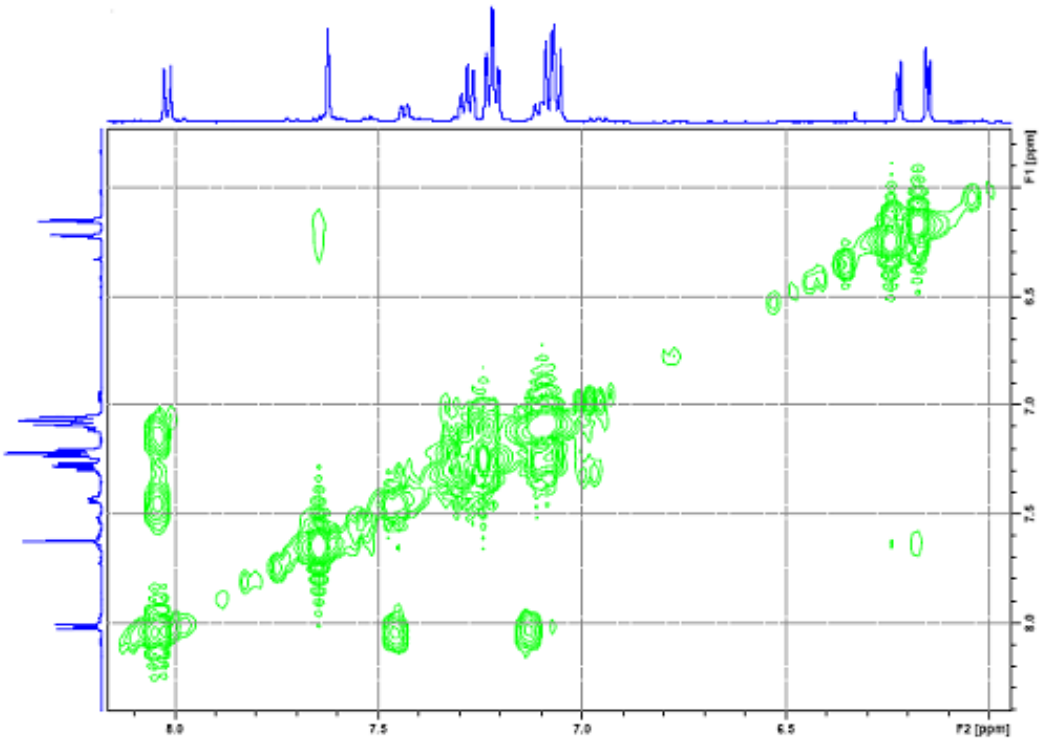

Figure E29. 2D-COSY NMR spectrum of **74** generated by irradiation of **60** with 355 nm excitation for 2 hours.

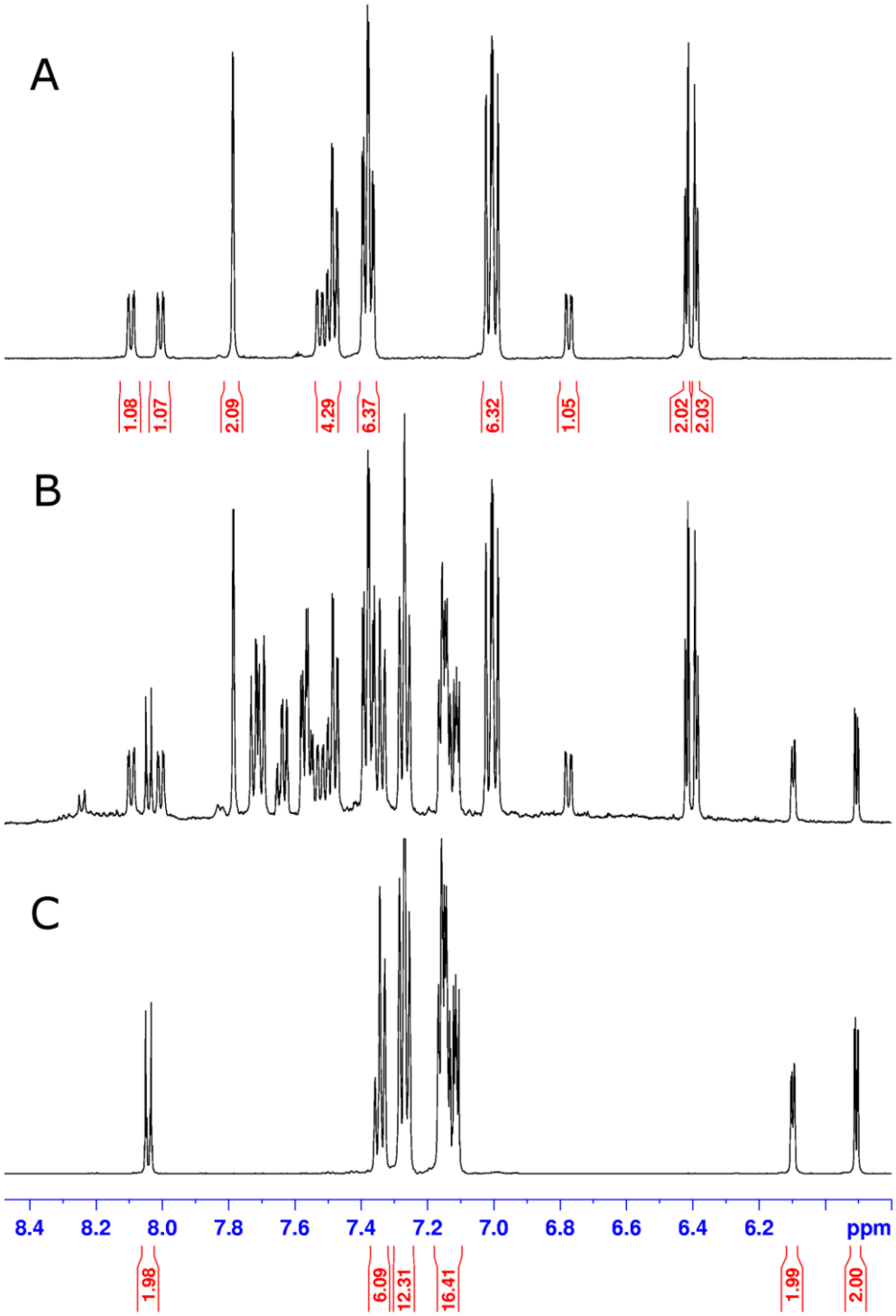

Figure E30. Aromatic region of the ^{1}H NMR spectrum ($(CD_3)_2CO$) of the PLS reaction of **60**. (A) Starting material, **60**; (B) 120 mins irradiation, (C) **67**.

Appendix F

General Experimental Details

F1 NMR spectroscopy

The first characterisation technique for the dipyrrin ligands and dipyrrinato complexes was ^{1}H NMR, followed by ^{13}C NMR. Samples were prepared in $CDCl_3$, d_6-DMSO, D_2O/NaOH, d_6-acetone or CD_3CN and spectra were recorded on 400 or 500 MHz Bruker Avance instruments utilising TOPSPIN 2.0 software. Spectra were calibrated using solvent peaks. Where appropriate COSY-^{1}H NMR were collected.

F2 Mass Spectrometry

Mass spectrometry was used to confirm the identity of all dipyrrinato complexes. Masses were obtained using either a Micromass ZMD 400 electrospray spectrometer in the appropriate mode or a Waters Micromass MALDI using a matrix system such as α-cyano-4-hydroxycinnamic acid (CHCA), retinoic acid or 2-(4'-hydroxybenzeneazo)benzoic acid (HABA) were used.

F3 Microanalysis

Microanalysis of all dipyrrinato complexes was carried out by the Campbell Microanalytical laboratory at the University of Otago.

F4 UV-Vis Absorption Spectroscopy

Solution UV-Vis spectroscopy was recorded for all dipyrrinato complexes using either a Shimadzu UV-3101PC UV-Vis-NIR-scanning spectrophotometer or a CARY 100Bio UV-Vis spectrophotometer. Either 1 cm or 0.1 cm quartz cells were utilised for measurements. Solid state absorption spectroscopy was carried out on the Ru(II)- and Rh(III)-dipyrrinato complexes at the University of Wollongong.

F5 Fluorescence spectroscopy

Emission spectra were collected for degassed CH_2Cl_2 solutions of the Re(I)-dipyrrinato complexes using FluoroMax-4 spectrofluorimeter from Horiba scientific running FluorEssence software.

F6 Infrared spectroscopy (IR)

IR spectra were recorded for all dipyrrinato complexes on a Nicolet 5700 FT-IR from Thermo Electron Corporation using an ATR attachment.

F7 Electrochemistry

Electrochemistry experiments were carried out for the Ru(II)- and Rh(III)- dipyrrinato complexes targeted as solar cell dyes. An Autolab Potentiostat Galvanostat PGSTAT30 ADC 164 with Autolab GPES software (Eco Chemie B. V. Utrecht, The Netherlands, version. 4.9) was used to for electrochemistry experiments. Solution state (staircase) cyclic voltammetry (CV) measurements were performed using a three electrode system comprised of a two platinum macro electrodes (one as the working electrode and one as the auxiliary electrode) and a silver wire (Ag/Ag^+) as a pseudo-reference electrode.

F8 Raman spectroscopy

Non-resonant Raman spectra (1064 nm) were collected at University of Otago by Dr Cushla McGoverin on powder samples and solutions in methanol, using a Bruker IFS-55 FT-interferometer bench equipped with an FRA/106 Raman accessory and utilising OPUS (version 4.0) software. A Nd : YAG laser with 1064 nm excitation wavelength was used. An InGaAs diode (D424) operating at room temperature was used to detect Raman photons. Spectra were typically measured using 256 scans at a power of 90 mW and a resolution of 4 cm^{-1}.

Resonance Raman spectra (413 nm, 444.2 nm, and 532 nm excitation at University of Otago) were collected using either a continuous-wave krypton-ion laser (413 nm) (Innova I-302, Coherent Inc.) or a solid-state 444 nm diode laser (Crystal Laser) or a solid state Nd:YAG laser (532 nm) (B & W Tec Inc.). Resonance Raman and SERS spectra (458 nm, 488 nm, 514.5 nm, and 633 nm excitation at Massey University) were collected using either a

ModuLaser Stellar-Pro argon laser (458 nm, 488 nm, and 514.5 nm) or a HeNe laser (633 nm) (ThorLabs). Raman and Rayleigh scattering light were collected from the sample cell using either a 180° backscattering geometry or 135° back-scattering geometry. Rayleigh scattering was rejected using Raman edge filters from Iridian Technologies or notch filters from Kaiser Optical Systems. The scattered photons were focused onto the entrance slit of an Acton Research SpectraPro® 2550i, 0.500 m imaging single stage monochromator/spectrograph and detected with a Roper Scientific Spec-10:100B CCD detector, controlled by WinSpec software. A combination of cyclohexane and a 50/50 v/v mix of toluene and acetonitrile (ASTM E 1840 Raman Shift Standard) were used for the frequency calibration. Frequency calibration was accurate to 0.5-1 cm^{-1}. Resolution ranged from 2 – 4 cm^{-1} depending on spectral position. Peak positions were reproducible to within 1 cm^{-1}.

Power at the sample ranged from 1 – 20 mW. Solutions for resonance Raman studies were typically prepared in dichloromethane or DMSO. Raman and Rayleigh scattering light were collected from the sample cell using either 180° back-scattering geometry or 135° back-scattering geometry. Rayleigh scattering was rejected using Raman edge filters from Iridian Technologies or notch filters from Kaiser Optical Systems. The scattered photons were focused onto the entrance slit of an Acton Research SpectraPro® 2550i, 0.500 m imaging single stage monochromator/spectrograph and detected with a Roper Scientific Spec-10:100B CCD detector controlled by WinSpec software. A combination of cyclohexane and a 50/50 v/v mix of toluene and acetonitrile (ASTM E 1840 Raman Shift Standard) were used for the frequency calibration. Frequency calibration was accurate to 0.5-1 cm^{-1}. Resolution ranged from 2 – 4 cm^{-1} depending on spectral position. Peak positions were reproducible to within 1 cm^{-1}.

F9 Solvents and reagents

Unless specified, commercial reagents and solvents (typically Sigma-Aldrich) were used without purification.